Aerodynamic and Aeroacoustic Analysis of Side-by-Side Rotor Urban Air Mobility Vehicles in Hover

By

Jared Delatorre Wakefield Sagaga

Dissertation

Submitted in partial satisfaction of the requirements for the degree of

Doctor of Philosophy

in

Mechanical and Aerospace Engineering

in the

Office of Graduate Studies

of the

University of California

Davis

Approved:

Prof. Seongkyu Lee, Chair

Prof. C.P. (Case) van Dam

Dr. Roger Strawn

Committee in Charge

2023

Abstract

Aerodynamic interactions between spinning rotor blades, rotor wake systems, and the fuselage present formidable challenges to rotorcraft designers. These interactions underpin much of the noise and aerodynamic challenges faced by such vehicles. With the emergence of urban air mobility (UAM) aircraft, especially vehicles with multiple rotors, the complexities and challenges of these interactions have increased dramatically when compared to simpler single-rotor helicopter designs. The need for quieter urban air vehicles requires an in-depth understanding of these interactions. This dissertation seeks to bridge existing knowledge gaps through the application of high-fidelity computational fluid dynamics (CFD) models combined with a high-fidelity model to predict resultant rotorcraft noise. By accurately simulating the aerodynamics and the noise generated by multi-rotor UAM aircraft, this research aims to pave the way for innovative low-noise designs that not only meet technical benchmarks but also fit seamlessly into urban settings by securing the acceptance of city dwellers.

A foundational step in this investigation is to ensure the robustness and accuracy of the employed CFD models. To achieve this, the models are meticulously validated against experimental data. A keen emphasis is placed on examining rotor-vortex interactions, especially parallel blade-vortex interactions (BVI). These BVIs are of particular interest because of their propensity to induce rapid aerodynamic changes and significant noise, which can be detrimental to the efficacy and acceptance of UAM vehicles. Progressing from this foundational step, the research delves deeper into a case study involving NASA's proposed side-by-side rotor vehicle. This study comprehensively evaluates the hovering rotor performance,

aerodynamics, and the associated noise generation under varied design scenarios, specifically considering rotor overlaps of 0%, 5%, 15%, and 25%.

Furthermore, simulations are performed for scenarios in both free-air and in proximity to the ground, reflecting the varied conditions that urban aerial vehicles might encounter. In out-of-ground situations, higher rotor overlap leads to more intense noise, primarily because of the rotor-to-rotor BVIs. However, for in-ground scenarios, lower or no overlap results in increased noise levels. This rise in noise is attributed to the interaction between the rotor and the upwash flow created by the ground, especially when the rotor is in closer proximity to the ground. This dissertation also undertakes an all-encompassing analysis of the UAM side-by-side rotor aircraft design. This involves not just the rotors, but also the fuselage and wing and its interplay with the aerodynamics and noise. Similar to the ground effect, the upwash flow from the fuselage significantly influences noise generation in scenarios with low or no overlap. The outcomes of this research shed light on the physical mechanisms behind noise generation, the directional patterns of noise propagation, and the intricacies of aerodynamic interactions.

In essence, this dissertation offers more than just a deep dive into the technical aspects. It provides invaluable insights, robust models, and guidance for engineers and designers striving to create the next generation of low-noise UAM rotorcraft, ensuring they are both effective, quiet, and amenable to urban integration.

This dissertation is dedicated to my parents,

Sopoaga Tu'utu'ulima Sagaga and Lilieni Tuialulu'u Sagaga,

for their unwavering support and encouragement throughout my academic career.

Contents

List of Figures

List of Tables

Acknowledgments

I want to express my gratitude to everyone who has helped me in this journey to earning my Ph.D. I want to first and foremost express deep gratitude to my advisor, Dr. Seongkyu Lee, for providing me the opportunity to work on research projects that are both challenging and exciting. His constant support has helped me gain confidence in myself when taking on new challenges. I have learned greatly from his extensive knowledge in various facets of rotorcraft and acoustics. Not only has it sparked my enthusiasm in rotorcraft research, but developed my expertise in those areas of research which has become an invaluable asset in my career. He always challenged me to think critically, push myself, and to try and reach my full potential in order to perform ground-breaking research. Second, I would like to thank Dr. C.P. van Dam and Dr. Roger Strawn for serving in my dissertation committee and fruitful conversations throughout my academic career.

I want to especially thank Dr. Roger Strawn during his time at the U.S. Army Technology Development Directorate (TDD) for providing me support, access to computational resources, and pursuing a career in rotorcraft research. I also would like to give thanks to experts in modeling rotorcraft aeromechanics and acoustics from TDD and the Helios Development Team that include Dr. Andrew Wissink, Dr. Buvana Jayaraman, Dr. Roget Beatrice, Dr. Jay Sitaraman, Dr. Zhongqi Henry Jia, Jain Rohit, and Mark Potsdam. I want to also thank Dr. Sicheng Kevin Li, Dr. Austin Thai, Jagdeep Batther, Nikos Trembois, and Donghun Kang for the countless conversations and advice onto my next career.

This journey would not have been possible without the support of my family, friends, colleagues, and lab mates. To my fiancée, Allie Wampler, thank you for always believing in

me especially for being by my side throughout all highs and lows from beginning to end of my PhD journey. My parents, Sopoaga and Lilieni Sagaga, I want to give them a special thank you for their never-ending love, encouragement, and support throughout my academic career.

List of Symbols

A	Rotor disk area, m^2
A_{proj}	Projected area, m^2
c	Speed of sound in the undisturbed medium, $\frac{m}{s}$
C_{tip}	Tip chord length, m
c_b	Blade chord length, m
$C_n M^2$	Nondimensional sectional normal force
c_{vg}	Vortex generator wing chord m
d	Hub separation distance, m
D	Rotor diameter, m
C_T	Thrust coefficient, $\frac{T}{\rho A R^3 \Omega^2}$
C_Q	Torque coefficient, $\frac{Q}{\rho A R^3 \Omega^2}$
FM	Figure of merit, $\frac{T_{total}}{P_{total}} \sqrt{\frac{T_{total}}{2\rho A_{proj}}}$
F_z	Sectional normal force, N/m
Γ_{v}	Vortex circulation, $\frac{m^2}{s}$
$\vec{l}$	Blade surface loading vector, N/m
$\dot{l}_r$	$\dot{l} \cdot \hat{r}$, $\frac{N}{deg \cdot m}$
l_r	$\vec{l} \cdot \hat{r}$, $\frac{N}{m}$
l_M	$\vec{l} \cdot \vec{M}$, $\frac{N}{m}$
L_{ref}	Grid unit reference length
M_{tip}	Mach number at the blade tip
$\vec{M}$	Local Mach number vector

M_r	$\vec{M} \cdot \hat{r}$
T	Thrust, N
Q	Torque, $N \cdot m$
P_{Total}	Total power, W
p'	Total acoustic pressure, Pa
p'_L	Loading noise acoustic pressure, Pa
p'_T	Thickness noise acoustic pressure, Pa
Q	Q-criterion, $\frac{1}{2}(\|\|W_{ij}\|\|^2 - \|\|S_{ij}\|\|^2), \frac{1}{s^2}$
W_{ij}	Spin-rate tensor
S_{ij}	Strain-rate tensor
r	Radial position, m
R	Rotor radius, m
Re	Reynolds Number
T_{Total}	Total thrust, N
t	Observer time, s
υ	Local fluid velocity on the blade surface, $\frac{m}{s}$
$\vec{x}$	Observer location, m
$\vec{y}$	Acoustic source location, m
V_∞	Tunnel free stream velocity, $\frac{m}{s}$
y^+	Dimensionless wall distance
ζ_{v}	Non-dimensional core size
$\frac{Z_v}{c}$	Non-dimensional vortex miss distance

Greek Symbols

λ_i	Induced inflow ratio
Ω	Rotor rotation rate, $\frac{rad}{s}$
Ψ	Azimuth angle, deg
Γ	Phase shift, deg
ρ_∞	Air density, $\frac{kg}{m^3}$
μ	Advance ratio
α_V	Vortex generator angle of attack, deg

Acronyms

BVI	Blade-vortex interaction
CFD	Computational fluid dynamics
CCW	Counterclockwise
CW	Clockwise
OASPL	Overall sound pressure level
RWTS	Rotary Wing Test Stand
SbS	SbS
SPL	Sound pressure level
UAM	Urban Air Mobility
VTOL	Vertical take-off and landing

Chapter 1

Introduction

A new era of aviation is on the horizon which will transform multiple industries, most notably (in no particular order) aerospace, defense, and transportation. The emergence of transformative aerial technology brought in by Advanced Air Mobility (AAM) with a burst of innovation is introducing new ways of transporting people and goods in both urban and rural environments [1]. AAM represents an inflection point in the ongoing evolution of the aerospace industry and a significant change in mobility as well as possibly impacting the economy on a global scale. The success of this new transportation system will rely on overcoming the critical barriers of overall safety along with the public acceptance of the noise generated by proposed modern multi-rotor civil vehicles [1–4]. In this thesis work, the Side-by-Side (SbS) rotor Urban Air Mobility (UAM) aircraft is considered as a multi-rotor configuration from a class of electric Vertical Take-off and Landing (eVTOL) or hybrid air vehicles that are a part of UAM (which is a subset of AAM) A detailed investigation on the performance, aerodynamics, and acoustics of SbS rotor UAM aircraft is performed based on high-fidelity computational methodology including a verification and validation of the approach used. This chapter presents the background and objectives of this thesis work.

1.1 Background and Motivation

This section provides a brief introduction into the background and motivation of multi-rotor UAM aircraft. A subsequent section provides a literature review related to the rise of the new emerging UAM market, including proposed conceptual designs.

1.1.1 Urban Air Mobility

In the past decade, interest in VTOL or multi-rotor air vehicles using electric powered or hybrid propulsion has been rapidly growing due to the potential to be the vehicle platform for UAM. UAM focuses on providing on-demand transportation through the air in urban and suburban areas. As a subset of AAM, UAM is the segment projected to have most economic benefit albeit the most difficult to develop. Many entities worldwide including government agencies, companies, and universities have been working on creating safe, environmentally conscious, efficient, and universally affordable UAM vehicles. This new class of aircraft could potentially make a major contribution by relieving congested ground traffic, especially in densely populated locations as well as by creating an efficient bridge between urban and suburban regions.

While these classes of air vehicles were originally designed for military purposes, they has been increasingly accessible to the civil market due to their affordability and simplicity, especially with small drones or Unmanned Aerial Vehicles (UAVs). Many have used varying scales of these multi-rotor air vehicles for recreational purposes as well as film recording, photography, etc. The initial UAM concept has as promoted early on by Uber Technologies Inc., subsequently launching a burst of VTOL companies worldwide with a large range

of UAM aircraft designs including Joby Aviation, Wisk, Archer, Lilium, EHang, etc. For this new market to be successfully sustainable, it must address and solve technical, logistical, and policy challenges that arise from a new integration into existing transportation networks. These challenges include safety, emissions, noise, performance, cost of travel, air traffic control, certification, and infrastructure [1–3]. Among these challenging hurdles in performance is battery technology, since batteries are known to have a lower energy density compared to traditional fuels for aircraft. This low energy density along with limitations on charging capacity, narrows down aircraft range which is important for convenience on a commercial level as seen in the auto industry with electric cars. Another challenge is aircraft noise which ties strongly to public acceptance. Embrace of UAM from the general public is a necessity for it to be widely implemented. In order for that to happen, there needs to be constant communication between government officials, community residents, and UAM operators. It should also be mentioned a socioeconomic impact of the UAM market, that should serve all communities including marginalized and isolated, not just the wealthy. For example, historically road infrastructure has been shown to contribute to socioeconomic and racial segregation, which is important that UAM does not end up having similar negative consequences.

A wide range of UAM aircraft have been developed, most having configurations that are unlike conventional helicopters. Although there is no simple way of generalizing across the large variety of concepts, here are some common characteristics for these UAM aircraft including distributed electric propulsion, and low noise rotor blades, to state a few [1–3]. Distributed electric propulsion is typically used for these vehicles due to low weight and low complexity of electric motors, allowing for multiple rotors to be integrated across an air-

craft. There are designs proposed by different companies such as a lift+cruise configuration which uses separate propulsion systems for vertical flight and for forward flight (cruise) [5]. Although not overlapped, there are other interesting studies about SbS rotors [6–9]. Other configurations have rotors capable of tilting when transitioning from vertical to forward flight leveraging the advantage of electric propulsion systems with a reduced complexity simplifying the mechanisms for tilting rotor nacelles or wings. However, these advantages are not without technical challenges that arise from increased unsteady aerodynamic interactions for the vehicle as a result of multiple rotors/propellers interacting with other components on an aircraft such as a rotor-to-rotor interactions or propellers installed in front of a wing. These interactions are not yet fully understood due to the breakdown, instability, and turbulent nature of the rotor wake systems. Furthermore, as UAM aircraft transition from vertical to forward flight, there will be a wide range of operating conditions with the potential for a variety of the different aerodynamic interactions. Not only will UAM aircraft have different aerodynamic characteristics compared to a conventional helicopter, it could also possibly induce different noise sources including rotor-to-rotor blade-vortex interactions, blade-wake interactions, etc.

An examination of notional VTOL aircraft optimized for lower emissions and acoustics was conducted by NASA scientists in order to study the feasibility of aircraft for UAM missions [10]. Rotorcraft designs were created with the intention of creating less than half of the climate-impacting emissions of today's fielded technology. Three aircraft size classes were developed for reduced-emissions rotorcraft concepts. The SbS rotor UAM aircraft, the subject of interest in this dissertation is classified as a class B aircraft. Figure 1.1 shows NASA's SbS rotor UAM aircraft design. The SbS rotor configuration has two main rotors

that physically overlap and intermesh, resulting in a more compact design, which makes it a suitable candidate for UAM operations. It achieves a 65% reduction in emissions while using less power compared to a conventional single main rotor helicopter [5, 10, 11]. Additionally, the SbS rotor maintains a low disk loading, and compared to a tilt-rotor configuration and also has significant improvements in cruise efficiency [10, 11]. All of the rotorcraft concept vehicles' models have some of the features and technologies that are anticipated to be found in a UAM aircraft. These features include muffling the engine and drive system to minimize noise to a level lower than the rotor system, with corresponding weight and performance penalties. Additional details of technologies for concept UAM aircraft may be found in [5].

Figure 1.1: Six-passenger SbS air taxi VTOL concept design from NASA [5]

1.1.2 UAM Aircraft Noise

Several barriers could negatively affect the success of UAM as outlined in the previous section, with noise generation as the primary issue to be addressed in this dissertation. The focus of this dissertation is on aerodynamically-induced rotor noise which is expected to be the dominant noise source for eVTOL aircraft as opposed to engine noise. Noise from UAM aircraft is not only important for certification, but also for public acceptance of this newly proposed mode of air transportation for urban operations.

Historically, conventional helicopters (most widely used and akin to eVTOL rotary wing aircraft) are required to have aircraft certification as well as community acceptance and both are important. Public acceptance for UAM operations must minimize the unwanted effects of aerodynamic noise which can trigger many public complaints. In the past, helicopter noise has been reduced through low noise design (e.g. reduction in the blade tip speed) and noise abatement measures on quietly operating aircraft. Accurate noise prediction methods and/or experimental data are required to provide insight on procedures for mitigating noise. However, many of aircraft configurations proposed for UAM are both new and unique, for which acoustic data are not available (due to it being a new platform). As a result, noise prediction methods are especially important for these new aircraft designs, even more so in the early stages of the design process with experimental data not being available. Noise prediction methods for conventional helicopters are often applied as starting points for UAM aircraft noise prediction.

1.2 Research Goals and Objectives

This section highlights the objectives of the research study in this thesis and includes a detailed description of the SbS rotor UAM aircraft.

1.2.1 NASA SbS Rotor UAM Aircraft

The objective of this investigation is to utilize high-fidelity CFD coupled with acoustics to enhance our understanding of the fundamental aerodynamics and acoustics of these multi-rotor air vehicles with an emphasis on the effects of varying amounts of overlap between

rotors. Specific goals are outlined below:

- Establish and validate a methodology to analyze the acoustics of aerodynamically interacting rotors.
- Based on the results from the high-fidelity CFD and acoustics approach, analyze the noise source mechanisms (e.g. rotor-to-rotor interactions) that include the examination of the strength and location of acoustic source(s).
- Conduct a full detailed analysis on the acoustics that include a study of the noise directivity based on the results of different overlap configurations and quantify the strength of different noise mechanisms.
- Investigate and compare the rotor performance, flow physics, aerodynamics, and acoustics for each overlap configuration as well as characterize the effect of the overlap, influence of a ground plane at different rotor heights, and presence of a fuselage.
- Perform a validation study of a canonical case with the same methodology used in the SbS rotor UAM aircraft studies.

Completion of these goals can help provide answers to three essential questions as it pertains to UAM. These questions are important to consider as it relates to contributions from the studies performed for this thesis work:

- Can we accurately model complex problems like blade-vortex interactions (BVI) using current state-of-the-art CFD/acoustics technology?
- Can current state-of-the-art analyses be used to make informed design decisions regarding rotorcraft performance and noise?

- Are there fundamental physical insights that can be gained from this thesis work that can help future UAM vehicle designers?

1.3 Outline of Thesis

This dissertation is composed of seven chapters that summarize a number of the author's previously published technical papers. Chapter 1 first discusses the background and motivation on the research studies of the SbS rotor UAM aircraft. It also outlines the scope of this thesis work including objectives and specific goals. Chapter 2 provides a brief background on the principals of rotorcraft acoustics and then it describes the aeroacoustic formulations used in this dissertation. Chapter 3 discusses the computational tools used in this thesis work including Helios, a multi-disciplinary and high-fidelity rotorcraft simulation software suite, and PSU-WOPWOP, an acoustics prediction tool. Chapter 4 presents the properties of the SbS rotor UAM aircraft including the aircraft model, CFD mesh, and numerical setup. Chapter 5 discusses validation of the computational tools through comparisons with an idealized parallel BVI wind tunnel experiment. A description of the simulation is provided followed by results from the validation study. Comparison of the acoustic predictions and experiment data are presented for a number of the experimental test cases. At the end of the chapter, discussion is provided on the effect of the numerical parameters on the acoustic predictions. Chapter 6 discusses the performance, aerodynamics, and acoustic simulation results of the NASA SbS rotor UAM aircraft, a six-passenger multi-rotor configuration based on high-fidelity CFD simulations coupled with acoustics. Comparisons of the UAM aircraft noise against a single isolated rotor and various background noise levels are shown. Chap-

ter 7 provides details on the study of ground effect and its impact on rotor performance, aerodynamics, acoustics including the directivity with comparisons to the isolated SbS rotors in free-air. Chapter 8 presents the investigation on the presence of the fuselage on performance where the presence of the fuselage causes increased aerodynamics interactions, acoustic intensity, and interactional aerodynamics as a function of different overlaps. Chapter 9 summarizes the studies presented in this dissertation including contributions to the field as well as recommendations for future work.

Chapter 2

Aeroacoustic Theory and Formulations

The fundamental theories and formulations for rotorcraft acoustic predictions are discussed and reviewed in this chapter. The chapter briefly covers the formulations developed by Lighthill, Ffowcs Williams, Hawkings, and Farassat, which are implemented in many acoustic prediction models.

2.1 Lighthill's Acoustics Analogy

Applied mathematician, Sir Michael James Lighthill, is known for his pioneering work in the field of aeroacoustics. He is often regarded by many in the field as the father of aeroacoustics. His work on acoustic theories of sound generated from turbulence known as Lighthill's acoustic analogy explains the origins and propagation of aerodynamically induced noise. Lighthill's acoustic analogy was derived by rearranging the governing equations of fluid mechanics: conservation of mass and momentum, into an in-homogeneous wave equation. As derived, Lighthill's acoustic analogy is used to model sound generation and propagation from turbulent flows or noise radiating from a distribution of equivalent sources in a stationary

medium, such as jet noise.

2.1.1 The Ffowcs Williams – Hawkings Equation

The original formulation of Lighthill's acoustic analogy could not be used in noise prediction of moving surfaces (e.g. rotor blade). Ffowcs Williams and Hawkings extended Lighthill's acoustic analogy by adding the capability to compute sound generated by moving solid surfaces of any geometry. This extension by Ffowcs Williams and Hawkings is commonly referred to as the Ffowcs Williams – Hawkings (FW-H) equation [12] as shown in Eq. 2.1.

$$\begin{aligned} \bar{\Box}^2 p'(\vec{x},t) = \frac{\partial}{\partial t}\left\{\left[\rho_o \upsilon_n\right]\delta(f)\right\} - \\ \frac{\partial}{\partial t}\left\{\left[P_{ij}\hat{n}_j + \rho u_i(u_n - \upsilon_n)\right]\delta(f)\right\} + \\ \frac{\bar{\partial}^2}{\partial x_i \partial x_j}\left[T_{ij}H(f)\right] \end{aligned} \tag{2.1}$$

The left hand side of Eq. 2.1 represents the wave operator and the right hand side is where the sound source terms reside. The source terms (right hand side of Eq. 2.1) are known as the monopole, dipole, and quadropole terms respectively. The monopole term is often labeled as the thickness term and the dipole term is often labeled as the loading term when acoustic source data surface, f, coincides with the actual surface. The $\bar{\Box}^2$ is the d'Alembert operator which can be expressed in its mathematical form as $(1/c^2)(\frac{\partial^2}{\partial t^2}) - \bar{\nabla}^2$ (where c is the speed of sound and the Laplace operator is denoted as $\bar{\nabla}^2$); p' is the acoustic pressure (this is the difference between the fluid pressure p and ambient pressure p_o); ρ_o is the fluid density of an undisturbed medium; υ_n is the normal component of the velocity of a surface at $f = 0$; the Dirac delta function is denoted as $\delta(f)$, which is zero ubiquitously

except when $f = 0$. P_{ij} is the compressive stress tensor; ρ is for fluid density; u_n is the normal component of the fluid velocity on the surface $f = 0$. T_{ij} is the Lighthill's stress tensor where $T_{ij} = \rho u_i u_j + P_{ij} - c^2(\rho - \rho_o)\delta_{ij}$; $H(f)$ is the Heavyside function, where $H(f) = 1$ where $f > 0$ and $H(f) = 0$ where $f < 0$. As seen in monopole and dipole source terms of Eq. 2.1, the Dirac delta function implies that only information from a surface is needed for computation. However, the Heaviside step function, which is present in the quadropole source term, implies information from a volume source outside of a surface where $f > 0$. For many rotorcraft acoustic predictions, the nonlinear quadropole source term is often neglected in low-speed flow regimes where speed of sound shows little variation throughout the flowfield. This low-speed assumption is valid for the cases studied in this thesis where the rotor tip speeds remain below $M_{tip} = 0.8$.

2.2 Farassat Formulation 1A

The Farassat Formulation 1A (FF1A) [13, 14], derived by Farassat using the free space Green's function of the wave equation, is an integral solution of the Ffowcs Williams – Hawkings equation. There are other solutions that can be obtained for the FW-H equation, however, FF1A provides simplicity and not requiring the observer time derivatives of integrals, making it an obvious choice for rotorcraft acoustic predictions in the subsonic flow regime.

As mentioned earlier, the quadropole source term from the FW-H equation is often neglected in many rotorcraft acoustic predictions and, Farassat's Formulation 1A neglects this quadropole term as well. As a result, the FF1A equation consists of the thickness

(Eq. 2.3) and loading (Eq. 2.4) terms from Eq. 2.2. The thickness and loading terms are decomposed into the far field ($\frac{1}{r}$) and near field ($\frac{1}{r^2}$) terms as shown in the right hand side of equations 2.3 and 2.4. Detailed derivations of equations 2.3 and 2.4 are given in [13].

$$p'(\vec{x},t) = p'_T(\vec{x},t) + p'_L(\vec{x},t) \tag{2.2}$$

$$\begin{aligned} 4\pi p'_T(\vec{x},t) = &\int_{f=0} \left[\frac{\rho_\infty \left(\dot{\upsilon}_n + \upsilon_{\dot{n}}\right)}{r\left(1-M_r\right)^2} \right]_{ret} dS \\ + &\int_{f=0} \left[\frac{\rho_\infty \upsilon_n \left(r\dot{M}_r + c\left(M_r - M^2\right)\right)}{r^2\left(1-M_r\right)^3} \right]_{ret} dS \end{aligned} \tag{2.3}$$

$$\begin{aligned} 4\pi p'_L(\vec{x},t) = &\frac{1}{c}\int_{f=0} \left[\frac{\dot{l}_r}{r\left(1-M_r\right)^2} \right]_{ret} dS \\ &+ \int_{f=0} \left[\frac{l_r - l_M}{r^2\left(1-M_r\right)^2} \right]_{ret} dS \\ + &\frac{1}{c}\int_{f=0} \left[\frac{l_r \left(r\dot{M}_r + c\left(M_r + M^2\right)\right)}{r^2\left(1-M_r\right)^3} \right]_{ret} dS \end{aligned} \tag{2.4}$$

In Eq. 2.2, the total acoustic pressure, denoted as p' consists of components that are thickness (p'_T) and loading (p'_L) terms as seen in the right hand side. ρ_∞ is the density of freestream; c is the speed of sound; r is the distance between the source and observer; $\dot{\upsilon}_n$ and $\upsilon_{\dot{n}}$ is the rate of change in the blade velocity in the normal direction and the inner product of the velocity vector and the source time derivative of the normal vector, respectively; M_r is the Mach number of the blade surface in the radiation direction toward the observer. l_r is the loading on the surface of the blade in the radiation direction; $\dot{l}_r$ is the rate of the change in the blade loading with respect to the change of time of noise emission (also known as "retarded" time) in the radiation direction.

In Farassat's Formulation 1A, it is important to note that the magnitude of the acoustic pressure is significantly influenced by two key terms:

- Doppler amplification factor, $\frac{1}{|1-M_r|}$.
- The sudden change within the airloads in the radiation vector with respect to the retarded time, $\dot{l}_r$.

The Doppler amplification factor depends on both the unit radiation vector ($\hat{r}$) and the magnitude of the blade surface Mach number (M). However, the second term is more important regarding impulsive loading due to interactional aerodynamics such as BVI as it becomes significant at the onset of BVI events. This can lead to the $\dot{l}_r$ term having a large magnitude resulting in impulsive loading noise. As mentioned earlier, the quadrupole source term is neglected when the advancing blade tip Mach number in the simulations remains below 0.8 or 0.9, and the speed of sound shows little variation throughout the computational domain as discussed in reference [15].

2.3 Rotorcraft Noise Sources

This sections provides a brief overview of rotor noise sources including a discussion of noise characteristics, the underlying physical mechanisms responsible for the noise, and noise prediction methods.

2.3.1 Discrete Frequency Noise

The complicated operating environment of a rotorcraft contributes to both discrete frequency (also referred to as tonal noise) and broadband aerodynamic noise generation and both of these types of noise can arise from multiple noise generation mechanisms. Discrete frequency noise is associated with the blade passing frequency (BPF) and its harmonics and can be divided into the deterministic components of thickness and loading noise, blade-vortex interaction noise (part of loading noise), and high-speed impulsive noise (quadrupole noise). Broadband noise sources arises from aerodynamic sources such as turbulence, blade self-noise, and blade-wake interaction noise. However, discrete frequency noise as calculated by the FW-H equation or Farassat's Formulation 1A is typically the largest component of rotorcraft community noise annoyance and, as such, it remains the primary focus of study in this dissertation.

Rotors or rotary-wings are used as a primary means of lift production with the capability to take-off and land vertically allowing a rotorcraft to fly virtually in any direction. However, this flexibility also comes with a cost. Compared to a fixed wing aircraft, the helicopter, requires more flight training, generates higher vibrations, produces more noise, suffers from more complex aeromechanical effects, and is slower in forward flight.

This additional aerodynamic complexity of a rotorcraft makes it more difficult to analyze and design than its fixed-wing counterpart. These aerodynamic complexities result from the interactions between the rotor blades, the rotor wake systems and the fuselage. In addition, rotors in forward flight often experience dynamic stall, interactions between the hub and upwash or rotor wake, and blade-vortex interactions. These interactional aerodynamics effects,

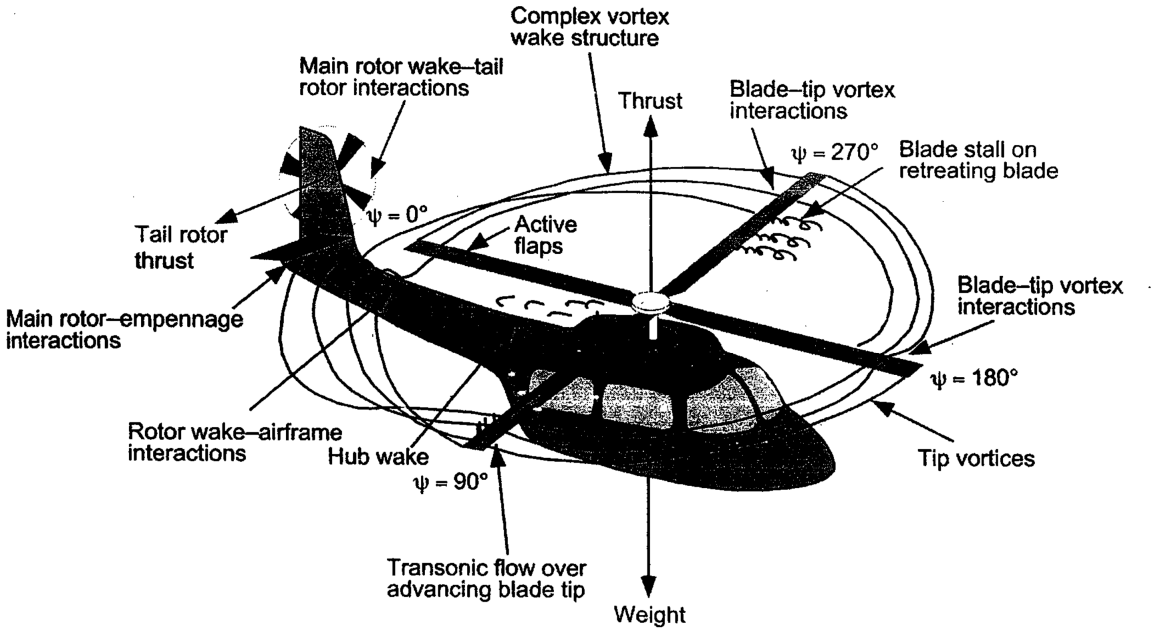

Figure 2.1: A schematic depicting flow structure including complex problems for a helicopter in forward flight [16].

along with unsteady blade loading, act as significant noise sources during the operation of a conventional rotorcraft as shown in Figure 2.1.

Other than flow noise or aerodynamics interaction noise being an external source of noise for rotorcraft, mechanical vibrations and engine or motor also contribute as noise sources. However, the dominant noise source comes mainly from aerodynamically induced noise or interactional aerodynamics. These dominant interactional aerodynamics sources originate primarily from the rotor blades and their interactions with surrounding air. Other components of a rotorcraft may also contribute to the overall noise, however, the most significant rotorcraft noise generation mechanisms result from the displacement of air by the moving rotor blades along with blade loading changes due to interactions between the rotor and its wake system. These two aerodynamic noise sources correspond to the "thickness" and "loading" noise terms in Farrassat's Formulation 1A and they play a large role in the

acceptance from the community regarding the success of UAM operations.

Aerodynamic noise sources from rotorcraft can also be characterized as either tonal noise and broadband noise. Tonal noise is typically associated with harmonics of the blade passing frequency. Broadband noise tends to have much higher frequencies and typically arises from aerodynamic turbulence in the surrounding air. As a result, the noise generated from rotor blades due to blade-vortex interaction(s) is considered to be tonal noise and the noise generated from the interaction between rotor blade and small scale turbulence in the rotor wake also known as blade-wake interaction (BWI) is considered to be broadband noise.

Tonal noise can be decomposed into several parts: thickness noise, loading noise, blade-vortex interaction noise, and high-speed impulsive noise. However, UAM rotorcraft typically operate without the transonic flow conditions that are required to produce high-speed impulsive noise. It occurs when the blade tip Mach number results in transonic flow, which is not the case for UAM aircraft as it operates in subsonic conditions. On the contrary, broadband noise consists of loading noise sources like blade self-noise and blade-wake interaction noise, which are non-deterministic. An example of how these noise sources for a conventional helicopter are shown in Figure 2.2 comparing one another.

Thickness and loading noise, two components of tonal noise are described by linear aerodynamic theory where the cause of thickness noise is from the displacement of the fluid due to the rotor blade and loading noise is caused by the accelerated force due to the moving surface of a rotor blade. As seen in Figure 2.2, loading noise is dominant at low frequencies including high impulsive loading noise such as blade-vortex interaction. As per the cause of loading noise, either steady or unsteady accelerated forces generated by a moving blade surface contributes to the generation of loading noise. Given that a rotorcraft operates in

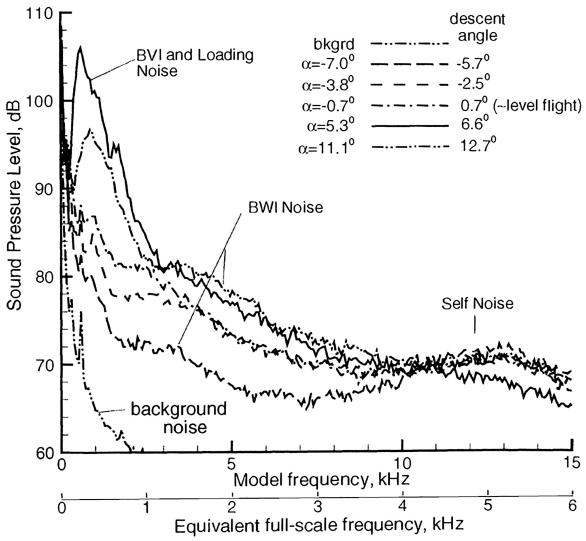

Figure 2.2: Schematic of a sound pressure level spectrum for a four bladed hingeless rotor of a 40% scale experimental model of the BO-105 helicopter [17].

an environment with a complicated flow field, it is more often or naturally inherent that unsteady aerodynamics occur in this operating environment. With blade-vortex interactions being more dominant at low frequencies contributing to loading noise and also a more dominant noise source during the operation of a rotorcraft, it is obvious what needs to be addressed for the success of UAM operations. Knowing this, it can become more compelling to address this issue when dealing with multi-rotor configurations. There is a possibility of multiple new sources of noise such as rotor-to-rotor blade-vortex interactions. Blade-vortex interactions exist in all flight operating conditions of a rotorcraft. However, the significance of the noise depend on several parameters including distance between the shedding tip vortex of the preceding rotor blade and the following blade, tip vortex strength, position of the shedding tip vortex relative to the following rotor blade or the interaction angle, and blade tip Mach number. The significance of the noise generated during a blade-vortex interaction event becomes evident when the shedding tip vortex is positioned parallel with the following blade.

For broadband noise, as mentioned earlier, self-noise (e.g. trailing edge noise) and blade-wake interaction are two non-deterministic loading noise sources. With varying multi-rotor configurations in the UAM space, broadband noise becomes more and more prominent as the total number of rotors increase. As shown by Zawodny et al. [18] and Intaratep et al. [19] broadband noise increases significantly from a single rotor to multi-rotors. In the present work for the SbS rotor UAM aircraft, only tonal noise is considered in the acoustic predictions. Begault [20] showed it is likely that broadband noise from UAM aircraft to be concealed from background noise (e.g. street noise) at low frequencies. However, at mid to high frequencies, this might not be the case.

2.3.2 Rotorcraft Noise Directivity

Figure 2.3 shows a typical pattern of the different types of rotorcraft noise discussed in the previous section, Section 2.3.1. As shown in the Figure 2.3, loading and broadband noise tend to direct noise in the downward direction below the rotor disk plane, thickness and high-speed impulsive noise propagate in a forward directivity which also increases in intensity with flight speed, and then blade-vortex interactions are directed in a conical region out of the rotor disk plane. Loading noise is generally more dominant in the downward direction from the rotor disk plane or in a conical region especially for BVI noise (e.g. elevation angles of 30° to 45°) whereas thickness noise is mostly in the rotor disk plane. The importance of each noise source may vary depending on the operation of the rotorcraft in both civilian and military operations. For example, in a military operation scenario, thickness or high-speed impulsive noise could be problematic for detection. UAM operations in a populated

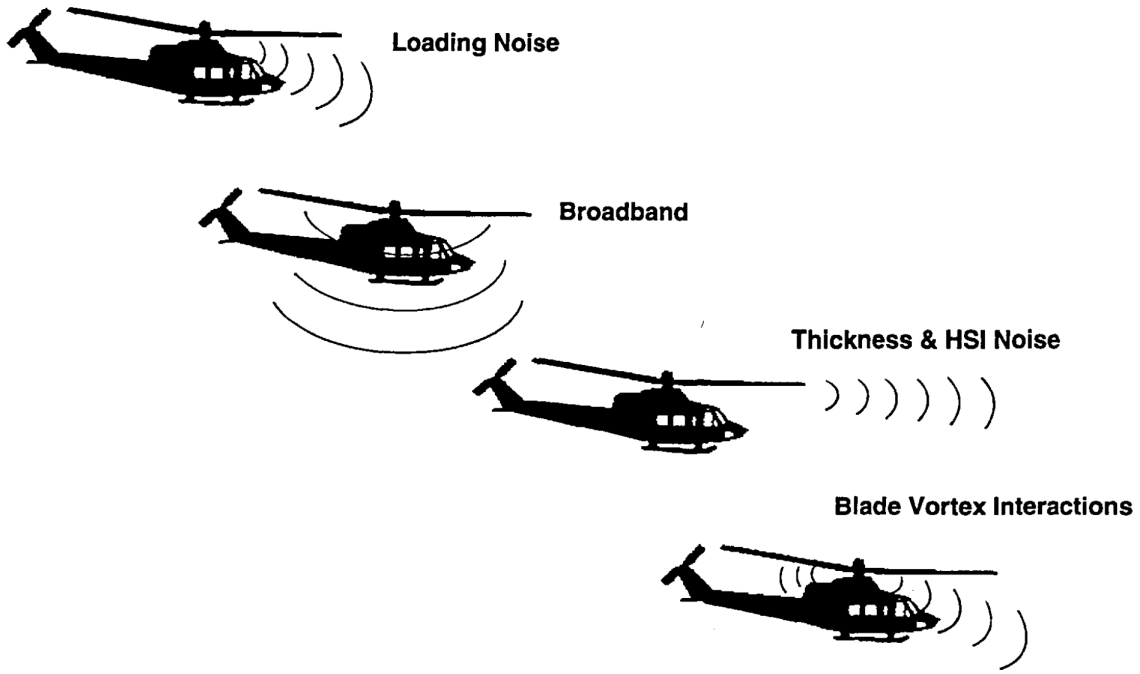

Figure 2.3: A depiction of typical noise directivity [21].

operating environment would cause a concern about downward noise directivity. Different solutions for various operating conditions are being proposed to incorporate modified flight path maneuvers, etc.

Chapter 3

Computational Methodology

This chapter presents details of the methodology used in the studies of the SbS rotor UAM aircraft and the parallel BVI validation study.

3.1 Computational Fluid Dynamics (CFD)

3.1.1 Helios

Helios (**HELI**copter **O**verset **S**imulations) is a high-fidelity and multidisciplinary rotorcraft modeling software suite. It is developed under the U.S. DoD Computational Research Engineering Acquisition Tools and Environments - Air Vehicles (CREATE-AV)^{TM} program and sponsored by the DoD HPC Modernization Program (HPCMP) Office and the US Army [22]. The CFD simulations of this dissertation as mentioned are performed using Helios. It supports a variety of solvers within its overset grid framework which includes interfaces to different types of software modules – near-body CFD solver, off-body CFD solver, structural dynamics, visualization, fluid-structure interface, etc. as seen in Figure 3.1. Colored in red are the main components of Helios' framework, colored in green are native modules (e.g. CFD/CSD codes) within Helios, and colored in blue consists of computational codes (e.g.

CFD, CSD, etc.) that are developed and maintained by external groups. Helios uses a dual mesh methodology, as seen in Figure 3.2, where the near-body solver(s) captures the viscous flow around a complex geometry, and the off-body solver resolves the wake by utilizing a combination of high-order algorithms and adaptive mesh refinement (AMR) [22]. These meshes from the near- and off-body form an overset mesh system with the domain connectivity that is fully automated and supported by PUNDIT (Parallel Unsteady Domain Information Transfer). PUNDIT manages the parallel overset mesh communication including possible relative motion between two mesh systems. Besides controlling the data transfer between the two mesh domains, it also performs the hole cutting and solution interpolation between the near- and off-body grids. It identifies a donor cell of each fringe point for interpolating the solution using a weighted function in the overlapped mesh regions. The near-body solvers currently supported in Helios include mStrand [23], Helios' native structured/unstructured solver, OVERFLOW [24], a high-order structured solver from NASA, FUN3D [25], NASA's unstructured solver, and CREATE^{TM}-AV's Kestrel unstructured solver, KCFD [23].

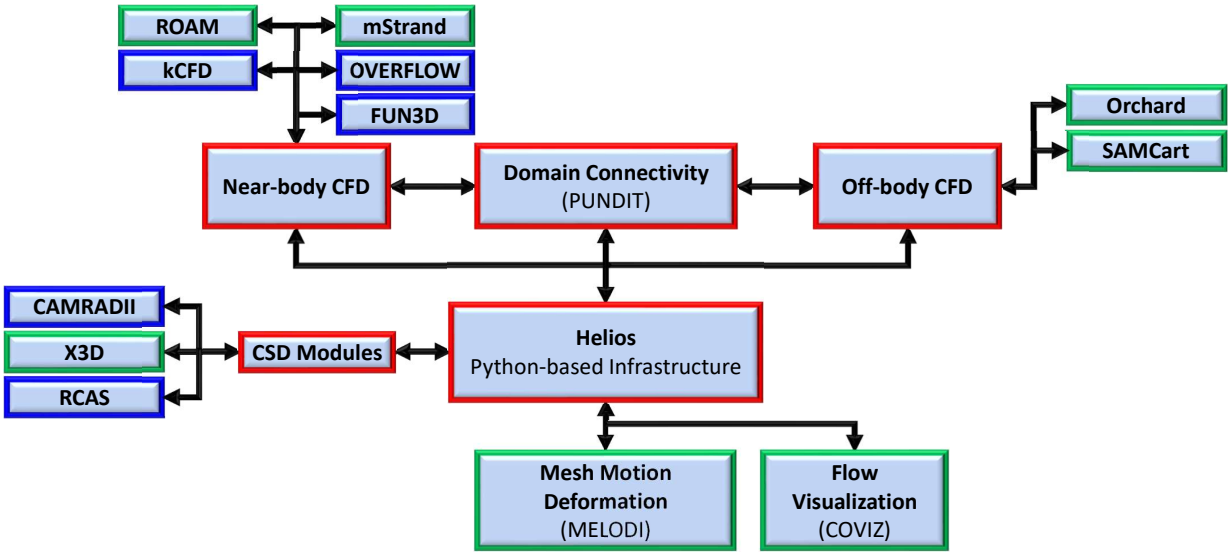

Figure 3.1: Software architecture of Helios.

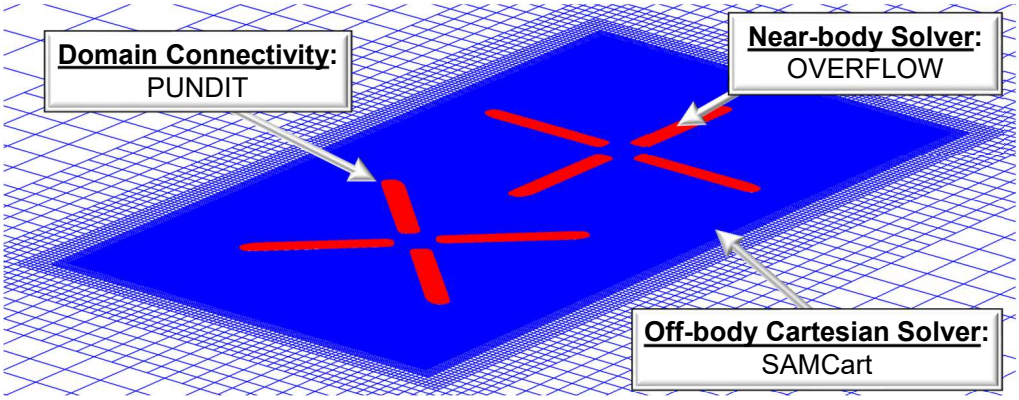

Figure 3.2: Dual paradigm methodology used in Helios.

Another module in Helios handles the mesh motion interface, Melodi (**ME**sh motion **LO**ading and **D**eformation **I**nterface), that provides support for aeroelastic motion with complex body dynamics. The Melodi module supports a generic hierarchical definition of the bodies and relative motions. It constructs a model of the problem using two basic entities, bodies and frames. Bodies are physical components associated with a body-conforming mesh, to which deformations can be applied. Frames are orthonormal triads, used as a tool for specifying the relative rigid motions of bodies. The model hierarchy is constructed successfully adding child nodes (e.g. frames, bodies, etc.), which inherent parent frame motions and coordinate system transformations. As example of how this hierarchy functions, starting from the top, a global CFD inertial frame is initially defined in Melodi. For the simulation of a rotor, a staionary rotor frame is defined under the global CFD frame, followed by a rotating frame with a rotation rate which is a child node of preceding stationary rotor frame. The rotor blade surfaces are then added under the rotating frame as a child node. Each body has a mesh frame associated with the mesh coordinates and a body frame associated with the blade motion. This blade motion can either be based on a mathematical expression or prescribed motion. Moreover, the blade motions and deformations can also be acquired

via CFD and CSD loose coupling approach in which the calculated airloads (from CFD near-body solver) are coupled with CSD airloads obtained using a rotorcraft comprehensive analysis code. However, this thesis work does not employ this approach.

3.1.1.1 Near-body Solver

In this section, a brief description of the CFD solvers, OVERFLOW and mStrand, both used throughout this dissertation work are provided. OVERFLOW is a three-dimensional, structured overset and curvilinear grid flow solver developed and maintained by NASA which is part of the first component of Helios' dual mesh paradigm. It is a node-centered, finite difference unsteady Reynolds-Averaged Navier-Stokes solver. The dissertation work uses a central difference spatial schemes of up to 5^{th} order accuracy with scalar dissipation. Time-accurate calculations employ a 2^{nd} order optimized backwards Euler time stepping scheme along with dual-time stepping subiterations.

The internal structured/unstructured near-body solver in Helios, mStrand, is a specialized strand grid solver that uses a vertex-centered finite-volume spatial discretization. It can accommodate both quadrilateral or triangular surface elements and handles general prismatic meshes in the normal direction. It currently uses a second-order gradient-based discretization in the streamwise direction and a limiter-based second-order discretization in the normal direction. The solver incorporates a second-order implementation of the full Navier-Stokes for the viscous terms and the Spalart-Allmaras turbulence model with first order discretization while the Roe approximate Riemann solver is used for the inviscid conservative fluxes. It solves the Reynolds-averaged Navier-Stokes equations in a general moving coordinate system in three dimensions.

3.1.1.2 Off-body Solver

This section provides background on the solver used in the off-body, SAMCart, a high-order and block-structured Cartesian grid solver with AMR capability. AMR allows for SAMCart to automatically refine the grids locally within the rotor wake region capturing essential flow features such as blade tip vortices. The off-body domain is generated based on a hierarchy scheme of nested Cartesian mesh refinement levels in which the finest level oversets the outer boundaries of the near-body mesh whereas the coarsest level is located in the far-field boundaries of the off-body domain. Uniform grid spacing between the refinement levels are refined or coarsened by a factor of two with each level.

3.2 Acoustics Simulation

This section briefly discusses the tool used to perform acoustic simulations for rotorcraft noise predictions.

3.2.0.1 PSU-WOPWOP

PSU-WOPWOP [26–28], is an advanced rotorcraft noise simulation software that is used in this thesis work to perform acoustic predictions. Farassat's Formulation 1A of the FW-H equation is numerically implemented in PSU-WOPWOP. PSU-WOPWOP can be coupled with other computational codes including CFD solvers (e.g. OVERFLOW) and rotorcraft comprehensive analysis codes (e.g. RCAS, CAMRADII, etc.). Existing capabilities include:

- Rotorcraft acoustic predictions of varying operating conditions such as foward flight, manuvering flight, and hover based on the observer time algorithm ($t = \tau + r(t, \tau)/c$).

- Coupling with various unstructured/structured CFD solvers (e.g. OVERFLOW, mStrand, etc.) and comprehensive rotorcraft analysis codes (e.g. CAMRADII, RCAS, etc.).

- Computation of rotorcraft noise at multiple observers (e.g. hemispherical grid, rectangular grid, etc.) in parallel mode.

- Transformation of geometry coordinates and performing a change of body motion.

- Simulate acoustic reflections for in-ground effect creating a mirrored image of solid surface bodies below the ground plane using an image source method.

- Calculations of permeable and impermeable surfaces. Permeable surface approach considers the noise sources on a permeable surface away from moving blade surfaces whereas impermeable surface approach considers all noise sources at the hard surfaces of the rotor blades. This dissertation only uses the impermeable surface approach.

- Having an effective acoustics post-processing tool facilitates understanding of the noise sources and PSU-WOPWOP provides a "sigma surface," for debugging simulation issues and identification of noise sources. The sigma surface shows the blade surface quantities (e.g. thickness and loading noise source terms) at the time of emission and it can be visualized as an iso-surface for a given observer/source time as seen in Figure 3.3.

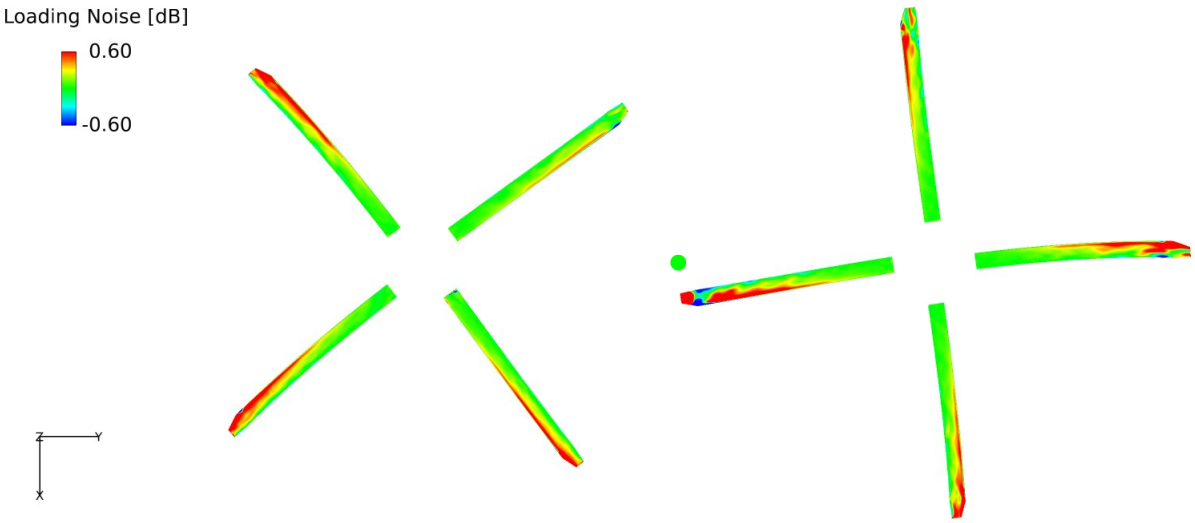

Figure 3.3: Sigma surface of the 0% overlap configuration at the 90° elevation angle and colored by the loading noise generated from the acoustic simulations.

Chapter 4

NASA Urban Air Mobility Aircraft

This chapter presents details of the SbS rotor UAM aircraft including the cases studied for the different rotor overlap configurations considered.

4.1 Multirotor Configurations

The design space for UAM VTOL aircraft is vast and offers many unexplored possibilities, unlike conventional helicopters that rely on a single main rotor and a tail rotor. With countless variations for UAM vehicles proposed including potential designs, NASA released a list of configurations to serve as reference UAM vehicles that demonstrate specific vehicle attributes that are representative of those proposed across the UAM community. However, these NASA notional designs are not proprietary to any private company which facilitates the sharing of independent analyses for the various designs. Typically, all of these NASA VTOL aircraft designs feature multiple rotors, making it crucial to consider multi-rotor interactional aerodynamics in their analysis.

Early studies on UAM aircraft designs using high-fidelity CFD simulations primarily focused on forward flight conditions, leaving hover performance relatively unexplored. How-

ever, hover performance is a critical aspect of rotorcraft operation and an essential component in rotorcraft design [29–31]. Significant advancements in helicopter hover performance predictions have been made recently through AIAA's S-76 helicopter hover prediction workshops [29]. These studies, which included direct comparisons with measurement data, demonstrated the maturity of high-end computational simulations in predicting hover performance for single rotor systems. Recent research on multi-rotor hover performance conducted by Healy et al. [32] for SbS rotors (no overlap) revealed that turbulent mixing between the rotors, caused by wakes from each rotor, leads to penalties on the thrust in the outboard sections as they pass over the inter-rotor region. Smith et al. [33] on the acoustics of SbS rotors (no overlap) in hover conditions found that strong interactions between the rotors result in a significant increase in noise due to the unsteadiness of loading. Rotor interaction effects become more prominent as the separation distance between the rotors is reduced, leading to adverse effects on rotor performance and increased noise levels due to unsteady loading, as found in a study of a small-scale multirotor configuration by Lee and Lee [6]. Zhou et al. [7] conducted an experimental investigation of rotor-to-rotor interactions of small-scale propellers for an Unmanned Aerial Vehicle (UAV). They found that the separation distance between the rotors had minimal effect on the thrust coefficient, except for an increase in thrust fluctuations as the separation distance decreased. A wind tunnel experiment carried out by Dingeldein [8] compared the power requirements of a coaxial rotor system to a tandem rotor system (same plane and no rotor overlap). The tandem arrangement demonstrated an improvement in hover efficiency, likely due to a reduction in induced power. Additionally, an experimental investigation by Dekker et al. [9] on SbS rotors without any rotor overlap in proximity to a ground plane found an increase in induced velocity with rotors spaced tip-

to-tip. They also observed that the formation of a fountaining flow, which is a component of upwash due to the presence of the ground (a similar effect provided by a fuselage), increased as the separation distance between the rotors widened.

4.2 Reference Vehicle Model: SbS Rotor

A series of studies on the conceptual design of UAM aircraft were conducted by Johnson et al. [5, 34, 35], exploring lift+cruise VTOL, quadrotor, and SbS rotor configurations. Among these, the SbS rotor configuration, as depicted in Figure 4.1, is anticipated to be the lightest vehicle with the lowest fuel consumption, although it would be slower than other conceptual vehicles [11]. Ventura Diaz et al. [36–38] performed high-fidelity CFD using OVERFLOW [24] loosely coupled with a Computational Structural Dynamics (CSD) comprehensive analysis code, CAMRAD II, on NASA's six-passenger SbS hybrid VTOL configuration (rotors and fuselage) in forward flight. Their results indicated that the percentage of the overlap region is a key parameter for rotor airloads and cruise performance. They found that the 15% overlap configuration yielded the best lift-to-drag ratio. Jia and Lee [4, 39] investigated NASA's quadrotor and SbS rotor concept design studies, focusing not only on aerodynamic performance predictions but also on acoustic predictions in forward flight conditions. Their findings revealed that blade vortex interaction (BVI) events generate significant noise. For instance, in the SbS rotor study, increasing the overlap region considerably amplified rotor-to-rotor BVI noise. They also examined the effect of the finest grid spacing (5% C_{tip} and 10% C_{tip}, where C_{tip} denotes the blade tip chord length) in the refinement off-body region on aerodynamic and acoustic predictions, determining that 10%

Figure 4.1: Six-passenger SbS air taxi VTOL concept design from NASA [34].

C_{tip} is sufficient to capture BVI noise. These initial studies on various UAM aircraft noise focused solely on forward flight conditions. However, noise can also be significant in hover, which is particularly important for UAM operations due to the close proximity to people on the ground. For example, Li and Lee [40] used UCD-Quietfly to predict rotor trailing-edge noise [41] and highlighted the importance of broadband noise for the SbS rotor in hover.

The NASA UAM reference vehicle, SbS rotor, is used in all the studies performed in this dissertation. The SbS rotor UAM vehicle can hold up to six passengers with a range of 200 nm, capable of performing four 50 nm trips without needing to refuel [35]. The propulsion system is hybrid with two turboshaft engines including a motor and a battery. At low speed flight or hover, the motor is used, and in cruise flight, the turboshaft engine drives the motor as a generator to charge the battery. The fundamental properties of the SbS rotor aircraft are shown in Table 4.1 which is also well-documented in previous studies of Ventura Diaz et al. [37] and Jia et al. [42]. A total of three different investigations are conducted of the SbS rotor UAM vehicle for the analysis of the rotor overlap effect on the performance, aerodynamics, flow physics, and acoustics: the isolated SbS rotor (without rotor hubs) in free air, the isolated SbS rotor (without rotor hubs) in- and out-of-ground effect, and full vehicle configuration in free air. Figure 4.2 shows the rotors of 0% overlap configuration for

Table 4.1: Basic properties for the SbS air taxi rotors.

Rotors	2
Blades per Rotor	4
Rotor Radius	10.5 ft (3.2 m)
Tip Chord Length	0.43 ft (0.13 m)
Nominal Rotor Speed	499.97 RPM
Nominal Rotor Tip Speed	550 ft/s (167.64 m/s)
Gross Weight	3,950 lb (1,792 kg)

the SbS rotor from the top view. This figure provides a detailed look at the orientation of the rotors and position of each of the four rotor blades for each rotor. There is a 45° phase shift applied on the left rotor to prevent collision between the left and right rotor shown in Figure 4.2 as well as offering a more compact design, which will be discussed in the full vehicle study. Details on the CFD grids and CFD/acoustics simulations setup of each investigation carried out will be provided and discussed in later chapters of this dissertation.

There are four overlap configurations of the SbS rotor consisting of the 0%, 5%, 15%, and 25% overlap percentage with two rotors each having four blades. The overlap distance is measured from the separation distance between the rotor hubs of each rotor and defines the overlapping percentages, and these distances are non-dimensionalized using the rotor's radius (R). The hub separation distances for the 0%, 5%, 15%, and 25% overlapping cases correspond to $2R$, $1.9R$, $1.7R$, and $1.5R$, respectively, as shown in Figure 4.3 for all overlap configurations. The rotor blades are modeled as rigid, without elastic deformation, since the material properties are not available during the vehicle's initial design phase. However,

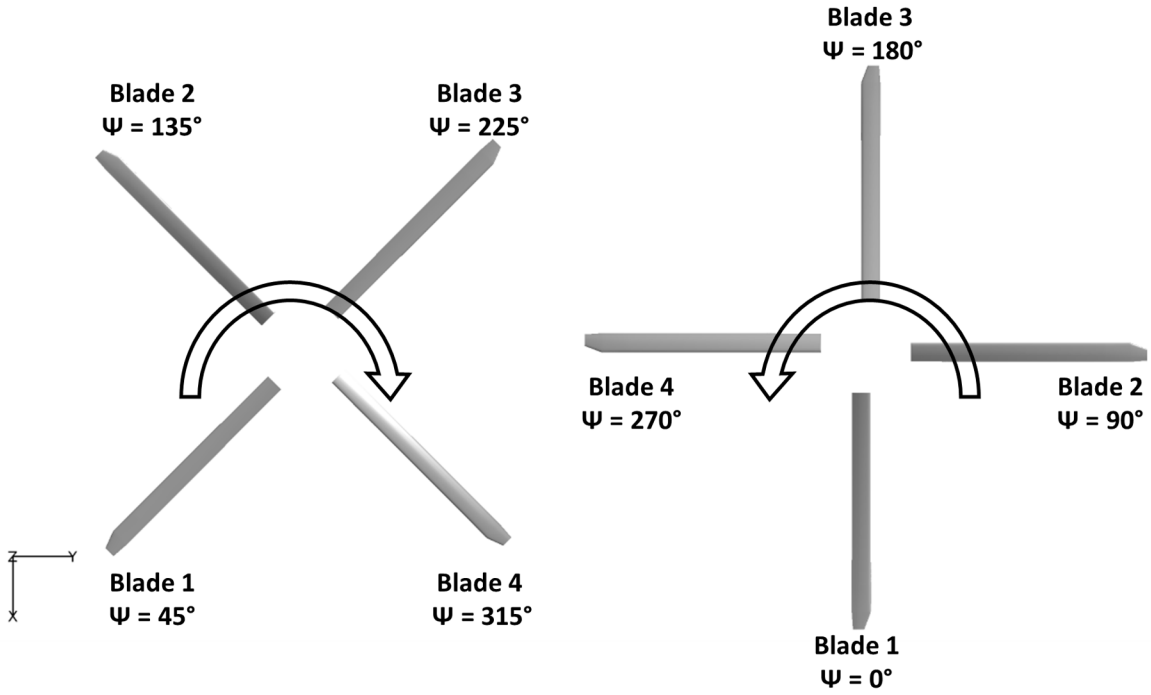

Figure 4.2: SbS rotor configuration and the definition of rotation of each rotor and blade position.

fundamental properties of the vehicle are presented in Table 4.1. Two modern airfoils, Boeing VR-12 and Sikorsky SSC-A09, are utilized for the rotor blades. The VR-12 is used along the span at $R < 85\%$, and the SSC-A09 is used at $R > 95\%$. Linear interpolation between the SSC-A09 and VR-12 is assumed for spanwise locations between 85% and 95%. Following the original blade design from previous studies [10, 35, 37], the blade chord remains constant from 0% to 94% of the blade span. From 94% to 100% of the blade span, there is a 15°linearly swept-tapered ratio where the chord varies linearly. This is illustrated in Figure 4.4, which displays the blade planform. In Appendix A, the chord and twist distributions for the rotor blade of the SbS rotor are provided in Figure A.1.

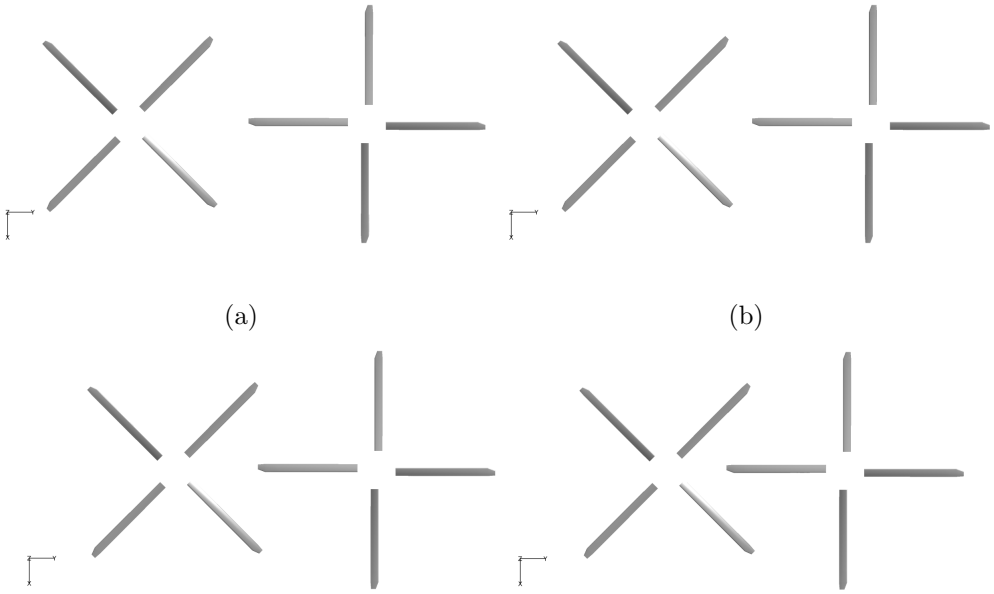

(a) (b) (c) (d)

Figure 4.3: SbS rotor configuration for each overlap: (a) 0% overlap, (b) 5% overlap, (c) 15% overlap, and (d) 25% overlap.

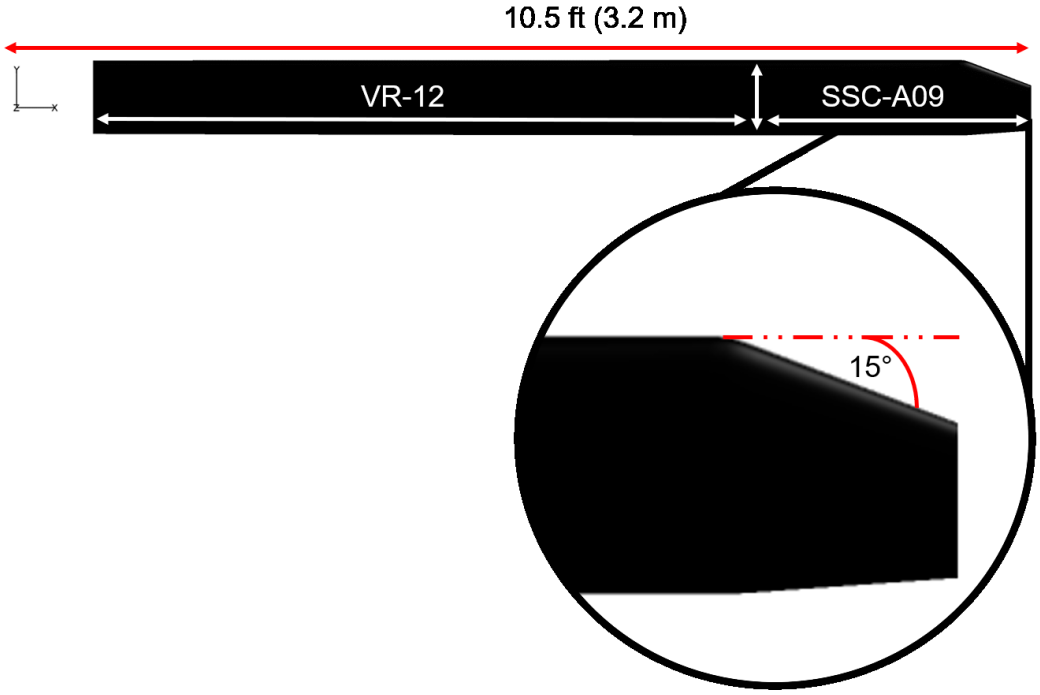

Figure 4.4: Rotor blade planform.

Chapter 5

Parallel Blade-Vortex Interactions

This chapter presents validation of numerical tools for an experimental investigation of an isolated parallel rotor blade-vortex interaction (BVI). Although this validation study does not exactly mimic all of the complex blade vortex interactions for the SbS rotor case, it directly addresses the accuracy of the high-fidelity CFD and acoustics solvers for a representative BVI event. In particular, these comparison cases will be used to validate the ability of the CFD aerodynamics and acoustics methods to 1) accurately model the formation of a tip vortex from a wing or rotor blade, 2) accurately convect this tip vortex over significant distances with little to no artificial numerical dissipation from the CFD method, 3) accurately model the aerodynamic interactions between a rotor and a vortex, and 4) accurately model the resultant noise that results from this BVI event. This methodology validation for BVI events is important because BVI is the primary source of noise for the SbS rotor. Four experimental and computational comparison test cases are presented where each case shows different combinations of vortex rotation direction and miss-distance between the rotor blade and the isolated vortex. In addition to the comparisons of computational and experimental results, this section also provides details of the wind tunnel experiment and computational

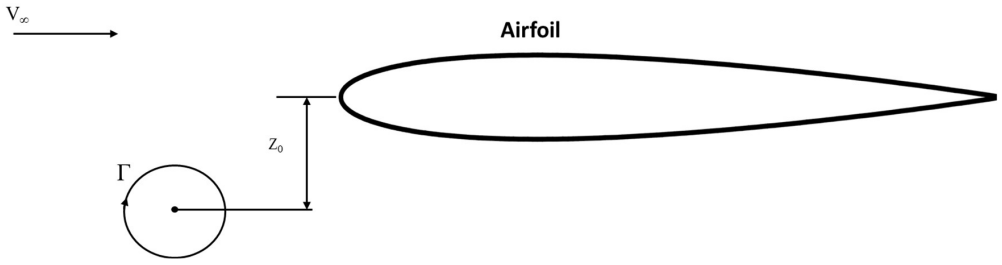

Figure 5.1: A simple two-dimensional model of parallel BVI.

model.

5.1 Motivation

Interactions between a rotor with one or more of its tip vortices can occur in many ways and these interactions significantly contribute to rotor loading and rotorcraft noise. Of all the possible blade-vortex interaction orientations, these parallel blade-vortex interaction (BVI) (as seen in Figure 5.1) events create the most rapid changes in loading on the rotor blade and they cause the highest levels of BVI-generated noise. As a result, both the wind tunnel experiment and the computational model validation in this chapter focus on these isolated parallel BVI events. These interactions are particularly strong when the rotor blade and the tip vortex are close to each other and even stronger when the tip vortex is parallel to the rotor blade. A representative wind tunnel experiment was conducted by Kitaplioglu et al. [43] as shown in the schematic of the experiment setup in Figure 5.2. This experiment has a wing-based vortex generator upstream of a two-bladed rotor that interacts with a tip vortex convecting downstream in parallel to the oncoming rotor blade. A detailed description of the experiment and of the computational model are provided in the section(s) below.

Numerous aerodynamic and acoustic computational codes have been developed that en-

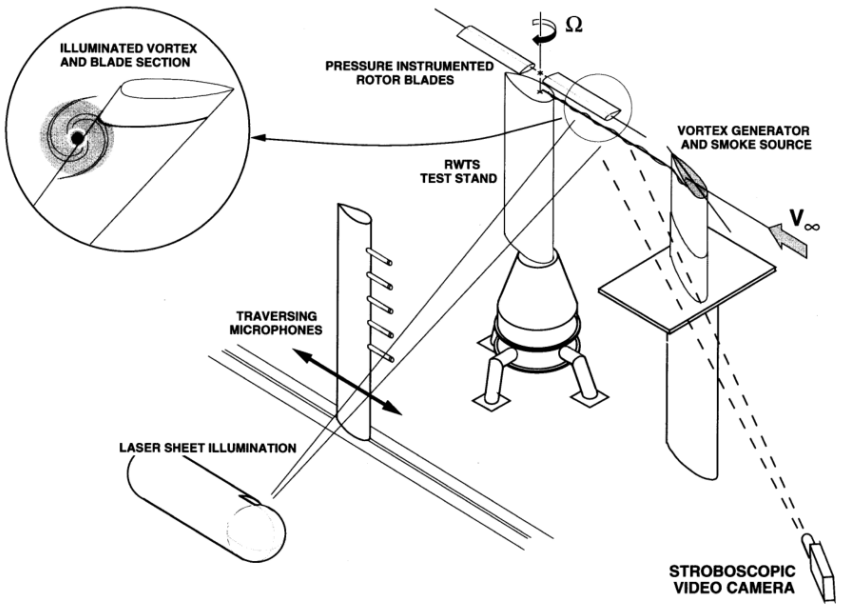

Figure 5.2: The schematic of the BVI experiment setup [44].

compass a wide of range of physical models of BVI. For example, the aerodynamic models include incompressible two-dimensional, vortex-cloud methods that employ conformal mapping solutions to three-dimensional, compressible Euler/Navier-Stokes (NS) CFD codes. As for computational acoustic methods, two types of methods primarily used include: acoustic analogy methods [43] and the Kirchoff methods [45]. Although direct CFD methods can be used for acoustic predictions, it is still limited in accuracy as well as in the far-field in which the acoustics is primarily the concern. However, CFD is a great choice of method for providing input for acoustic prediction methods. Which method to use is dependent on the extent to which flow field non-linearity dominates the overall solution. Aerodynamics in the near-field has a significant role in determining the essential flow physics and the type of acoustic method that should be used.

Confidence in these methods require clear validation using the simplest of tests. In the past, most BVI experimental tests have involved the use of rotor models operating at

typical flight conditions. Instead of analyzing a (multi-)rotor under typical flight conditions which result in complex BVI, a simpler geometry was created which could be more easily tested in the wind tunnel and modeled using various computational methodologies. With this approach, if a computational methodology is unable to generate good correlation with this simplified BVI experiment, there is little confidence to expect accurate results when analyzing a more complex rotor interaction problem at full-scale flight conditions.

This experiment is fitting for the current study because of available surface pressure and acoustic data for both the near- and far-field. Details on the location, strength, and structure of the steady tip vortex are provided in the next section, making it ideal for comparison and validation of the methodology employed in the studies of the SbS rotor UAM aircraft. In the current study, the tip vortex generated is more representative of a realistic rotor undergoing self-induced BVI, which is more complex as opposed to previous validation studies [45–55] that used analytical methods to insert a vortex into the simulation helping maintain its strength without concern of dissipation among other factors that can influence it.

The primary purpose of this investigation of the parallel BVI experiment is to validate that the results from the computational methodology used for simulation are in agreement with experimental data. This can be done by answering questions on whether the computational methodology employed is capable of achieving these essential aspects using modern CFD:

- Accurately capture the roll-up of a tip vortex.
- Accurately convect a tip vortex downstream to the location(s) where it interacts with a rotor blade.

- Accurately model the complex aerodynamic interactions when the rotor passes over a tip vortex.

- Accurately propagate the resulting acoustics signals to a far-field observer.

Previous validation studies [45–55] of the parallel BVI experiment used a variety of computational methods to which they were observed good agreement with the experiment data. However, to the author's best knowledge, there are no other published validation studies of parallel BVI wind tunnel experiment [43] that has captured (or capable of doing so) in a CFD simulation, a trailing tip vortex convecting downstream from a wing-based vortex generator interacting with a rotor blade in a parallel manner. The validation study performed for this dissertation considered four primary cases from the experiment that include ± 12 degrees with miss distances of $\frac{Z_v}{c} = 0$ and $\frac{Z_v}{c} = -0.25$. The measured acoustic data considered are from the far-field microphones with details of the acoustic setup provided in later subsections. This thesis work can help advance our understanding of the underlying physics, noise source origin, and mechanism of intricate/real world rotor configurations which can eventually lead to improved confidence in existing and future CFD models and simulations of rotor configurations.

5.2 Experiment

Several wind tunnel experiments were performed by Kitaplioglu and Caradonna [56, 57] for the study the interactions between a rotor blade and tip vortex. The purpose of the experiment was to simulate the aerodynamics and acoustics of a parallel, unsteady blade-vortex interaction. The main reason for the experiment was to match as closely as possible

Figure 5.3: BVI experiment apparatus in the NASA Ames 80-by-120-Foot Wind Tunnel [57].

the conditions for a simplified model of a rotor blade undergoing an unsteady and parallel interaction with a vortex. The vortex was generated from a wing placed upstream of the rotor and set to an angle of attack. This was done to provide independent control of the major parameters that influence the parallel, unsteady blade-vortex interaction such as vortex strength, vortex-blade separation distance, rotor advance ratio, and hover tip Mach number. Figure 5.3 shows the experimental arrangement in the test section of the NASA Ames 80- by 120-Foot Wind Tunnel or National Full-Scale Aerodynamics Complex (NFAC) and a descriptive schematic can seen in Figure 5.2.

5.2.1 Wind Tunnel Installation

The test section of the NFAC wind tunnel are acoustically treated in the floor and ceiling of approximately six inches and 10 inches in the walls, with a cutoff frequency of approximately

250 Hz (90% absorption). The U.S. Army Rotary Wing Test Stand (RWTS) and rotor system were installed on the horizontal centerline of the test section with rotor hub approximately 5.0 meters above the floor. The wing generating the vortex was installed upstream of the RWTS with the trailing edge 1.219 meters (approximately three chords of the wing) upstream of the rotor blade tip at its 180 degrees azimuth position. The length (span) of the wing was set such to place the tip vortex for direct impact with the rotor blade. A smoke generator for flow visualization of the vortex was mounted inside the wing. The vortex and blade during the interaction were illuminated with a long-range laser that was also used to document the blade-vortex separation distance.

5.2.2 Rotor and Vortex Generator

A small-scale, two-bladed, teetering rotor with a 2.134 meter diameter was used. The blades are untwisted with a rectangular planform, NACA0012 airfoil, 0.152 meter chord, an aspect ratio of 7.125, and a chord Reynolds number of the order of 10^6. The rotor was mounted on the RWTS capable of driving up to 2,300 RPM with a tip Mach number of 0.7. Rotation of the rotor was in the clockwise direction (as viewed from above the rotor). Each blade was equipped with 30 absolute pressure transducers on the upper and lower surfaces distributed in three spanwise sets of 10 chordwise locations. The blades were stiffened to minimize any aeroelastic effects and set at a 0°angle of attack to minimize the creation of any tip vortices from the blades.

The vortex was generated using a short rectangular wing (vortex generator) with a NACA0015 airfoil, an 18-inch (0.4572 meters) chord, and a chord Reynolds number of the

order of 10^5. The vortex generator is constructed in a telescoping arrangement (remotely controlled with a total travel of nine inches) to allow for height adjustment of the vortex relative to the rotor blade. Theatrical fog was used to make the vortex visible. The generated vortex had a core size (ζ_{V}) of approximately 0.15 of the blade chord and an estimated strength (Γ_{v}) shown below.

The characteristics of the tip vortex were not measured during the experiment. However, McAlister and Takahashi [58] conducted detailed laser velocimetry studies of a similarly generated vortex. Based on their experiment and several additional studies [43], the vortex characteristics can be estimated as follows:

- $\Gamma_{\mathrm{v}} = 0.35 V_{\infty} c_{vg}$
- $\zeta_{\mathrm{v}} = 0.05 c_{vg}$

The BVI experiment conducted by Kitaplioglu and Caradonna had a freestream Mach number of 0.142. A vortex is generated from a vortex generator (wing), which is then convected downstream toward the rotor to the point of the parallel interaction that occurs when the position of the rotor is at the 180 degree azimuth angle. This interaction occurs at about 1.2192 meters, measuring from the tip of the vortex generator to tip of the blade. The rotor was set to the height equal to the span of the vortex generator aligned to the wing tip at an azimuth of 180°. A total of 32 rotor revolutions were run with surface pressure collected from the chordwise absolute pressure transducers previously mentioned located at three radial locations. A total of seven microphones were used to obtain acoustic data in both the near- and far-field. Two microphones were positioned in the near-field in close proximity of the interaction to provide information on the detailed evolution of the acoustic

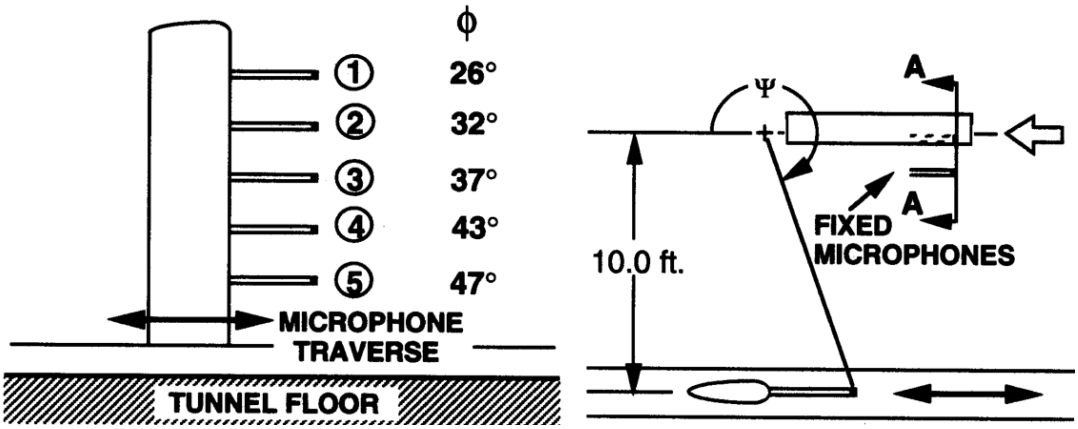

Figure 5.4: Far-field microphone positions (not to scale) [44]: (a) side view and (b) top view.

field. The other five microphones were located on a movable array that is able to traverse parallel to the rotor and vortex generator to obtain a survey of the acoustic far-field. The parameters of the experiment are summarized in [44].

5.2.3 Acoustics Setup

There are two sets of microphones that were installed for measuring the acoustics in the wind tunnel experiment. One set has a total of five microphones installed at different heights on a traversing vertical strut can be controlled remotely and was mounted on a tunnel floor 3.06 meters to the starboard side of the rotor aligned with the direction of the incoming freestream. This vertical strut is capable of traversing upstream and downstream parallel to the rotor and vortex generator. The five microphones were mounted at elevation angles of 26, 32, 37, 43, and 47 degrees as shown in Figure 5.4.

Another set of microphones were installed on a short sting just under the rotor close to the side of the interaction position. The positions of these two near-field microphones are shown in Figure 5.5.

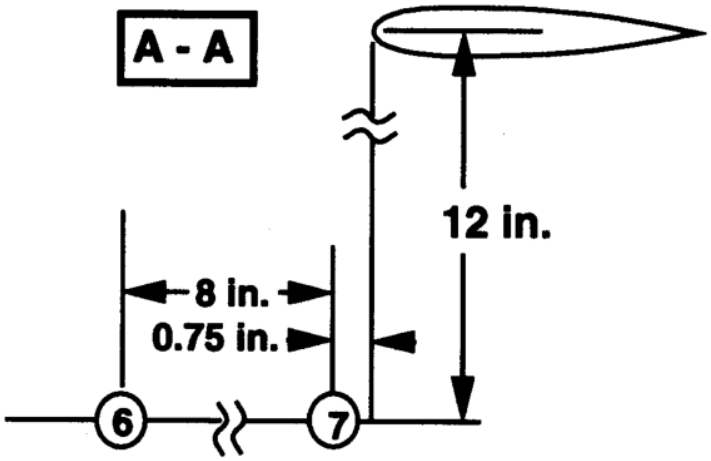

Figure 5.5: Near-field microphone positions (not to scale) [44].

5.3 Parallel Blade-Vortex Computational Study

This section presents details of the CFD and acoustics setup for the validation study of the acoustic data measured at the far-field microphone locations from the parallel BVI wind tunnel experiment.

5.3.1 Methodology

The methods employed in the CFD study of the SbS rotor UAM aircraft are used in this validation study. OVERFLOW is used via Helios in the near-body with SAMCart in the off-body without AMR. PSU-WOPWOP is used to perform acoustic simulations for all five microphone locations in the far-field.

5.3.2 Wing and Rotor Model

Simulations include the rotor (2 bladed) which rotates in the clockwise direction with wing (vortex generator) positioned 1.2192 meters upstream from the rotor blade tip in its 180° azimuth position as shown in Figure 5.6. The wing is set at an angle of attack of ±12 degrees in each of the cases considered. The rotor is set to a zero degree collective resulting in near-zero thrust in order to minimize the generation of a wake or tip-vortex system from the rotor. Orientation of the rotor relative to wing ensures parallelism of the interaction of the tip vortex and rotor blade tip.

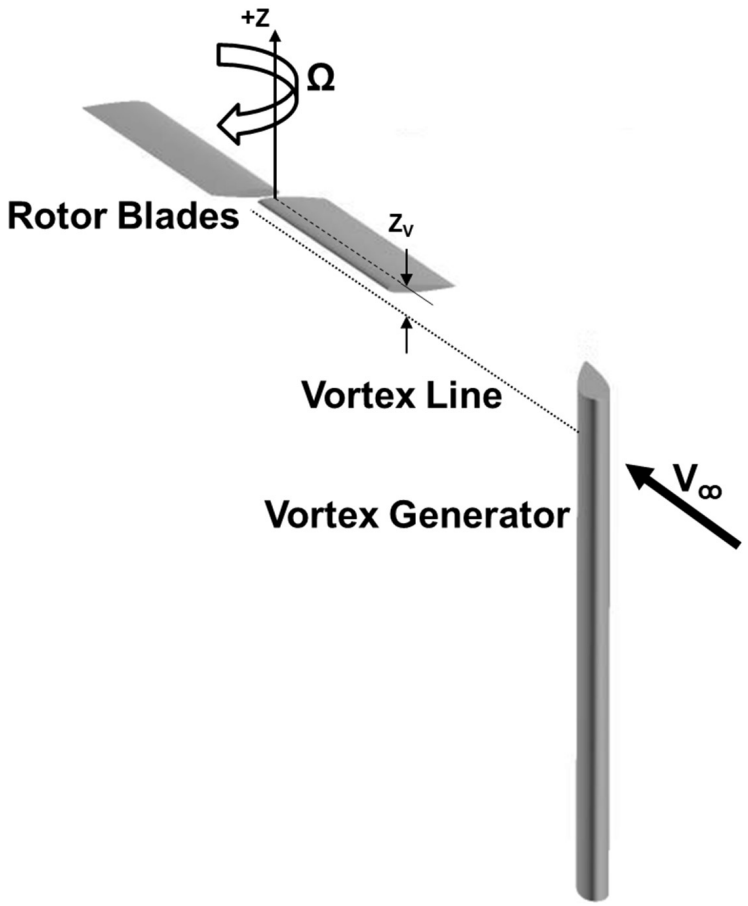

Figure 5.6: Setup of the model depicting the rotor, wing, and parallel tip vortex.

5.3.3 Grids

The rotor blades and wing (vortex generator) are modeled using a high-order overset structured mesh with an O-grid topology for the near-body with a high-order Cartesian grid for the off-body in the far-field. For the rotor blades, each blade consists of three sections that make up the grid: the main blade, blade tip, and blade root as shown in Figure 5.7. The wing shown in Figure 5.8, however, consists only grids of the main wing and wing tip, on the wing root side there is no grid cap as it is as an open-body interfacing with the ground plane. For the grid resolution, the spacing used in modeling the near-body grids of the SbS

rotor blades are invoked on the rotor blades and wing including the number of points in the spanwise, chordwise, and normal direction. Clustering at the leading and trailing edges are enforced as well using the blade's tip chord set at 0.05% C_{tip} and 0.02% C_{tip} respectively. The number of grid points in the volume of the near-body for each rotor blade is approximately 14.6 million, 11.5 million for the wing, and approximately 40.7 million for both the wing and rotor.

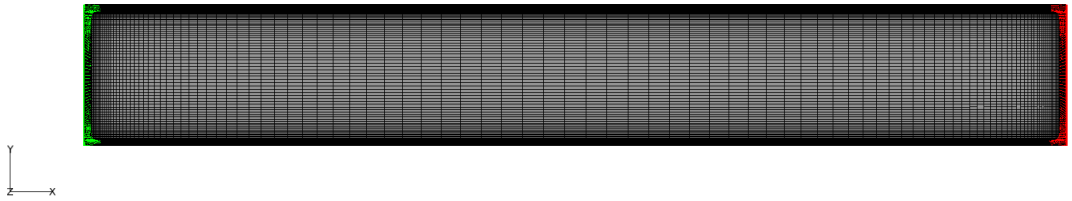

Figure 5.7: Near-body overset structured grids of the rotor blade.

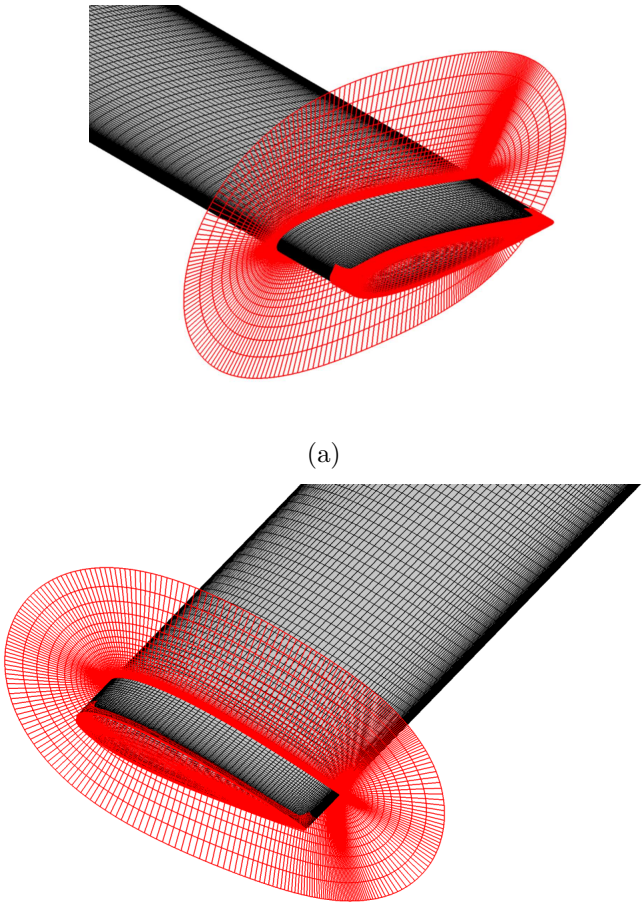

(a)

(b)

Figure 5.8: Near-body cap grids of the rotor blade and wing: (a) Rotor blade and (b) Wing.

The off-body Cartesian grid is shown in figures 5.9 and 5.10. It has seven refinement levels and a fixed refinement region. A fixed refinement box surrounds the rotor and the wingtip of the vortex generator. The spacing in the fixed refinement box is set to 10% C_{tip} of the rotor blade, matching the spacing on the outer boundary of the near-body volume grids. The refinement box dimensions are $1.25R$ in the x-direction, $2.5R$ in the y-direction, and $0.25R$ in the z-direction. The x, y, and z coordinates are displayed in figures 5.9 and 5.10. After 12 rotor revolutions, the off-body grid has approximately 11 million grid points with a size measuring 20 rotor radii away from the origin in the x, y, and +z direction.

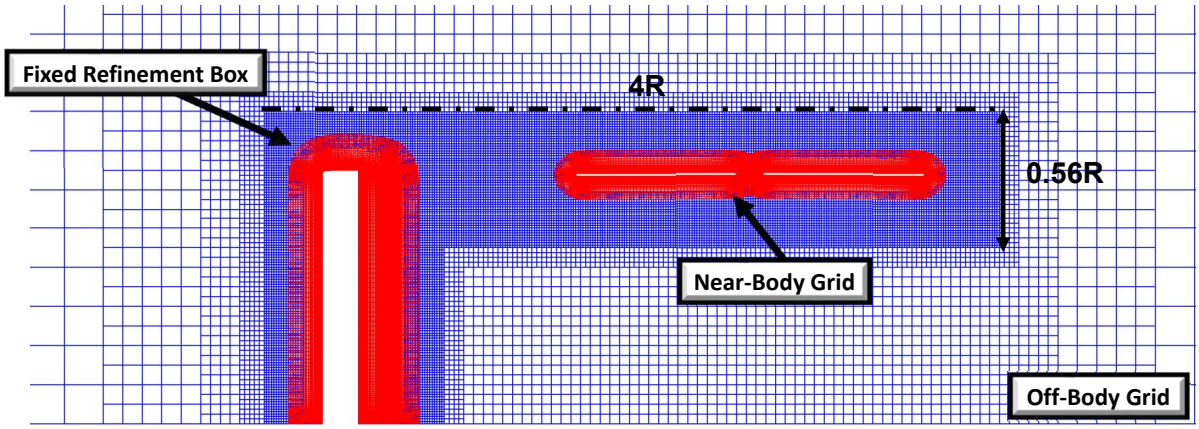

Figure 5.9: Side view of the off-body mesh.

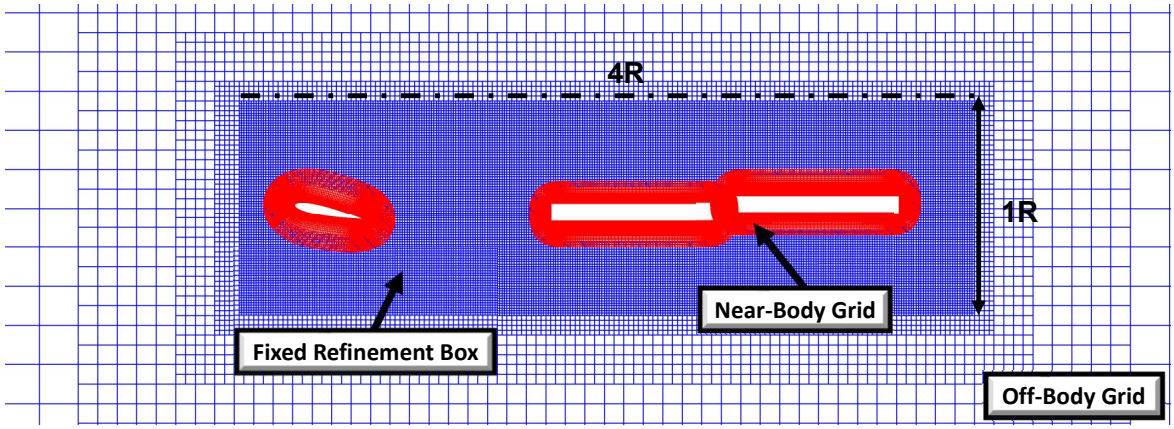

Figure 5.10: Top view of the off-body mesh.

5.3.4 CFD Setup

OVERFLOW is used for the near-body solver in Helios with SAMCart selected as the solver in the off-body. , Spalart-Allmaras Detached Eddy Simulations (SA-DES), turbulence model is used in the studies of SbS rotor (as discussed in Chapter 3) in both the near- and off-body solvers including the rotation curvature correction model. The two different timestep sizes used in prior studies (see Chapters 6,7,8) are also used in this validation study in order to minimize computational time. In the first 2,880 timesteps, we use a timestep size of 1°

Table 5.1: Computational size and cost — All overlap cases

Near-body grid	
Per rotor blade	9 million
Rotor (2 blades)	18 million
Wing	7.8 million
Off-body grid	
Grid points (Initial to final timestep)	11 million
Number of processors	720
Simulation time per rotor	2 — First 8 revs
revolution (hrs)	5 — Last 4 revs

which is 8 rotor revolutions and then after initiating a restart for the next 5,760 timesteps, we reduce the timestep size to 0.25° for 4 rotor revolutions, resulting in a total of 12 rotor revolutions. The CFD simulations were run on Mustang (HPE SGI 8600) HPC located at the Air Force Research Laboratory. A total of 15 nodes (720 processors) were used for each case considered in this validation study. Details on the cost of each simulation are presented in Table 5.1.

5.3.5 Acoustic Simulation Setup

PSU-WOPWOP is used for all acoustic simulation with an impermeable surface approach as used in the study of the SbS rotor cases. Aside from the tool(s) used for the acoustic predictions, the rest of the acoustics setup is clearly different and specific to the wind tunnel

Table 5.2: Location of Microphones (Coordinates in chords).

Microphone	x	y	z
Mic 2	15.135	20	9.46
Mic 3	15.135	20	11.41
Mic 4	15.135	20	14.1
Mic 5	15.135	20	16.23

experiment. Four cases from the experiment are considered as discussed in Chapter 5, Section 5.1. Acoustics from a total of 4 out of the 5 far-field microphone locations are studied due to unavailability of the data from one of the microphones. The microphone locations are shown in Subsection 5.2.3 of Chapter 5 including the elevation angle. Table 5.2 presents the locations of the microphones in the x, y, and z directions in blade chord lengths of the rotor. The origin (global reference frame), (0, 0, 0), is set to the quarter chord location of the wing-based vortex generator.

5.4 Parallel Blade-Vortex Interactions Results

In this section, the acoustic results are presented for the validation study of the methodology employed in the investigation of the SbS rotor UAM aircraft.

5.4.1 Acoustic Results

The four primary BVI cases from the parallel BVI wind tunnel experiment are considered where the advance ratio and tip Mach number are fixed at $\mu = 0.198$ and $M_{tip} = 0.712$. These four cases exhibit the interaction occurring with tip vortices of opposite swirl direction, which are obtained by setting the wing at an angle of attack of $+12°$ and $-12°$for both the head-on interaction and an interaction of the tip vortex at 0.25 blade chord below the rotor blade.

Acoustic time histories of the predictions and measurements for the far-field microphones of the head-on interaction ($\frac{Z_v}{c} = 0$) case with the wing set to $+12°$ are shown in Figure 5.11. In the figure, the predictions are shown in a solid line colored in red and the experiment are shown in squares colored black. Acoustic predictions for microphones 3 and 4 show good agreement while microphones 2 and 5 show a slightly lower maximum peaks by 5 to 7 Pa in the acoustic pressure compared to the experiment. However, comparisons of the pulse width between predictions and experiment are in good agreement.

Figure 5.12 shows the acoustic predictions and measurements from the far-field microphones for one of the miss-distance cases, $\frac{Z_v}{c} = 0.25$ with the wing set to $+12°$. All four microphones show slight overprediction of the maximum peak by 8 to 10 Pa in the acoustic pressure from the acoustic simulations. Similar to the head-on interaction ($\alpha_v = +12°$ and $\frac{Z_v}{c} = 0$) case, the predicted pulse width is in good agreement with the measured pulse width.

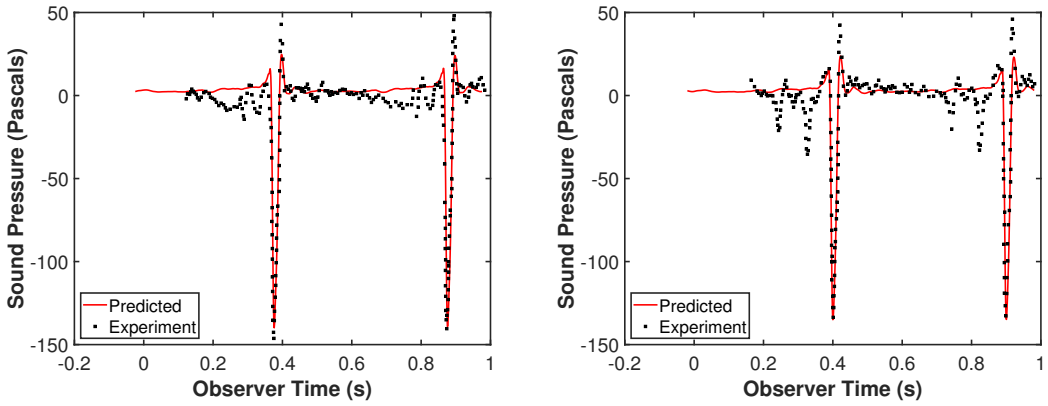

(a)

(b)

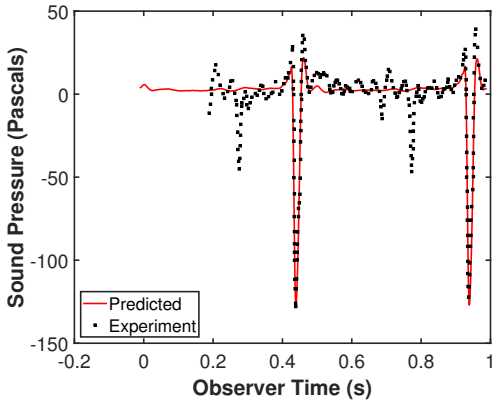

(c)

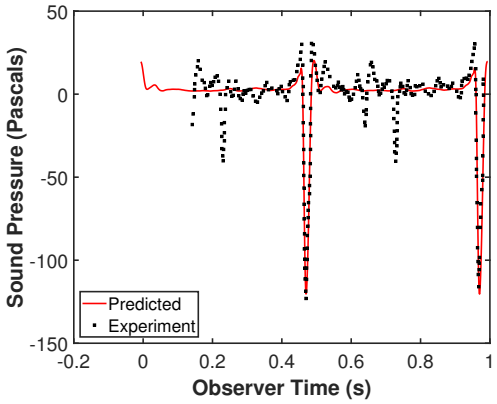

(d)

Figure 5.11: Acoustic predictions for the head-on interaction case — $\alpha_v = +12°$, $\frac{Z_v}{c} = 0$: (a) Mic. 2, (b) Mic. 3, (c) Mic. 4, and (d) Mic. 5.

In Figure 5.13, the acoustic time histories are shown for both measured and predicted of the far-field microphones for the head-on interaction case, $\alpha_v = -12°$, $\frac{Z_v}{c} = 0$. Acoustic predictions for microphone 2 and 3 show larger underpredictions, as much as 18 Pa difference compared to the measured data, and even more so when compared to the underpredictions from cases presented in figures 5.11 and 5.12. In contrast, the pulse width between the predictions and experiment shows good agreement.

Figure 5.14 presents the time histories of acoustic pressure from the experiment and

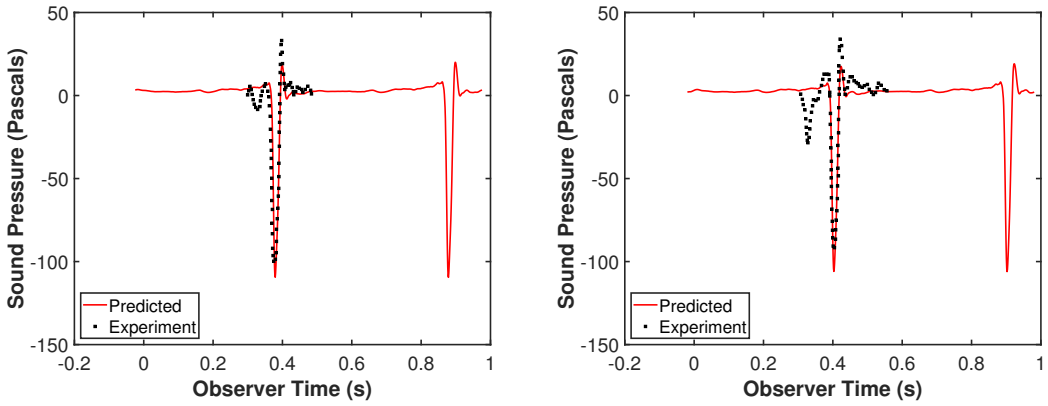

(a)

(b)

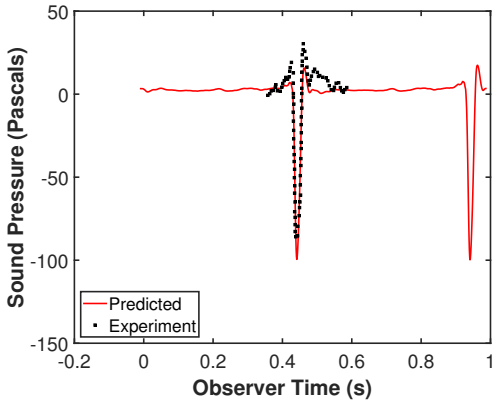

(c)

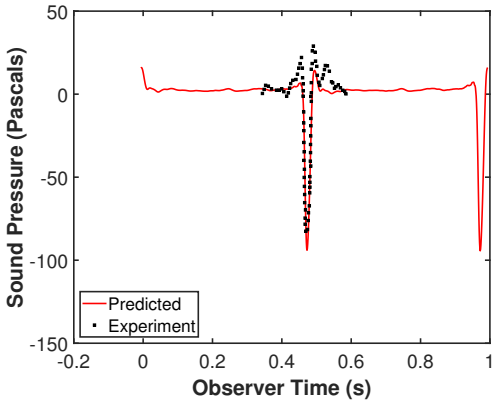

(d)

Figure 5.12: Acoustic predictions for the vortex with a miss-distance case of 0.25 blade chords below the blade — $\alpha_v = +12°$, $\frac{Z_v}{c} = -0.25$: (a) Mic. 2, (b) Mic. 3, (c) Mic. 4, and (d) Mic. 5.

acoustic simulations of the four far-field microphones in the miss-distanc case, $\alpha_v = -12°$, $\frac{Z_v}{c} = 0$. Microphones 2 and 3 show slight overprediction (10 to 13 Pa) in the simulations while the acoustic predictions for microphones 4 and 5 show slight underprediction (2 to 3 Pa) of the maximum peaks in acoustic pressure. Similarly to the other cases, the predicted pulse width is in good agreement with the measured pulse width.

Overall, the predicted pulse width and character show very good correlation with the measurement data in all of the four cases simulated. The use of a finer spacing in the

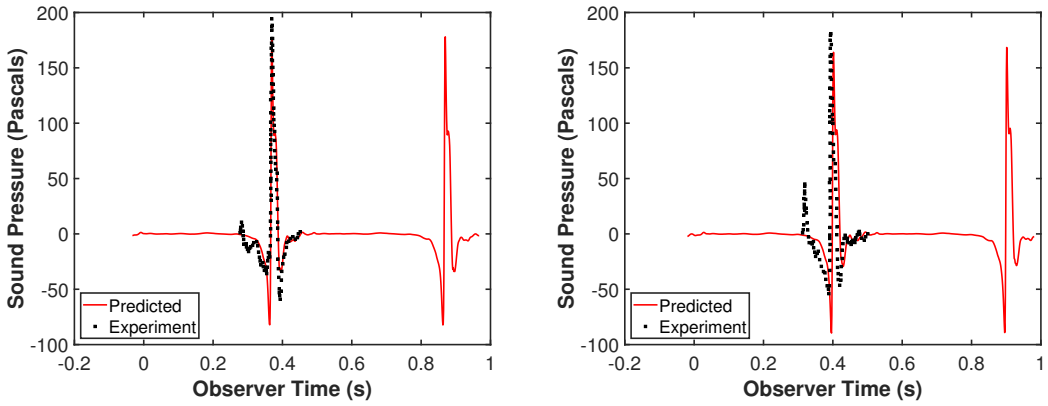

(a)

(b)

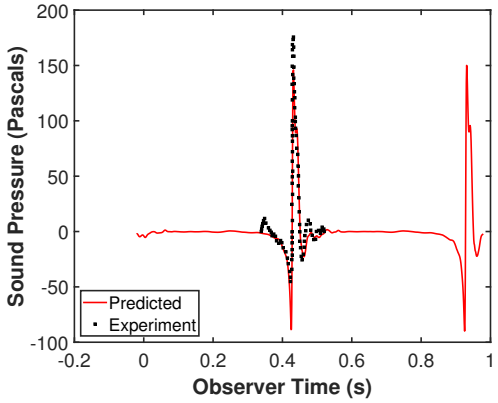

(c)

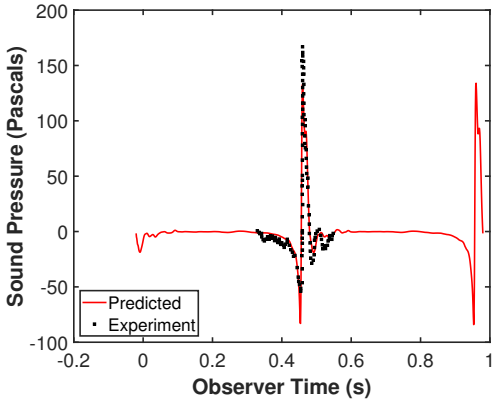

(d)

Figure 5.13: Acoustic predictions for the head-on interaction case — $\alpha_v = -12°$, $\frac{Z_v}{c} = 0$: (a) Mic. 2, (b) Mic. 3, (c) Mic. 4, and (d) Mic. 5.

off-body mesh or increasing the number of grid points for the surface of the rotor blade might improve the predictions. This detailed grid resolution study is not conducted in this dissertation.

5.4.2 Summary

The parallel BVI wind tunnel experiment has been analyzed for four primary cases at ±12 degrees with miss distances of $\frac{Z_v}{c} = 0$ and $\frac{Z_v}{c} = -0.25$ to validate the computational method-

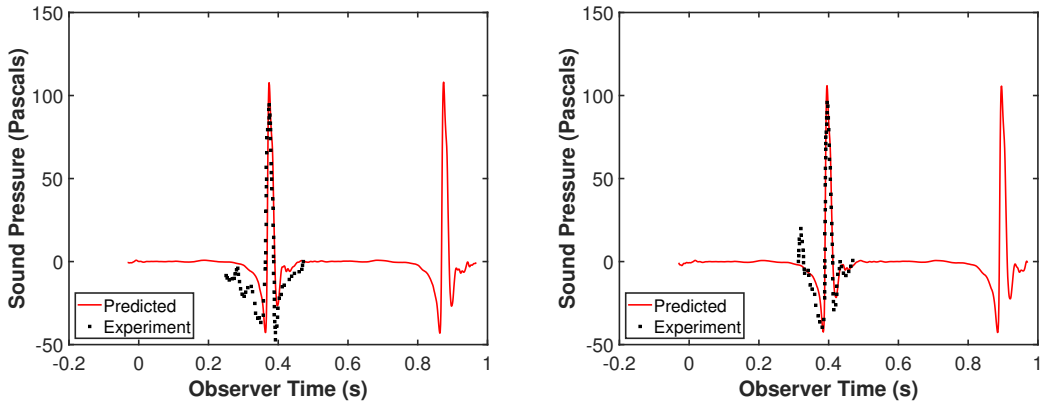

(a)

(b)

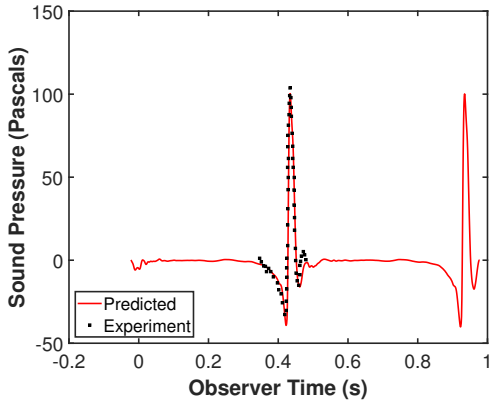

(c)

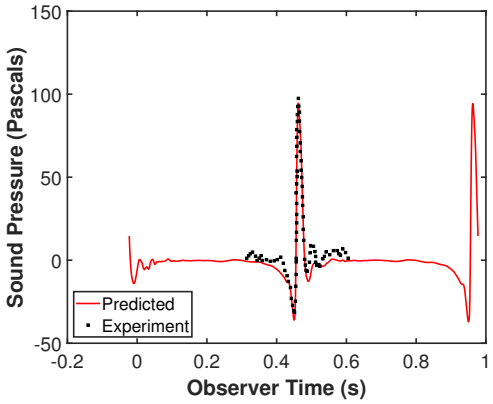

(d)

Figure 5.14: Acoustic predictions for the vortex with a miss-distance case of 0.25 blade chords below the blade — $\alpha_v = -12°$, $\frac{Z_v}{c} = -0.25$: (a) Mic. 2, (b) Mic. 3, (c) Mic. 4, and (d) Mic. 5.

ology used to perform the studies of the SbS rotor UAM aircraft. Measured data of the acoustics were compared to acoustic predictions from the high-fidelity CFD and acoustics coupling approach. The simulations yielded good results in all four cases for the far-field microphones. The peak-to-peak amplitudes were predicted well within approximately 7.67% or better in most cases. Pulse widths from acoustic predictions were computed well in comparison to measured data.

For the case of an isolated parallel blade-vortex interaction event, these results demon-

strate that the CFD and acoustics models used in this thesis work can achieve all of the four goals set out at the beginning of this chapter:

- Accurately capture the roll-up of a tip vortex.
- Accurately convect a tip vortex downstream to the location(s) where it interacts with a rotor blade.
- Accurately model the complex aerodynamic interactions when the rotor passes over a tip vortex.
- Accurately propagate the resulting acoustics signals to a far-field observer.

Chapter 6

Isolated Side-by-Side (SbS) Rotor

This chapter presents the CFD and acoustic results from the simulations of the isolated SbS rotor (in free air with no ground plane) based on high-fidelity CFD coupled with acoustics analysis. These investigations cover different overlap configurations in hover at several collective pitch angle. Details of the setup for the CFD and acoustic analysis were discussed in Chapter 4 with additional details being provided here.

6.1 Isolated SbS Rotor Configuration: Goals and Objectives

The goal of this study is to investigate the impact of SbS rotor overlap on rotor performance, aerodynamics, and aeroacoustics in hover. Specifically, high-fidelity CFD and aeroacoustic simulations are employed to reveal the detailed flow fields and unique noise sources associated with the six-passenger hybrid VTOL SbS taxi UAM configuration. By examining the various overlapping cases and their effects on hover performance, aerodynamics, and aeroacoustics, this study aims to identify aerodynamic noise sources of overlapping rotors, based on flow physics, as well as to provide detailed analyses of performance and aerodynamics.

The findings can be used to optimize the design and performance of future VTOL air taxi configurations in the rapidly expanding UAM industry.

6.2 Methodology

High-fidelity CFD modeling is employed in this study to calculate the performance and flow field of the rotors for the six-passenger hybrid VTOL SbS air taxi UAM configuration. The unsteady and compressible Navier-Stokes equations, based on first principles, are used to capture complex flow fields, such as unsteady flow, radial flow, swirl flow, compressibility, flow separation, and blade-vortex interaction. The simulations conducted in this research study assume a fully-turbulent flow. Consequently, this study does not model any laminar flow in the rotor blades' leading edge region, followed by transition to turbulent flow. CFD calculations are performed using CREATE^{TM}-AV Helios [23], with NASA's OVERFLOW module [24] serving as the near-body solver and SAMCart as the off-body solver. In the off-body mesh, a fine structured mesh is employed, incorporating an adaptive Cartesian mesh refinement to resolve the wake. Aeroacoustic predictions are obtained using an acoustic analogy in PSU-WOPWOP [26–28].

The simulations focus on the left (clockwise rotating) and right (counter-clockwise rotating) rotors, excluding the fuselage and rotor hubs, to examine the flow fields and any interactional aerodynamics between these rotors. Comparisons between each overlap configuration are performed including a total of five collective pitch angles for each rotor overlap configuration that are considered for investigation in analyzing the effect of the rotor overlap on performance, flow physics, aerodynamics, and acoustics at varying range of thrust.

6.2.1 Grids

Helios utilizes a dual-mesh paradigm, dividing the entire computational domain into near-body (structured or unstructured) and off-body (structured) mesh systems. The rotor blades are modeled using an overset structured mesh with an O-grid topology for the near-body, while an adaptive Cartesian grid is used for the off-body far-field. NASA's Chimera Grid Tools (CGT) [59], an overset grid generation software, is employed to create the near-body mesh. Each blade consists of three sections/components: the blade root, blade tip, and main blade (as shown in Figure 6.1). Regarding grid resolution, there are 265 points around the airfoil, 165 points in the spanwise direction, and 65 points in the normal direction. The chordwise spacings at the leading and trailing edges are set to 0.05% C_{tip} and 0.02% C_{tip}, respectively, where C_{tip} represents the blade's tip chord. Surface grids are clustered in the leading and trailing edges along the chordwise direction to accurately resolve gradients of the flowfield quantities. These same grid spacing characteristics are also applied along the spanwise direction near the root and tip. The wall spacing is set at 1.0×10^{-5} meters to achieve a y+ (dimensionless wall distance) of 1.0. For the near-body volume grids extending to the chord length in the wall-normal direction, the end spacing at the overset boundary is set to 10% C_{tip}. The number of near-body volume grid points for each rotor blade is approximately 4.9 million, and the total number of grid points for all eight rotor blades is approximately 39.2 million.

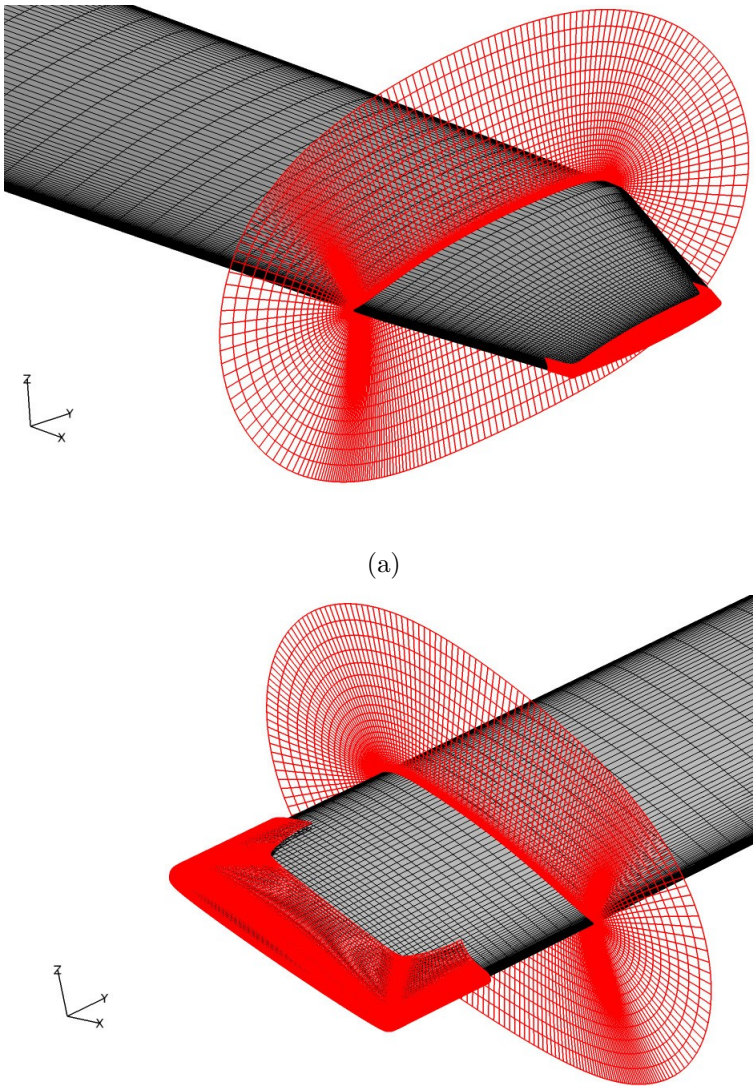

(a)

(b)

Figure 6.1: Near-body overset structured grids with the cap grids at the root and tip: (a) blade tip and (b) blade root.

The off-body Cartesian grid is shown in figures 6.2 and 6.3. It is automatically generated by SAMCart with 8 refinement levels and adaptive mesh refinement (AMR) activated after 2,880 timesteps, or 8 rotor revolutions. AMR is a feature in SAMCart that helps capture the detailed physics of rotor wakes, including vortices shedding from the blades. A fixed refinement box surrounds the two rotors to resolve and capture the flow physics and wake

near the blades. The spacing in the fixed refinement box is set to 10% C_{tip}, matching the spacing on the outer boundary of the near-body volume grids. Utilizing a fixed refinement box along with a grid adaptive region for tracking the shedding vortices, particularly in the far-wake, can help reduce computational costs for these types of cases. The refinement box dimensions are $1.25R$ in the x-direction, $2.5R$ in the y-direction, and $0.25R$ in the z-direction. The x, y, and z coordinates are displayed in figures 6.2 and 6.3. After 12 rotor revolutions, the off-body grid has approximately 800 million grid points. The domain size for the off-body is 20 rotor radii away from the origin in every direction.

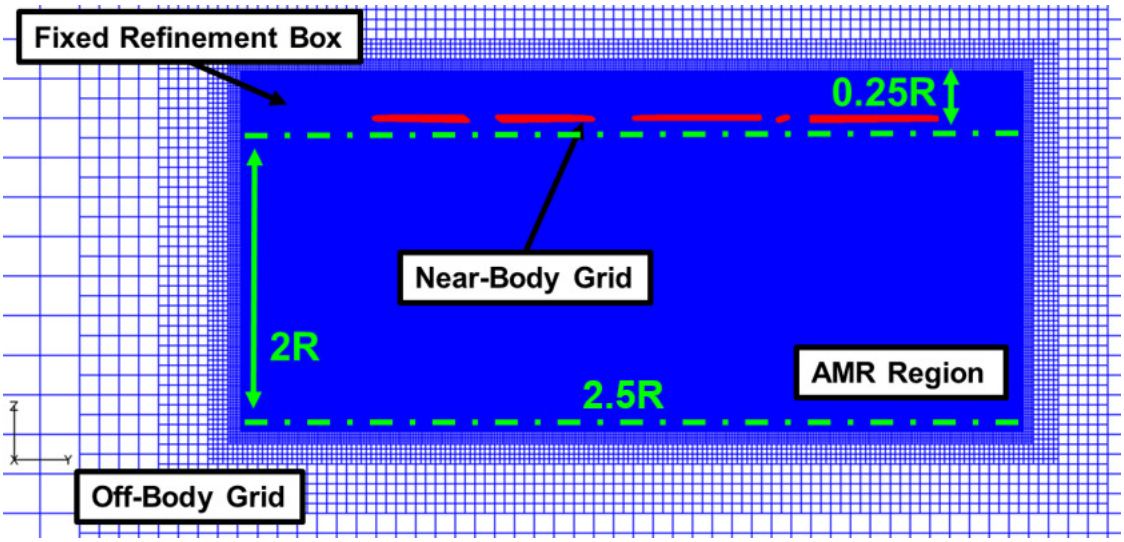

Figure 6.2: Side view of the off-body mesh.

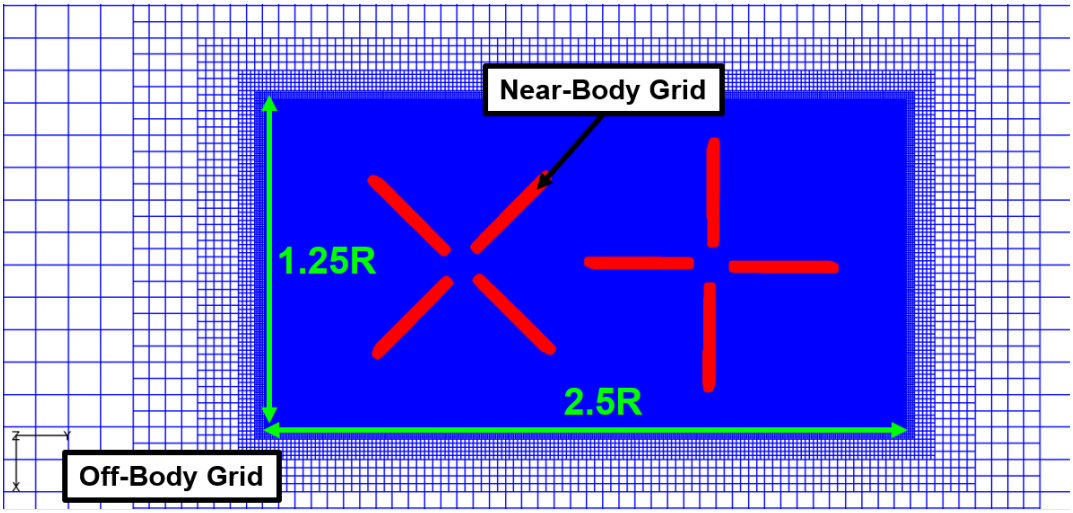

Figure 6.3: Top view of the off-body mesh.

6.2.2 CFD Setup

OVERFLOW [24], a high-fidelity and overset structured flow solver developed and maintained by NASA, is used as the near-body solver in Helios. To capture rotor wakes and tip vortices, SAMCart, an off-body Cartesian solver, is used in conjunction with AMR. For the inviscid terms in OVERFLOW, a fifth-order central difference spatial scheme is applied, while a second-order discretization scheme is used for the viscous terms. Temporal discretization involves a second-order diagonalized Beam Warming penta-diagonal scheme [60], along with dual-time stepping subiterations. The Spalart-Allmaras DES [61] option is utilized in the near-body to resolve viscous turbulent flows near the wall and the wake in the off-body. A rotation curvature correction model is also employed. Time-accurate simulations for this study are divided into two different time-step simulations to minimize computational time. In the initial run, the time-step size is set to 1.0° azimuth for 2,880 timesteps, or 8 rotor revolutions. A restart is then initiated for the second run, during which the time-step size is switched to a finer 0.25° azimuth for 5,760 timesteps, or 4 rotor revolutions. This method

Table 6.1: Simulation settings — All overlap cases

Near-body settings	
Grid type	Structured grid
Spatial scheme	fifth-order accurate
Turbulence model	SA-DES
Off-body settings	
Grid type	Cartesian AMR
Finest wake-grid spacing	10% C_{tip} spacing
Spatial scheme	Fifth-order accurate
Turbulence model	SA-DES

allowed us to reduce the overall computational time from 96 hours (4 days) to less than 24 hours.

All CFD simulations were conducted on either the Centennial (SGI-ICE-XA) or Excalibur (Cray XC40) high-performance computers (HPCs), located at the U.S. Army Research Laboratory and the U.S. Department of Defense (DoD) Supercomputing Resource Center (DSRC). For all simulations, a total of 20 nodes (800 cores) on Centennial or 25 nodes (800 cores) on Excalibur were employed. Tables 6.1 and 6.2 present the simulation settings, mesh size, and a breakdown of the computational cost for each simulation, respectively.

Table 6.2: Computational size and cost — All overlap cases

Near-body grid	
Per rotor blade	4.9 million
Both rotors (8 blades)	39.2 million
Off-body grid	
AMR OFF	153.5 million
AMR ON	625.9 million
Number of processors	800
Simulation time per rotor	2.5 — First 8 revs
revolution (hrs)	19 — Last 4 revs

6.2.3 Acoustic Simulation Setup

For acoustic prediction, PSU-WOPWOP [26–28] is used for the acoustic predictions. PSU-WOPWOP is a numerical implementation of Farassat's Formulation 1A [13, 14] of the Ffowcs Williams and Hawkings (FW-H) equation [12]. An impermeable surface approach is used, which takes into account only the blade surface loading from high-fidelity CFD results as well as the motion of the blades.

In one of the two acoustic calculations performed, a single observer is positioned at a 90°elevation angle, 500 ft (152.4 m) below the rotor disk plane which can be seen in Figure 6.4 to assess Uber's noise guidelines [1]. A hemispherical grid is generated for multiple observers (total of 1000) at a distance of 10R (105 ft or 32 m) as shown in Figure 6.5. The hemispherical case is used to investigate the acoustic directivity of the SbS rotors and the

impact of the overlap on noise directivity.

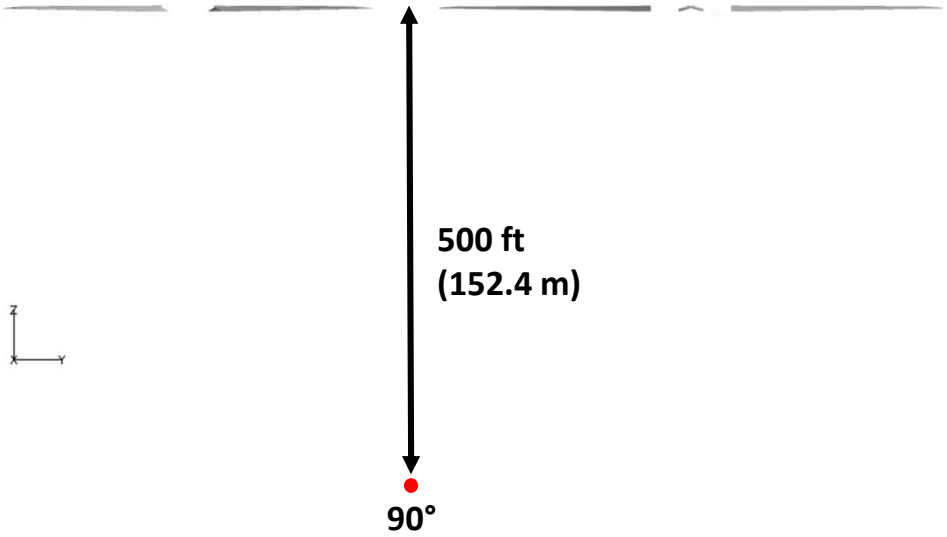

Figure 6.4: Observer location in the single observer case.

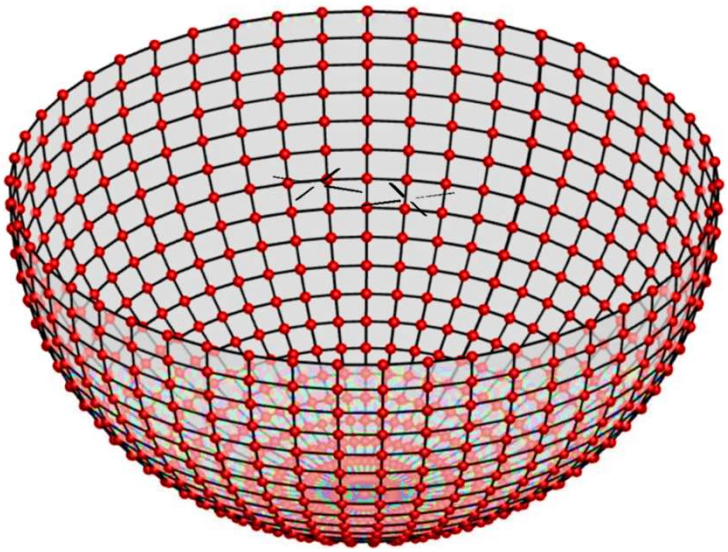

Figure 6.5: Observer location in the multiple observers case.

6.3 Isolated Side-by-Side (SbS) Rotor Results

This section presents results for performance, flow physics, aerodynamics, and aeroacoustics of the isolated SbS rotor configuration in hover and free-air ($M_{tip} = 0.5$, $Re_{tip} = 1.44$ million).

6.3.1 Performance

The rotors (without the hub) of the six-passenger SbS air taxi are simulated in hover for different overlap configurations as mentioned before, from 0%, 5%, 15%, and 25% using OVERFLOW via Helios (V8.1.1). All overlapping configurations are simulated with a range of collective angles of 4°, 6°, 8°, 10°, and 12°. The rotor forces and moments for all simulation cases converge after 12 rotor revolutions, with a total of 8,640 timesteps. Tables 6.1 and 6.2 show the settings used for all simulation cases as well as the number of cores used including wall-clock time. From a previous study, Sagaga and Lee [62], used the modified Figure of Merit (FM) definition, which was originally developed for coaxial rotors [63], to represent total FM for SbS rotors. However, in a recent study performed for SbS rotors, Wright et al. [64] introduced a new definition of FM for overlap rotors using the projected area or A_{proj} (see Appendix B), as seen in Eq. C.1 (see Appendix C).

Figures 6.6 and 6.7 show both the thrust and torque coefficients of the left rotor for each overlap case. The thrust and torque are very similar for different overlap cases. There is a slight drop in both the thrust and torque for a single rotor in the 15% and 25% overlap cases. However, in figures 6.6(b) and 6.7(b) for the combined rotors the results show the opposite in which the thrust and torque are higher for the 15% and 25% overlap than the 0% and 5% overlap cases. This difference is associated with the area equations that are used in

calculating the thrust and torque coefficients for a single rotor, πR^2, and combined rotors, A_{proj}.

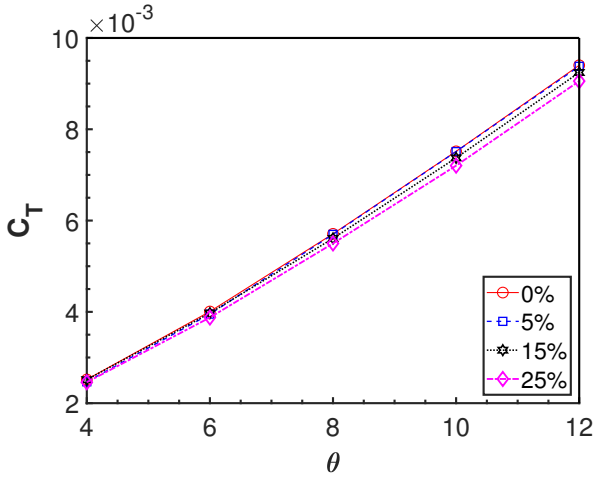

(a)

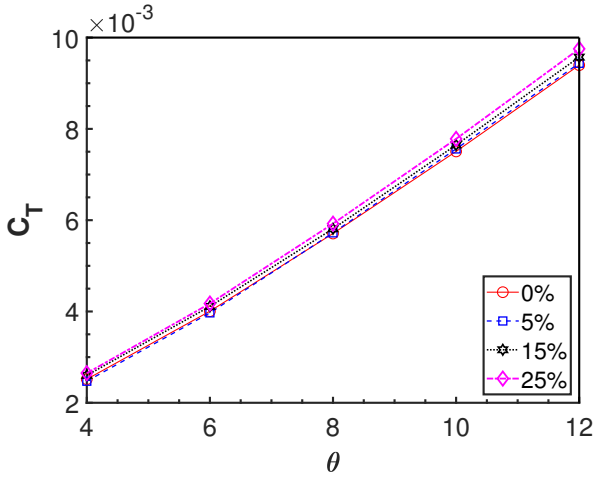

(b)

Figure 6.6: Thrust coefficient for different overlap cases (between overlap 0% – 25%) at all collective pitch angles (between 4°– 12°): (a) Single Rotor and (b) Combined Rotors.

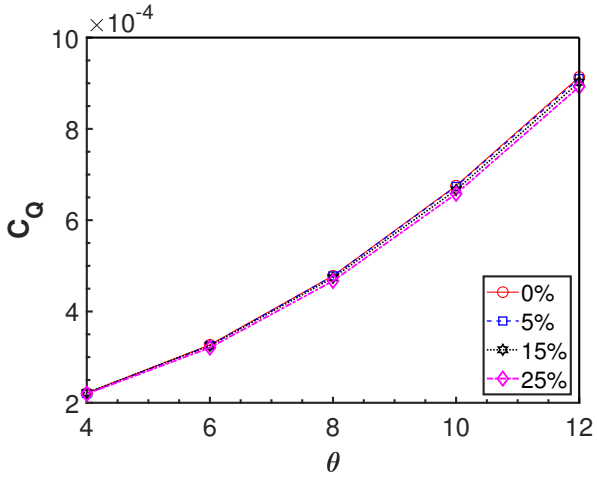

(a)

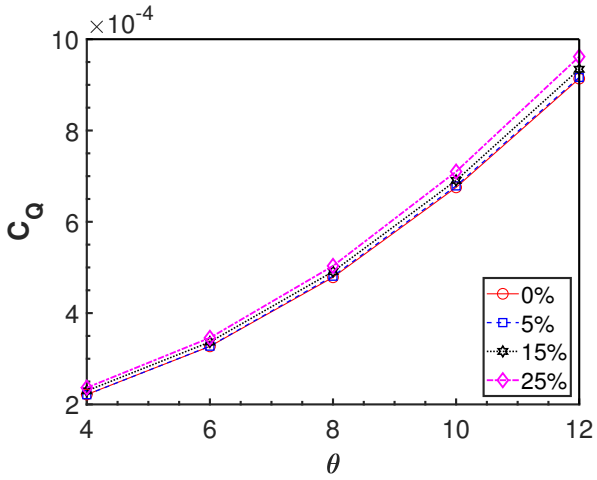

(b)

Figure 6.7: Torque coefficient for different overlap cases at all collective pitch angles: (a) Single Rotor and (b) Combined Rotors.

Figure 6.8 shows FM as a function of $\frac{C_T}{\sigma}$ for a single rotor and combined rotors for different overlap cases. The blade loading coefficient or $\frac{C_T}{\sigma}$, where C_T is thrust coefficient and sigma is rotor solidity which is the ratio of the total blade area to rotor disk area. The maximum FM is approximately 0.7. At lower thrust values, the FM is almost the same for all overlap cases. For higher thrust values, 25% overlap case shows a drop in FM for a single

rotor, which is mainly due to the increased induced velocity in the overlap region, which will be shown later. However, for a combined rotor, FM increases with the overlap percentage due to the increase in A_{proj}, which is consistent with experimental data [64].

Figure 6.9 shows the comparison of FM for the combined rotors as a function of the blade-loading coefficient between all the overlap cases at every collective pitch angle. Here, FM of the SbS rotors is shown for the last rotor revolution. FM increases with increasing the collective pitch angle and overlap region.

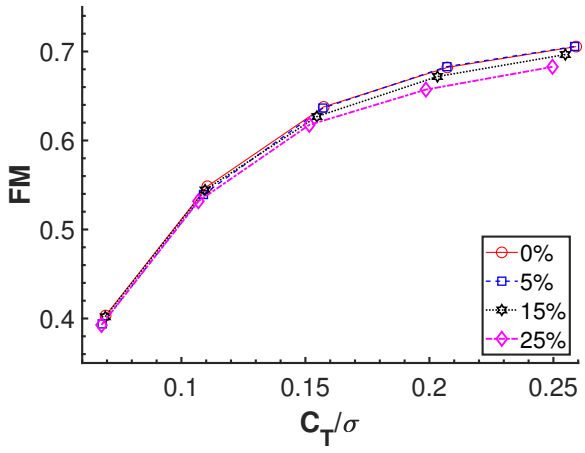

(a)

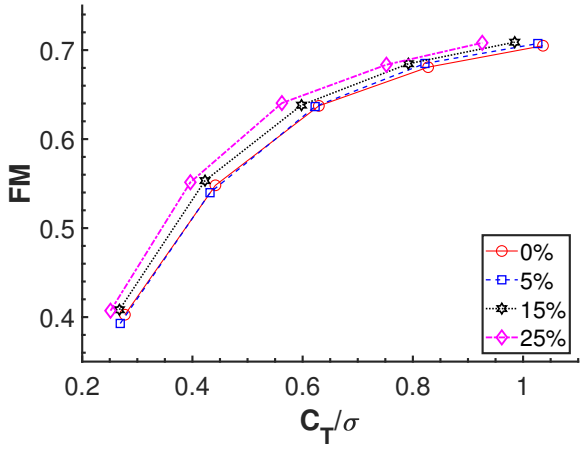

(b)

Figure 6.8: Figure of merit vs. the blade-loading coefficient for different overlap cases at every collective pitch angle: (a) Single Rotor and (b) Combined Rotors.

Table 6.3 shows the percentage difference of FM for all overlap cases and collective pitch angles for combined rotors. The 0% overlap case is used as the baseline in which all other overlap cases are compared to. The 5% overlap case for the 4° and 6°collective pitch angle, shows a difference in FM from 1% to 2%. For the 15% and 25% overlap cases at the 4° collective pitch angle, there is a 1% difference in FM. For all overlap cases at collective pitch

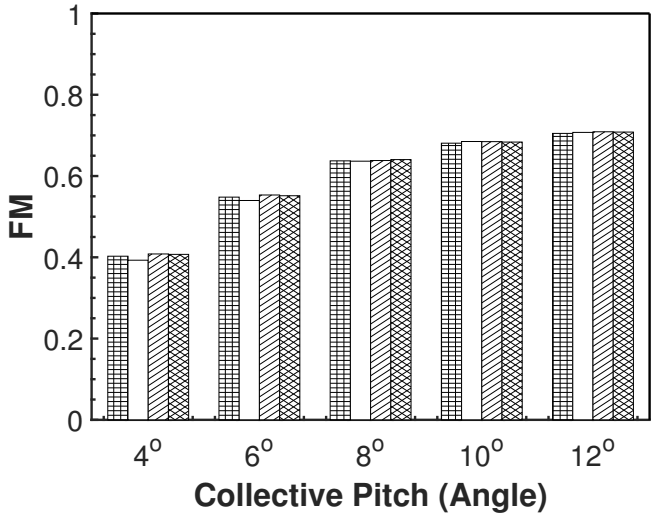

Figure 6.9: FM comparison of the combined rotors vs. the collective pitch angle between all the overlap cases: 0% overlap case (plus bar), 5% overlap case (empty bar), 15% overlap case (hatched bar), and 25% overlap case (cross bar).

Table 6.3: FM difference for all overlap cases and collective pitch angles of the combined rotors

Figure of Merit				
OL / **CP**	0%	5%	15%	25%
4°	0.403	0.393 (2.441%)	0.408 (1.379%)	0.407 (1.124%)
6°	0.548	0.540 (1.511%)	0.553 (0.958%)	0.551 (0.623%)
8°	0.637	0.636 (0.126%)	0.638 (0.127%)	0.640 (0.491%)
10°	0.681	0.685 (0.607%)	0.685 (0.563%)	0.684 (0.403%)
12°	0.705	0.707 (0.349%)	0.709 (0.568%)	0.708 (0.465%)

angles, 8°, 10°, and 12°, the difference in FM is less than 1%. Ventura Diaz et al. [37] showed that 15% overlap configuration achieves the highest lift-to-drag ratio in forward flight. However, how much FM varies in hover with different overlap percentages should be

carefully considered for the final selection of the best overlap case.

6.3.2 Flow Physics

Figures 6.10 – 6.13 show the iso-surface of the Q-criterion with the vorticity magnitudes colored for the 0% and 25% overlap cases at three collective pitch angles (4°, 8°, 12°). Highly complicated flow patterns are observed in the middle of the two rotors even at 0% overlap, which will induce the variance and fluctuation of the performance and blade aerodynamics. As shown in Figure 6.14, the rotor tip vortex is found to be broken down in the overlap region or the wake age of 360° (when the first blade from both rotors reach the 270°azimuth). This broken-down tip vortex develops into worm-like eddy structures, as seen in figures 6.10 – 6.14. As the overlap distance reduces, the rotor-to-rotor interactions intensify. It can be seen that the flow structures are similar for all the overlap cases at each collective angle. However, the distinct difference of the tip vortex and blade interaction is visualized.

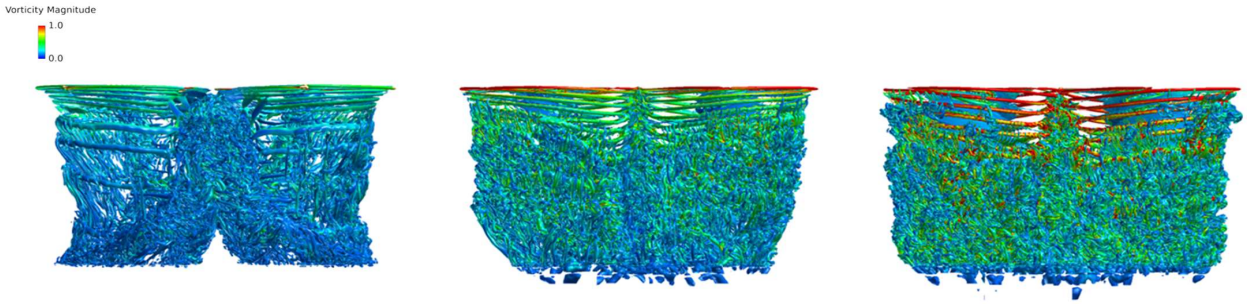

Figure 6.10: Iso-surfaces of the Q-criterion colored by vorticity magnitude for the 0% overlap case at 4°, 8°, and 12°.

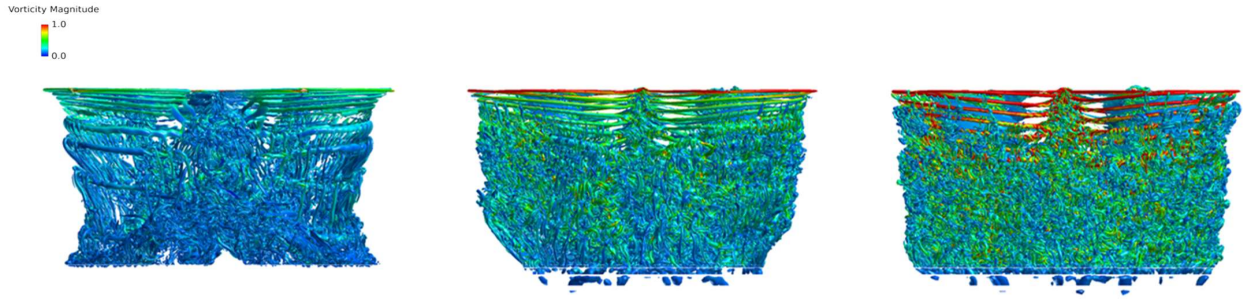

Figure 6.11: Iso-surfaces of the Q-criterion colored by vorticity magnitude for the 5% overlap case at 4°, 8°, and 12°.

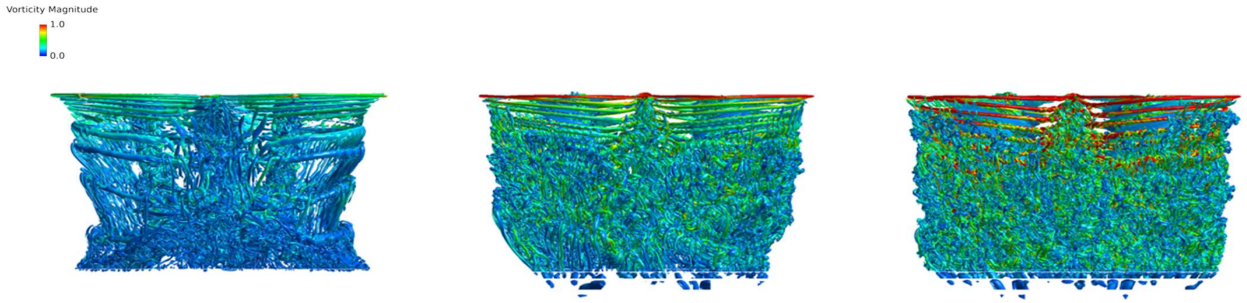

Figure 6.12: Iso-surfaces of the Q-criterion colored by vorticity magnitude for the 15% overlap case at 4°, 8°, and 12°.

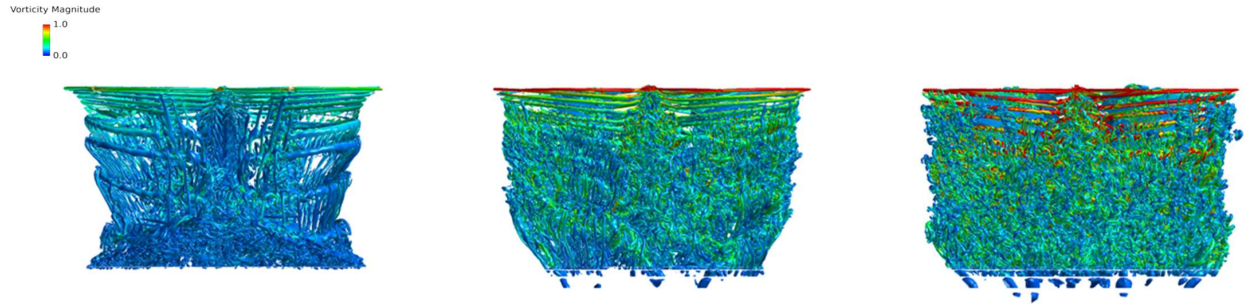

Figure 6.13: Iso-surfaces of the Q-criterion colored by vorticity magnitude for the 25% overlap case at 4°, 8°, and 12°.

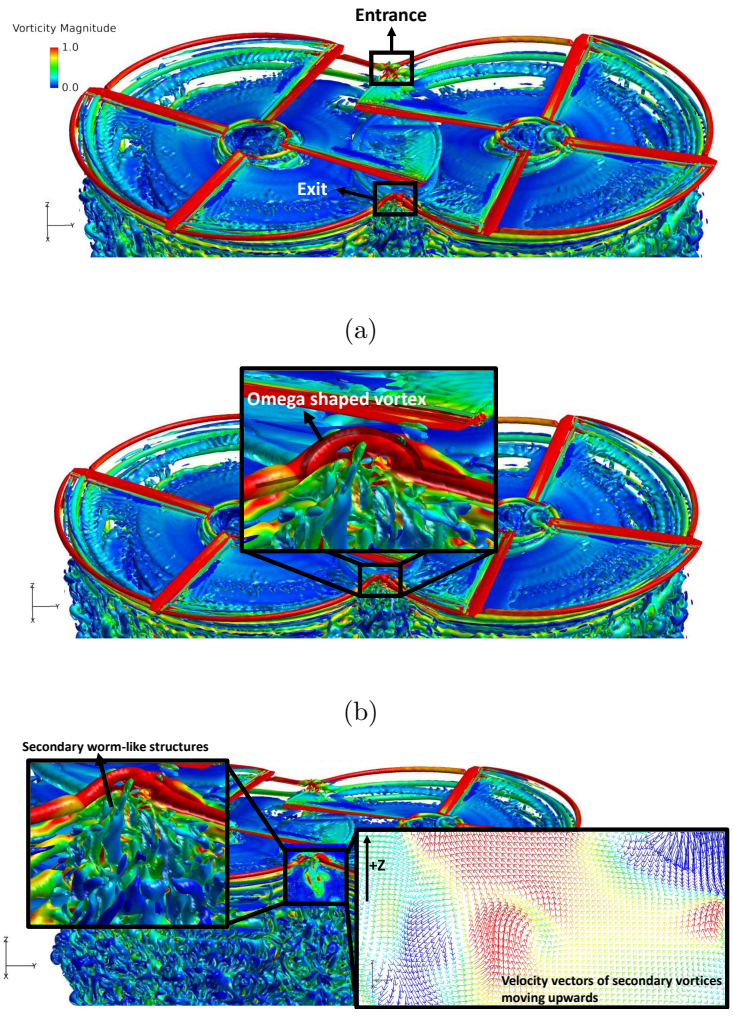

Figure 6.14: Iso-surface Q-criterion colored by the vorticity magnitude for 25% overlap case: (a) entrance and exit points of the overlap region, (b) Omega shaped vortex structure, and (c) small secondary worm-like structures.

Figure 6.14(a) shows the entrance and exit of the overlap region at the 25% overlap case. The tip vortices are not clearly visible within the overlap region since they are rapidly convected to the downstream due to high induced velocities in the overlap region as shown in Figure 6.15. Also, in Figure 6.14(b), a formation of an Omega shaped vortex structure is shown as a result of a merge of the two tip vortices from each rotor when they enter and exit the overlap region. There are also smaller secondary worm-like structures moving

upwards in the +Z direction as seen in Figure 6.14(c), which are pulled by the circulation of the tip vortices. These small secondary worm-like structures were investigated in previous studies for isolated rotor cases [65–68], in which the grid resolution and sub-iteration convergence were studied on how each affects the formation of these secondary structures. For instance, Bodling et al. [65] leveraged Helios in conjunction with OVERFLOW to explore the impact of sub-iteration convergence and grid resolution. Their research suggested achieving an OVERFLOW sub-iteration residual decrease within the scope of 2.4 orders of magnitude and a SAMCart sub-iteration residual decrease within 1.25 orders of magnitude to effectively capture minuscule secondary vortex structures. They also advised utilizing the finest off-body grid resolution of 2.5% of the blade tip chord length. In our investigation, we implemented a total of 50 sub-iterations in OVERFLOW and 20 sub-iterations in SAMCart. We accomplished an OVERFLOW sub-iteration residual decrease of roughly 1.8 orders of magnitude and a SAMCart sub-iteration residual decrease of about 2.2 orders of magnitude. Even though the SAMCart residual decrease meets the suggested value, the OVERFLOW sub-iteration residual decrease is below the recommended value. Furthermore, our grid resolution of the 10% C_{tip} for the finest grid spacing is considerably coarser than the suggested value. Therefore, our simulations are not designed to accurately or quantitatively capture secondary vortex structures, and a qualitative behavior, such as upstream movement of secondary vortex structures, is only discussed in this section.

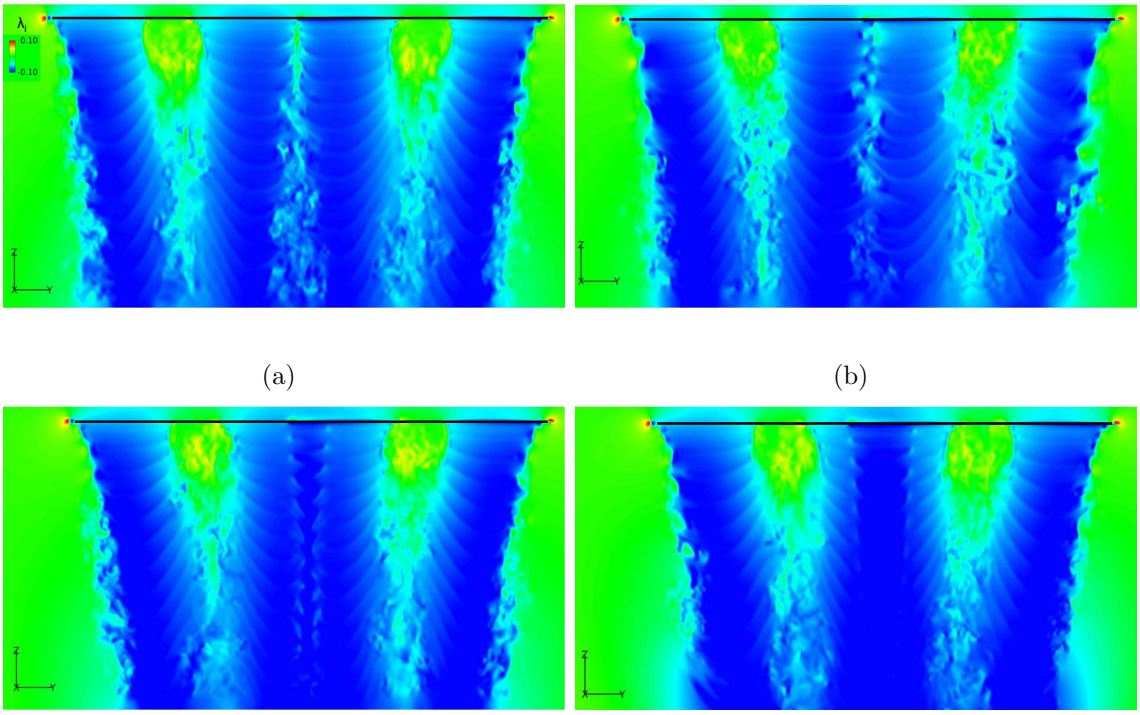

(a) (b)

(c) (d)

Figure 6.15: Comparison of λ_i (inflow ratio) between all of the overlap cases at 8° collective pitch angle. The black bar represents the rotor disk plane: (a) 0% overlap, (b) 5% overlap, (c) 15% overlap, and (d) 25% overlap.

Figure 6.15 shows a comparison of the induced inflow ratio for all the rotor overlap configurations at 8° of the collective pitch angle. It can be seen that the induced inflow ratio increases significantly at the center or the overlap region as the overlap region increases. The increased induced inflow ratio is due to the overlapped tip vortex and wake effects from both rotors. Furthermore, the higher induced inflow ratio in the overlap region pushes the blade-tip vortices in the downward direction. The increase in the induced inflow at the rotor disk in the overlapped region with increasing the overlap percentage reduces the angle of attack in the region. As a result, a significant reduction in the sectional thrust is expected in the overlap region as the overlap percentage increases. This will be further analyzed in

the following subsection.

Figure 6.16(a) shows a contour plot of the induced inflow ratio for the 0% overlap case at 8° collective pitch angle. Several horizontal planes below the rotor disk are added to quantify the inflow ratio downstream locations, as seen in figures 6.16(b) – (f). A slight asymmetry of the inflow ratio is found between the left and right rotors. As the overlap increases, the inflow ratio is contracted inward. There is consistent increase of the induced velocity at the center of the vehicle as the overlap percentage increases.

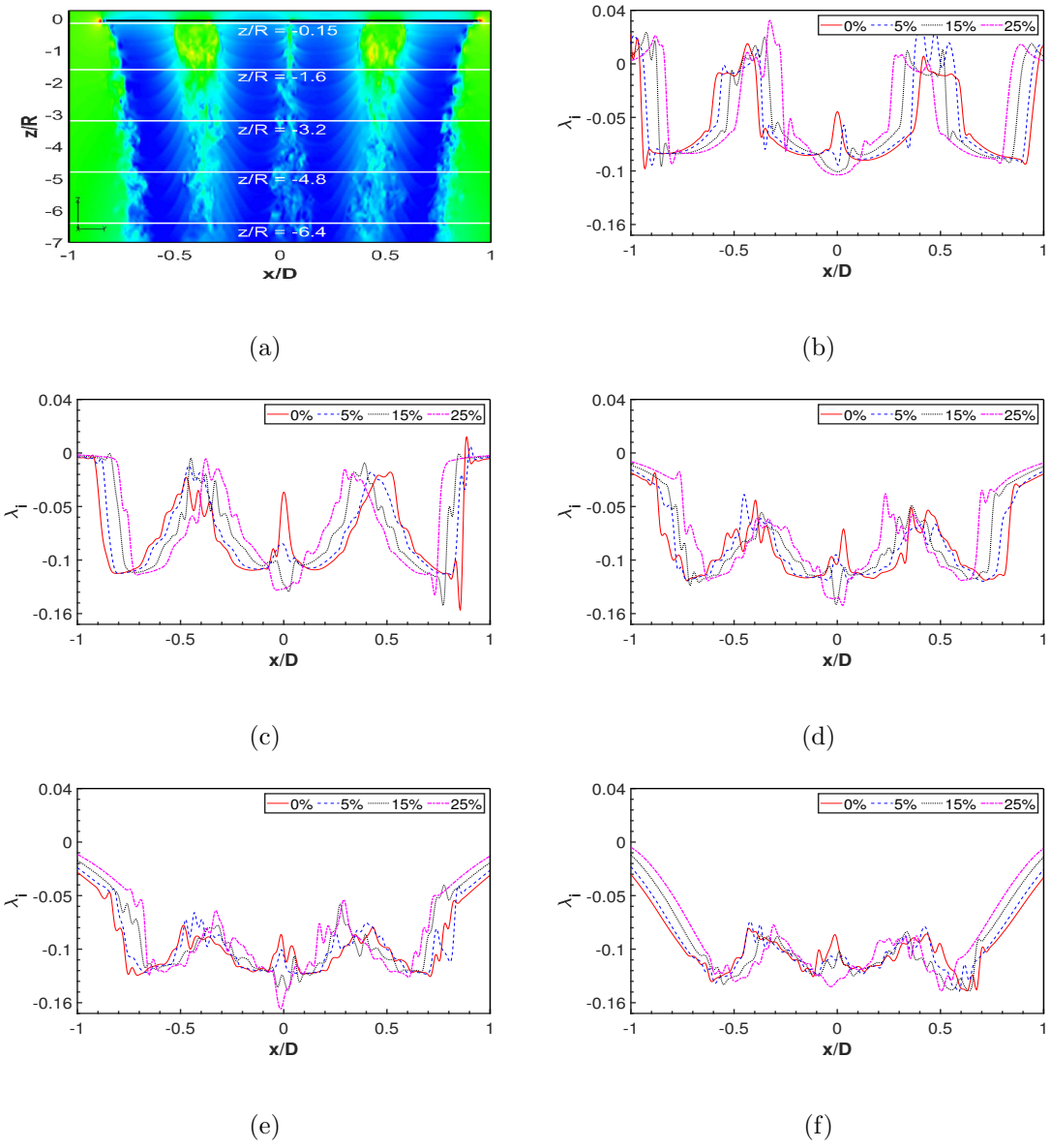

Figure 6.16: Comparison of λ_i (inflow ratio) between all of the overlap cases for the 8° collective pitch angle: (a) Measurement locations of inflow ratio, (b) z/R = -0.15, (c) z/R = -1.6, (d) z/R = -3.2, (e) z/R = -4.8, and (f) z/R = -6.4.

6.3.3 Aerodynamics

We investigate the variation of the aerodynamics, especially in the overlap region. Figures 7.14 – 6.20 show the normal force, chordwise force, and pitching moment on the rotor disk

for only one of the rotors (left rotor) due to symmetry at 8° collective pitch angle. There is a drop in the magnitude of the normal force at $\psi = 270°$ where the overlap region exists. The effect of overlap is more pronounced as the overlap region is increased. The negative chordwise force is found near the tip outside the overlap region. Within the overlap region, the positive chordwise force is observed, which contributes the increase in the torque and the degradation in FM. The distribution of the pitching moment also shows the change of the sign or near zero values in the overlap region.

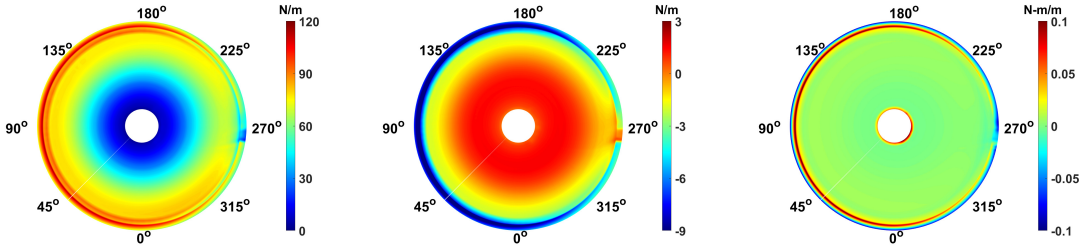

(a) (b) (c)

Figure 6.17: Normal force, chordwise force, and pitching moment for the 0% overlap case at 8°.

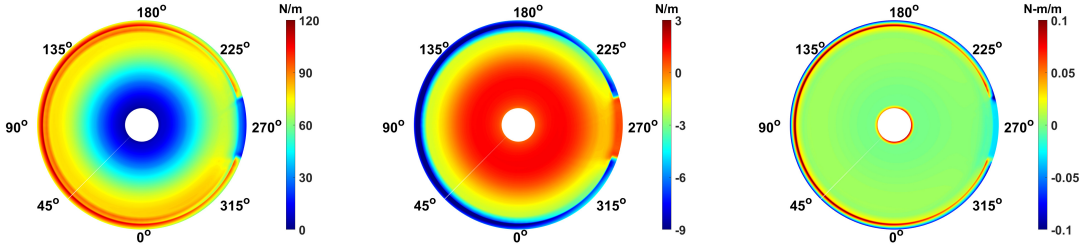

(a) (b) (c)

Figure 6.18: Normal force, chordwise force, and pitching moment for the 5% overlap case at 8°.

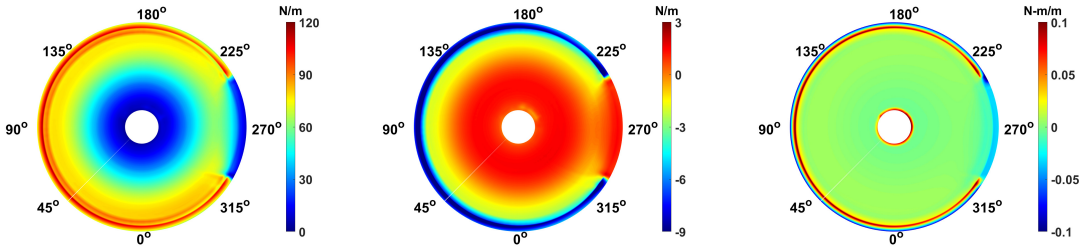

(a) (b) (c)

Figure 6.19: Normal force, chordwise force, and pitching moment for the 15% overlap case at 8°.

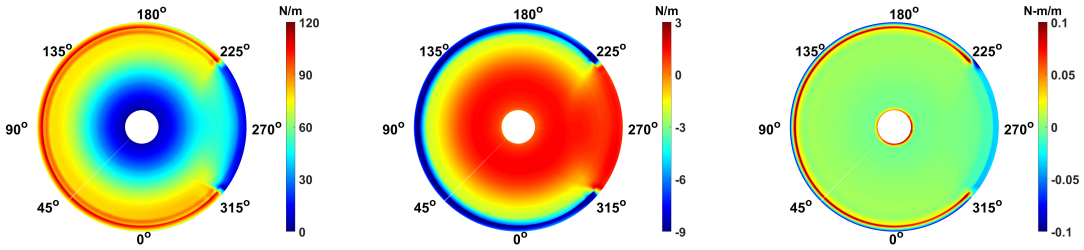

(a) (b) (c)

Figure 6.20: Normal force, chordwise force, and pitching moment for the 25% overlap case at 8°.

Figures 6.21 and 6.22 show how the normal force is significantly affected by the increase in the overlap region. Figure 6.21 compares the normal force for all overlap cases at different radial locations along the blade. It can be seen that the width, depth, and the rate of the change of the normal force significantly increase with increasing the overlap, especially for the 15% and 25% overlap configurations.

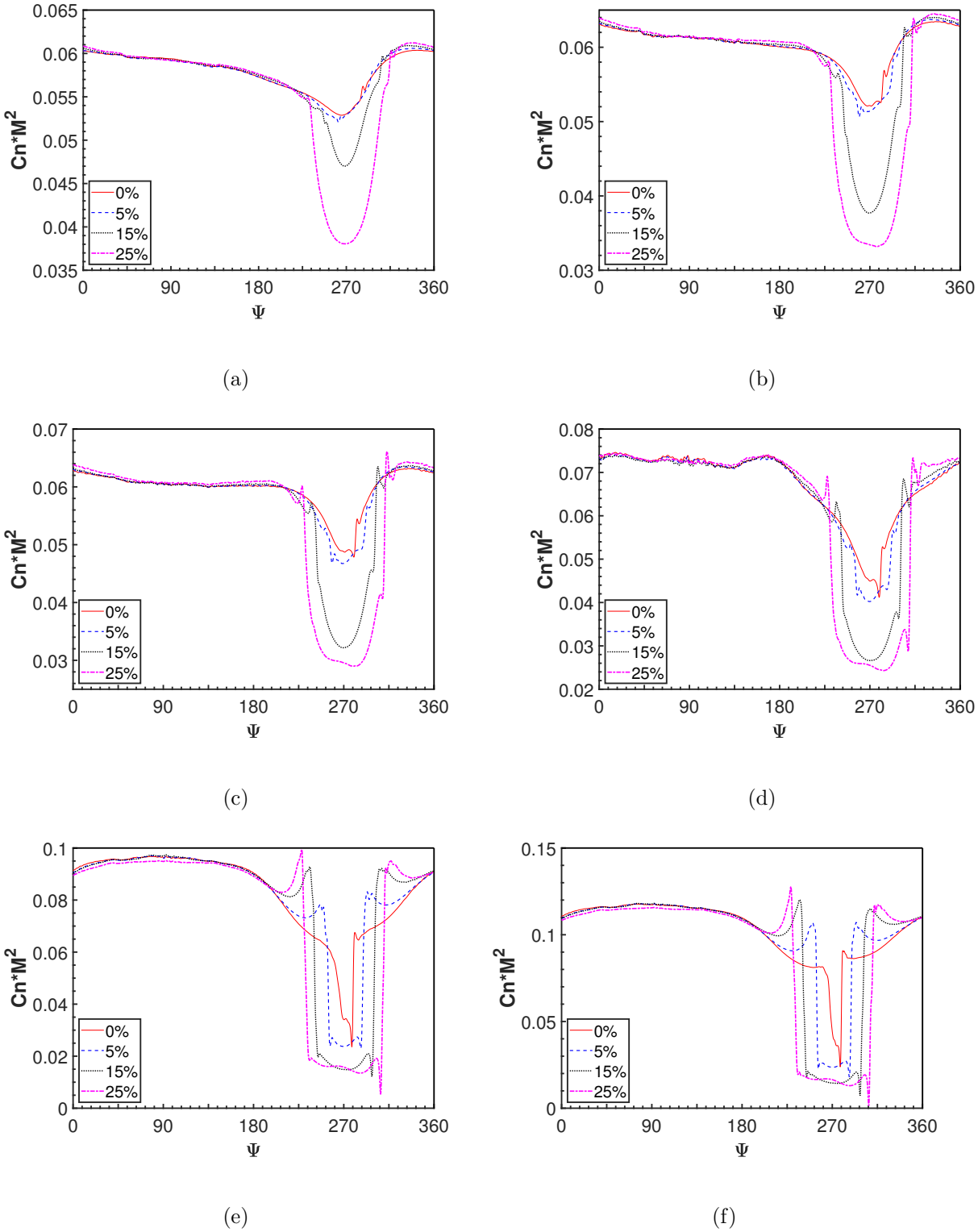

Figure 6.21: The effect of rotor overlap for all of the overlap cases on the normal force: (a) $r/R = 0.75$, (b) $r/R = 0.84$, (c) $r/R = 0.87$, (d) $r/R = 0.90$, (e) $r/R = 0.95$, and (f) $r/R = 1.0$.

Figure 6.22 shows how much the normal force (or thrust) is affected by the increase in the overlap region: the azimuthal range where it is affected, or width, (Figure 6.22(a)) and the extent of the change, or depth (Figure 6.22(b)). In figure 6.22(a), even 0% overlap case shows the overlap width, which is reduced near the tip. There is a significant increase in the width for 15% and 25% overlap cases. For the 25% case, the width is about 85° azimuthal angle and it is nearly constant along the blade radius. In figure 6.22(a), the depth significantly increases near the blade tip for all overlap cases. The 15% and 25% overlap cases show a similar depth near the tip, which is much larger than that of 0% and 5% cases.

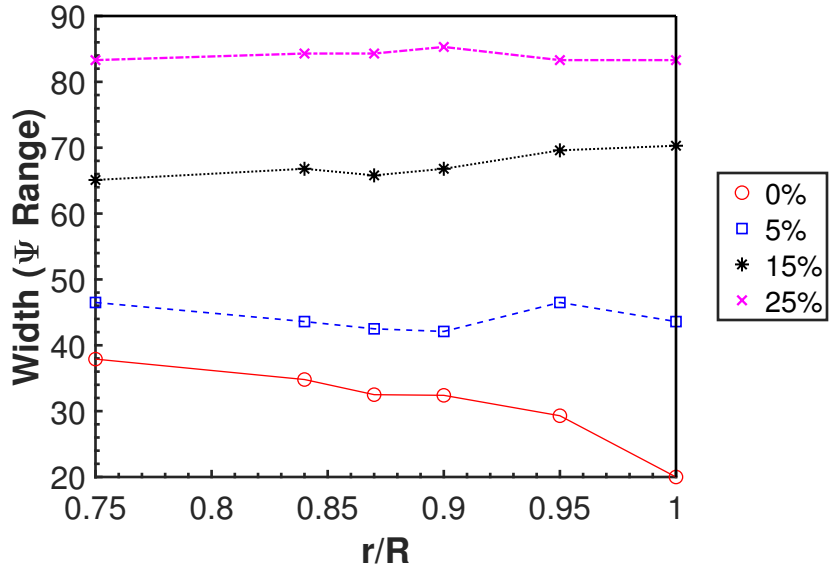

(a)

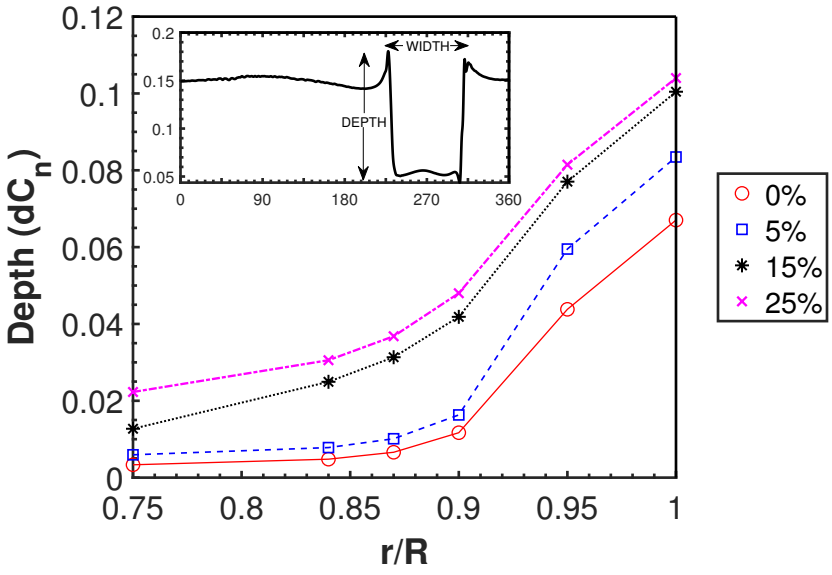

(b)

Figure 6.22: Overlap effect on the aerodynamic performance for all overlap cases: (a) Width and (b) Depth.

The calculated blade sectional thrust coefficient, $\frac{dC_T}{dr}$, can be seen in Figure 6.23 for all the overlap cases at a collective pitch angle of 8° for the azimuthal degrees of 0°, 90°,

180°, and 270°, only for the left rotor due to symmetry. It is shown that the sectional thrust decreases at $\psi = 270°$ with increasing an overlap region, which correlates with the normal force distribution in figures 6.17 – 6.20. The thrust reduction is more pronounced with increasing an overlap region in terms of both the magnitude and the extent toward the inboard section of the thrust drop. This thrust reduction is thought to be due to the increased induced velocities with two rotor tip vortex effects as shown in figures 6.15 and 6.16. Due to the periodic variation of the rotor thrust with the azimuthal angle, FM oscillates as shown in Figure C.1 (see Appendix C). A slight peak at about 95% of the blade radius is seen due to the swept tip.

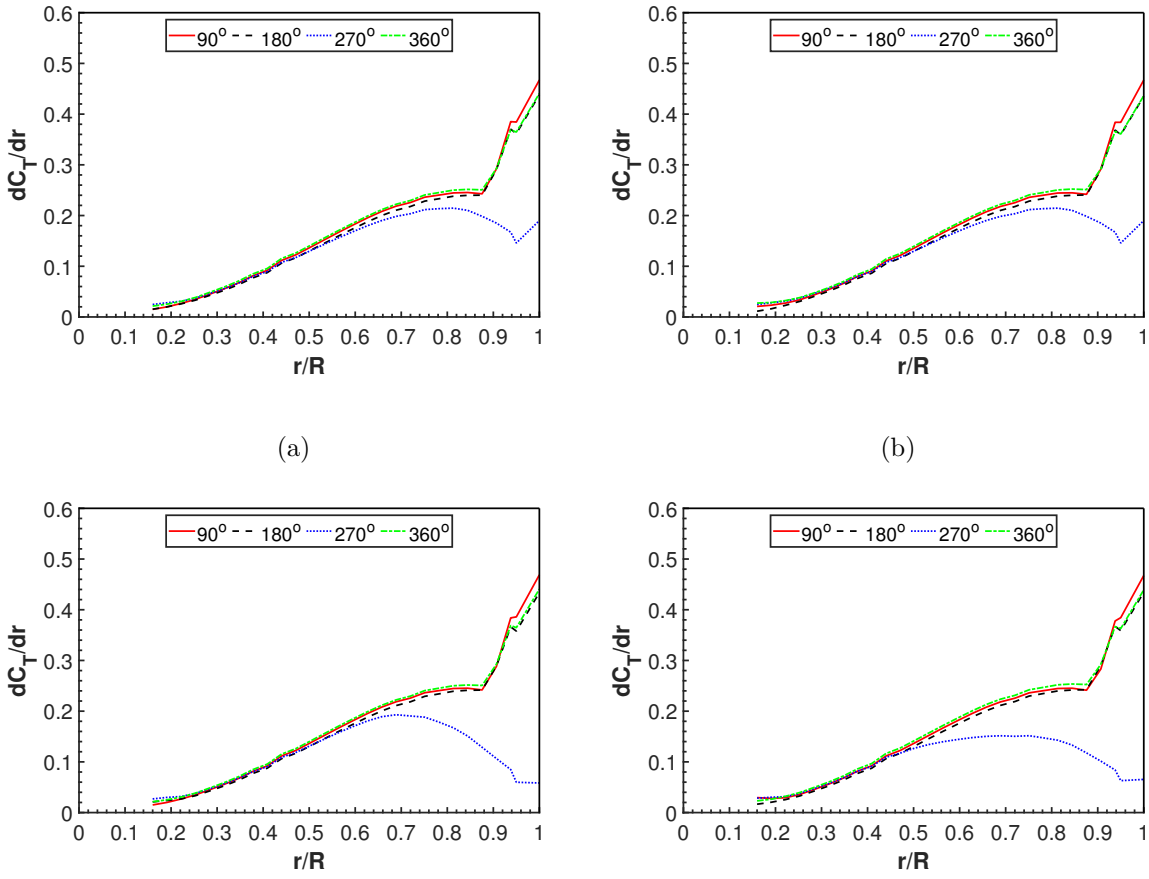

(a) (b)

(c) (d)

Figure 6.23: Blade sectional thrust coefficient at 8° collective pitch angle: (a) 0% overlap, (b) 5% overlap, (c) 15% overlap, and (d) 25% overlap.

6.3.4 Aeroacoustics

6.3.4.1 Acoustic Prediction and Noise Source Identification

Figure 6.24 shows a quantitative comparison of $dF_z/d\Psi$ of the right rotor for all rotor overlap configurations at the 75% span. Note that this derivate of the normal force is the main source of the loading noise as shown in Eq. (2.4). Due to symmetry between the left and right rotor of the distribution of $dF_z/d\Psi$, only the right rotor is analyzed here. It is clear that the magnitude of the BVI events are located within 225° and 315° azimuths or in the

range between the entrance and exit of the overlap. As the overlap percentage increases, the duration between the two peaks increases. It will be shown later that these peaks are associated with the rotor-to-rotor BVI at the entrance and exit of the overlap. The 25% overlap case shows significantly higher rotor-to-rotor BVI peaks located near 225° and 315° azimuths compared to the other overlap cases. It is anticipated that the 25% overlap configuration would result in the highest sound pressure level.

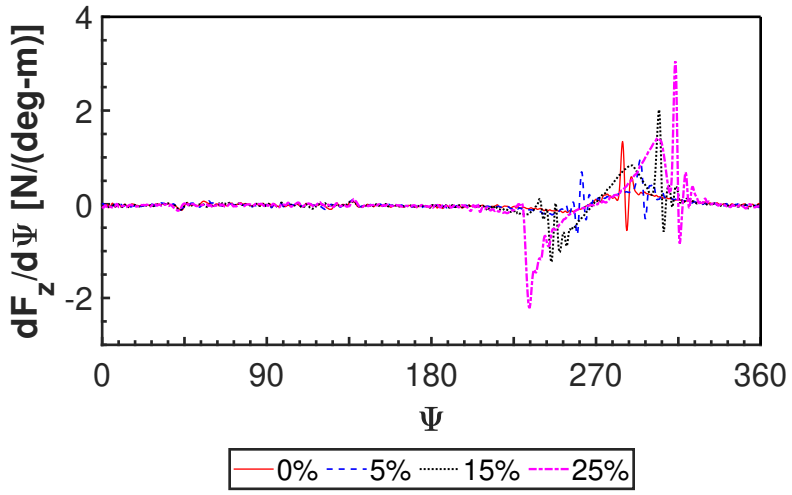

Figure 6.24: Comparison of $dF_z/d\Psi$ of the right rotor at the 75% span.

Figure 6.25 shows the acoustic pressure time history at an observer of 500 ft below the rotor for all the overlap cases at 8° collective pitch angle. It is found that the acoustic pressure magnitude increases as the overlap percentage increases. The large and distinct acoustic peaks occur when the rotor blades either enter or exit the overlap region, as will be shown in detail later. It is also found that the rotor-to-rotor BVIs at these two locations, as shown in figure 6.14(a), are the source of the large acoustic peaks. The isolated rotor acoustic results are added as a reference since this isolated rotor does not exhibit rotor-

to-rotor BVI. It is clearly seen that the acoustic pressure from the isolated rotor is almost negligible, which demonstrates the importance of the role of rotor-to-rotor BVI on the noise generation. In addition, there are also small pressure variations between each of the peaks, which are most likely to be from the interaction of the rotor blades with the small secondary worm-like structures as shown in figure 6.14(c).

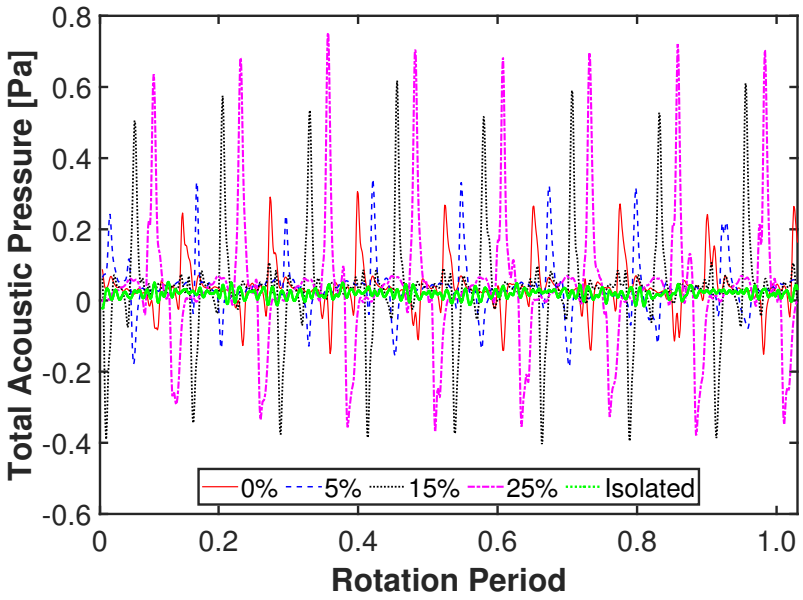

Figure 6.25: Comparison of the total acoustic pressure of all rotor overlap cases and an isolated rotor case at 8°.

The A-weighted sound pressure level (SPL) in the first 50 blade passing frequency (BPF) harmonics are shown in Figure 6.26, where the observer distance is set to 500 ft. It is found that the dominant tone noise occurs at the even BPF harmonics, which indicates the rotor-to-rotor interaction noise source as discussed earlier. At the 2nd, 4th, and 8th harmonics, the 25% overlap case has the highest noise levels. At higher harmonics, both the 15% and 25% cases show higher noise levels compared to the 0% and 5% overlap cases. For an isolated rotor, the tonal noise occurs at each harmonic of BPF, but the magnitude is significantly

lower than that of overlap cases.

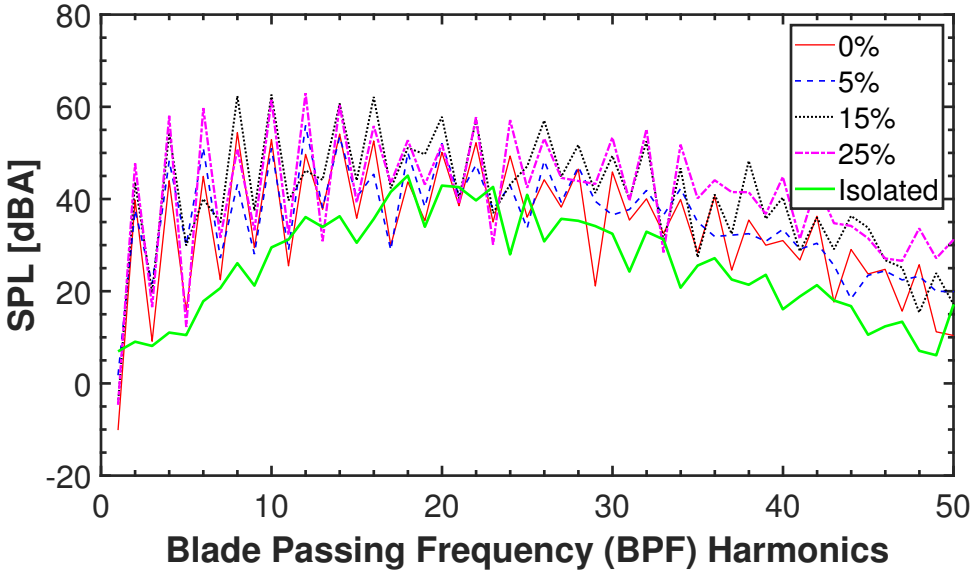

Figure 6.26: Comparison of A-weighted SPL between all overlap configurations at 8°.

Figure 6.27 shows the further correlation between the noise source contour map and the acoustic pressure time history at the 0% and 25% overlap cases. The blade from the right rotor coming out of the overlap region at the exit location just past the 270° azimuth (0% overlap in the first row of the second column) and about 315° azimuth (25% overlap in the second row of the first column) contributes to the large positive acoustic peaks at t = 0.1289 sec and t = 0.1389 sec respectively. In contrast, at t = 0.1242 sec and t = 0.1422 sec for the 0% overlap (first row of the first column) and 25% overlap (second row of the second column) cases respectively, the blade can be seen entering the overlap region, which contributes to the large negative acoustic peaks at the observer times. Figure 6.27 illustrates not only what is causing the large spikes in the total acoustic pressure, but also the effect of blades on the acoustic peaks. For the 0% overlap, one blade contributes a pair of the negative and positive peaks at a relatively short time as it passes through the entrance and exit of the overlap.

For the 25% overlap, a pair of the positive and negative peaks is contributed by two blades as one blade exits and the other blade enters the overlap region in a short period of time.

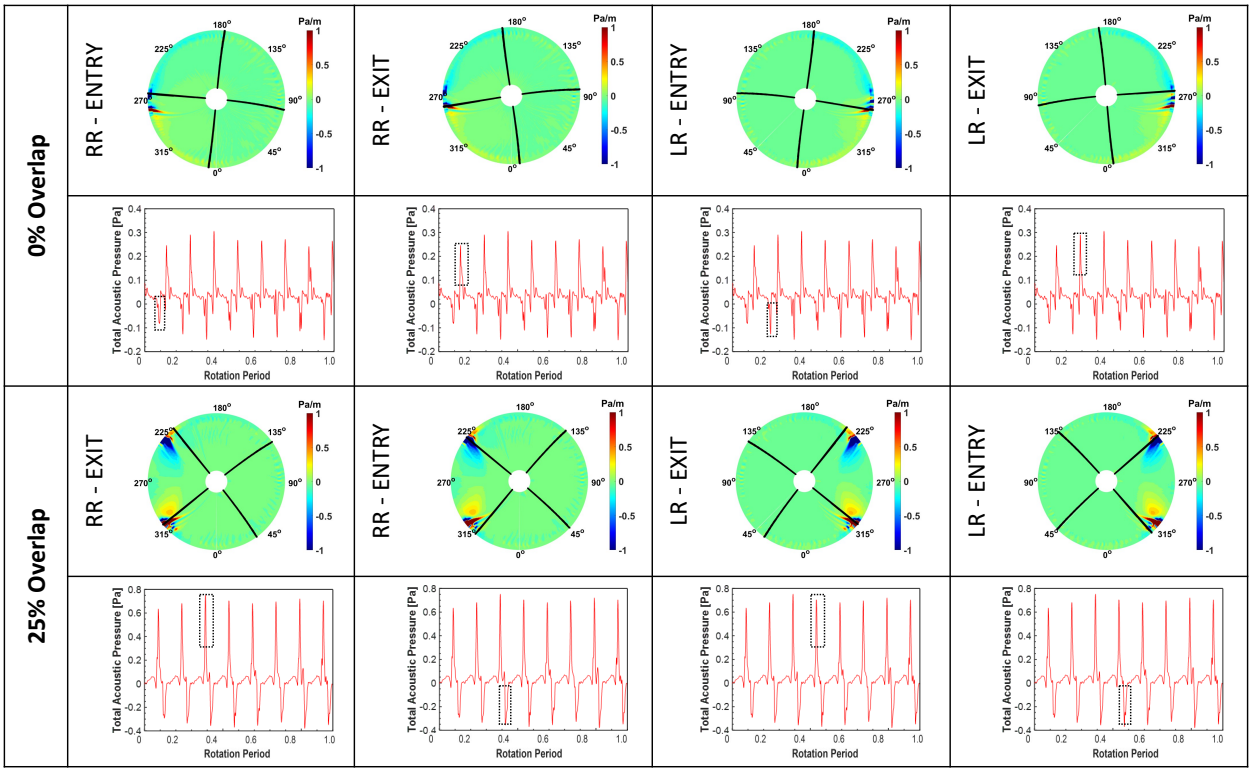

Figure 6.27: Acoustic pressure as a function of the observer time with entrance and exit locations visualizing the cause of the positive and negative peaks for both rotors (0% and 25% overlap case).

6.3.4.2 Noise Directivity

In this subsection, the noise directivity is studied. Figure 6.28 shows the A-weighted OASPL of each overlap case on a hemisphere with the radius of 10 times the rotor radius. In all the overlap cases, the color bar is kept the same for comparison purposes. The contour plots represent results from the top view of the hemispherical grid simulation cases with multiple observers. The front of the contour plots are near the entrance region of the rotors and the rear are near the exit region. All the overlap cases show a different radiation patterns from minor to significant differences. The contour plots of the 0% and 5% overlap cases in figures

6.28(a) and 6.28(b) respectively show asymmetry differences. However, the 15% and 25% overlap cases in figure 6.29(c) and 6.29(d) show significant discrepancies. These discrepancies are due to an acoustic interference, which can be seen as a strip or a line that begin from one end to the other end of the hemisphere. The regions of the interference is located near x = +10 m and y = +/- 20 m for the 15% overlap case and near x = -10 m and y = +/- 20 m for the 25% overlap case. This acoustic interference is investigated further by analyzing the left and right rotors individually. Acoustic simulations are performed for left and right rotors of the 15% and 25% overlap cases on a hemispherical grid. Similar acoustic interference is observed in a study from Poggi et al. [69] of a propeller configuration investigating not only Mach number effects, but also separation distance. From their analysis on the noise, they noticed wavy noise distribution resulting from constructive and destructive interference mainly due to the effect of the phase angle between the blades of the two propeller system examined.

The contour plots of the A-weighted OASPL for the left rotor and the right rotor of the 15% and 25% overlap cases are shown in Figure 6.29(a) – (d) respectively. It is seen that for 15% overlap the combination of each rotor generates the strong strip pattern due to the acoustic destructive interference between the two rotors while for 25% overlap the acoustic destructive interference is already visible in each rotor noise map, which indicates the acoustic destructive interference occurs between the blades rather than between the rotors. This will be proved by analyzing the pressure time history and noise source contour maps below.

Figure 6.30 shows the total acoustic pressure from the observer located in the acoustic interference region for the 15% and 25% overlap cases respectively. Figure 6.30(a) show for

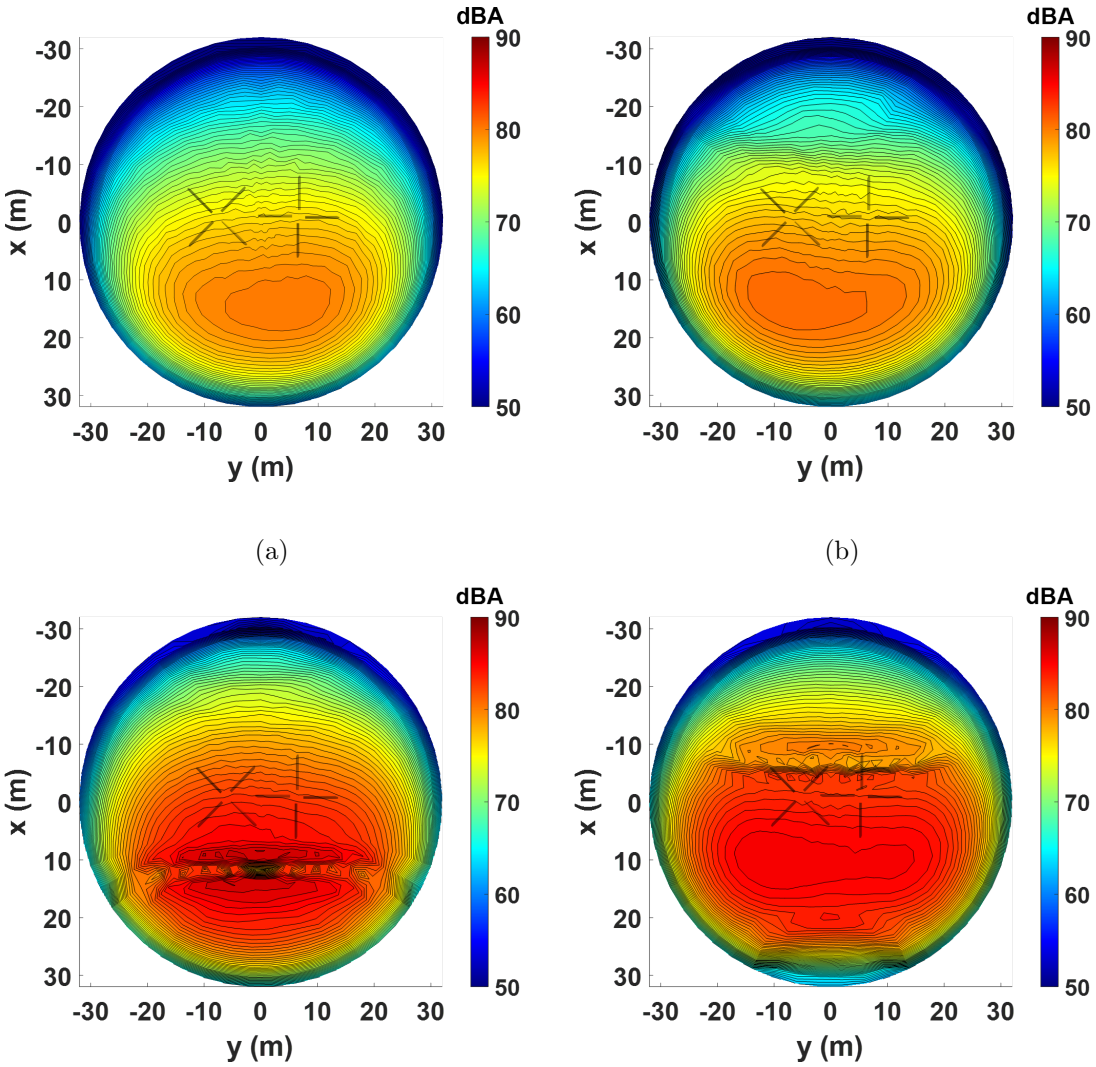

Figure 6.28: Comparison of OASPL on hemisphere grids: (a) 0% overlap, (b) 5% overlap, (c) 15% overlap, and (d) 25% overlap.

the 15% overlap case the positive and negative peaks from each rotor occur at almost the same time, resulting in the cancellation of the acoustic pressure or the acoustic destructive interference. However, in figure 6.30(b), the acoustic destructive interference or noise cancellation is not visible from each rotor for 25% overlap. Figure 6.31 shows the noise source contours of the left and right rotors including the location of events causing the acoustic radiation at the observer time in the interference region for 15% and 25% overlap cases. It can

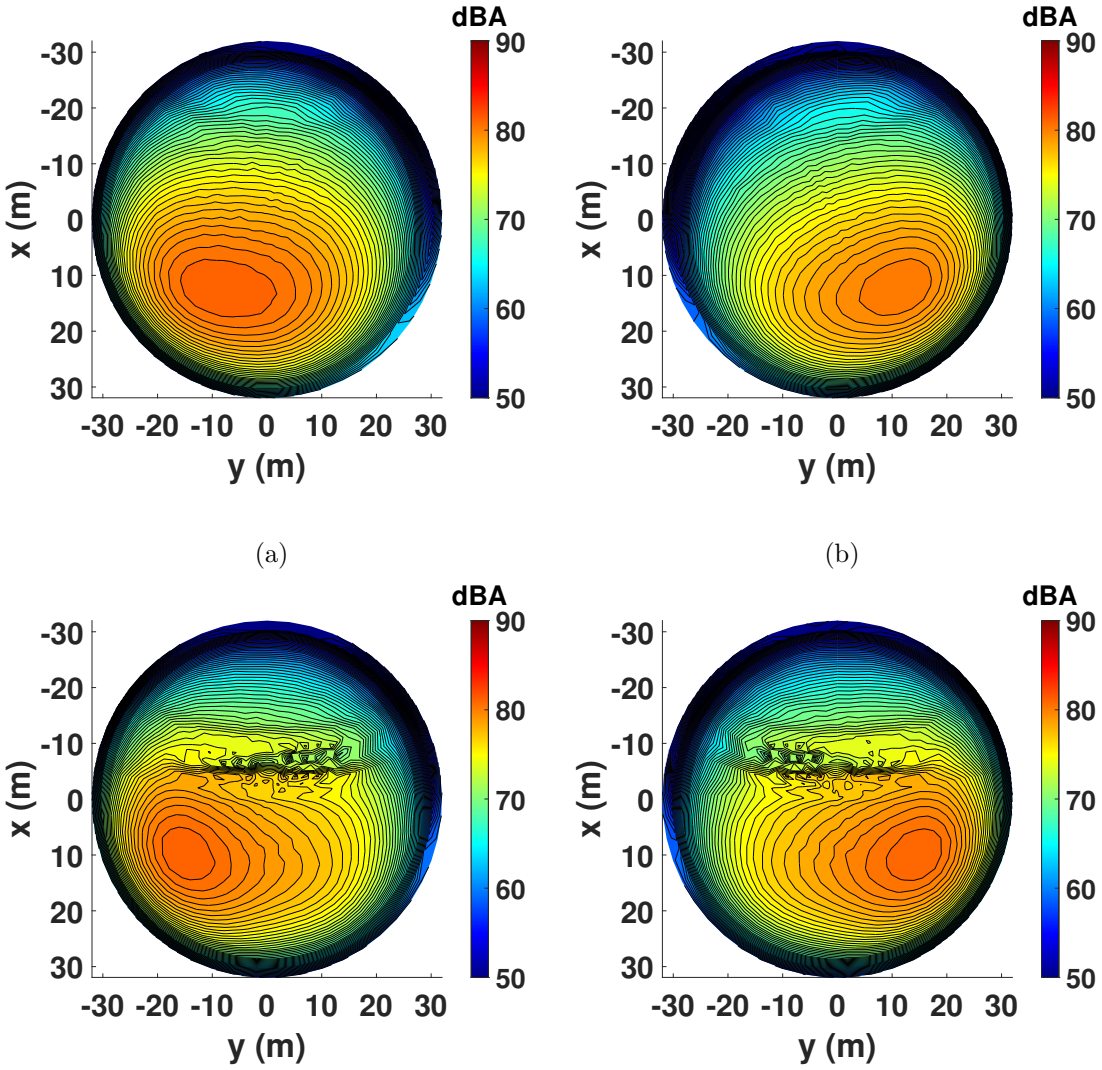

Figure 6.29: Comparison of OASPL: (a) Left rotor — 15% overlap, (b) Right rotor — 15% overlap, (c) Left rotor — 25% overlap, and (d) Right rotor — 25% overlap.

be seen for the 15% overlap case each blade generates either the positive or negative acoustic radiation at one observer time. However, for the 25% overlap case, two blades generate both the positive and negative peaks almost simultaneously so that the noise cancellation occurs in the interference region. This in-depth analysis reveals that the far-field noise propagation characteristics for rotor is very different for each overlap case so that the noise directivity can be distinct for each overlap case.

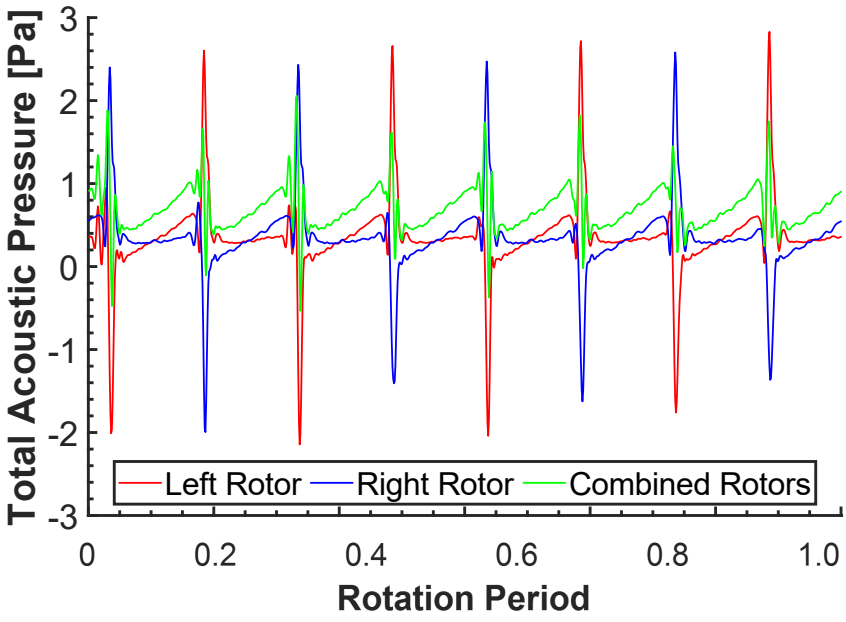

(a)

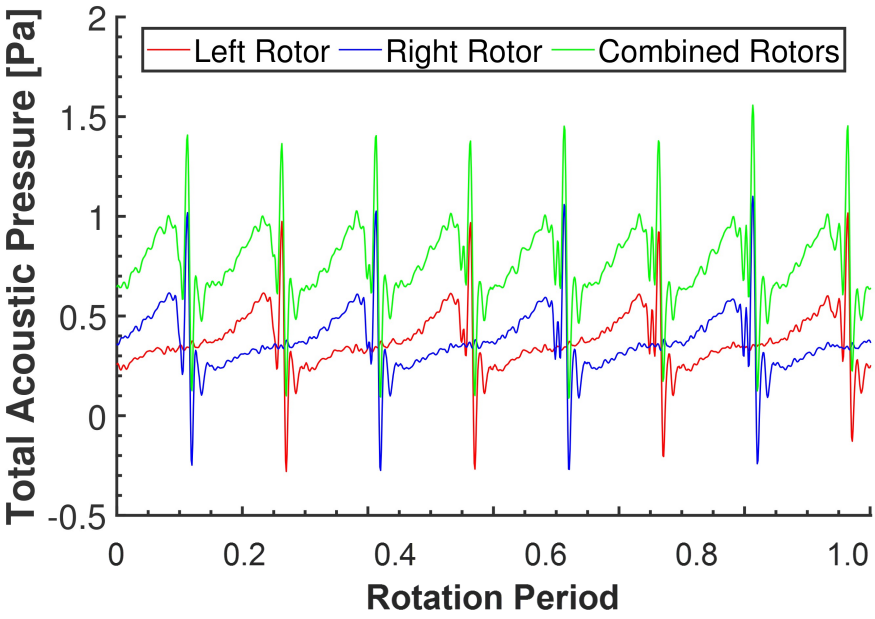

(b)

Figure 6.30: Comparison of the total acoustic pressure in the interference region: (a) 15% overlap and (b) 25% overlap.

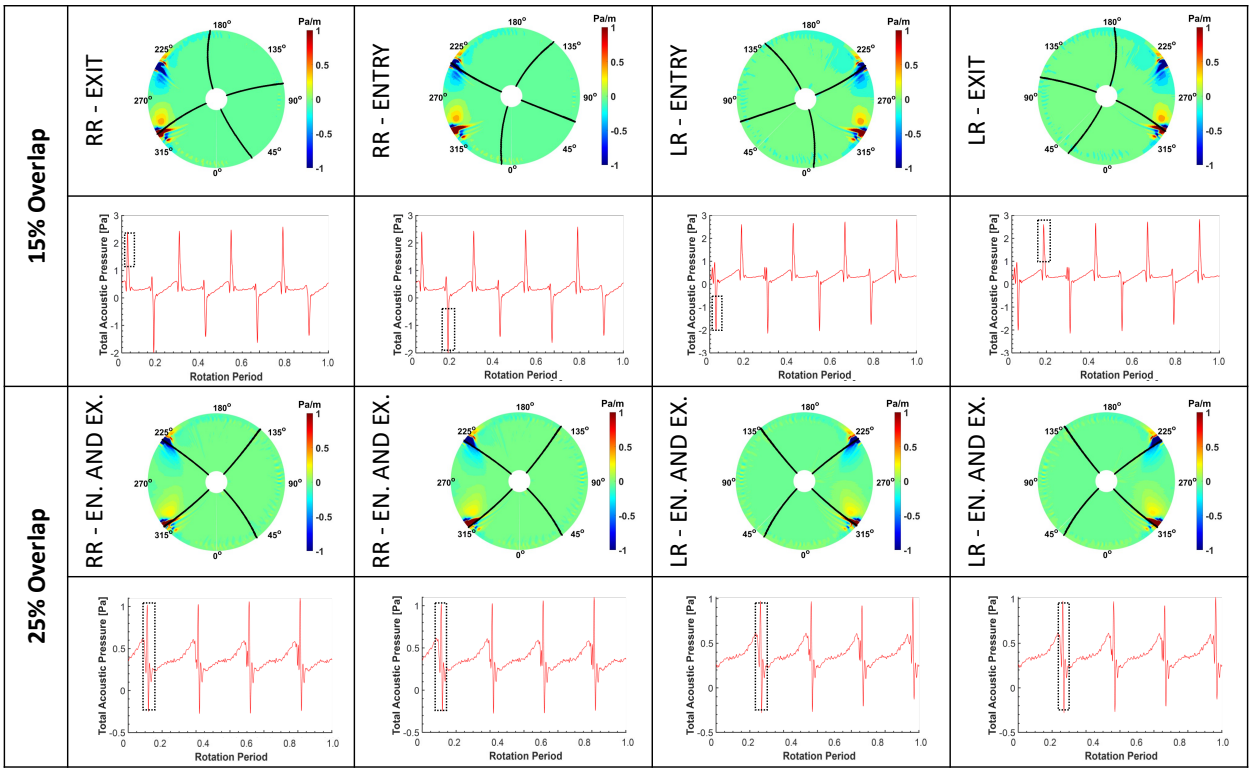

Figure 6.31: Acoustic pressure at the region of the acoustic interference visualizing the cause of the interference from the left and right rotors (15% and 25% overlap case).

6.3.4.3 Comparison with Background Noise Levels

As discussed in earlier sections, UAM aircraft noise can be one of the main barriers in gaining public acceptance especially if it exceeds background noise in a route where UAM aircraft will fly. In addition, as guidelines from one of the largest promoters of UAM, Uber Technologies Inc., the A-weighted SPL of UAM aircraft noise should be below 62 dBA at an altitude of 500 ft (152.4 m), needing to be 15 dB lower than that of a similar-sized helicopter noise at the same altitude and flight operating conditions [70]. Figures 6.32 and 6.33 show the unweighted one-third octave band sound pressure level (SPL) and A-weighted overall sound pressure level (OASPL) respectively for each overlap case. Both plots show a comparison of each rotor overlap configuration to the background noise, which include freeway, community,

park, and rural areas [20]. Figure 6.33 clearly shows that all of the overlap cases exceed the Uber noise guideline of 62 dBA at an altitude of 500ft (152.4 m). It can be seen that the OASPL is lower for the 0% and 5% overlap cases by about 3.2 and 2.7 dB respectively compared to the freeway noise when operating at 500 ft (152.4 m). Yet it exceeds the community, park, and rural noise. The same can be said for the one-third octave band SPL of the 0% and 5% overlap cases where, at lower frequencies, noise is lower than the freeway, rural, community, and park noise. However, there is a small range of frequency, where for all the overlap configurations, noise exceeds the freeway background noise. The 15% and 25% overlap cases show as much as 20 dB larger than all background noise, especially in a 100-2,000 Hz frequency range. It should be noted that the current calculations do not take into consideration broadband noise. As demonstrated in previous studies by Li and Lee [40, 71, 72] UAM broadband noise could increase significantly, especially at high frequencies, which is associated with trailing-edge noise [41].

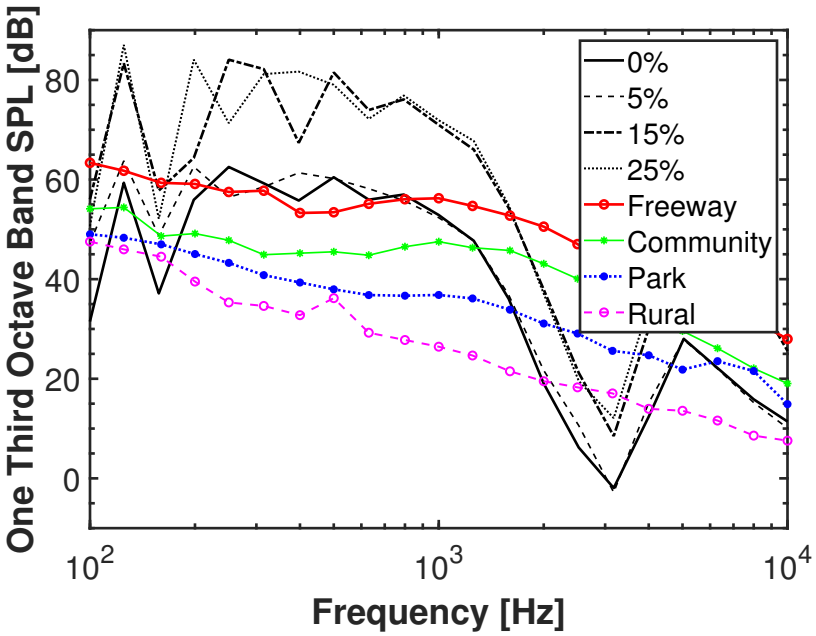

Figure 6.32: One-third octave band SPL for all the overlap cases in comparison with various background noise levels at 500 ft below the rotor.

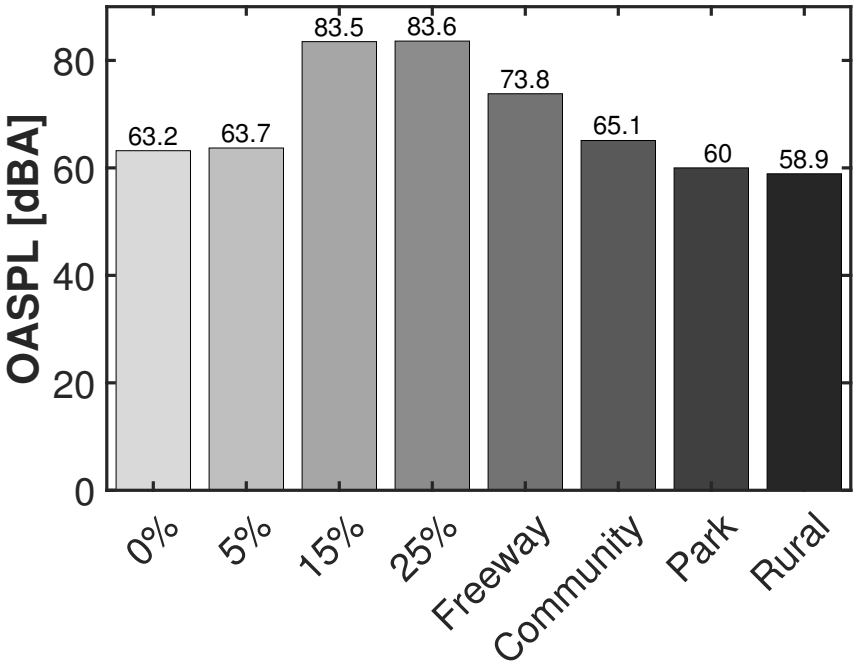

Figure 6.33: OASPL of each rotor overlap case along with background noise.

6.3.5 Conclusions

For a state-of-the-art UAM twin rotor configuration in hover, the effect of rotor overlap on the performance, aerodynamics, and aeroacoustics has been studied. CFD simulations were performed using a high-fidelity tool, CREATE^{TM}-AV Helios, in order to study the performance, aerodynamics, and acoustics of NASA's rotor configuration with 0%, 5%, 15%, and 25% overlaps in hover condition. Acoustic simulations based on an impermeable approach were carried out using an acoustics prediction tool, PSU-WOPWOP. The thrust, torque, and FM were analyzed at different overlap cases with various collective pitch angles. The tip vortex and induced velocity were analyzed. The effect of the overlap on the blade sectional aerodynamic loads were investigated. Connections between the different acoustic sources and the resulting noise were investigated for each overlap case. Comparisons between the rotor noise and various background noise were also carried out in order to assess UAM aircraft noise as well as its impact on urban communities.

The findings drawn from the results presented and analyzed in this work are as follows:

1. The area of overlap had discernible effects at both low and high collective pitch angles. At low collective pitch angles, FM experienced an increase ranging roughly between 1% and 2%. At high collective pitch angles, the FM increase was more marginal, at around 0.5%.

2. As the rotors enter and exit the overlap region, a merging of the two tip vortices from each rotor occurs, leading to the formation of an Omega-shaped vortex. Inside the overlap region, these tip vortices disintegrate, resulting in secondary worm-like structures that are drawn upward due to the circulation of the tip vortices. It was

determined that the induced velocity in the overlap region beneath the rotor plane intensifies with an increase in overlap percentage, largely attributed to the effect of the twin rotor tip vortices.

3. There was a noticeable decrease in the normal force exerted by the rotor in the vicinity of the overlap region. This reduction was found to result from the impact of the wakes from both rotors, which induced higher velocities on the rotor blades.

4. The primary sources of noise in the rotor with rotor overlap resulted from rotor-to-rotor BVIs as the blade enters and exits the overlap region, exhibiting strong even BPF harmonic noise. These interactions significantly intensify as the overlap increases, with the highest increase in noise observed at a 25% overlap.

5. Acoustic interference was closely examined for both the 15% and 25% overlap scenarios, which resulted from destructive interference. This phenomenon was noted as a significant decrease in acoustic pressure at certain observer points. The origins of this destructive interference varied between the 15% and 25% overlap scenarios, leading to distinct noise directivity patterns.

6. None of the rotor overlap configurations met Uber's noise guideline of 62 dBA at an altitude of 500 ft (152.4 m). In addition, at an altitude of 500 ft (152.4 m) in hover condition, various background noises did not fully mask the noise produced by the rotor. This necessitates the development of noise reduction technologies to improve public acceptance of UAM operations.

Chapter 7

Isolated Side-by-Side (SbS) Rotor In-ground Effect

This chapter presents the CFD and acoustic predictions from the simulations of the isolated SbS rotor with in-ground effect. It considers configurations with no rotor overlap and maximum rotor overlap in the hover condition at different heights above the ground. Details of the setup for the CFD and acoustic analysis are provided. The results presented in Chapter 6.3 for the isolated SbS rotor out of ground effect (OGE) are used here for comparison. Therefore, the in-ground effect cases are only simulated in this study.

7.1 Ground Effect: Goals and Objectives

Recent research has employed computational and experimental methods to develop a comprehensive understanding of UAM aircraft acoustics, focusing on key noise sources, noise directivity, broadband noise, and aerodynamic interactions in small, fixed-pitch, variable RPM rotor configurations [4, 39, 40, 72–77]. Acoustics also plays a crucial role in UAM aircraft design [78] and trajectory optimization [79], typically employing low-fidelity acoustic prediction tools for implementation [80]. However, most UAM noise studies did not

consider the ground effect on aerodynamics and acoustics. As the UAM field expands and produces diverse multi-rotor designs, significant interactional aerodynamics will occur when operating near ground surfaces. A few recent investigations have highlighted the importance of in-ground-effect (IGE) on performance, aerodynamics, control, and acoustics for dual rotors [32, 33] and quadcopter [81].

Ground effect affects rotorcraft performance due to the presence of a boundary (e.g., ground) inhibiting rotor wake development. However, the aerodynamics and acoustics of multi-rotor vehicles in these conditions are not yet fully understood. Previous experimental studies reported improvements in rotor thrust and power when a ground plane was present at distances of one or two rotor radii. When a rotorcraft hovers near the ground surface (e.g., at rotor heights of one or half-rotor diameter), the rotor wake initially propagates downward before rapidly expanding upon approaching the ground. This expansion changes the flow from vertical downwash to radial outwash, developing a radial wall jet that alters induced and slipstream velocities, affecting thrust and power [82]. Figure 7.1 compares wake behaviors. On the left, an out-of-ground-effect (OGE) rotor's wake is unaffected by the ground plane due to the large distance, except in the far wake region. Conversely, the right side shows an IGE rotor hovering near the ground surface (approximately two rotor radii) with substantial impact on thrust, power, and wake expansion. Although numerous past studies have investigated ground surface effects, most focused on isolated rotors or single main rotor full vehicle configurations.

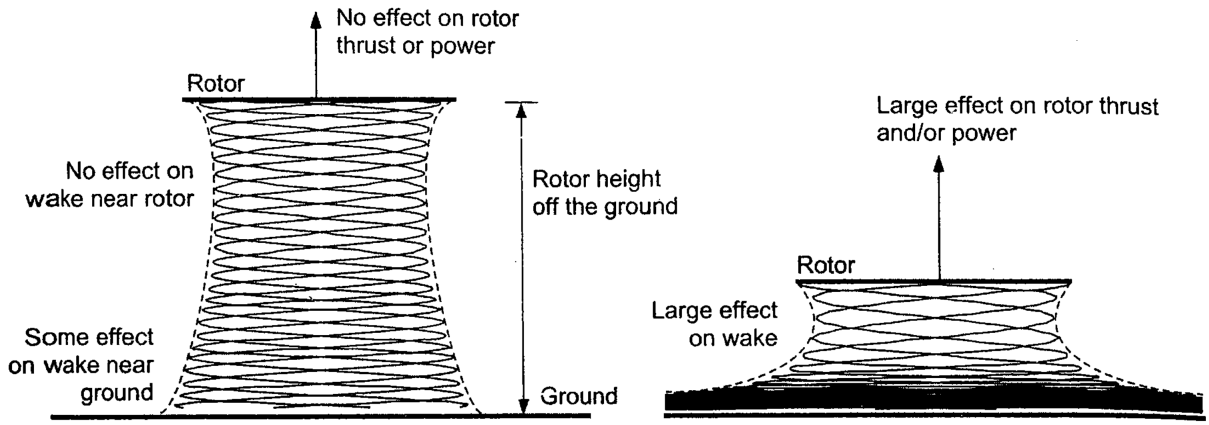

Figure 7.1: Wake from a hovering rotor [16]: (left) out of ground effect (OGE), (right) in ground effect (IGE).

The goal of this chapter is to investigate the impact of the ground plane on the performance, aerodynamics (including rotor-to-rotor interactions), aerodynamically induced noise of the SbS rotor (without the fuselage) in hover using high-fidelity computational fluid dynamics (CFD). The presence of the ground plane may cause significant variations in acoustic intensity and directivity at different SbS rotor heights above the ground and with distinct rotor overlap settings. We note that this investigation solely focuses on the tonal noise generated from rotor blades. Li and Lee [40, 71, 72, 83–85] highlighted the importance of broadband noise in rotorcraft noise including SbS rotor. However, broadband noise is not considered in this study.

7.2 Methodology

CFD simulations are performed again using CREATE^{TM}-AV Helios, with the OVERFLOW module for near-body calculations and SAMCart for off-body calculations as in the study of the isolated SbS rotor presented in the previous chapter (Chapter 6). However, there are some differences in the off-body meshes used in this study of ground effect including

boundary conditions and size of the computational domain.

7.2.1 CFD Simulation Setup

Time-accurate simulations of the present chapter employs a similar methodology from the isolated SbS rotor case study. Simulations of the in-ground effect cases has a time-step size varying from 10° to 2.0° azimuth in increments of 2° for 3,288 timesteps or the first 40 rotor revolutions. A restart is then initiated in the subsequent runs, switching to a finer timestep after we finish 40 rotor revolutions, where the finest timestep size of 0.25° azimuth is used for the final 5 rotor revolutions or 7,200 timesteps. We were able to reduce the overall computational time from 168 hours (one week) to 100 hours (about four days) by using this method. All CFD simulations were conducted on the Onyx (Cray XC40/50) high-performance computer (HPC) maintained by the U.S. Army Engineer Research and Development Center, one of the U.S. Department of Defense (DoD) Supercomputing Resource Centers (DSRC). A total of 21 nodes (924 cores) were utilized for all IGE simulations. Table 7.1 display the simulation settings and present the breakdown of the computational grid size and cost for each IGE simulation, respectively.

Table 7.1: Computational size and cost | All overlap cases

Near-body grid	
Per rotor blade	4.9 million
Both rotors	39.2 million
Off-body grid	
AMR OFF	179 million
AMR ON	705 million
Number of processors	924
Simulation time per rotor revolution (hrs)	28 | First 40 revs 72 | Last 5 revs

7.2.2 CFD Grids

The near-body grids of the SbS rotors used in the present work remain the same from the study in the previous chapter. However, the Cartesian grid in the off-body is set up differently for the in-ground effect cases while still using the automatically generated off-body computational domain by SAMCart using eight refinement levels with adaptive mesh refinement (AMR) activated after 40 rotor revolutions (3,288 timesteps). The spacing in the fixed refinement box is set to be 10% C_{tip}, matching the spacing on the outer boundary of the near-body volume grids, and its spacing does not change throughout the simulation duration, unlike the AMR region. Setting a fixed refinement box enveloping both rotors with an adaptive region set below the fixed refinement box for tracking the shedding vortices,

especially in the far-wake, can also help reduce the cost for these types of simulation cases. The size of the refinement box is set to $1.25R$ in the x-direction, $2.5R$ in the y-direction, $0.25R$ in the z-direction as shown in Figure 7.2. The AMR region has similar sizing to the refinement in the x and y directions; however, it is set to be $1R$ and $2R$ for H/D = 0.5 and H/D = 1 cases in the negative z-direction, as seen in Figure 7.2. The total number of grid points in the off-body grid is approximately 705 million grid points after 45 rotor revolutions. The domain size for the off-body is set to be 20 rotor radii away from the origin in every direction except in the negative z-direction due to the presence of the ground plane. Two heights are set for the rotors above the ground plane: half rotor diameter (H/D = 0.5) and one rotor diameter (H/D = 1), as shown in Figure 7.2.

The number of points for each rotor blade remain the same as the previous study at approximately 4.9 million, and a total of 39.2 million grid points are used for all eight rotor blades. For the off-body Cartesian volume grids, the finest spacing is still set to be 10% of the C_{tip}. However, both the off-body grid computational volume and the overall number of gridpoints is significantly larger when compared to the study conducted in the chapter prior to the present work as shown in Table 7.1.

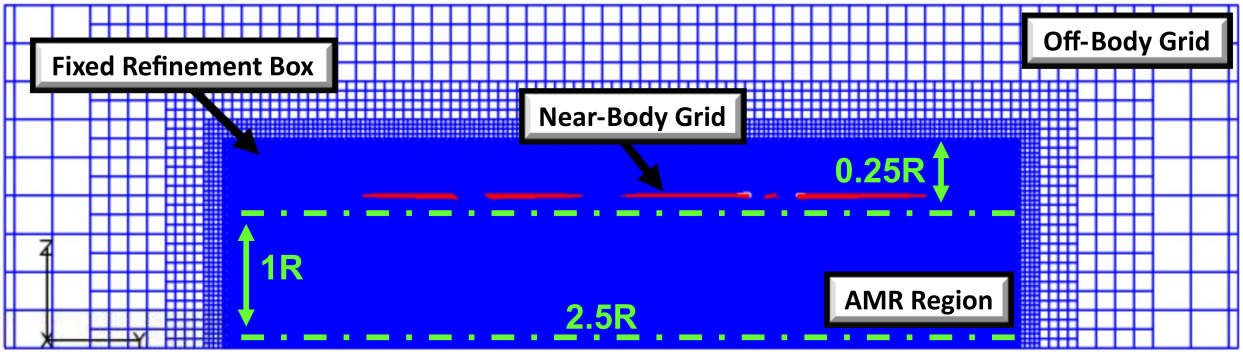

(a)

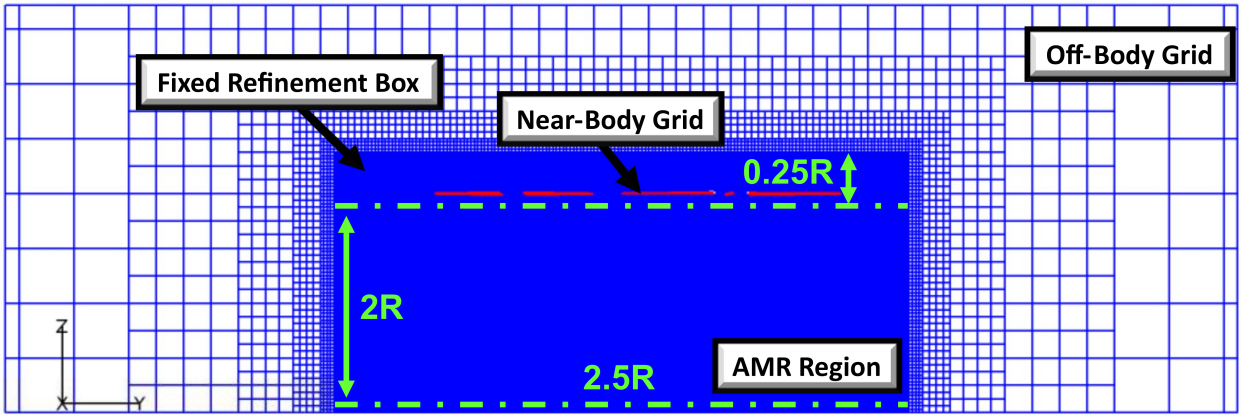

(b)

Figure 7.2: Off-body grids for the IGE cases for 0% overlap case: (a) H/D = 0.5 and (b) H/D = 1.

7.2.3 Acoustic Simulation Setup

An acoustic prediction tool, PSU-WOPWOP [26, 28], is used for the acoustic predictions in this chapter. Farassat's Formulation 1A [13, 86, 87] of the Ffowcs Williams and Hawkings (FW-H) equation [12] was numerically implemented in PSU-WOPWOP. The impermeable surface approach is used in the present work.

PSU-WOPWOP is used to perform all acoustic simulations for the single observer cases, an observer is positioned at the 90° elevation angle and half rotor diameter or one rotor

diameter below the rotor disk plane, as shown in Figure 7.3. Additionally, the effect of acoustic reflections off the ground is considered along with the aerodynamic influence of the ground. The acoustic reflections are simulated in PSU-WOPWOP using an image source method, creating a mirrored image of the SbS rotor below the ground plane at a distance equidistant to the SbS rotor located above the ground plane. For the multiple observer cases, a total of 2,500 ground observers are positioned in a rectangular grid at both one and two rotor radii below the rotor for both overlap cases to study the noise directivity as seen in Figure 7.4.

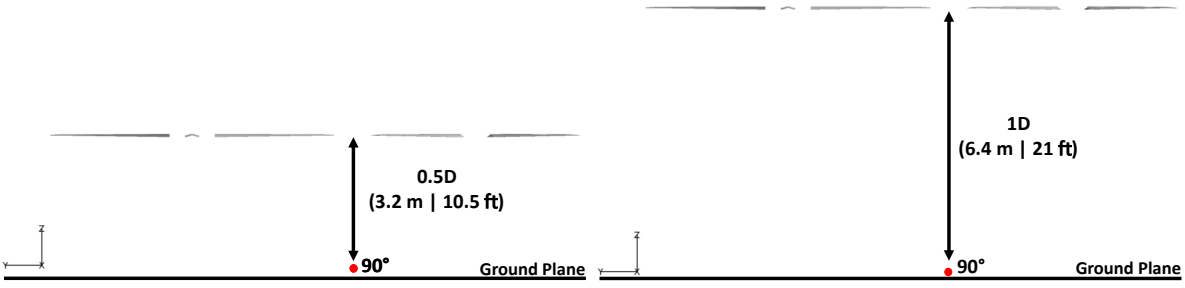

(a) (b)

Figure 7.3: Single observer location (Not to scale | Side view): (a) H/D = 0.5 and (b) H/D = 1.

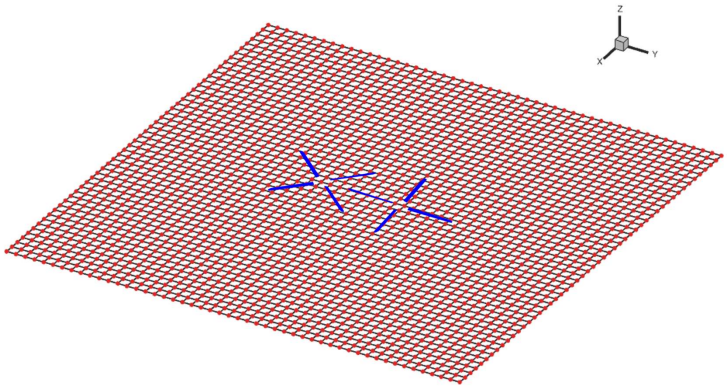

Figure 7.4: Location of the multiple ground observers (Not to scale).

7.3 Isolated Side-by-Side (SbS) Rotor In-ground Effect Results

This section presents the results for performance, flow physics, aerodynamics, and aeroacoustics for the in- and out-of-ground effect cases of the isolated SbS rotor configuration.

7.3.1 Performance

The rotors (excluding the fuselage and hubs) of the SbS rotor UAM aircraft were simulated in hover for the 0% and 25% overlap configurations using OVERFLOW in Helios, taking into account the ground effect. The simulations were performed with a collective pitch angle of 8° for both overlap configurations. A total of 45 rotor revolutions (10,488 time steps) were run to ensure full development of the flow field as the wake from the combined rotor system progressed towards the ground.-

Figures 7.5 shows a comparison between IGE and OGE scenarios for both the thrust and torque coefficients generated by the combined rotors, in both the 0% and 25% overlap cases. The maximum thrust and torque are achieved in IGE scenario with a rotor height of H = 0.5D. On the other hand, for the scenario with a rotor height of H = 1D, the thrust and torque at 0% overlap are comparable to those of OGE, however, the values are higher in the 25% overlap case compared to the OGE scenario. When comparing the 0% and 25% overlap scenarios, it can be observed that the 25% overlap scenario consistently results in higher values for both thrust and torque compared to the 0% overlap scenario.

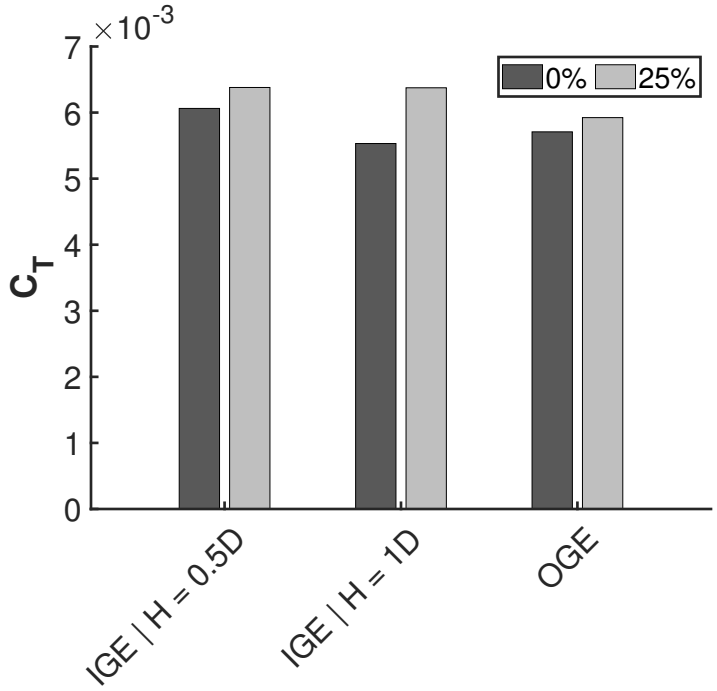

(a)

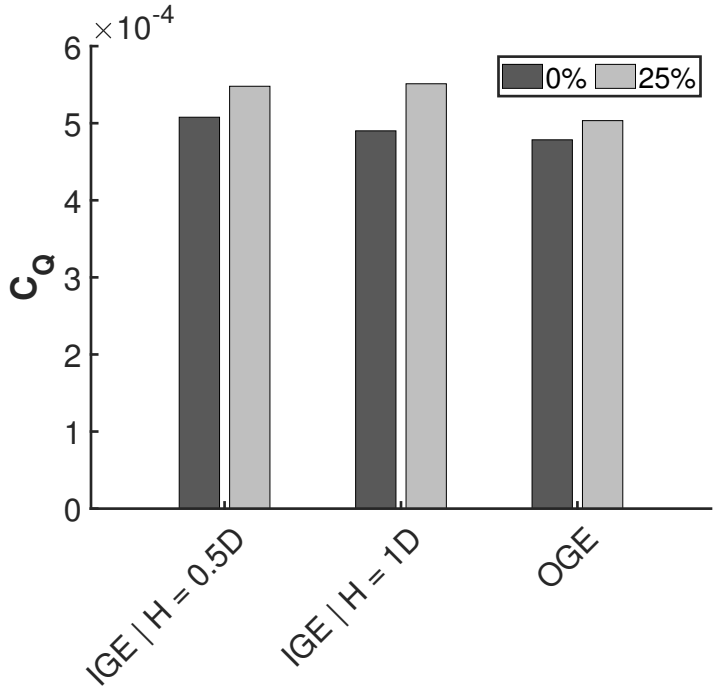

(b)

Figure 7.5: Performance comparison between IGE and OGE for the 0% and 25% overlap cases: (a) thrust coefficient and (b) torque coefficient.

Figure 7.6 displays the convergence of the Figure of Merit (FM) for the 0% and 25% overlap configurations, considering both rotor height cases of H = 0.5D and 1D, at a collective pitch angle of 8°. The definition of FM can be found in Eq. C.1 (see Appendix C). Similar to the thrust and torque coefficients, Eq. C.1 uses the projected overlap area A_{proj} (see Appendix B).

The convergence can be observed to be reached between 40 and 41 rotor revolutions. It is shown that the H = 0.5D case results in a higher FM compared to H = 1D for both configurations, but with increased fluctuations at the 0% overlap case. The 25% overlap case displays similar fluctuation magnitudes at both heights.

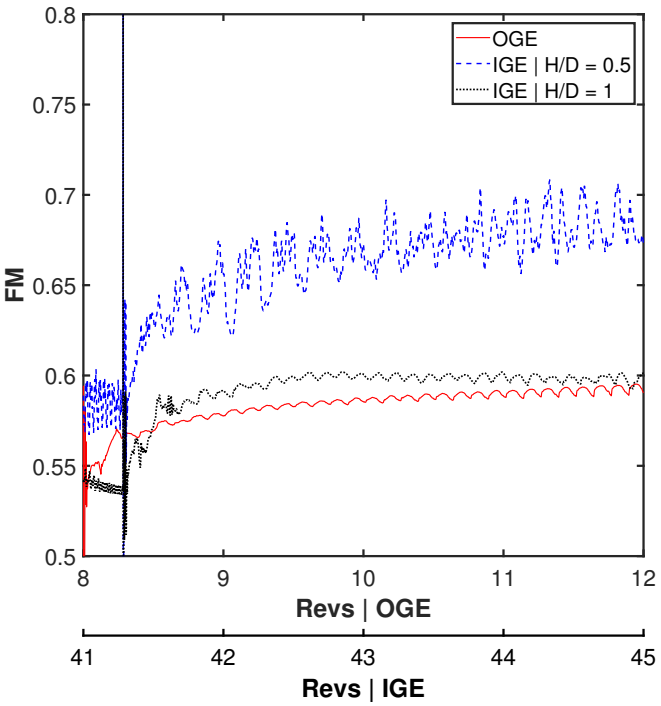

(a)

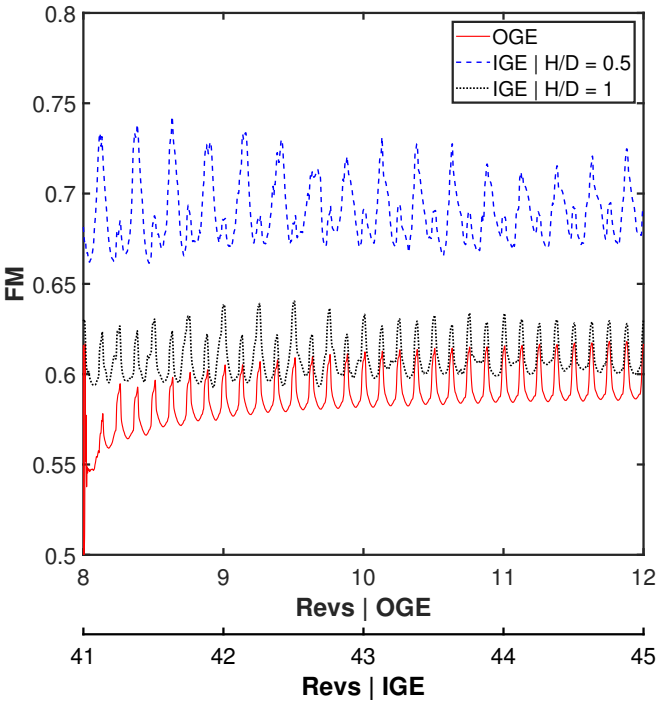

(b)

Figure 7.6: Figure of merit convergence plots for the 0% and 25% overlap cases: (a) 0% overlap and (b) 25% overlap.

Table 7.2 presents the percentage difference of FM for the 0% and 25% overlap configurations in IGE scenario, at a collective pitch of 8° for the combined rotors. The OGE cases for the 0% and 25% overlap configurations serve as the baseline for comparison with the IGE cases. The results show that the 0% overlap IGE case has a difference in FM ranging from about 9% to about 6% for rotor heights of H = 0.5D and 1D, respectively. The 25% overlap IGE case has a difference in FM ranging from about 3% to about 2% for rotor heights of H = 0.5D and 1D, respectively. As the overlap percentage increases, the influence of the ground plane on the performance decreases. The detailed flow physics related to this performance difference will be examined in the next subsequent section.

Table 7.2: FM difference for 0% and 25% overlap cases for the combined rotors

Figure of Merit						
CP\OL	0% (OGE)	0% (0.5D)	0% (1D)	25% (OGE)	25% (0.5D)	25% (1D)
8°	0.637	0.692 (8.621%)	0.674 (5.762%)	0.640	0.657 (2.689%)	0.653 (1.975%)

7.3.2 Flow Physics

Figures 7.7 and 7.8 depict the iso-surface of the Q-criterion, colored with the vorticity magnitude for the 0% and 25% overlap cases with in- and out-of-ground effect at 8° collective. The figures also show the entrance and exit regions of the overlap. In the 25% overlap configuration, there is a clear interaction between the tip vortices from the left rotor and right rotor blades at the entrance and exit regions at the given time step, which is a major source of noise and will be discussed in detail later. After this interaction, the tip vortices break down and become less discernible. The wake development exhibits significant differences, including the influence of not only the overlap region but also the ground plane on

the overall formation of the wake. It is shown that the vortices near the hub of each rotor move upwards, as well as the overlap entrance and exit regions at a rotor height of H = 0.5D, with the effect being more noticeable in the 0% overlap case than the 25% overlap case. In the outwash region, the flow transitions from mostly vertical to a radial outwash as it strikes the ground plane, developing into a radial wall jet moving away from the wake of both rotors. The reduced distance of the rotors to the ground plane can also intensify the interactions between the wake from the SbS rotors, upstream flow, and the rotor blades exiting and entering the overlap region. Additionally, smaller worm-like structures moving in the upward (+z direction) direction can be observed, which have been identified as secondary vortex structures and previously investigated in studies of isolated rotor cases [66, 68, 88]. The number of secondary vortex structures decreases as the rotors approach the ground. In other words, the wakes become more stabilized when the rotors operate near the ground.

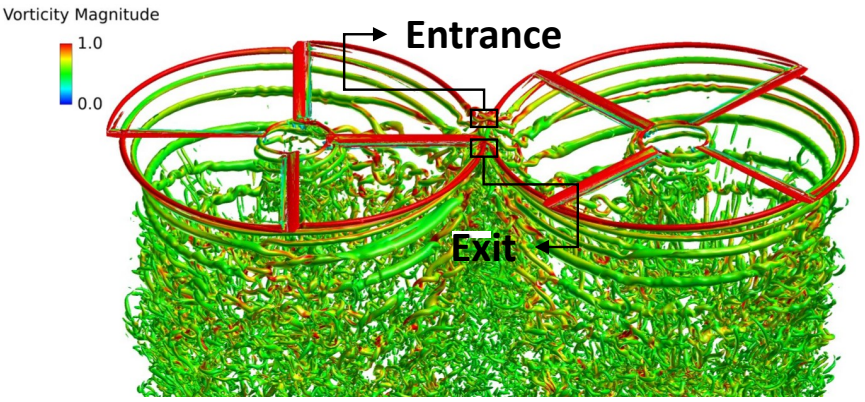

(a)

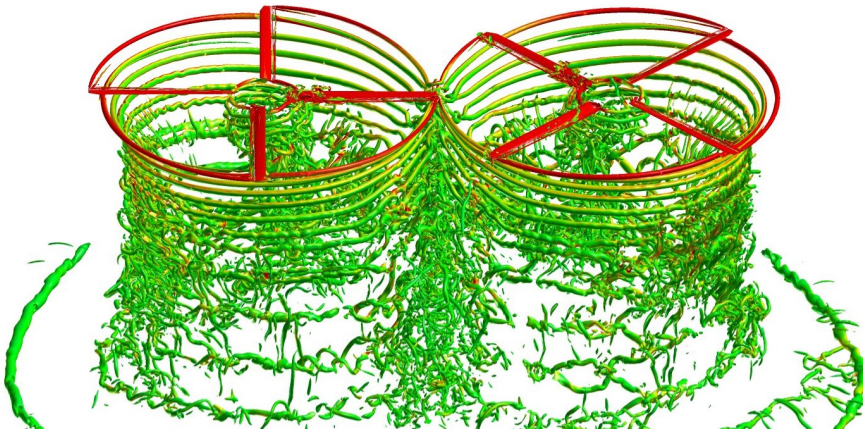

(b)

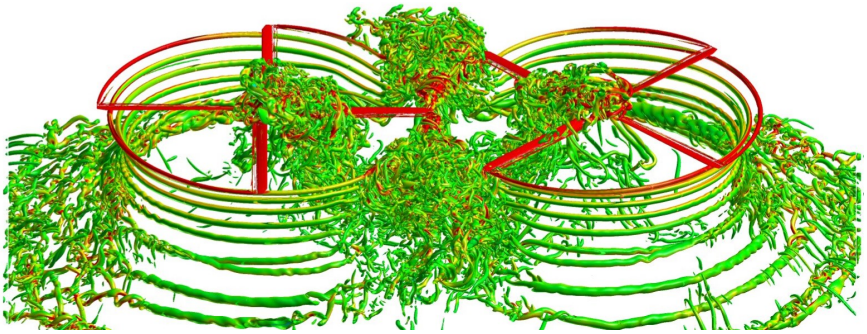

(c)

Figure 7.7: Iso-surfaces of the Q-criterion with the vorticity magnitude for the 0% overlap case: (a) OGE, (b) H = 1D, and (c) H = 0.5D.

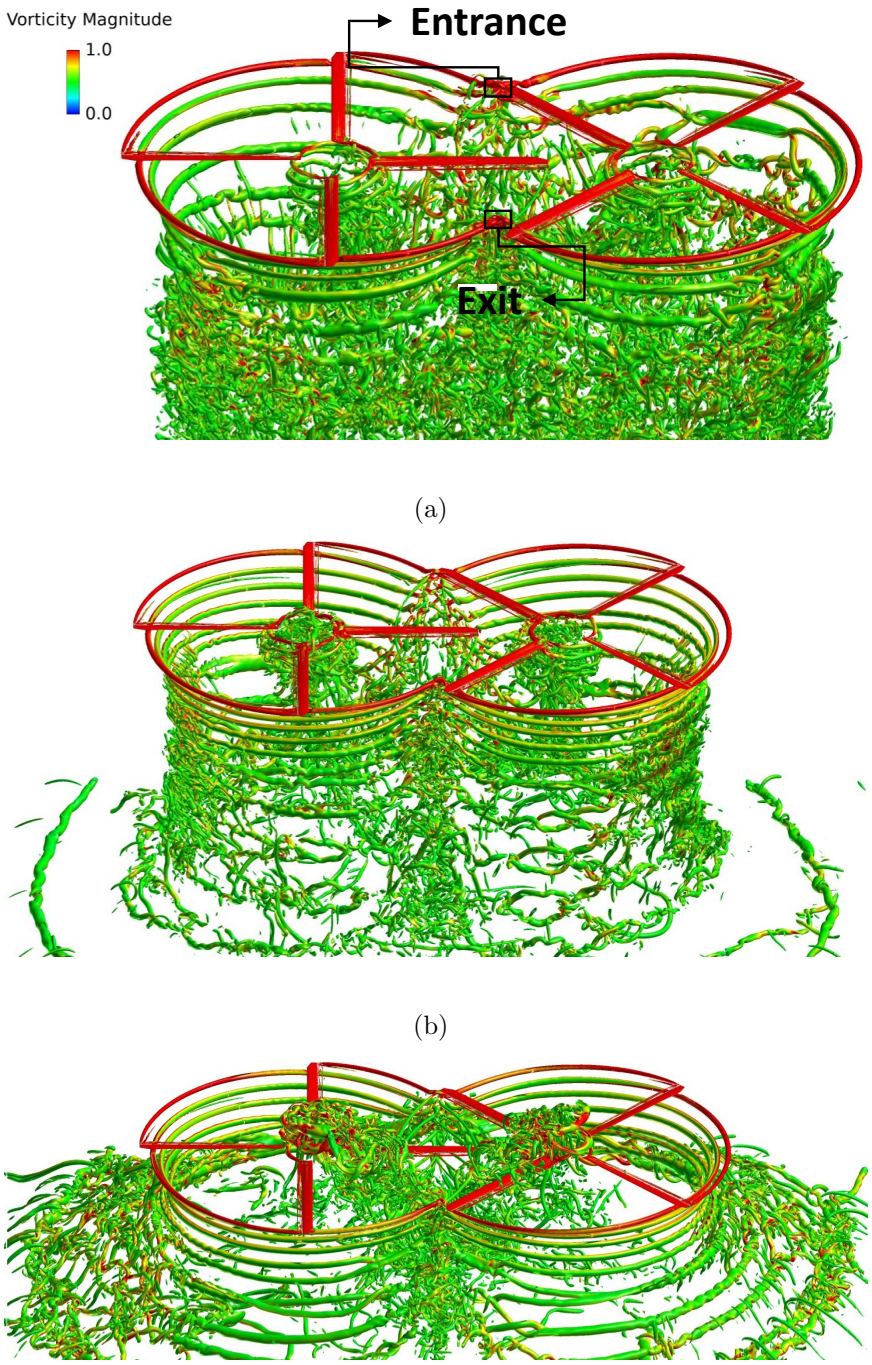

(a)

(b)

(c)

Figure 7.8: Iso-surfaces of the Q-criterion with the vorticity magnitude for the 0% overlap case: (a) OGE, (b) H = 1D, and (c) H = 0.5D.

Figures 7.9 and 7.10 provide a comparison of the induced inflow ratio at the rotor center plane for both in- and out-of-ground effect cases of the 0% and 25% overlap configurations.

The inflow ratio is defined in Eq. 7.1 [16]:

$$\lambda_h = \lambda_i = \frac{v_i}{\Omega R} \tag{7.1}$$

where v_i is the induced velocity, Ω is the angular velocity, and R is the rotor radius. The positive value (red color) indicates the upwash and the negative value (blue color) indicates the downwash. The figures show a substantial increase in upwash flow, as indicated in figures 7.9(b), 7.9(c), 7.10(b), and 7.10(c) for in-ground effect cases, especially in the hub region.

Both in-ground effect cases of the 0% overlap configuration generate more upwash than in-ground effect cases of the 25% overlap configuration. The downwash significantly increases in the overlap region in the 25% overlap configuration due to the overlapped tip vortices and wake effects from each rotor. The downwash is high and pushes the blade tip vortices downward, leading to reduced upwash in the overlap region for the in-ground effect cases of the 25% overlap configuration. This demonstrates the effect of overlap on the upwash influenced by the ground plane. In other words, as the rotor height increases for the in-ground effect cases of both overlap configurations, the amount of upwash decreases in both the hub and overlap regions. For the 25% overlap configuration, changing the rotor height from H = 0.5D to H = 1D results in an even greater increase in downwash, comparable to the out-of-ground effect 25% overlap case.

Figure 7.11 displays horizontal planes below the rotor disk in a contour plot of the induced inflow ratio for the 0% overlap configuration for both the in- and out-of-ground effect cases. Several horizontal planes below the rotor disk are added to extract the inflow ratio. The results of the inflow ratio at each downstream location are shown in figures 7.12 and 7.13.

A slight asymmetry in the inflow ratio is found between the left and right rotors. As the overlap increases, the inflow ratio contracts inward. Note that H = 0.5D is not shown in figures 7.12(c)-(e) and 7.13(c)-(e), and H = 1D is not shown in figures 7.12(e) and 7.13(e). The results demonstrate a clear reduction in downwash and noticeable upwash near the hub of each rotor in in-ground effect. Moreover, the 25% overlap configuration exhibits higher downwash near the center for both in-ground and out-of-ground effect cases.

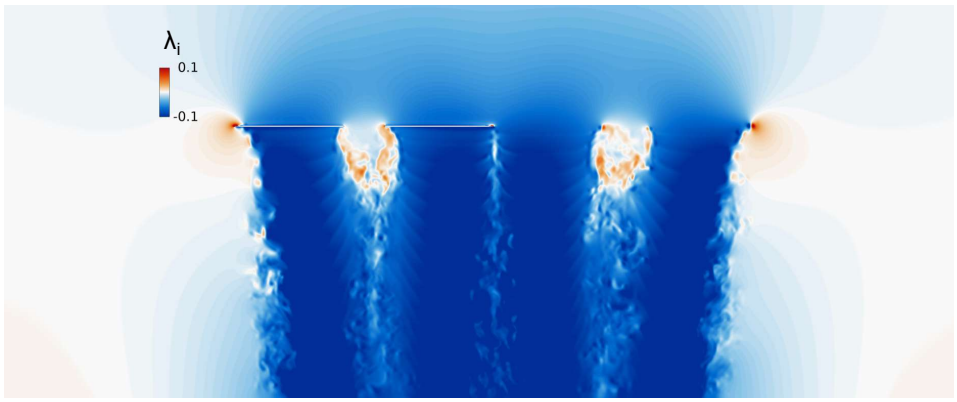

(a)

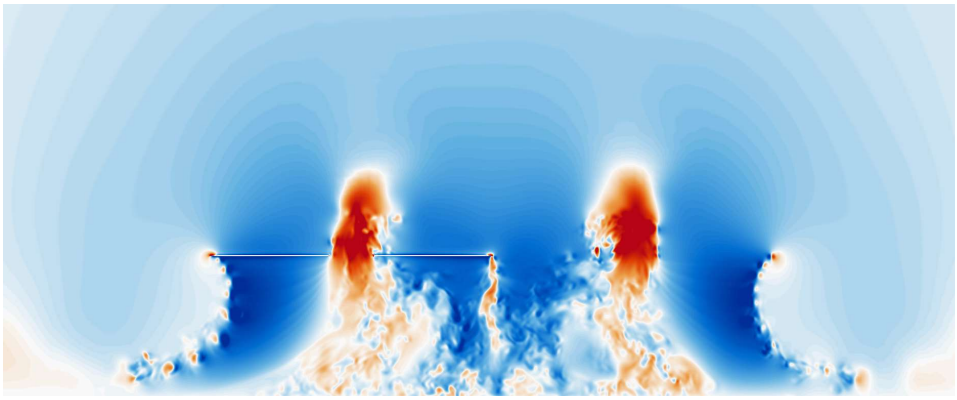

(b)

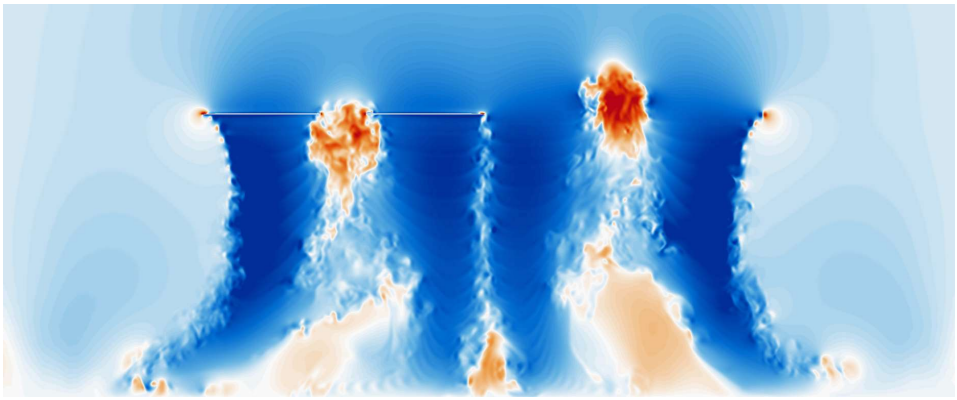

(c)

Figure 7.9: Comparison of λ_i (inflow ratio) between the OGE and IGE cases for the 0% overlap configuration. The black bar represents the rotor disk plane: (a) OGE, (b) H = 0.5D, and (c) H = 1D.

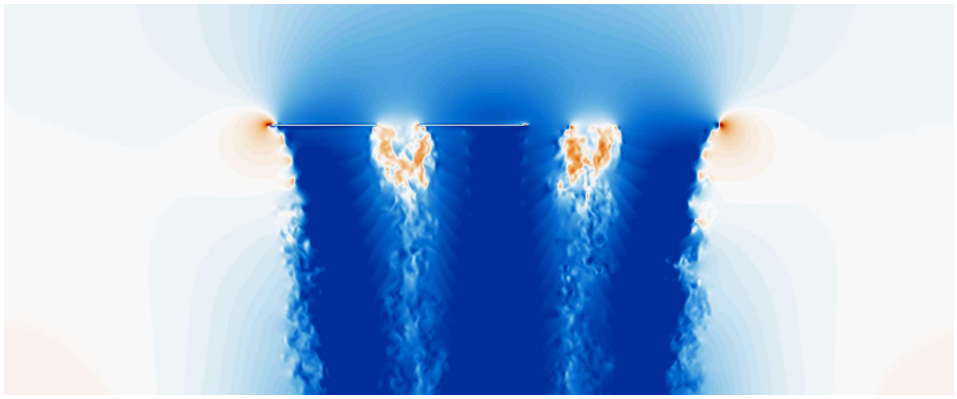

(a)

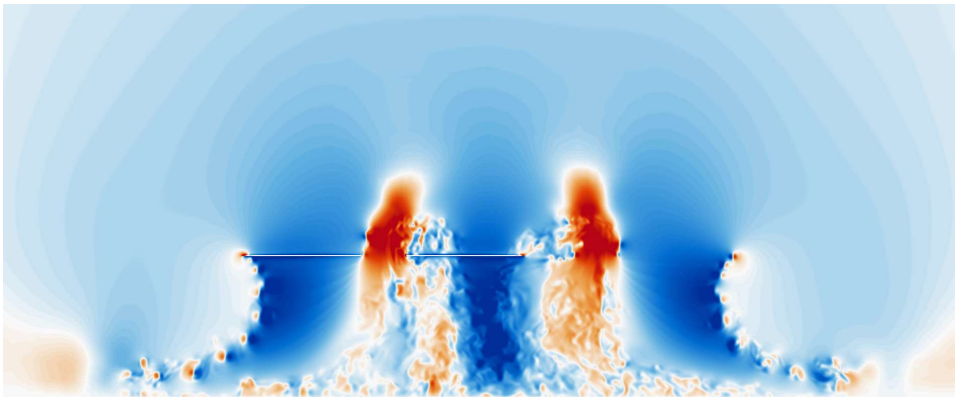

(b)

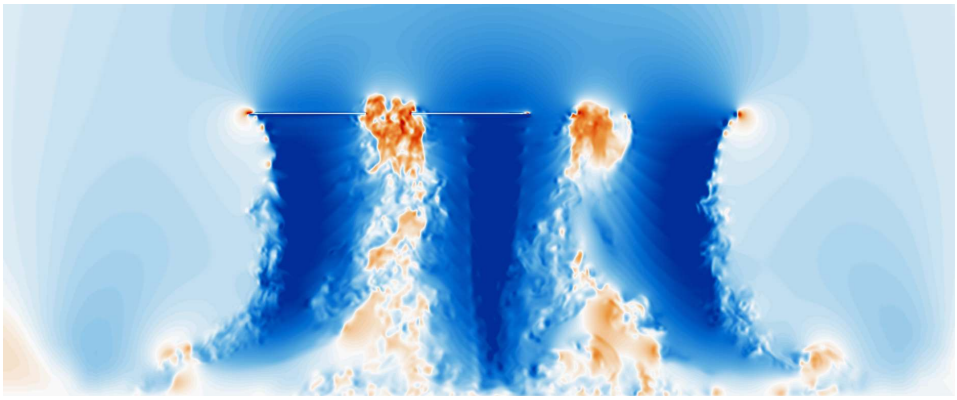

(c)

Figure 7.10: Comparison of λ_i (inflow ratio) between the OGE and IGE cases for the 25% overlap configuration. The black bar represents the rotor disk plane (a) OGE, (b) H = 0.5D, and (c) H = 1D.

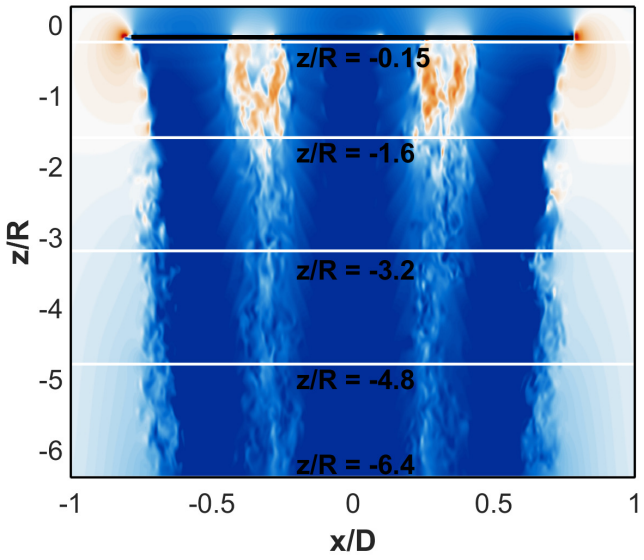

(a)

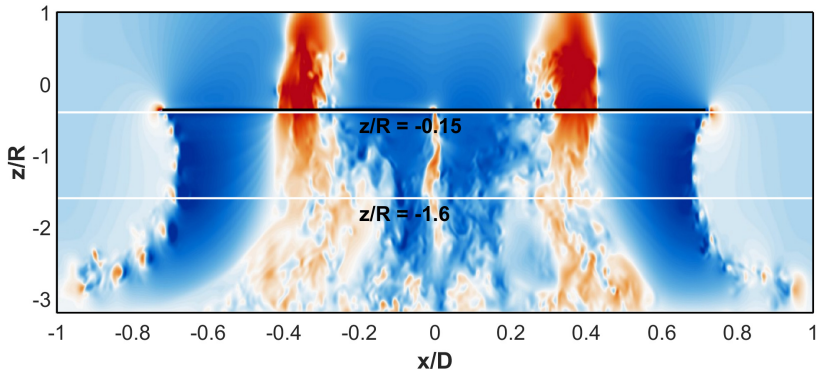

(b)

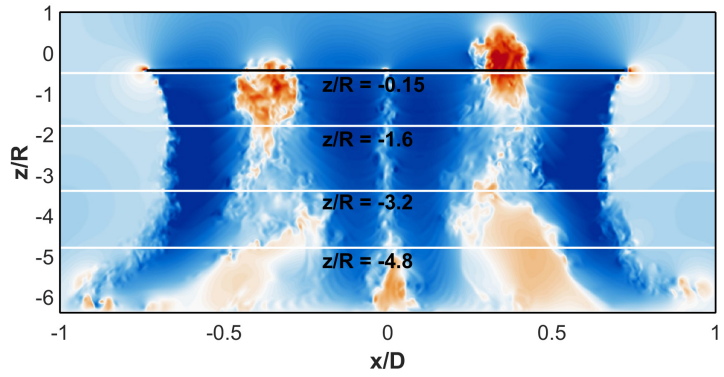

(c)

Figure 7.11: Measurement locations of inflow ratio.

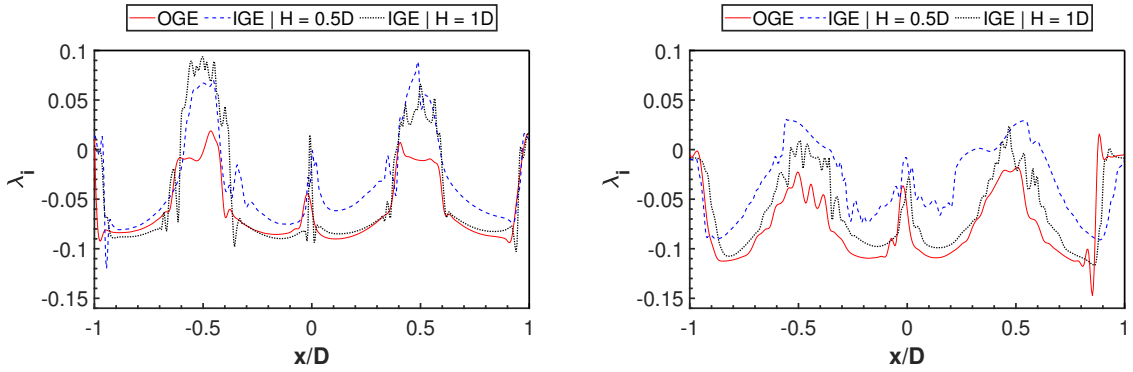

(a)

(b)

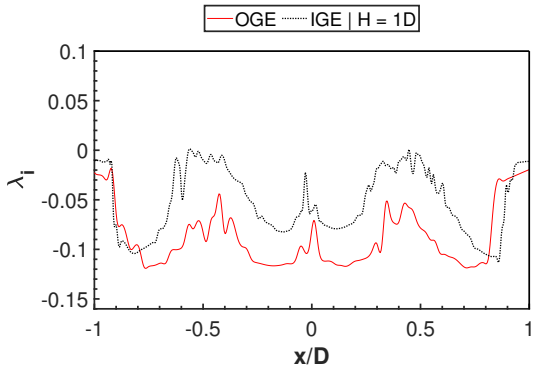

(c)

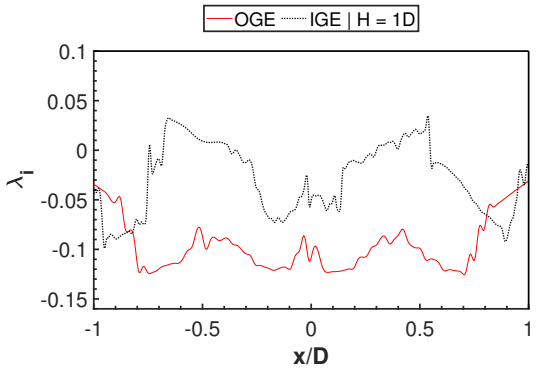

(d)

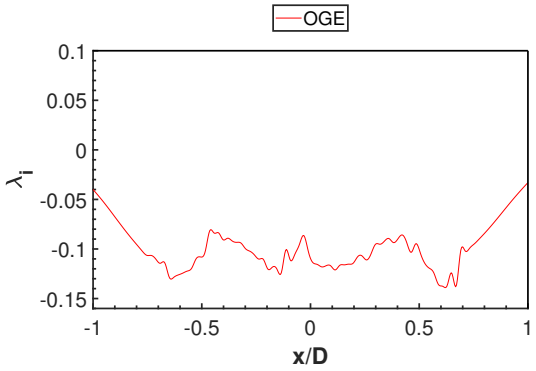

(e)

Figure 7.12: Comparison of λ_i (inflow ratio) of the 0% overlap configuration for in- and out-of-ground effect cases: (a) Measurement locations of inflow ratio, (b) z/R = -0.15, (c) z/R = -1.6, (d) z/R = -3.2, (e) z/R = -4.8, and (f) z/R = -6.4.

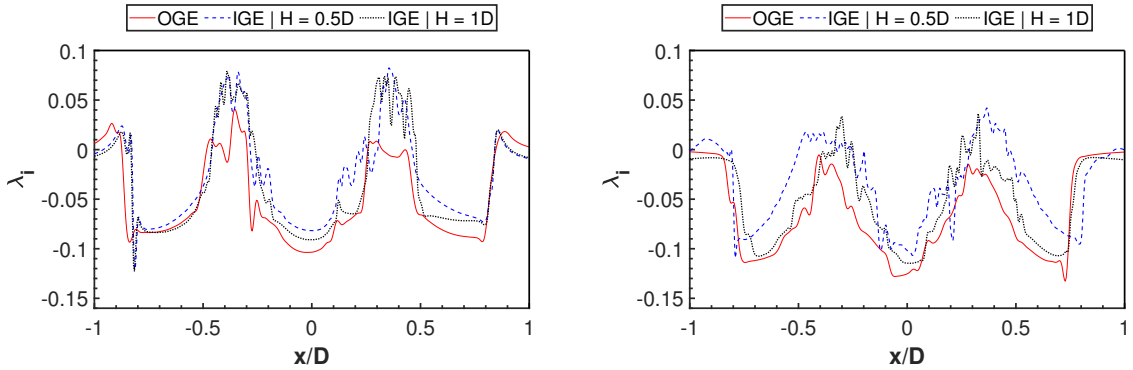

(a)

(b)

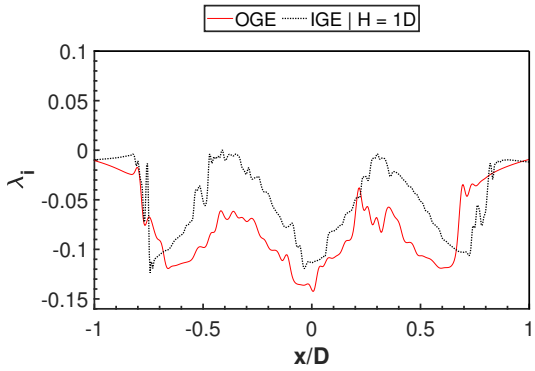

(c)

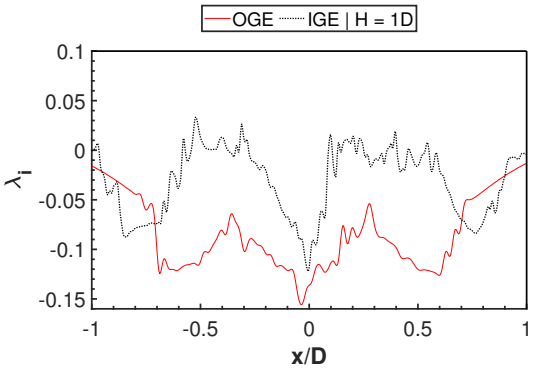

(d)

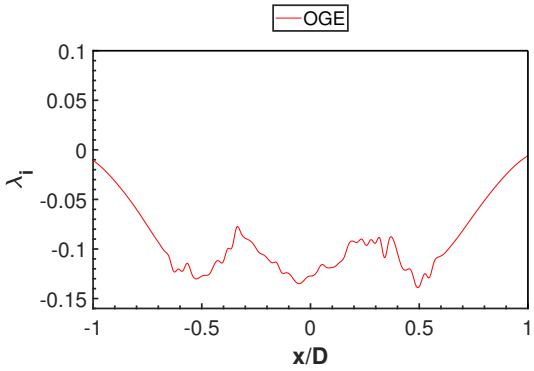

(e)

Figure 7.13: Comparison of λ_i (inflow ratio) of the 25% overlap configuration for in- and out-of-ground effect cases: (a) Measurement locations of inflow ratio, (b) z/R = -0.15, (c) z/R = -1.6, (d) z/R = -3.2, (e) z/R = -4.8, and (f) z/R = -6.4.

7.3.3 Aerodynamics

We investigate the variation in aerodynamics between the in-ground and out-of-ground effect cases of the 0% and 25% overlap configurations, with a focus on the overlap region. Figures 7.14 – 7.15 show the normal force on the left rotor disk, owing to symmetry. For the out-of-ground and H = 1D cases, a decrease in the normal force magnitude occurs at $\psi = 270°$, where the influence of the right rotor is dominant in all 0% and 25% overlap cases. At the 25% case, the impact of overlap becomes more pronounced, as evidenced by the greater azimuthal range in which the thrust deficit arises. Figures 7.14(c) and 7.15(c) depict the increase in the normal force in the hub region and interaction near the overlap region at H = 0.5D due to the strong upwash effect as discussed in the previous subsection, especially notable in the 0% case.

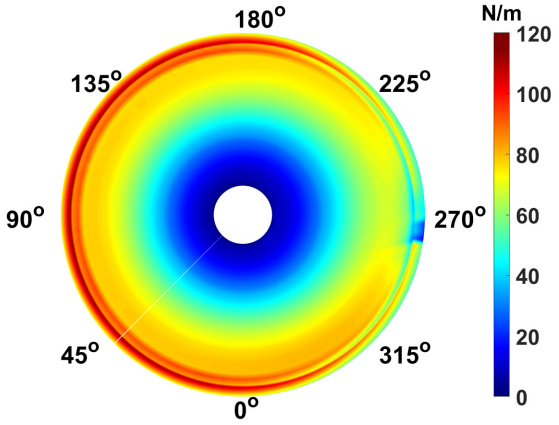

(a)

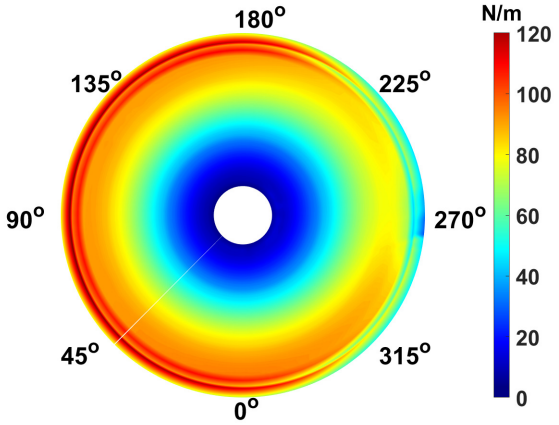

(b)

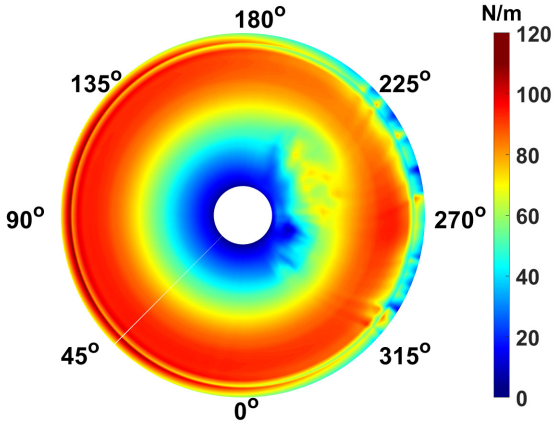

(c)

Figure 7.14: Normal force for the 0% overlap configuration comparing the in- and out-of-ground effect cases: (a) OGE, (b) H = 1D, and (c) H = 0.5D.

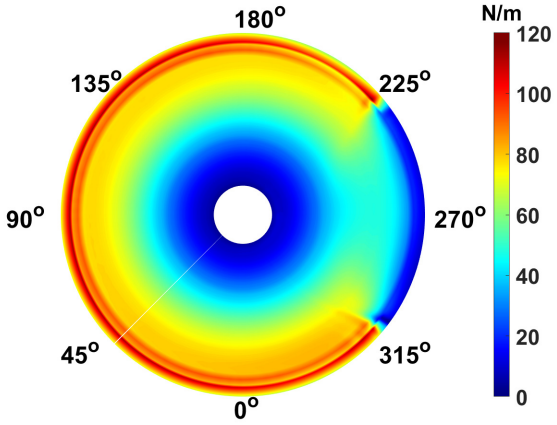

(a)

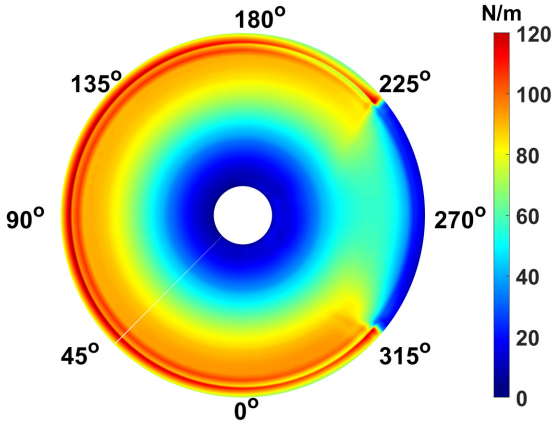

(b)

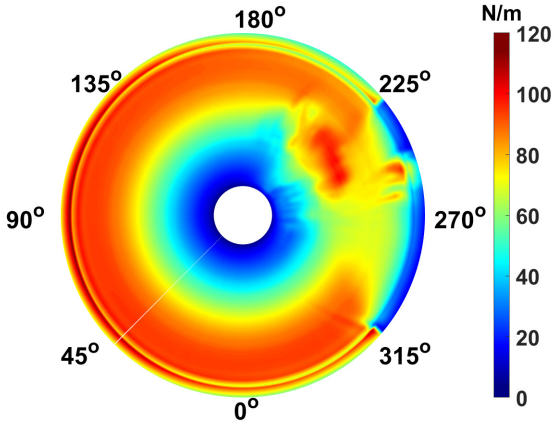

(c)

Figure 7.15: Normal force for the 25% overlap configuration comparing the in- and out-of-ground effect cases: (a) OGE, (b) H = 1D, and (c) H = 0.5D.

Figures 7.16 and 7.17 depict the non-dimensional normal force as a function of azimuthal angle at four radial locations ($r/R = 0.5, 0.75, 0.9$, and 1.0). The figures compare the normal force for in- and out-of-ground effect cases of the 0% and 25% overlap configurations. The width, depth, and rate of change of the normal force increase significantly with increasing overlap, as seen in the 25% overlap configuration. At $r/R = 0.5$, H = 0.5D significantly increases the normal force for both configurations. This increase is significant and leads to an improvement in thrust performance as discussed earlier. At the outboard locations, sharp peaks and fluctuations appear for the both configurations at H = 0.5D. However, as noted in the previous subsection, at H = 1D, both overlap cases show performance similar to the out-of-ground effect cases in the overlap region, although out-of-ground effect case shows larger normal forces than H = 1D outside the overlap region.

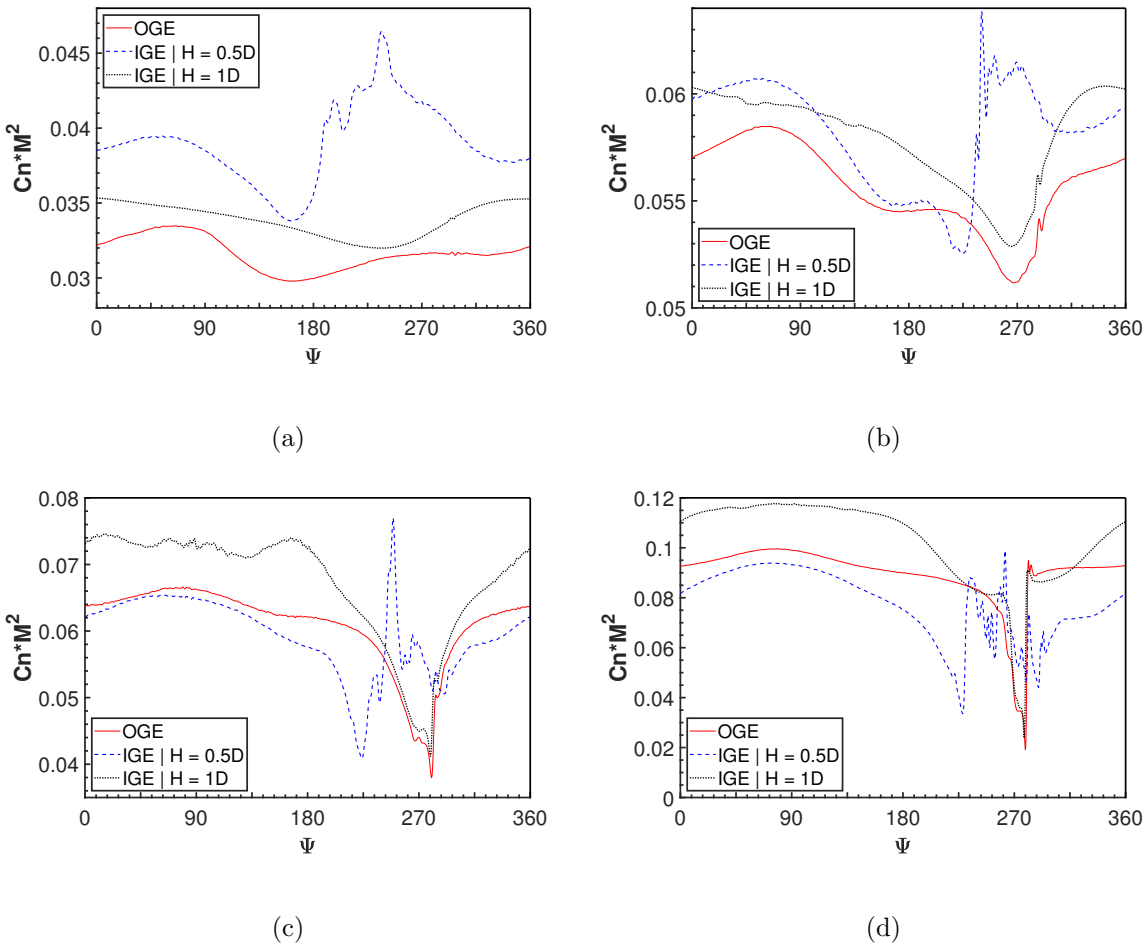

Figure 7.16: The non-dimensional normal force coefficient for the 0% overlap at four different radial locations: (a) $r/R = 0.5$, (b) $r/R = 0.75$, (c) $r/R = 0.90$, and (d) $r/R = 1.0$.

Figures 7.18 shows the blade sectional thrust coefficient, $\frac{dC_T}{dr}$ along the blade radius, at the azimuthal angle of 270°, where the thrust deficit mostly occurs within the overlap region. Due to symmetry, only the left rotor is shown. In the 0% overlap configuration, the blade section at H = 0.5D shows a higher thrust coefficient compared to H = 1D and out-of-ground cases along the entire blade section. H = 1D and out-of-ground cases have similar thrust coefficients. In the 25% overlap configuration, both in-ground cases have similar but higher thrust coefficients than out-of-ground case. A slight peak at approximately 95% of the blade radius is noticeable due to the swept tip.

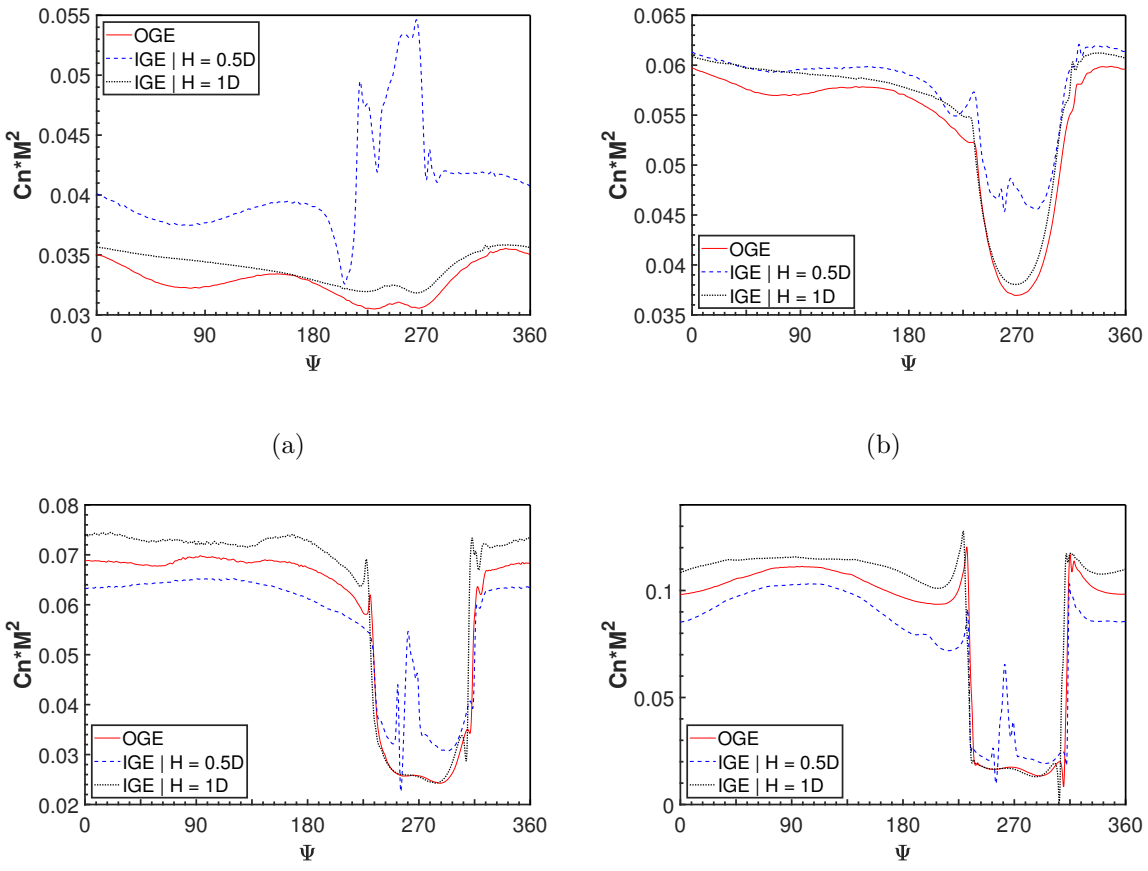

Figure 7.17: The non-dimensional normal force coefficient for the 25% overlap at four different radial locations: (a) $r/R = 0.5$, (b) $r/R = 0.75$, (c) $r/R = 0.90$, and (d) $r/R = 1.0$.

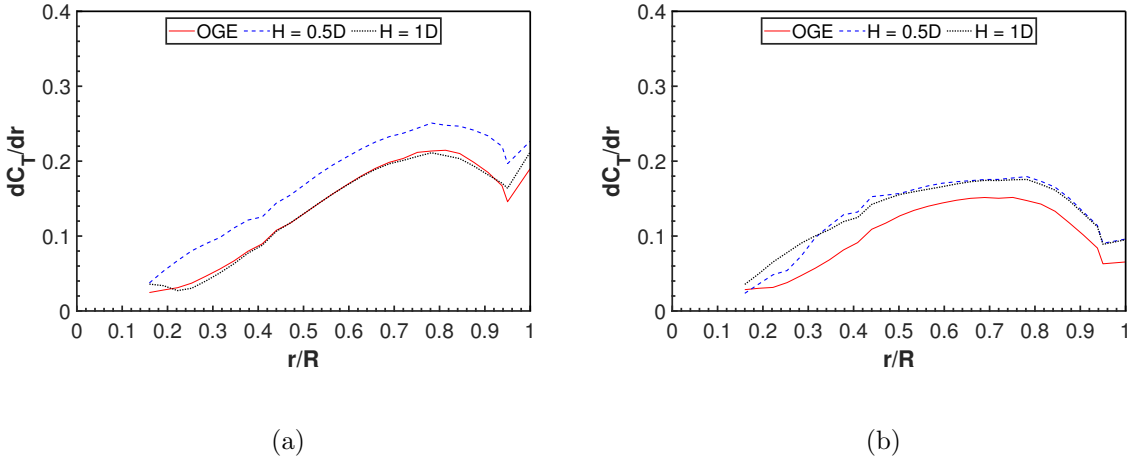

Figure 7.18: Blade sectional thrust coefficient for the in- and out-of-ground effect cases of the 0% and 25% overlap configurations at 270°azimuthal location: (a) 0% overlap and (b) 25% overlap.

In Figure 7.19, the blade sectional thrust coefficient is presented for the in-ground effect cases of the 0% and 25% overlap configurations at azimuthal angles of 0°, 90°, 180°, and 270°. There is a deficit in the sectional thrust that is more prominent at the 270° azimuthal angle, which increases as the overlap region expands. At H = 0.5D, the decrease in the sectional thrust at the 270° azimuthal angle is not noticeable, especially at the 0% overlap configuration. At the 25% overlap configuration, the decrease in the sectional thrust is more noticeable in both in-ground cases. The decrease in sectional thrust correlates with the normal force distribution shown in figures 7.14 and 7.15. The reduced thrust is thought to be due to the increased induced velocities caused by the two rotor tip vortex effects observed in figures 7.9, 7.10, 7.12, and 7.13. Due to the periodic variation of rotor thrust with azimuthal angle, FM oscillates, as demonstrated in Figure 7.6.

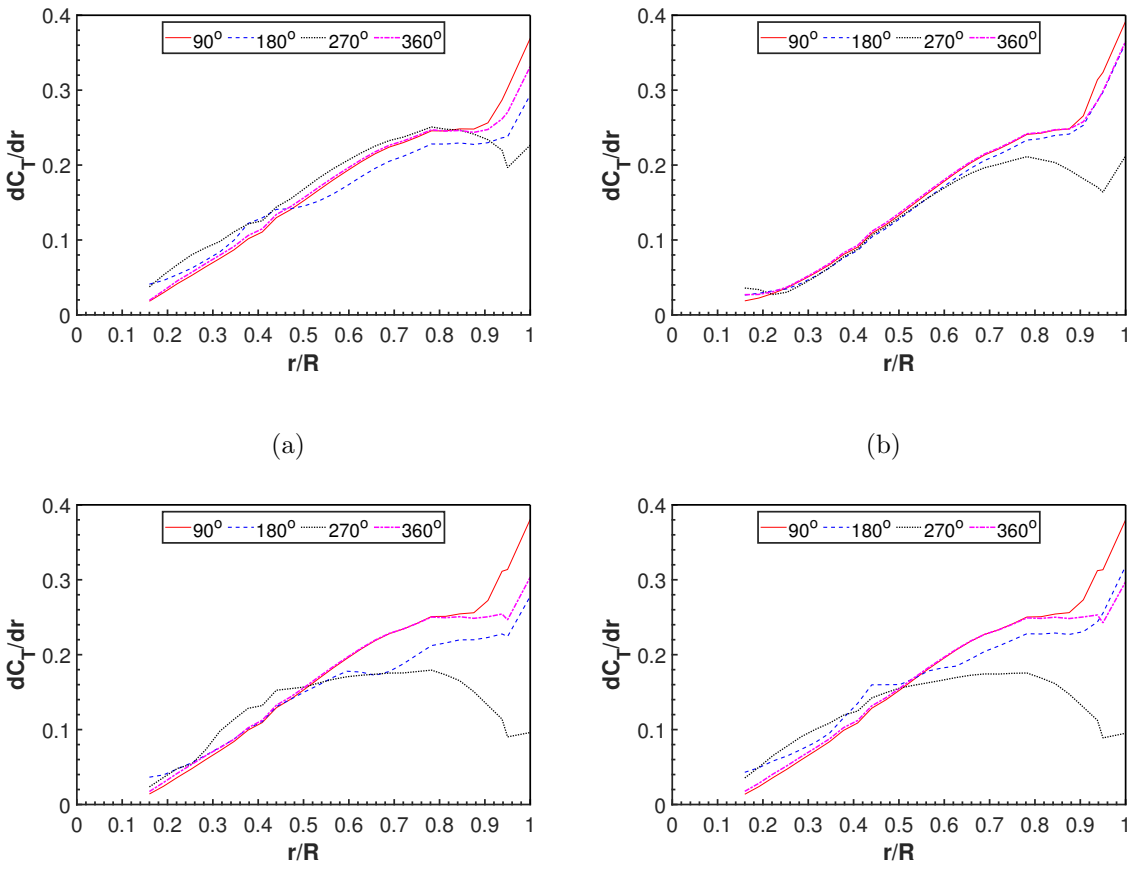

Figure 7.19: Blade sectional thrust coefficient for the in-ground effect cases: (a) 0% overlap at H = 0.5D, (b) 0% overlap at H = 1D, (c) 25% overlap at H = 0.5D, and (d) 25% overlap at H = 1D.

7.3.4 Aeroacoustics

Figure 7.20 shows a quantitative comparison of $dF_z/d\Psi$ of the left rotor at the 75% span for all in- ground effect cases of the 0% and 25% overlap configurations. It should be noted that this derivative of the normal force is the main source of the loading noise of Farassat's Formulation 1A [87]. Due to symmetry between the left and right rotor of the distribution of $dF_z/d\Psi$, only the left rotor is analyzed here. It is clear that the pressure fluctuation

events are located within 225° and 315° azimuths where there is a considerable amount of events that can be correlated to interactional aerodynamics due to interaction between the upwash and rotor wake, the upwash and rotor blades, and rotor to rotor vortex interactions. Some of rotor to rotor interactions include the interaction between the wake or vortices from one rotor with the other especially near the overlap entrance and exit regions as seen in figures 7.7 and 7.8. In Figure 7.20(a), at about the 290° azimuth angle for the 0% overlap configuration at H = 0.5D, there are peaks with a significantly large amplitude compared to the peaks in the 25% overlap case. The flow upwash interacting with blades at the 0% overlap in-ground and H = 0.5D case contributes to the strong pressure fluctuations.

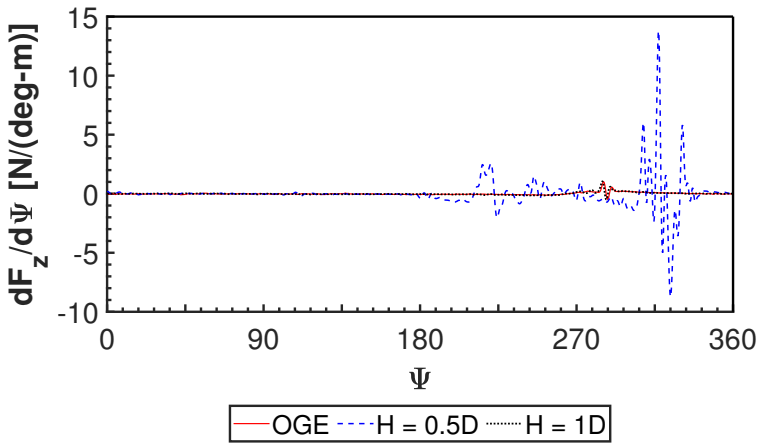

(a)

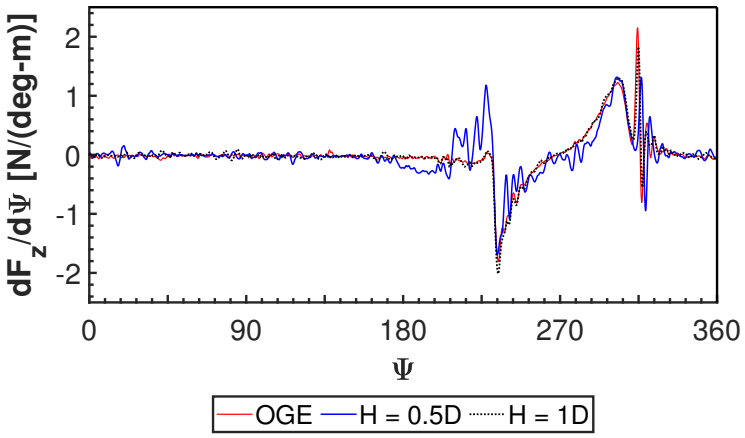

(b)

Figure 7.20: Comparison of $dF_z/d\Psi$ of the left rotor at the 75% span for the in- and out-of-ground effect cases of the 0% and 25% overlap configurations: (a) 0% overlap and (b) 25% overlap.

Figure 7.21 shows the total acoustic pressure of a single observer positioned H = 0.5D and H = 1D, below the rotor disk plane, for both the 0% and 25% overlap configurations. The in- and out-of-ground cases are included. The tonal peaks appear regularly during the

entrance and exit of the overlap for all the cases,except in-ground cases at H = 0.5D where there are irregular and multiple peaks. The additional frequency content present in the H = 0.5D cases are mainly due to the upwash effect as discussed.

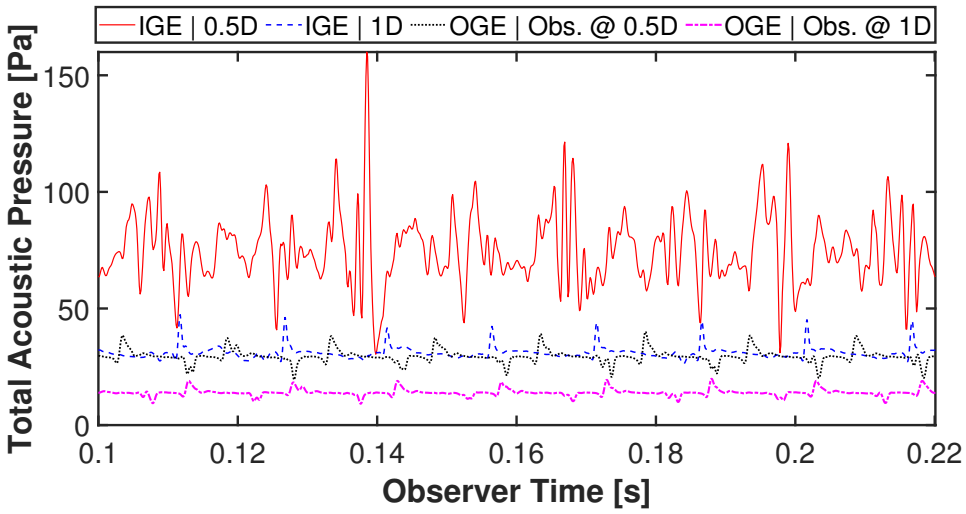

(a)

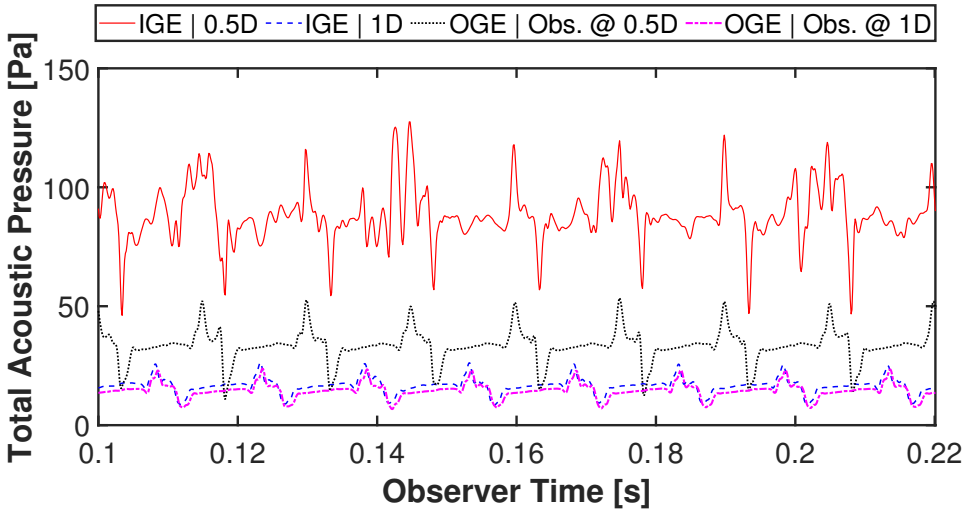

(b)

Figure 7.21: Comparison of the total acoustic pressure for the in- and out-of-ground effect cases of the 0% and 25% overlap configurations: (a) 0% overlap and (b) 25% overlap.

The A-weighted sound pressure level (SPL) for the first 50 blade passing frequency (BPF)

harmonics is depicted in Figure 7.22. For the out-of-ground cases, even harmonics represent the dominant tonal frequencies, suggesting the presence of rotor-to-rotor interaction noise. In contrast, for the in-ground cases at H = 0.5D, the tonal noise increases at both even and odd harmonics. This implies that the dominant noise sources include not only the rotor-to-rotor interaction noise but also the rotor and upwash flow interaction noise at each rotor, as illustrated in Figure 7.21. At H = 1D, even harmonics remain dominant; however, the magnitude for the in-ground cases surpasses that of the out-of-ground cases after the 25^{th} harmonics at the 0% overlap configuration.

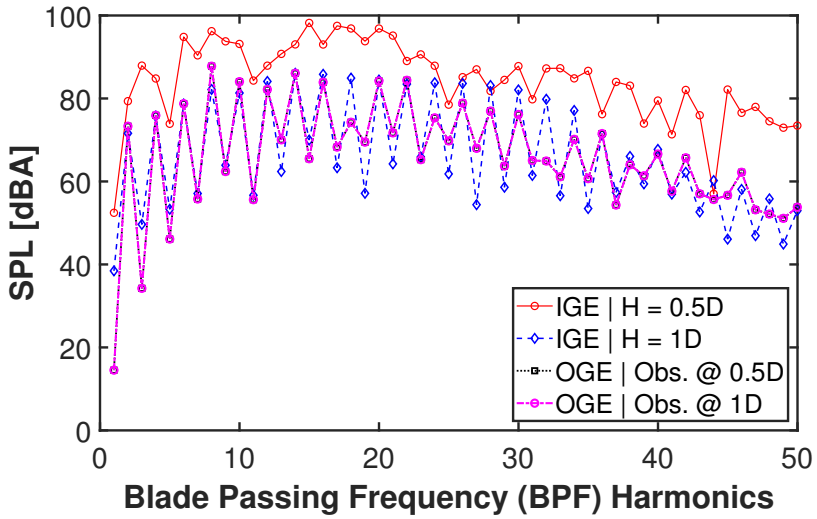

(a)

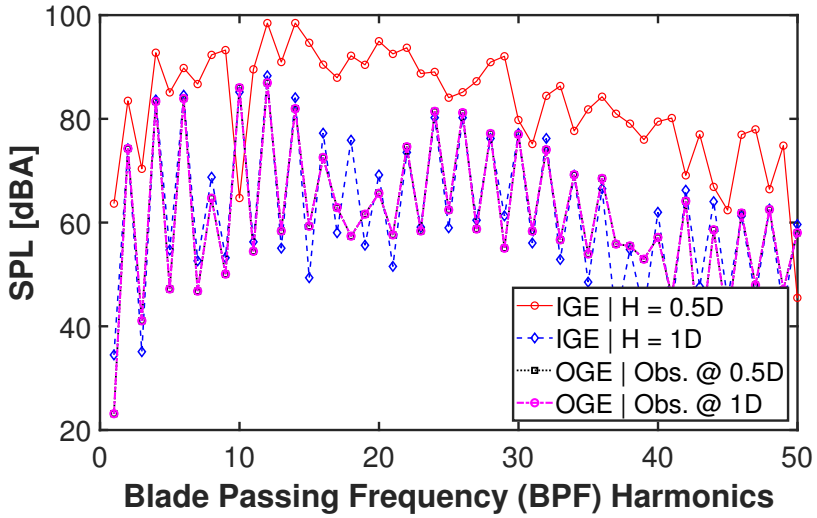

(b)

Figure 7.22: Comparison of A-weighted SPL for the in- and out-of-ground effect cases of the 0% and 25% overlap configurations: (a) 0% overlap and (b) 25% overlap.

Figure 7.23 displays the contours of the first integrand of the loading noise portion of Farassat's Formulation 1A [87] for the left rotor only, due to symmetry. This plot was first devised by Jia and Lee to investigate the loading noise sources in SbS rotor [4]. The black lines in the contour plots represent the rotor blades at an observer time (black dashed lines) when

the acoustic peaks are observed. It is noted that, at the given microphone position, for the in-ground effect cases at H = 1D for both overlap configurations, the primary aerodynamic interactions are rotor-to-rotor BVI events occurring when the blades enter (blue color) or exit (red color) the overlap region. However, for the H = 0.5D in-ground effect cases in both overlap configurations, numerous interactions other than rotor-to-rotor interactions are present, as discussed earlier. In particular, the H = 0.5D cases exhibit significantly greater impulsiveness compared to the strength of the rotor-to-rotor BVI events in the H = 1D cases.

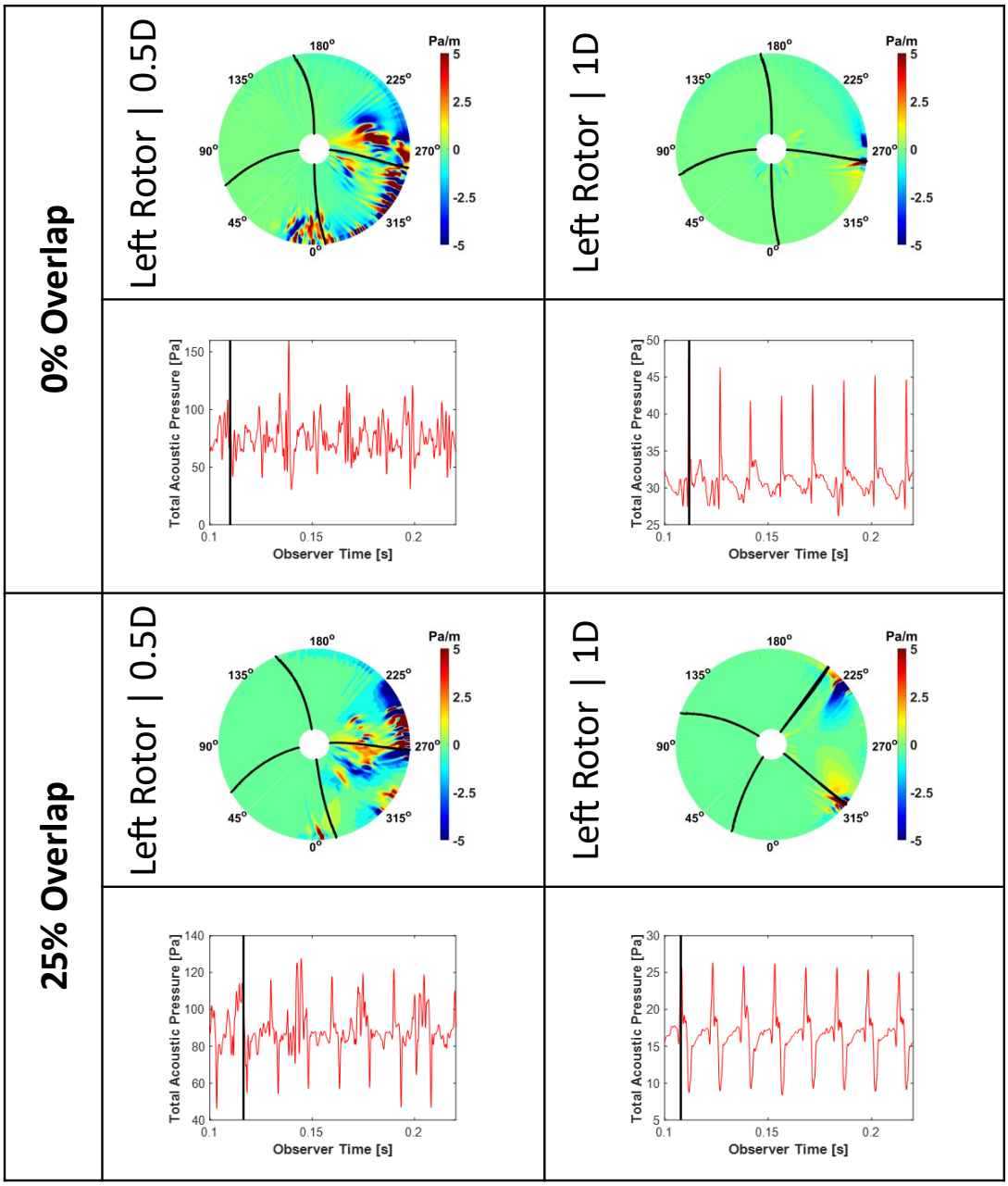

Figure 7.23: Comparison of noise intergrand results of the left rotor for all in-ground effect cases of the 0% and 25% overlap configurations.

Figure 7.24 shows the A-weighted overall sound pressure level (OASPL) for all in-ground effect cases of both the 0% and 25% overlap configurations, as well as the out-of-ground effect cases. It can be observed that for both overlap configurations, the H = 0.5D cases with in-ground effect exhibit the highest OASPL compared to the other cases, due to the additional

noise sources mentioned earlier. For the 0% overlap configuration, the H = 1D case with in-ground effect demonstrates a higher noise level than the out-of-ground case. Conversely, for the 25% configuration case, there is minimal difference between the in-ground at H = 1D and out-of-ground cases. In other words, the ground effect diminishes for the 25% overlap configuration after H = 1D due to a strong downwash effect.

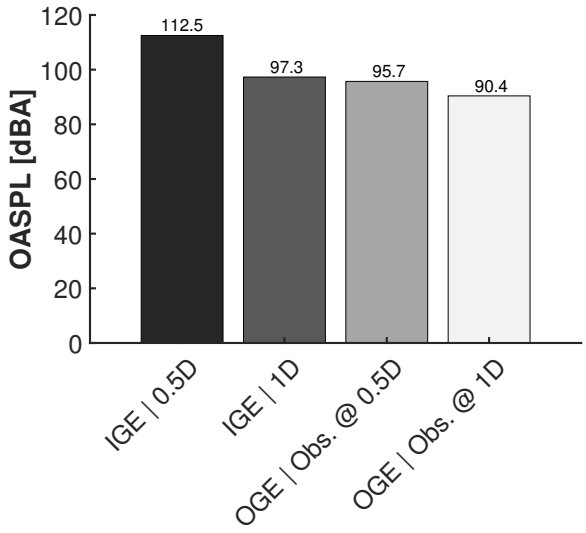

(a)

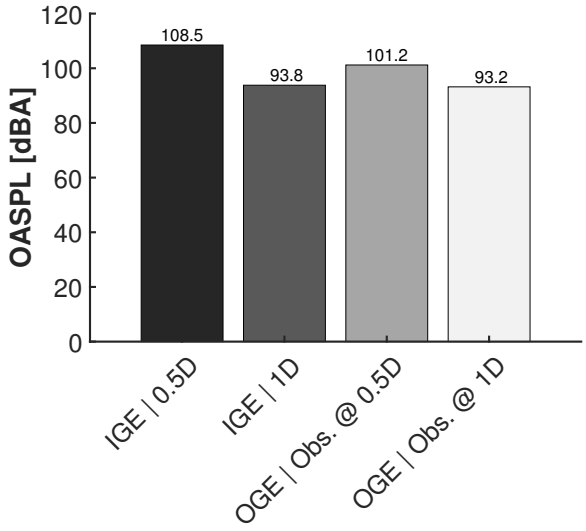

(b)

Figure 7.24: Comparison of A-weighted OASPL for the in- and out-of-ground effect cases of the 0% and 25% overlap configurations: (a) 0% overlap and (b) 25% overlap.

Figures 7.25 shows the directivity patterns of the OASPL and the total acoustic pressure at the peak and valley locations in the entrance region. These peaks and valleys are situated near the boundary of the rectangular grid, where both constructive and destructive interfer-

ence can be observed in all in-ground effect cases for both overlap configurations. In peak locations, constructive interference from both rotors results in a significant increase in noise levels. Conversely, destructive interference from both rotors in valley locations leads to a reduced overall noise level. There are differences in the directivity patterns and interference for the H = 1D cases in both the 0% and 25% overlap configurations. The majority of peaks and valleys appear near the entrance of the overlap region for the 0% overlap configuration. However, for the 25% overlap in-ground effect case at H = 1D, peak and valley locations also occur near the exit of the overlap region.

Figure 7.26 illustrates the directivity between A-weighted and unweighted noise levels. The peaks and valleys are not as distinct in the A-weighted plots since the constructive and destructive interferences primarily occur at the second harmonic waves. The A-weighted OASPL shows higher noise levels in the exit region compared to the entrance region. For the 25% overlap configuration at H = 1D, the A-weighted OASPL reveals interference patterns in the exit region, which also occur in the unweighted region with a lower amplitude. This indicates that the interference mainly takes place at high frequencies in this case.

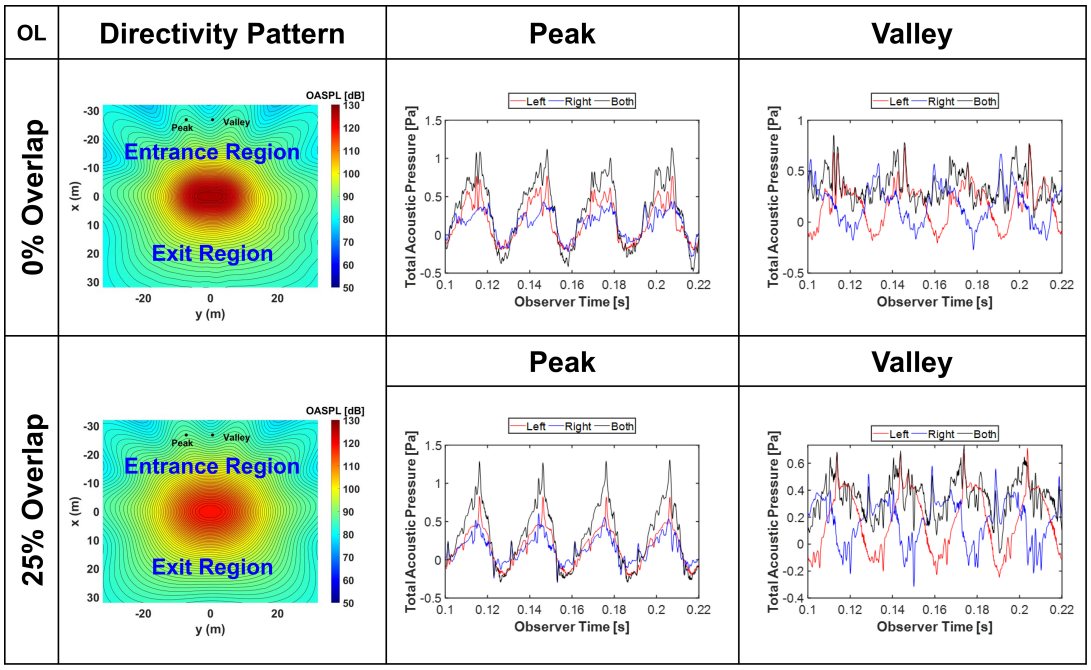

(a)

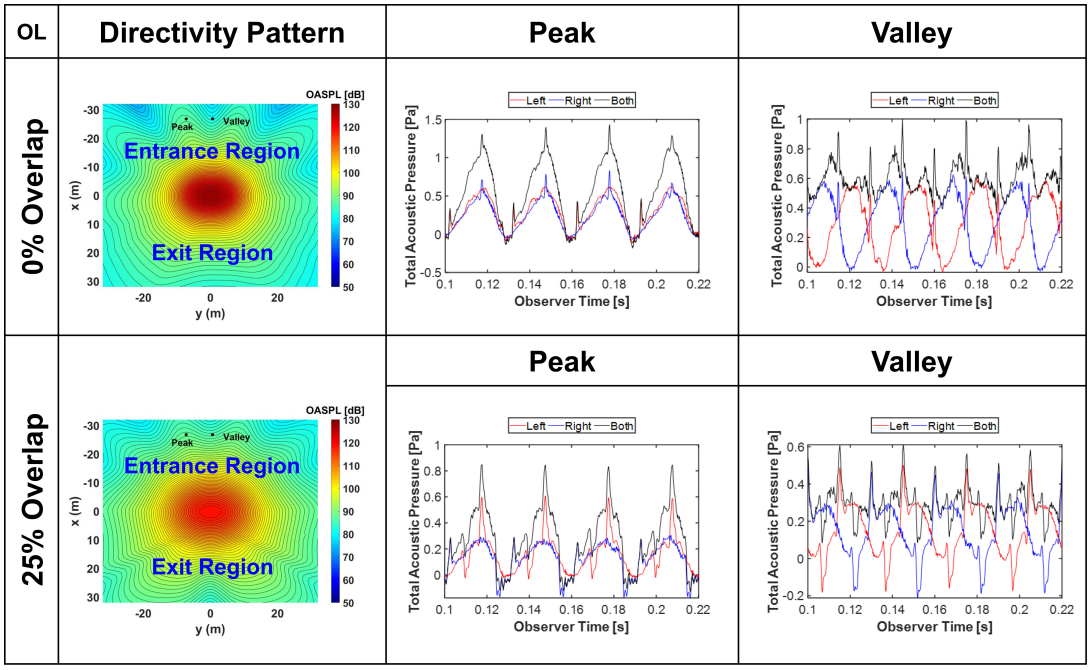

(b)

Figure 7.25: Comparison of the total acoustic pressure in the interference region for the in-ground effect cases of the 0% and 25% overlap configurations: (a) H = 0.5D and (b) H = 1D.

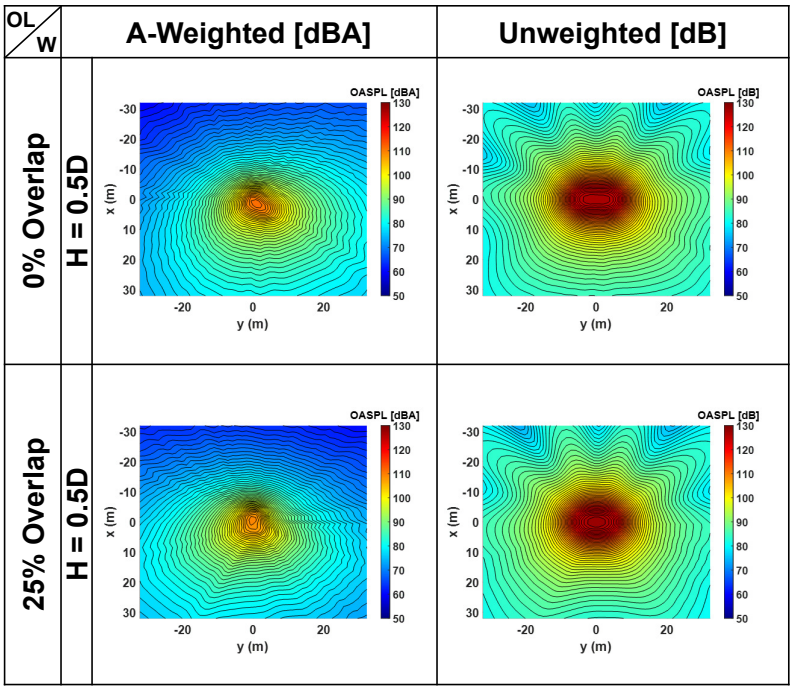

(a)

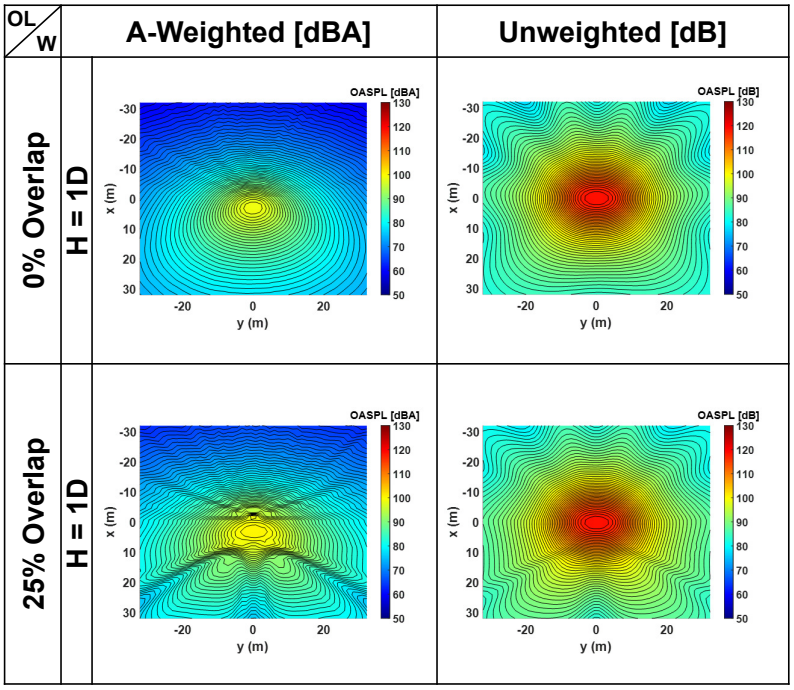

(b)

Figure 7.26: Comparison of OASPL (A-weighted and unweighted) for all in-ground effect cases of the 0% and 25% overlap configuration: (a) H = 0.5D and (b) H = 1D.

7.3.5 Conclusions

The impact of the ground surface on the six-passenger SbS rotors of NASA's UAM reference vehicle has been examined and analyzed in hover. High-fidelity CFD simulations were conducted using CREATE^{TM}-AV Helios to investigate the performance, aerodynamics, and acoustics of SbS rotor configurations with 0% and 25% overlap in both in- and out-of-ground effect cases during hover. Acoustic simulations using an impermeable approach were performed with the acoustic prediction tool PSU-WOPWOP. Thrust, torque, and FM were analyzed for different in-ground effect cases at two rotor heights of H = 0.5D and H = 1D. Tip vortex and induced velocity were also studied. The effect of the ground surface on blade sectional aerodynamic loads was investigated, and connections between various acoustic sources and the resulting noise were examined for each in-ground effect case. Directivity comparisons were made between both overlap configurations at H = 0.5D and H = 1D. Based on the results presented and analyzed in this study, the following conclusions can be drawn:

1. The presence of the ground surface has a clear impact on the hover performance, as evidenced by an increase in FM in all in-ground effect cases for both the 0% and 25% overlap configurations. Specifically, for the 0% overlap configuration at H = 0.5D and H = 1D, there is a significant increase of 8.6% and +5.8%, respectively, compared to the out-of-ground effect case. Similarly, for the 25% overlap case at H = 0.5D and H = 1D, there is a 2.7% and 2.0% increase, respectively, compared to the 25% overlap out-of-ground effect case. This indicates that as the overlap increases, the influence of the ground surface on rotor performance decreases.

2. In the vicinity of the overlap region, an increase in normal force was observed for the

H = 0.5D case, in contrast to the decrease seen in the out-of-ground effect cases. The increase in normal force, particularly for the 0% overlap case, can be attributed to the absence of overlap and the reduction in induced velocity due to the significant amount of upwash generated.

3. It was observed that the induced velocity decreases considerably in the overlap region for the H = 0.5D cases and shows a slight increase in the H = 1D cases for the 0% overlap configuration. In contrast, for the 25% overlap cases, it was observed that the increase in the induced velocity, thereby overshadowing the upwash generated.

4. At H = 1D, the most dominant source of noise in hover condition is the blade-tip interaction with the tip vortical structures as the blade enters and exits the overlap region for both overlap configurations. At H = 0.5D, due to the closer proximity to the ground and the upwash effect especially at the 0% overlap configuration, there is an increase in the number of aerodynamic interactions, such as rotor-to-rotor, rotor and wake, rotor and tip vortices, rotor and upwash, and upwash and rotor wake interactions, resulting in noise increase at all harmonics. For the 25% overlap configuration, the OASPL levels became similar between the in-ground case at H = 1D and the out-of-ground case, while the 0% configuration showed much higher noise levels in-ground at H = 1D compared to the out-of-ground case. Overall, the 25% configuration provides about 3-4 dB noise reduction compared to the 0% configuration near the ground. This indicates the noise reduction benefit of SbS rotor configurations with overlap near the ground.

5. Acoustic interference was examined for both 0% and 25% overlap cases at specific

observer locations identified as peaks and valleys, which resulted from constructive and destructive interference, respectively. The directivity patterns were found to be considerably different between the A-weighted and unweighted OASPL. The peaks and valleys in the A-weighted OASPL were significantly reduced or not as visible, except for the A-weighted OASPL of the 25% overlap case at H = 1D in the exit region.

Chapter 8

Side-by-Side (SbS) Rotor and in Full Configuration with Fuselage

This chapter presents the CFD and acoustic results from the simulations of the SbS rotor and fuselage configuration based on high-fidelity CFD coupled with acoustics investigating different overlap configurations in hover and out-of-ground effect at a collective pitch angle of 8°. Details of the setup for the CFD and acoustic analysis are provided.

8.1 SbS Rotor UAM Vehicle: Goal and Objectives

In the study of the ground effect in the previous chapter, it is found that the upwash effect due to the ground leads to a more significant influence on the 0% overlap configuration than the 25% overlap configuration in terms of aerodynamic noise. Based on these results, we would also expect the presence of the fuselage to play a substantial role on the SbS rotor UAM vehicle performance and noise since the fuselage interference with rotor downwash is in many ways similar to the presence of a ground plane.

The objective of this chapter is to build upon earlier studies on the SbS rotor configuration by including the fuselage and investigating the performance, aerodynamics, and acoustics

in full configuration. It should be noted that this paper focuses only on tonal noise and does not consider broadband noise, although broadband noise is also an important noise source in UAM aircraft as shown in references [40, 41, 71, 72]. Results from high-fidelity computational fluid dynamics (CFD) simulations are analyzed to identify possible sources of noise, including BVIs. The effect of the rotor-to-rotor overlap percentage on the strength of the generated noise and far-field noise directivity are presented. The noise generated from the aerodynamic interactions of the SbS rotors due to overlap, including the presence of the fuselage, is compared to that from an isolated rotor in hover condition. Ultimately, this work aims to assess and characterize tonal noise of the SbS rotor in full configuration in hover.

8.2 Numerical Methods

High-fidelity CFD modeling used in this study to calculate the performance and flow field of the SbS rotor and full configuration employ similar methodology used in the study of the isolated SbS rotor and in-ground effect. However, there are differences including the addition of a near-body solver using an unstructured approach. Acoustic calculations use the same methods applied in prior studies using an acoustic analogy in PSU-WOPWOP.

8.3 Rotor Model

Simulations include not only the same left (clockwise rotating) and right (counter-clockwise rotating) rotors (at a collective pitch angle of 8°) used in the prior studies, but the rotor hubs as well including the fuselage. We investigate the flow fields and any interactional aerodynamics mainly between the rotors and fuselage. Figure 8.1 shows various overlapping

cases: 0%, 5%, 15%, and 25%, which were considered in earlier research [4, 36, 37, 62, 74].

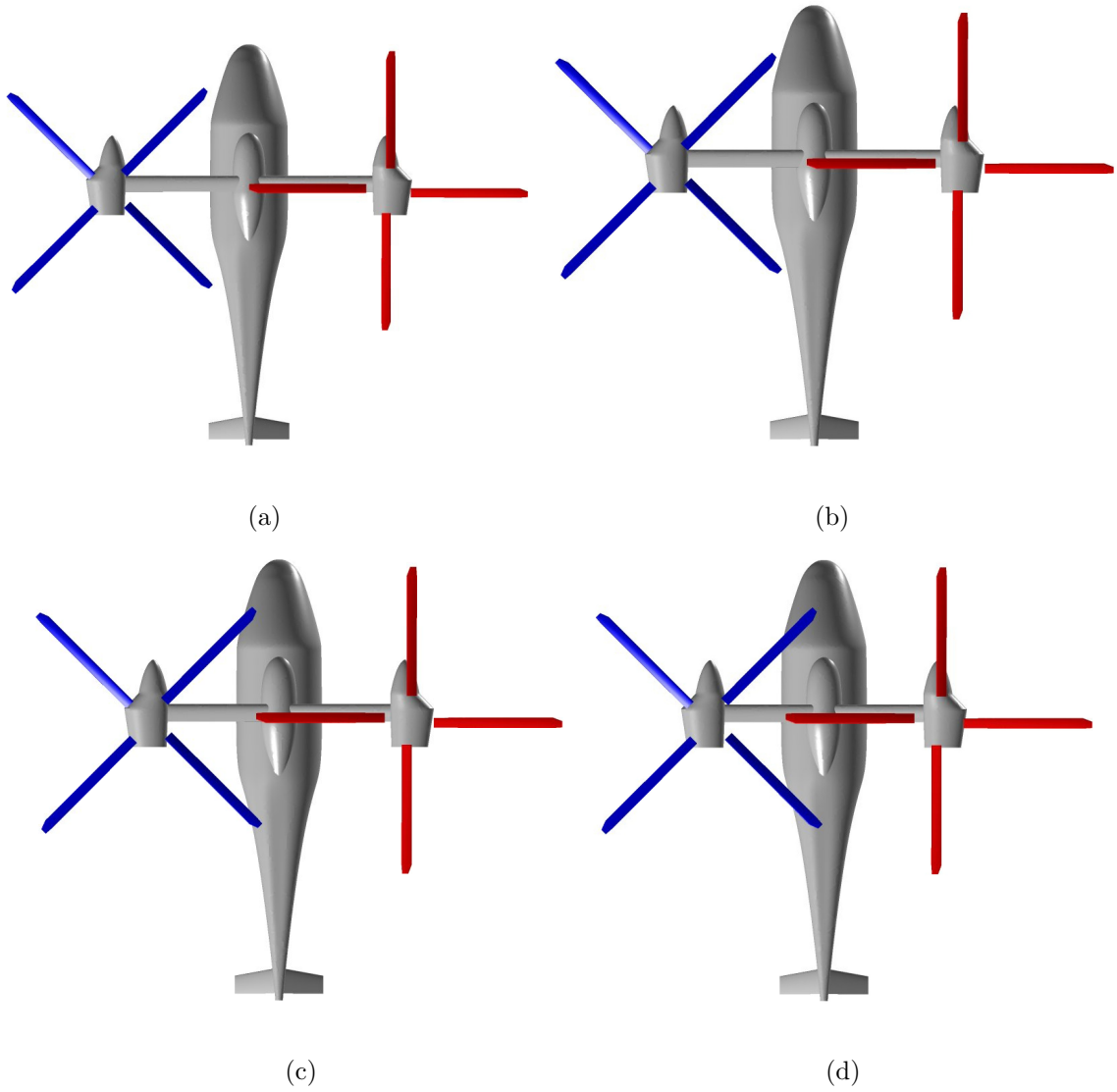

(a) (b)

(c) (d)

Figure 8.1: SbS rotor configuration for each overlap: (a) 0% overlap, (b) 5% overlap, (c) 15% overlap, and (d) 25% overlap.

8.3.1 Grids

For the near-body, the rotor blade are modeled using an overset structured mesh with an O-grid topology, while the fuselage is modeled using an unstructured mesh. The far-field is modeled using an adaptive Cartesian grid for the off-body. The near-body grids of the rotor

blades used in the previous studies of the SbS rotor are used in this study. For the fuselage, an unstructured surface mesh (mixed elements consisting of triangles and quadrilaterals) is generated using Pointwise's [89] grid generation tool, and the volume mesh is generated using mStrand [22], a native unstructured meshing system in Helios. The number of near-body volume grid points for each rotor blade is approximately 4.9 million, and for all eight rotor blades, it contains a total of 39.2 million grid points. For the near-body volume grid points of the fuselage (including rotor hubs), contains a total of 11.5 million grid points.

In the off-body mesh system, the Cartesian grid, as seen in figures 8.2 and 8.3, is automatically generated by SAMCart with the number of refinement levels set to eight and adaptive mesh refinement (AMR) turned on starting after 2,880 timesteps or 8 rotor revolutions. SAMCart has the capability, with AMR, to help capture the detailed physics of the rotor wakes, including vortices shedding off from the blade tips. There is a fixed refinement box that envelops both rotors in order to resolve and capture the tip vortices and wakes near the blades. The spacing in the fixed refinement box is set to 10% C_{tip}, which matches the spacing on the outer-boundary of the near-body volume grids. Setting a fixed refinement box along with a grid adaptive region for tracking the shedding vortices, especially in the far-wake, can help reduce the cost for these types of expensive numerical simulations. The size of the refinement box is $1.25R$ in the x-direction, $2.5R$ in the y-direction, and $0.625R$ in the z-direction. The x, y, and z coordinates are shown in figures. 8.2 and 8.3. The total number of grid points in the off-body grid is approximately 691 million grid points after 8,640 timesteps or 12 rotor revolutions. The domain size for the off-body is 20 rotor radii away from the origin in every direction.

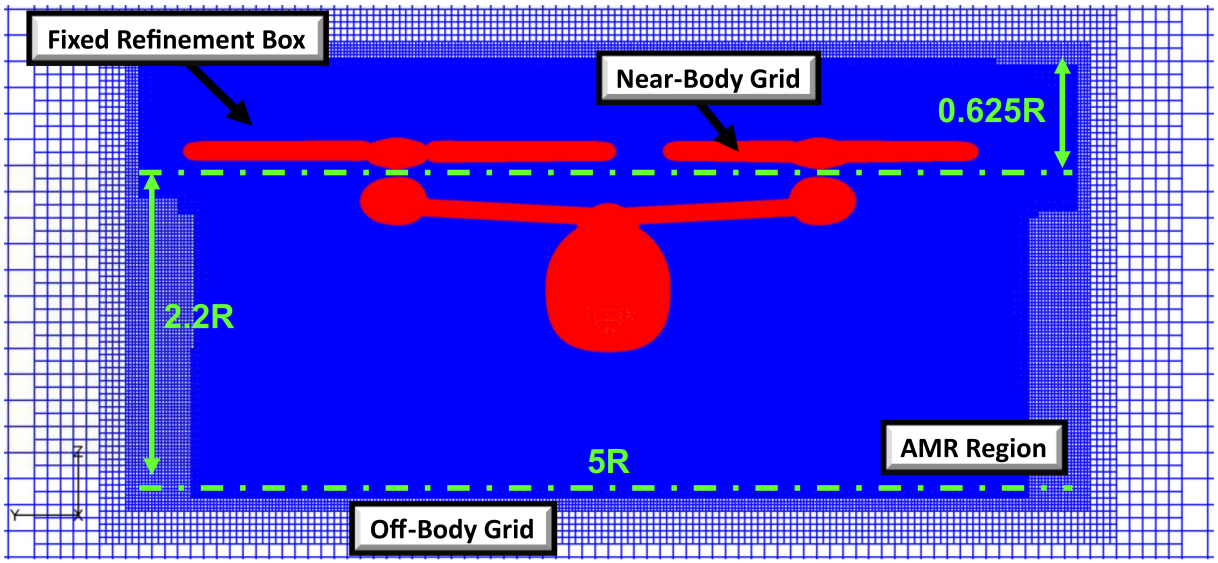

Figure 8.2: Front view of the off-body mesh.

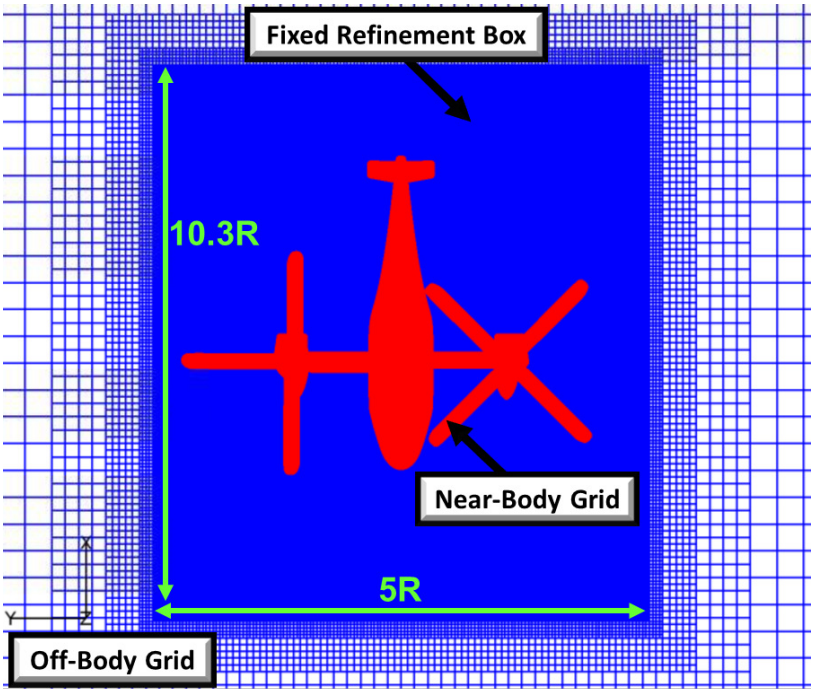

Figure 8.3: Top view of the off-body mesh.

8.4 CFD Setup

The strategy for reducing overall computational time used for the isolated SbS rotor study is also used in the current work. The time-accurate simulations are split into two separate time-step simulations. In the initial run, the time-step size is set at 1.0° azimuth for 2,880 timesteps or 8 rotor revolutions. Following this, a restart is initiated for the second run, during which a finer time-step size of 0.25° azimuth is employed for 5,760 timesteps or 4 rotor revolutions. This two separate time-step simulation was also recommended by Chaderjian [90] to achieve a quicker convergence of solutions. As mentioned earlier, AMR is activated after the initial run or 8 rotor revolutions. Using this method allowed us to reduce the total computational time from 168 hours (one week) to 100 hours (about four days).

All CFD simulations were conducted on Mustang, a HPE SGI 8600 high-performance computer (HPC) maintained by the U.S. Army Engineer Research and Development Center. Mustang is part of the U.S. Department of Defense (DoD) Supercomputing Resource Centers (DSRC). A total of 21 nodes (924 cores) were used for all simulations. Table 8.1 displays the mesh size and a detailed breakdown of the computational costs for each simulation, respectively.

Table 8.1: Computational size and cost | All overlap cases

Near-body grid	
Per rotor blade	4.9 million
Both rotors	39.2 million
Fuselage (with rotor hubs)	11.5 million
Off-body grid	
AMR OFF	272 million
AMR ON	691 million
Number of processors	924
Simulation time per rotor	28 | First 8 revs
revolution (hrs)	72 | Last 4 revs

8.5 Acoustic Simulation Setup

The same impermeable surface approach is used in chapters prior are used again in the current study. This approach considers only the loading from the rotor and fuselage surfaces of the SbS rotor vehicle, based on high-fidelity CFD results. In this paper, we do not fully take into account the acoustic scattering of rotor noise by the fuselage, although compressible RANS captures some of the acoustics pressure bounced off from the solid surface. Additionally, we do not address the broadband noise originating from rotor blades and the fuselage.

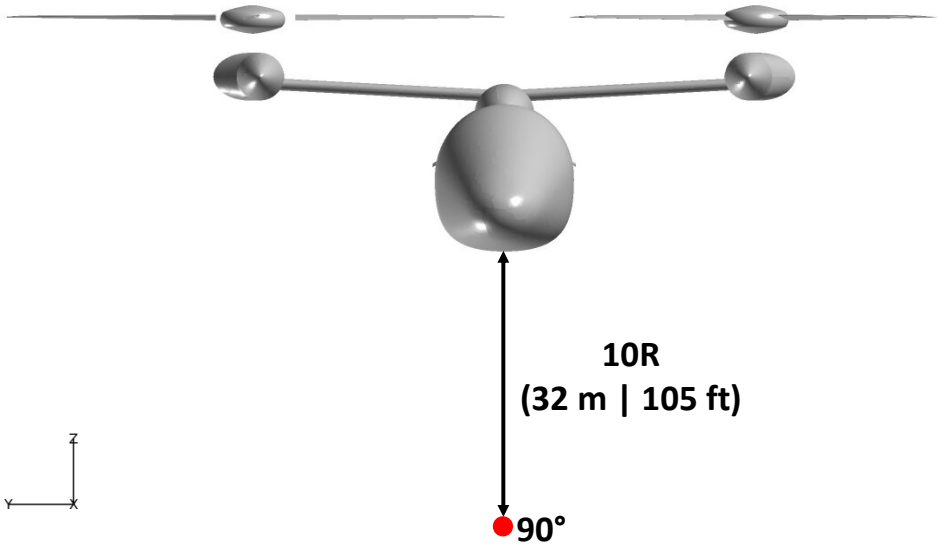

Figure 8.4: Observer location in the single observer case.

Two acoustic simulations are performed. In the first, a single observer is positioned at a 90°elevation angle and 10 rotor radii below the vehicle as shown in Figure 8.4. In the second acoustic simulation, a hemispherical grid is generated for multiple observers (a total of 1,000) at a distance of 10R (105 ft or 32 m) from the center of the vehicle seen in Figure 8.5. This hemispherical case is utilized to examine the acoustic directivity of the SbS rotors and the impact of overlap and fuselage on noise directivity.

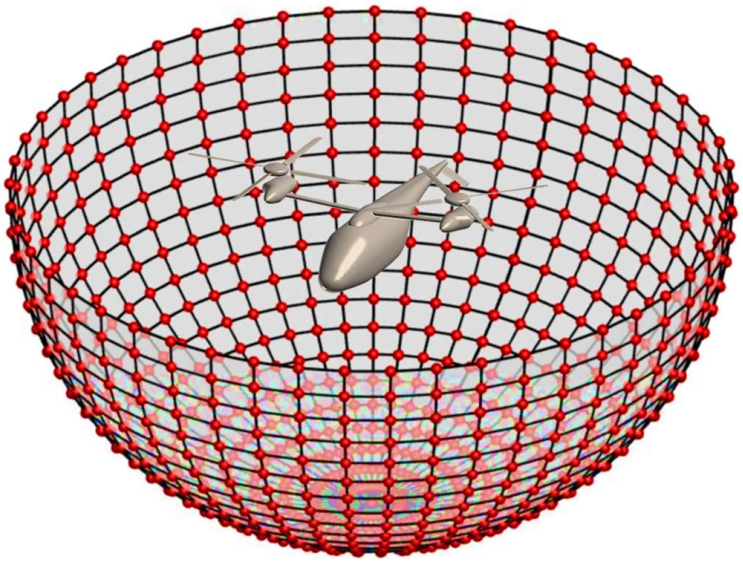

Figure 8.5: Observer location in the multiple observers case using a hemispherical grid.

8.6 Side-by-Side (SbS) Rotor in Full Configuration with Fuselage Results

This section presents results from the CFD and acoustic simulations of the SbS rotor UAM aircraft in full configuration. These simulations are based on high-fidelity CFD coupled with acoustics, and investigate performance, aerodynamics, and aeroacoustics for various overlap configurations in hover with the fuselage included.

8.6.1 Performance

The SbS rotor UAM aircraft was simulated in hover for the 0%, 5%, 15%, and 25% overlap configurations using OVERFLOW (rotors) and mStrand (fuselage) in Helios. The simulations were performed with a collective pitch angle of 8°for all of the overlap configurations. A total of 12 rotor revolutions (8,640 time steps) were run to ensure the full development of the flow field and the convergence of the forces and moments.

Figure 8.6 shows a comparison of the thrust and torque coefficients based on the projected area between the isolated SbS rotors and the full configuration for all of the overlap cases. In the 25% overlap case for both the isolated rotors and the full configuration, maximum thrust and torque are achieved. Meanwhile, there is a significant increase in thrust and torque for all of the overlap cases in the full configuration compared to the isolated rotor configuration. This is possibly due to the partial ground effect provided by the fuselage and support structure that holds the rotors. The partial ground effect can generate an upwash flow [91], which in turn increases the normal force as the rotor blades pass over the fuselage and support structure. The upwash and sectional blade loading will be investigated in detail

later. At the 8°collective pitch angle, the calculated thrust coefficient of the full configuration is about 50% more for all overlap cases compared to the expected thrust of NASA's notional design of the SbS rotor UAM aircraft with a 15% overlap [5]. Overall, the thrust increase is higher than the torque increase from the isolated rotors to full configuration, which yields a favorable effect in the Figure of Merit (FM), as will be discussed in the following paragraph.

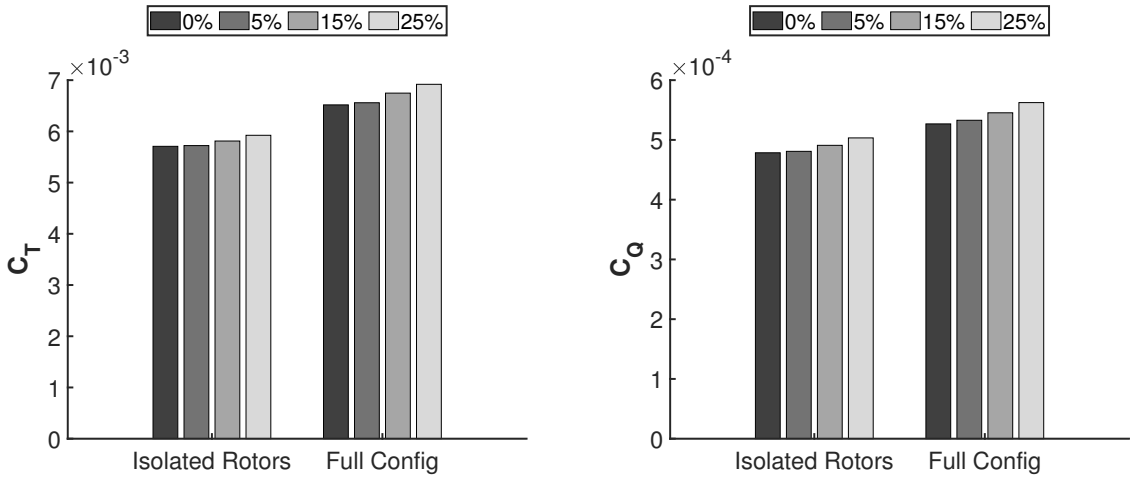

(a) (b)

Figure 8.6: Performance comparison between the isolated SbS rotors and the full configuration for all overlap cases: (a) thrust coefficient and (b) torque coefficient.

Figure 8.7 shows the convergence of FM for the four overlap configurations, including the isolated SbS rotors and the full configuration at a collective pitch angle of 8°. The definition of FM can be found in Eq. C.1 (see Appendix C). In Eq. (C.1), the projected overlap area A_{proj} (see Appendix B) is also used, similar to the thrust and torque coefficients.

In Figure 8.7, two simulations were run: a coarse time step size of 1° until 8 revolutions and a fine time step size of 0.25° after 8 revolutions. As a result, the variation of the x-axis value is not linear across 8 revolutions. It can be observed that convergence is achieved between 9 and 10 rotor revolutions for the isolated SbS rotors, and about 7 or 8 rotor revo-

lutions for the full configuration. However, additional rotor revolutions are added to ensure that the forces and moments are fully converged. Fluctuations are present in each overlap for both configurations and increase as the overlap percentage increases. These fluctuations are more pronounced in the full configuration cases. Overall, the full configuration exhibits much higher FM than the isolated rotors, which can be justified by the results in Figure 8.6.

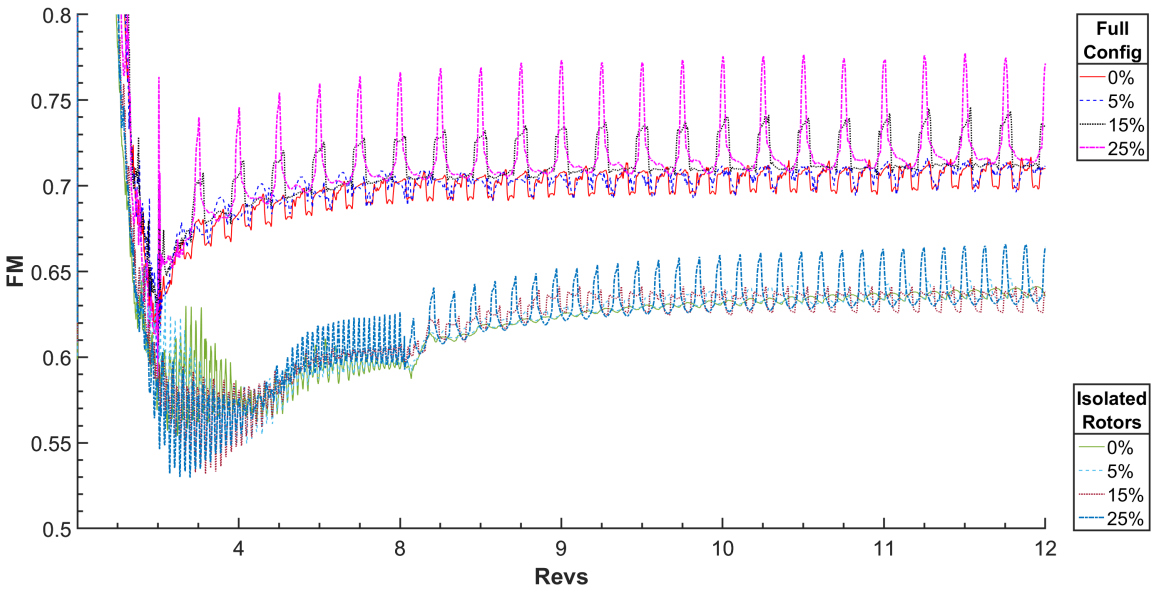

(a)

Figure 8.7: FM convergence plots for four rotor overlap cases for both isolated rotors and full configuration.

Table 8.2 presents the percentage difference of FM for different overlap configurations in the isolated rotors and the full configuration cases. The 0% overlap configuration serves as the baseline to which all other overlap configurations are compared. The results show that for the isolated SbS rotors, the 5% to 25% overlap cases have a difference in FM ranging from 0.126% to 0.5%, and for the full configuration, the FM difference ranges from 0.34% to 2.5%. In other words, the benefit of the rotor overlap is more distinct in the full configuration. In

addition, it is seen that not only does the rotor overlap have an influence on the increase of FM, but more notably, the presence of the fuselage provides a significant increase in FM. Overall, the inclusion of the fuselage increases FM by about 10 to 12% compared to the isolated rotors. This significant effect of the fuselage on FM is not typically apparent in the single rotor configuration. This indicates that for accurate prediction of FM in the SbS rotor configuration, it is essential to include the fuselage. Details on the flow physics are examined in the subsequent section to further investigate the correlation to this performance difference.

Table 8.2: FM difference for four overlap cases for both isolated rotors and full configuration.

Figure of Merit				
CP\OL	0%	5%	15%	25%
Iso Rotors	0.637	0.636 (0.13%)	0.638 (0.13%)	0.640 (0.49%)
Full Config	0.706	0.709 (0.34%)	0.719 (1.86%)	0.724 (2.53%)
ΔFM	0.069 (10.27%)	0.073 (10.85%)	0.081 (11.94%)	0.084 (12.32%)

8.6.2 Flow Physics

Figure 8.8 shows the iso-surface of the Q-criterion, colored by the vorticity magnitude of the full configurations, for all of the overlap cases. A clear interaction can be seen for the 25% overlap configuration in Figure 8.8(d) between the tip vortices from the left and right rotor blades at the overlap entrance and exit regions at a given time step. This interaction is considered a major source of noise, which will be discussed in detail later. The tip vortices break down and become less apparent right after the interaction. The wake development

exhibits significant differences, especially in the overlap region, due to the partial ground effect generated by the fuselage. The vortices near the hub of each rotor move upwards. This effect is more noticeable in the 0% overlap and 5% configurations, as seen in figures 8.8(a) and 8.8(b), respectively, compared to the other overlap configurations. Additionally, smaller worm-like structures can be observed, which have been identified as secondary vortex structures and previously investigated in studies of isolated rotor cases [65, 66, 68]. In a study by Bodling et al. [65] that used Helios with OVERFLOW to investigate the effect of sub-iteration convergence on the development of secondary vortex structures, it was recommended to achieve at least an OVERFLOW sub-iteration residual drop within the range of 2.4 order of magnitude and a SAMCart sub-iteration residual drop in the range of 1.25 order of magnitude to resolved the detailed secondary vortex structures. In the present work, a total of 50 sub-iterations in OVERFLOW and 20 sub-iterations in SAMCart are used. The OVERFLOW sub-iteration residual drop of about 1.8 order of magnitude and SAMCart sub-iteration residual drop of about 2.2 order of magnitude are attained in all of the overlap cases. Although the OVEFLOW residual drop is slightly lower than the recommended value, the SAMCart residual drop is sufficient to capture the secondary vortex structures in the off-body mesh.

For instance, Bodling et al. [65] leveraged Helios in conjunction with OVERFLOW to explore the impact of sub-iteration convergence and grid resolution. Their research suggested achieving an OVERFLOW sub-iteration residual decrease within the scope of 2.4 orders of magnitude and a SAMCart sub-iteration residual decrease within 1.25 orders of magnitude to effectively capture minuscule secondary vortex structures. They also advised utilizing the finest off-body grid resolution of 2.5% of the blade tip chord length. In our investigation, we

implemented a total of 50 sub-iterations in OVERFLOW and 20 sub-iterations in SAMCart. We accomplished an OVERFLOW sub-iteration residual decrease of roughly 1.8 orders of magnitude and a SAMCart sub-iteration residual decrease of about 2.2 orders of magnitude. Even though the SAMCart residual decrease meets the suggested value, the OVERFLOW sub-iteration residual decrease is below the recommended value. Furthermore, our grid resolution of the 10% C_{tip} for the finest grid spacing is considerably coarser than the suggested value. Therefore, our simulations are not designed to accurately or quantitatively capture secondary vortex structures, and a qualitative behavior, such as upstream movement of secondary vortex structures, is only discussed in this section

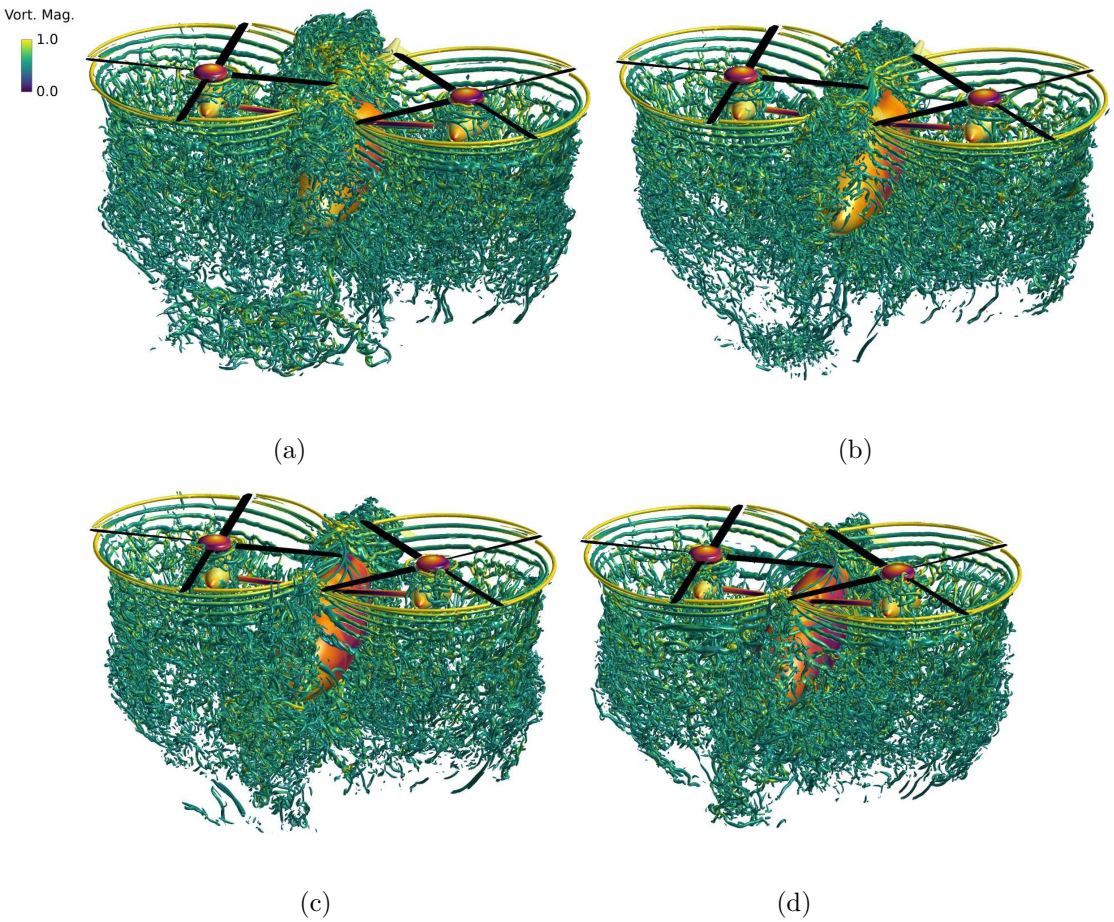

Figure 8.8: Iso-surfaces of the Q-criterion colored by vorticity magnitude of the full configurations for different overlap cases: (a) 0%, (b) 5%, (c) 15%, and (d) 25%.

Figures 8.9 provide a comparison of the induced inflow ratio at the rotor center plane for all of the full configurations. The inflow ratio is defined in Eq. 8.1 [16]:

$$\lambda_h = \lambda_i = \frac{v_i}{\Omega R} \tag{8.1}$$

where v_i is the induced velocity, Ω is the angular velocity, and R is the rotor radius. The positive value signify upwash (red color) and the negative value signify the downwash (blue color).

Figures 8.9(a) and (b) show a substantial increase in upwash flow for 0% and 5% overlap configurations, which was also visualized as upward-moving vortices in figures 8.8 (a) and (b). However, in the 15% and 25% overlap configurations, downwash significantly increases in the overlap region, as shown in figures 8.9(c) and (d), due to the overlapped tip vortices and wake effects from each rotor. The high downwash pushes the blade tip vortices downward, leading to reduced upwash in the overlap region, despite the partial ground effect from the fuselage, demonstrating the effect of rotor overlap. Hence, as rotor overlap increases, the amount of upwash in the overlap regions decreases. In other words, the rotor overlap negates the impact of the partial ground effect from the fuselage.

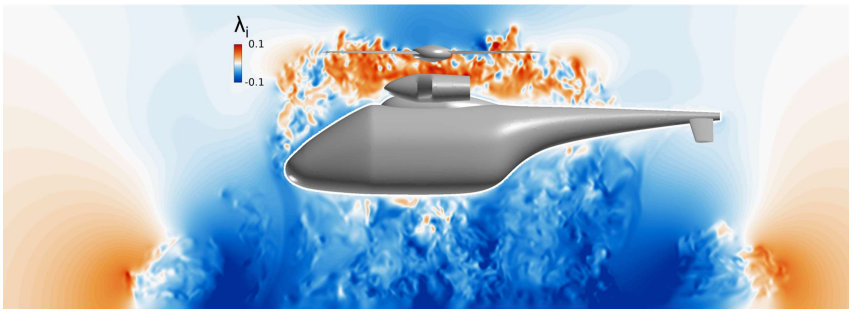

(a)

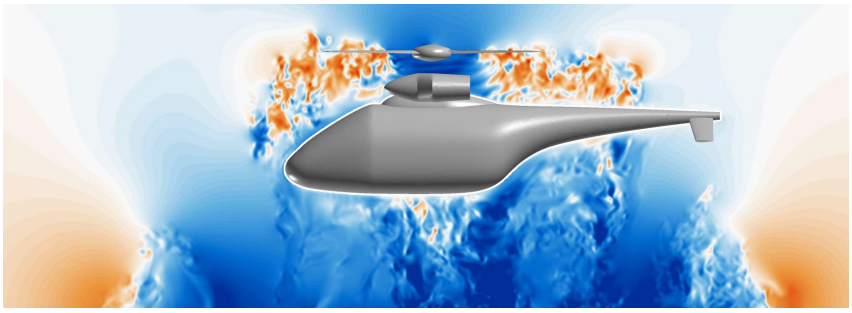

(b)

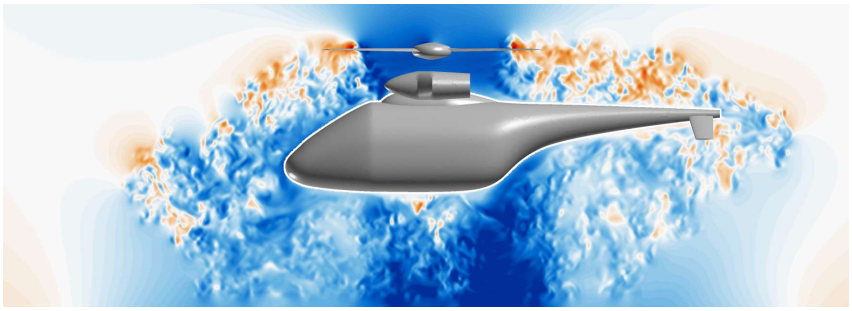

(c)

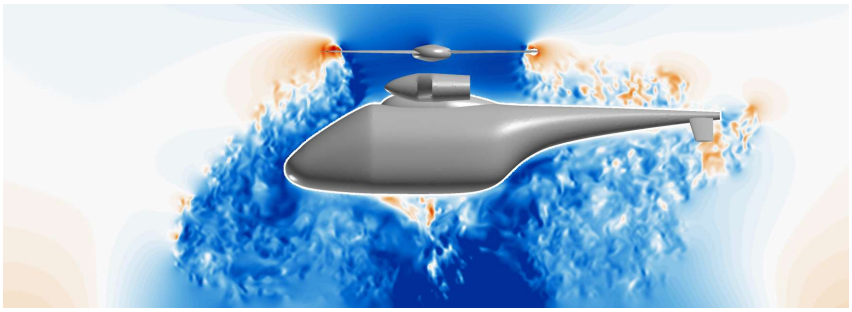

(d)

Figure 8.9: Comparison of λ_i (inflow ratio) for different overlap cases: (a) 0%, (b) 5%, (c) 15%, and (d) 25%.

Figure 8.10(a) shows a contour plot of the induced inflow ratio for the 0% overlap full configuration case. To quantify the inflow ratio downstream of the wake, various horizontal planes are added, and the results are shown in figures 8.10(b)–(f). A slight asymmetry in the inflow ratio is found between the left and right rotors. The inflow ratio contracts inwards as the overlap region increases. It is also shown that the downwash increases near the hub region as the overlap percentage increases. For the 0% and 5% configurations, the downwash is significantly reduced near the hub region.

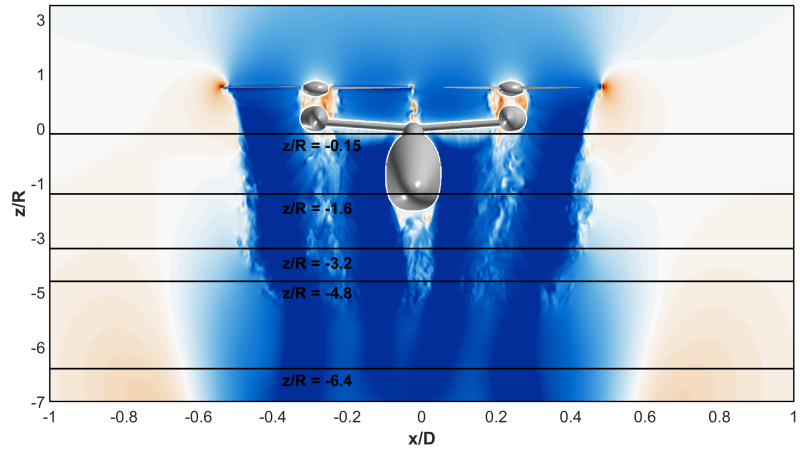

(a)

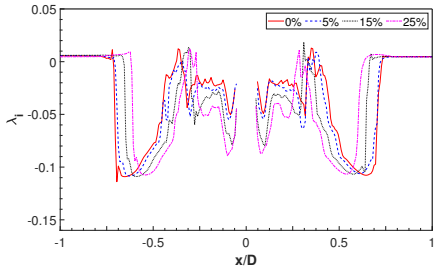

(b)

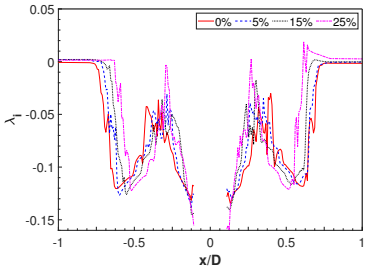

(c)

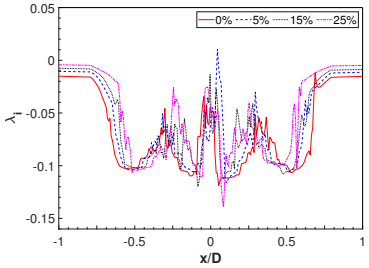

(d)

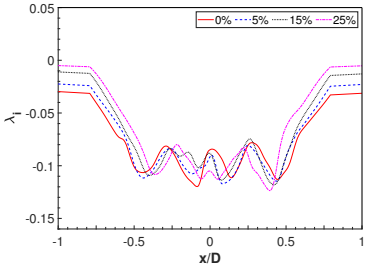

(e)

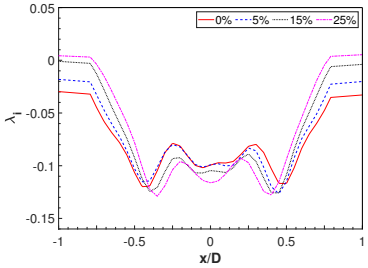

(f)

Figure 8.10: Comparison of λ_i (inflow ratio) between different overlap cases: (a) Measurement locations of inflow ratio, (b) z/R = -0.15, (c) z/R = -1.6, (d) z/R = -3.2, (e) z/R = -4.8, and (f) z/R = -6.4.

8.6.3 Aerodynamics

The fluctuation in aerodynamics is being investigated, especially in the overlap region. Figures 8.11 and 8.12 show the normal force on the rotor disk for the right rotor only, due to symmetry for both the isolated SbS rotors and the full configuration of all overlap cases. There is a reduction in the normal force magnitude at $\psi = 270^{\circ}$ within the rotor overlap region. The impact of the rotor overlap becomes more pronounced in the 15% and 25% cases, in which the azimuthal range increases for the thrust deficit. Even though the 0% overlap configuration does not have rotor overlap, it is evident from figures 8.11 and 8.12 that there is a decrease in normal force. Overall, the full configurations show an increase in the normal force compared to the isolated rotor, as shown in Figure 8.6(a). For the 0% and 5% overlap cases in full configuration, the thrust deficit region near the tip is extended in the azimuthal range similar to the 15% and 25% overlap cases. However, this extended thrust deficit is focused only at the tip region so that it does not negate the large increase in thrust, as shown in prior sections (see subsection 8.6.1). Additionally, multiple interactions are seen in Figure 8.12, especially in the 0% and 5% overlap cases, which correspond to interactional aerodynamics due to the interaction between the upwash wakes (influenced by the presence of the fuselage) and rotor blades. For the 15% and 25% configurations, the dominant interaction is still the tip vortices from one rotor with the other rotor, notably near the exit and entrance regions of the rotor overlap.

Figure 8.13 shows the root mean square of the pressure coefficient (Cp_{RMS}) on the fuselage, which indicates the source of unsteady loading noise. Across the majority of the span in the support structure that extends from the port to the starboard side of the vehicle, there is

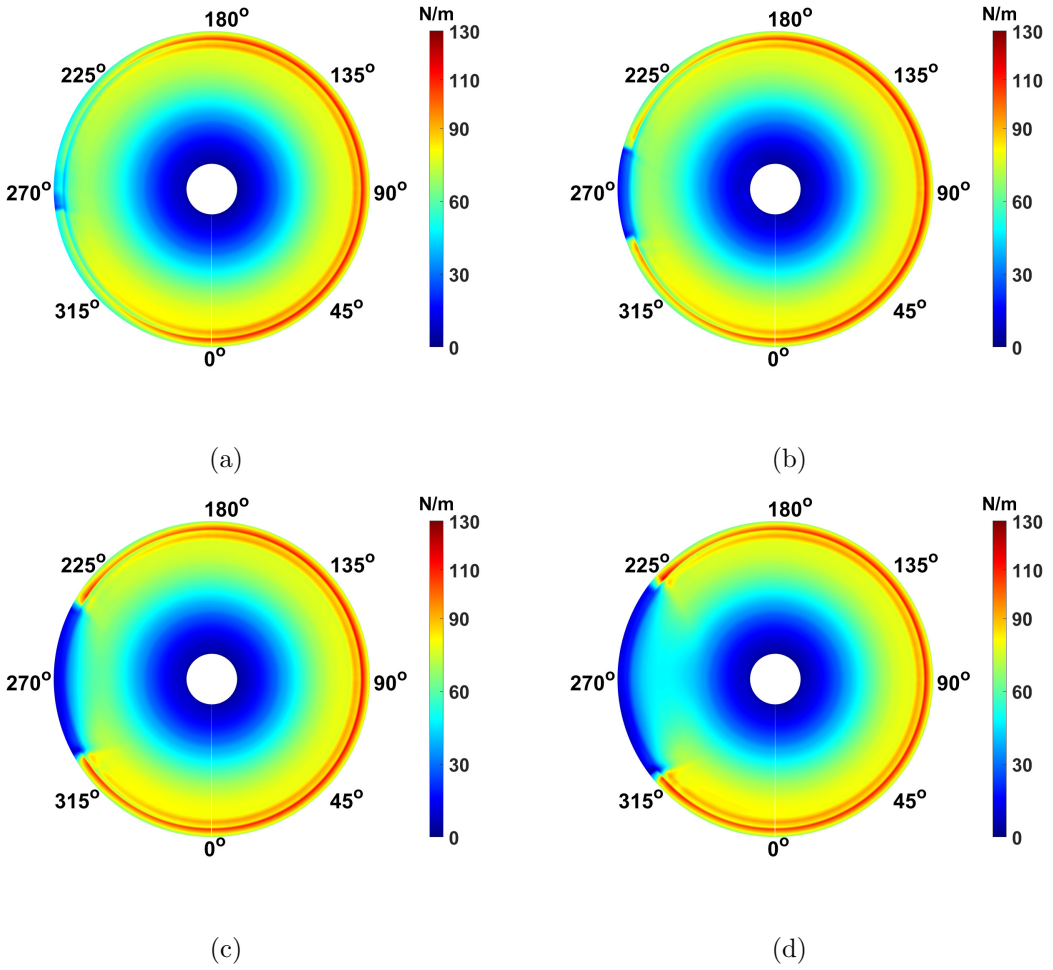

Figure 8.11: Normal force for different overlap configurations of isolated SbS rotors: (a) 0%, (b) 5%, (c) 15%, and (d) 25%.

higher unsteadiness in the surface pressure for the 0% and 5% overlap cases when compared to the 15% and 25% overlap cases. This is attributable to the increase in upwash within the overlap and hub regions for configurations with less rotor overlap. As demonstrated in figures 8.8 and 8.9, less rotor overlap leads to an increase in upwash, higher unsteadiness, and more intense aerodynamic interactions with rotor blades than cases with a greater degree of rotor overlap. The 15% and 25% overlap cases demonstrate high unsteadiness only at the leading edge of the support structure. From this result, it is expected that the 0% and 5% overlap cases would generate intense noise from the fuselage. However, despite the

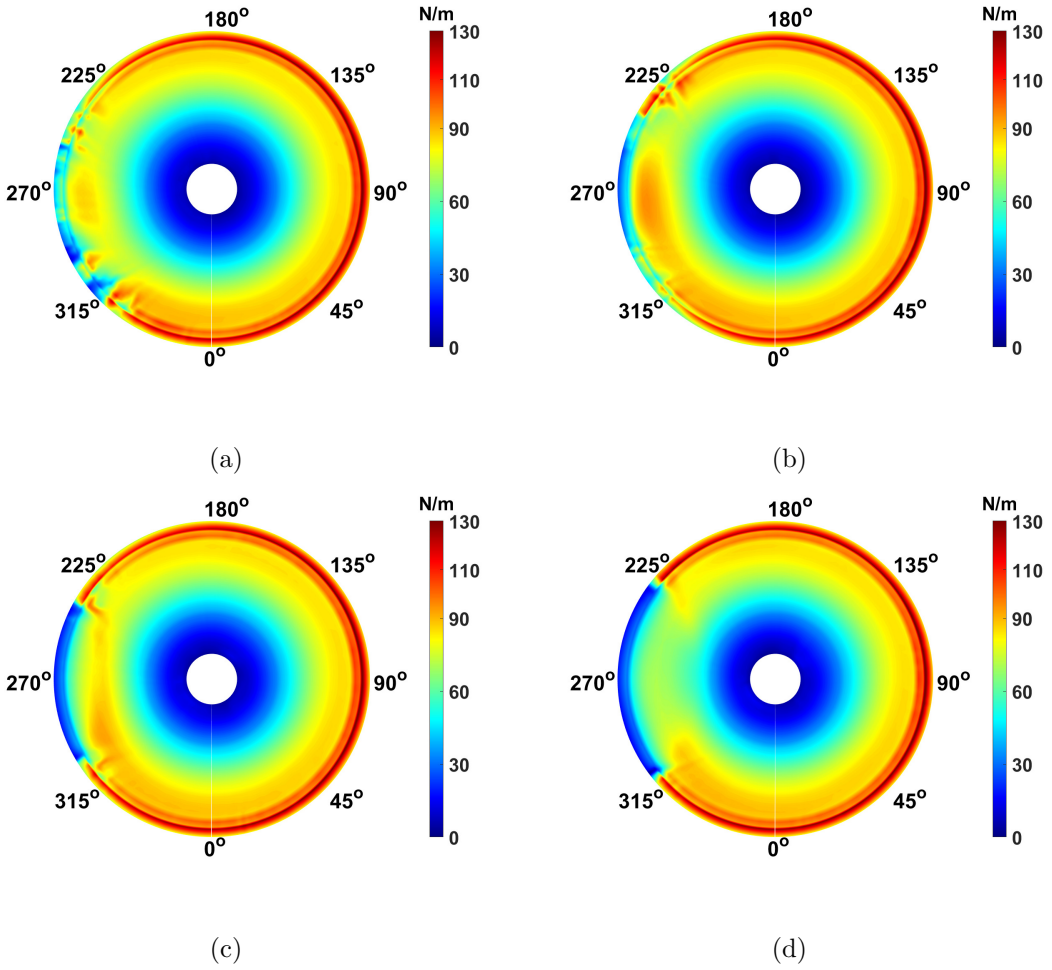

Figure 8.12: Normal force of full configurations for different overlap: (a) 0%, (b) 5%, (c) 15%, and (d) 25%.

significant unsteadiness observed on the fuselage surface, in all four overlap configurations, the rotor blades still contribute more to noise generation than the fuselage, as will be shown later, since the Mach number of rotor blades near the tip section is much higher than that of the fuselage.

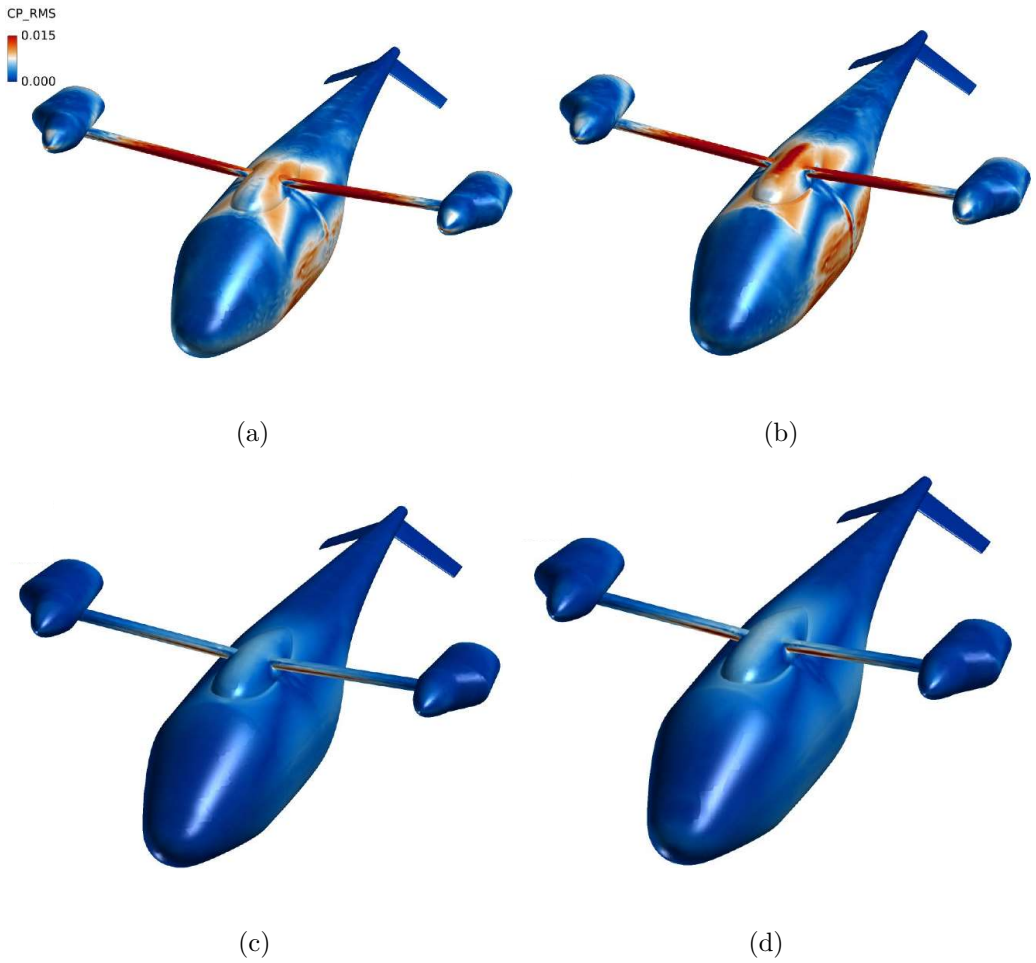

Figure 8.13: Cp_{RMS} of the full configurations for different overlap cases: (a) 0%, (b) 5%, (c) 15%, and (d) 25%.

Figure 8.14 shows the non-dimensional normal force as a function of azimuthal angle at four radial locations ($r/R = 0.5, 0.75, 0.9$, and 1.0) in full configuration. The normal force of different overlap is compared to one another. There is a significant increase in the width, depth, and rate of change of the normal force as the overlap region increases, especially for the 25% overlap configuration. At $r/R = 0.5$, the normal force substantially increases for all overlap configurations, with the 25% overlap case having the largest magnitude of the normal force, which leads to an improvement in the thrust performance as discussed earlier. In the outboard locations, sharp peaks and fluctuations are seen in the 0% and 5% overlap

cases, but more so for the 0% overlap configuration, due to having lower induced velocity as a result of having no rotor overlap compared to the other overlap configurations. Due to the presence of the fuselage, an upwash flow is formed and becomes a major contributor to the fluctuations shown.

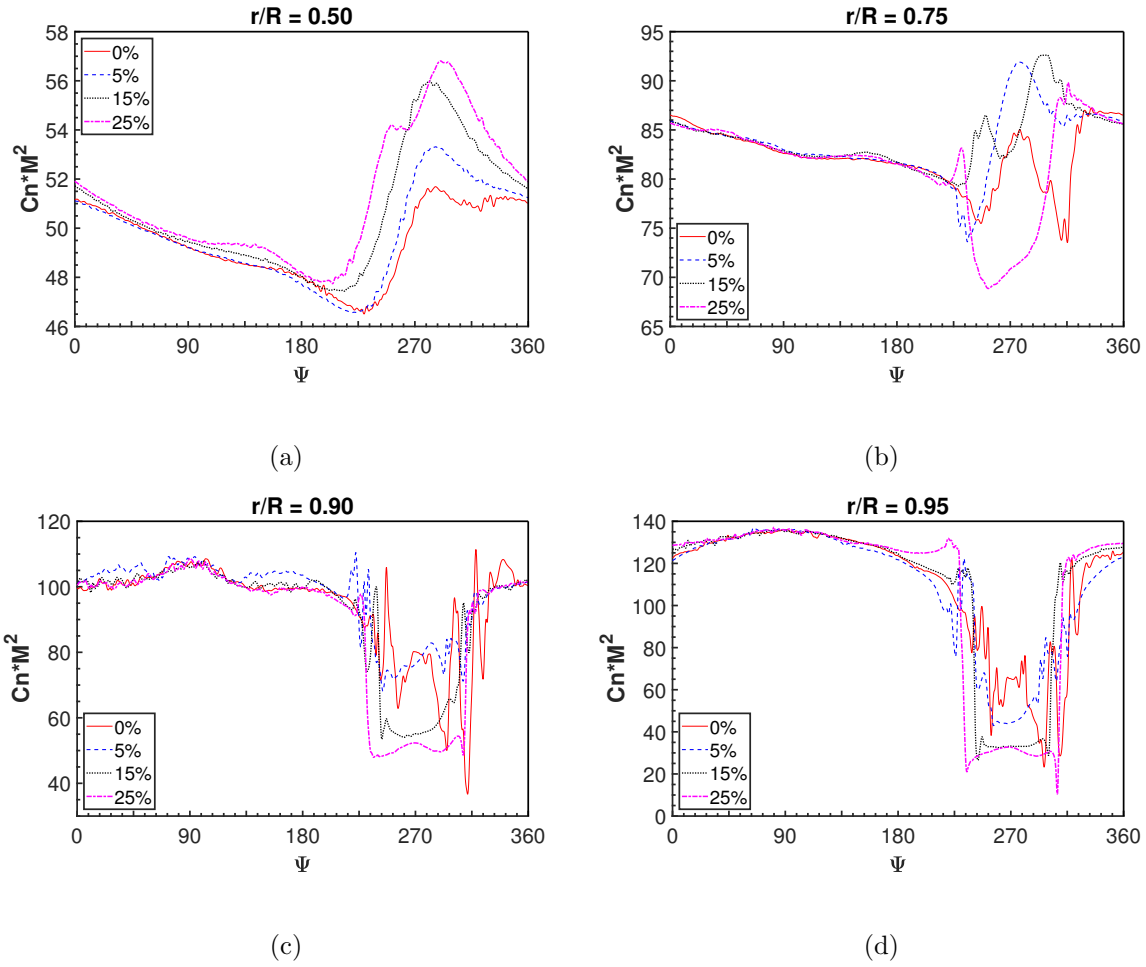

Figure 8.14: The non-dimensional normal force coefficient in full configuration for different overlap at four different radial locations: (a) $r/R = 0.5$, (b) $r/R = 0.75$, (c) $r/R = 0.90$, and (d) $r/R = 1.0$.

Figure 8.15 shows the blade sectional thrust coefficient, $\frac{dC_T}{dr}$, for all four overlap configurations along the blade radius in full configuration, at azimuthal angles of 90°, 180°, 270° and 360°. Due to symmetry, only the right rotor is shown. The 0% overlap case shows a greater

increase in the sectional thrust in the outboard section at 360° azimuth angle, compared to the other overlap configurations. It also shows that there is deficit in the sectional thrust at 270° as seen in the other cases that have rotor overlap, which is absent in the 0% overlap case. This thrust increase for the 0% overlap case corresponds to the amount of upwash flow or reduced downwash effect due to having no rotor overlap or the partial ground effect provided by the fuselage, as shown in Figure 8.10.

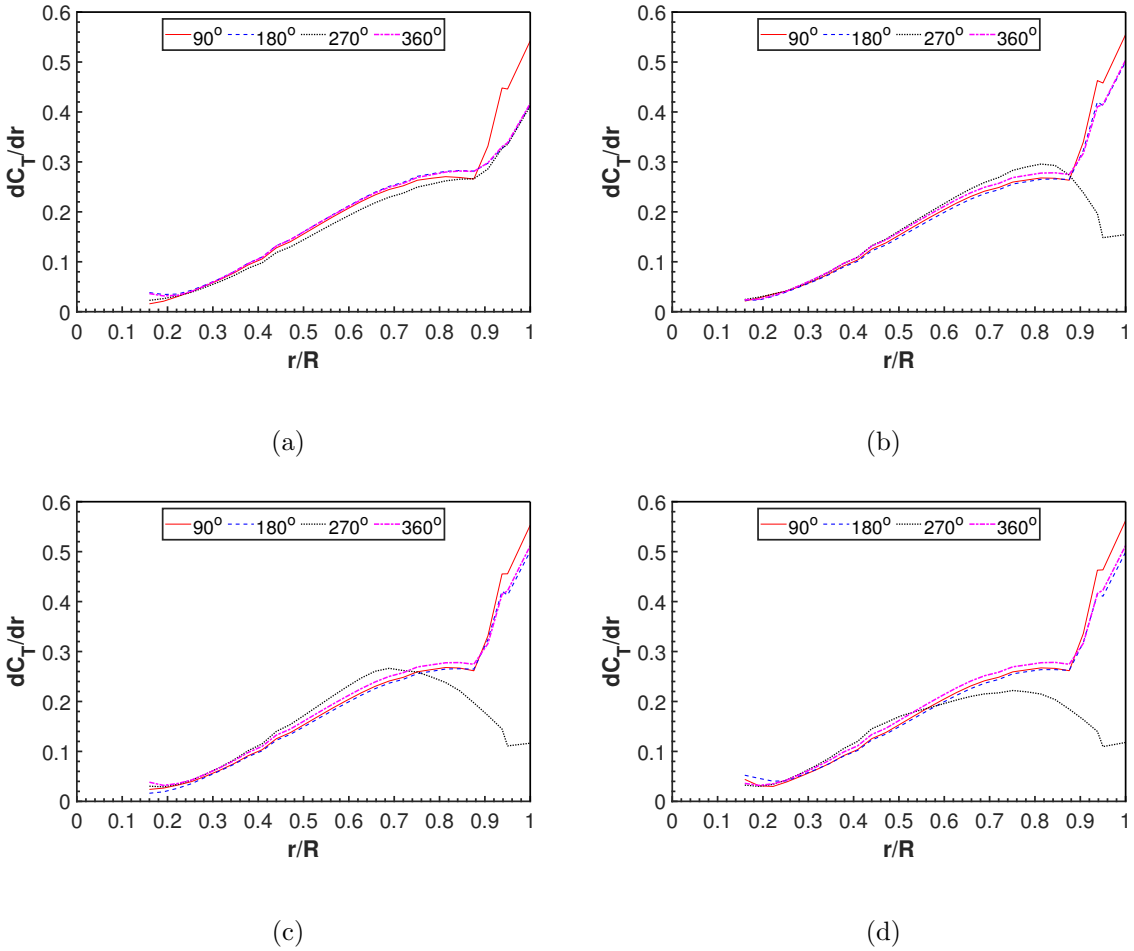

Figure 8.15: Blade sectional thrust coefficient in full configuration for different overlap at four different azimuthal angles: (a) 0% , (b) 5% , (c) 15%, and (d) 25%.

Figure 8.16 shows a comparison of the blade sectional thrust coefficient for both the isolated SbS rotors and the complete configuration with varying overlaps at a 270° azimuth

angle. As previously noted, there is a substantial increase in the blade sectional thrust near the 90% span location for the 0% overlap case in the full configuration, which can be attributed to the upwash flow influeced by the presence of the fuselage. In general, blade loading increases in the full configuration compared to the isolated rotors. As the overlap percentage grows, blade loading diminishes for both isolated rotors and full configuration, particularly in the outboard region.

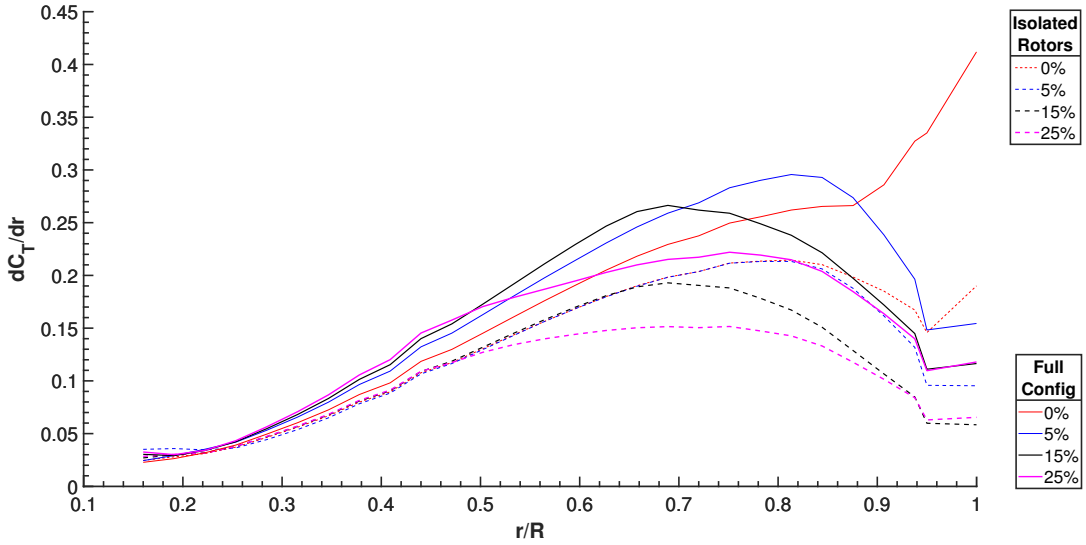

Figure 8.16: Blade sectional thrust coefficient for the isolated SbS rotors and full configuration at the 270° azimuthal location.

8.6.4 Aeroacoustics

Figure 8.17 provides a quantitative comparison of $dF_z/d\Psi$ for the right rotor at the 75% span across all full configurations with varying overlap. It is crucial to note that this derivative of the normal force constitutes the primary source of loading noise in Farassat's Formulation 1A [87]. Given the symmetrical distribution of $dF_z/d\Psi$ between both rotors, only the right rotor is analyzed here. Between 225° and 315° azimuths, a significant number of pressure

fluctuation events can be attributed to interactional aerodynamics resulting from interactions between the upwash and rotor blades as well as rotor-to-rotor blade vortex interactions. Rotor-to-rotor interactions encompass those between the tip vortices from one rotor and the other rotor blades, particularly near the overlap entrance and exit regions, as observed in Figure 8.8. For example, for the 25% configuration, the primary peaks only occur at the entrance and exit regions of the overlap. In Figure 8.17(a), however, around the 290° azimuth angle for the 0% overlap configuration, there are peaks with considerably larger amplitudes compared to other overlap configurations. The upwash flow interacting with the blades for the 0% overlap configuration near the exit point of the overlap region contributes to intense pressure fluctuations, which are also present in other overlap cases, albeit to a lesser extent.

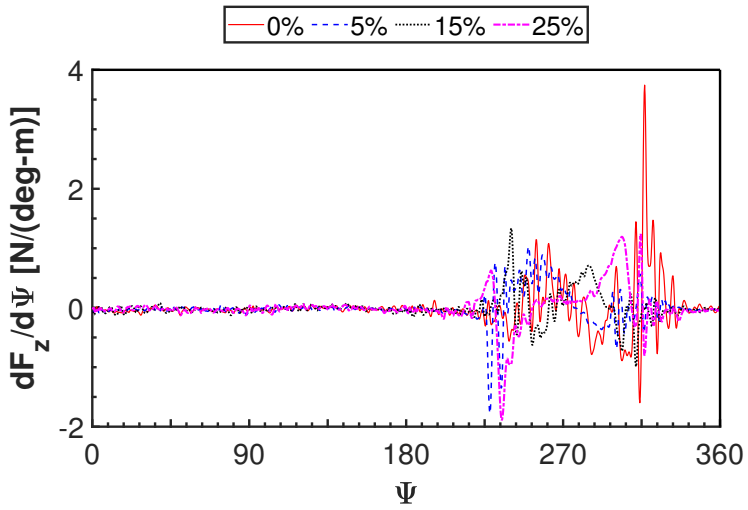

Figure 8.17: Comparison of $dF_z/d\Psi$ of the right rotor at the 75% span for the full configuration with different overlap.

Figure 8.18 displays the total acoustic pressure for a single observer situated 10 rotor radii below the rotor disk plane across all overlap configurations, taking into account noise contributions from the rotors and fuselage individually. The tonal peaks are regularly spaced for configurations with higher percentages of rotor overlap, as seen in figures 8.18(c) and

8.18(d) for the 15% and 25% overlap cases, respectively. The peaks are more distinct in the 25% overlap case. These peaks are attributed to rotor blades passing through the entrance and exit regions of the overlap region. However, multiple irregular peaks are present in the 0% and 5% overlap configurations, as shown in figures 8.18(a) and 8.18(b), potentially due to the fuselage providing a partial ground effect. The upwash effect, as previously discussed, contributes to the increase in the noise and, hence, the 0% configuration shows large multiple tonal peaks. Although the rotor noise is higher than the fuselage noise for the 0%, 5%, 15% overlap cases, the fuselage noise still contributes to the total noise noticeably. In the 25% overlap case, the fuselage noise is in phase with the rotor noise, and the magnitudes from both components are similar. This results in large positive peaks.

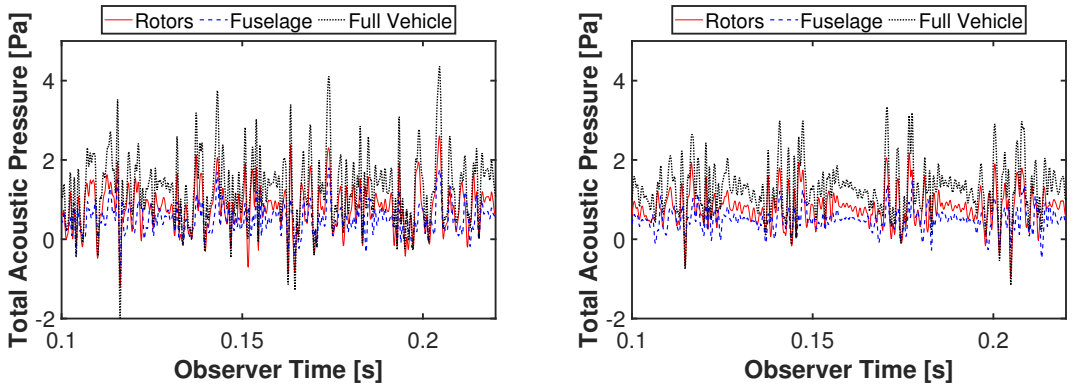

(a)

(b)

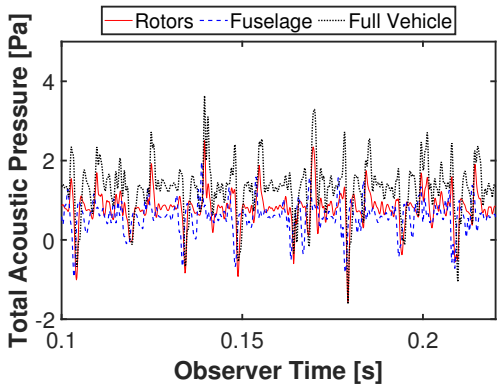

(c)

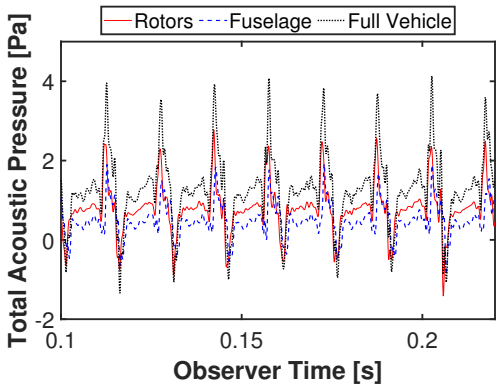

(d)

Figure 8.18: Comparison of the total acoustic pressure for the full configurations of different overlap configurations. The contributions from the rotors and fuselage only are also shown: (a) 0% , (b) 5% , (c) 15%, and (d) 25%.

In Figure 8.19, the A-weighted sound pressure level (SPL) for the first 50 blade passing frequency (BPF) harmonics of all overlap configurations is depicted, broken down into contributions from the rotors and fuselage. For the 0% and 5% overlap cases, the tonal noise occurs at both even and odd harmonics. This indicates that the dominant noise sources encompass not only the rotor-to-rotor interaction noise but also the noise resulting from the interaction between the individual rotor and upwash flow, as observed in Figure 8.18.

Conversely, in the 15% and 25% overlap configurations, the tonal noise occurs at only even harmonics, suggesting the rotor-to-rotor interaction noise. For the 0% and 5% overlap cases, the rotor noise is more important than the fuselage noise. For the 15% and 25% overlap cases, both the rotor and fuselage noise are almost equally important.

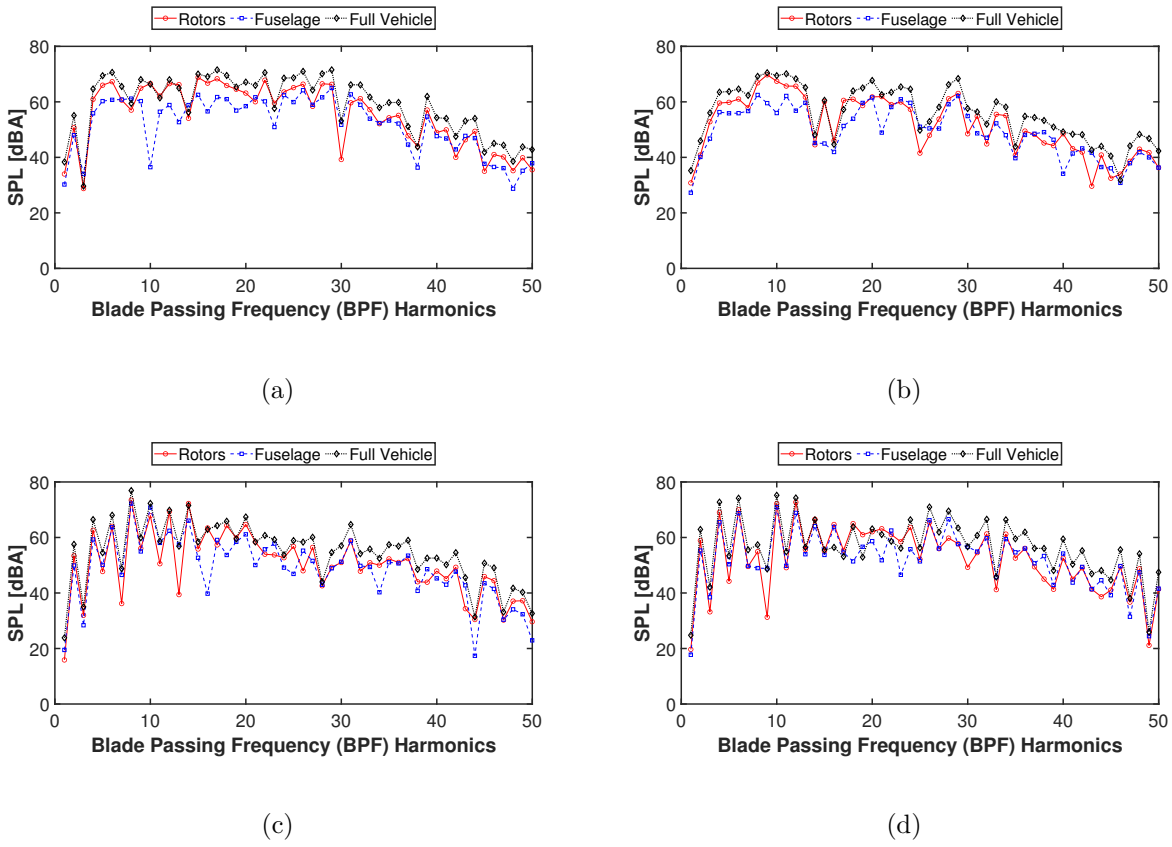

Figure 8.19: Comparison of the A-weighted sound pressure level for the full configurations of different overlap configurations. The contributions from the rotors and fuselage only are also shown: (a) 0% , (b) 5% , (c) 15%, and (d) 25%.

Figure 8.20 displays the contours of the first integrand of the loading noise portion of Farassat's Formulation 1A [87], or the rate of the change of the loading, for the right rotor only, due to symmetry. The black lines in the contour plots represent the rotor blades at an observer time (indicated by black dashed lines in the acoustic time history plots) when acoustic peaks are observed for the given microphone position (10R below the rotor disk

plane). This figure clearly shows the distinct noise source distributions for different overlap cases. For example, for the 25% overlap case, the dominant noise sources are rotor-to-rotor BVI events occurring when the blades enter (blue color) or exit (red color) the overlap region. However, as discussed earlier, the 0% overlap configuration features numerous interactions beyond rotor-to-rotor interactions, as evidenced by the multiple sporadic peaks.

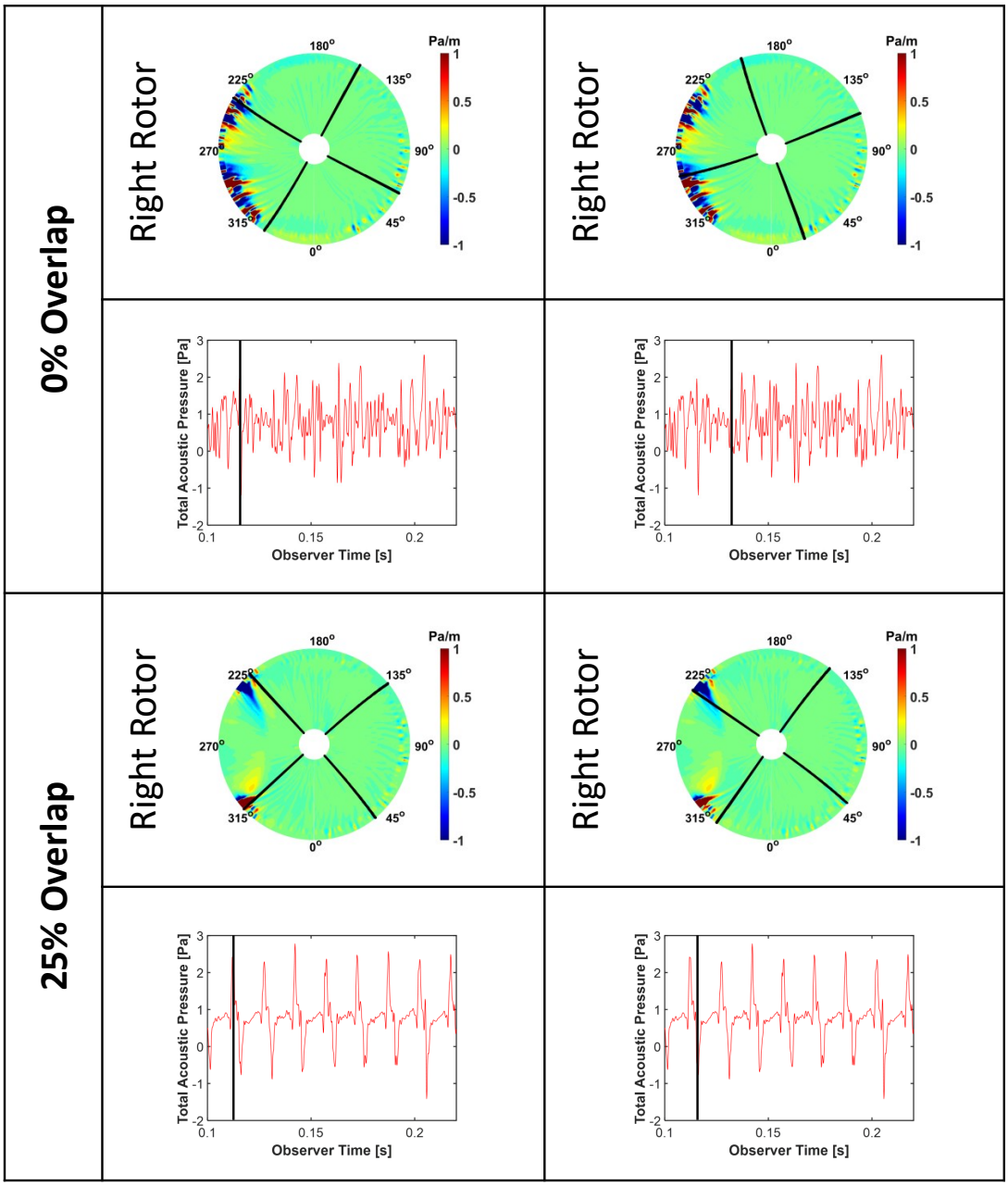

Figure 8.20: Comparison of noise intergrand results of the right rotor for the 0% and 25% overlap configurations.

Figure 8.21 shows the A-weighted overall sound pressure level (OASPL) for all overlap configurations. It is evident that the 0% overlap configuration exhibits the highest OASPL, which includes contributions from both the rotors and fuselage, compared to the other overlap configurations. This is due to the additional noise sources mentioned earlier. In the 0%

overlap configuration, the absence of rotor overlap allows for more upwash flow from the fuselage, leading to additional interactions and higher overall noise levels. Conversely, the 25% overlap configuration, which features maximum rotor overlap that prevents the passage of upwash flow and generates higher induced velocity from a strong downwash effect, reduces the partial ground effect provided by the fuselage, resulting in lower overall noise levels. The difference between rotor noise and fuselage noise becomes smaller as the overlap percentage increases. This figure demonstrates the noise reduction benefits associated with overlapping rotors. Interestingly, this is the opposite result for isolated rotors, in which the 25% overlap configuration exhibited the highest noise level [74]. Therefore, including the fuselage is crucial for a comprehensive noise assessment. However, it is worth noting that this research does not incorporate the acoustic scattering by the fuselage. A complete analysis of noise would need to account for this acoustic scattering as well.

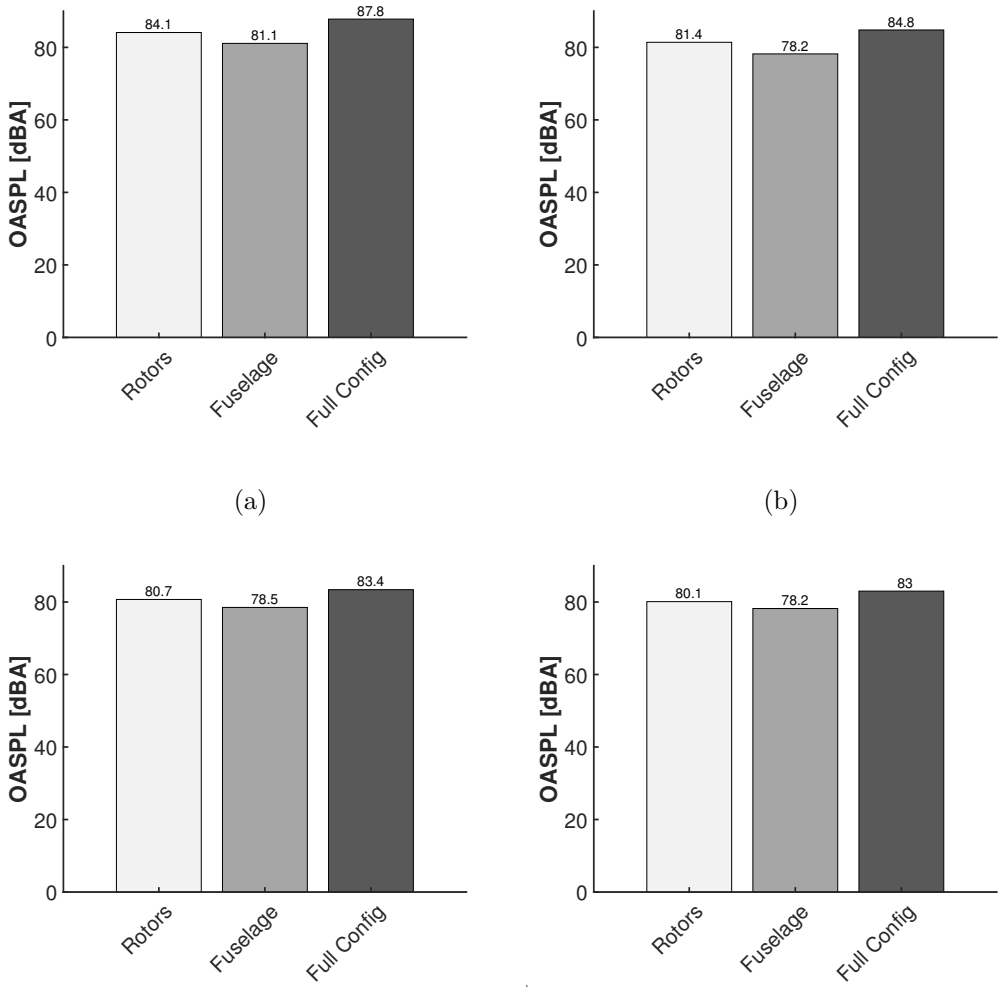

Figure 8.21: Comparison of the A-weighted overall sound pressure level for the full configurations of different overlap configurations. The contributions from the rotors and fuselage only are also shown: (a) 0% , (b) 5% , (c) 15%, and (d) 25%.

Figure 8.22 displays the directivity patterns of the A-weighted OASPL for each overlap case on a hemispherical grid with a radius of 10 times the rotor radius. To facilitate comparison, the color bar remains consistent. The top view of the hemispherical grid is shown in the contour plots. Various radiation patterns are depicted for each overlap case, with differences ranging from minor to significant. Asymmetry differences are evident in the contour plots for the 0% and 5% overlap cases, possibly due to the wake of the combined rotor system not

being stably symmetric. A similar phenomenon was observed in a study of SbS rotors with no rotor overlap by Healy et al. [32]. Additionally, the 15% and 25% overlap cases exhibit noticeable strips across the hemisphere grid. These strips are attributed to acoustic destructive interference between the two rotors, as investigated in-depth in a study of the same SbS rotors without the fuselage [74]. Interestingly, the destructive interference occurs at different locations for the 15% and 25% configurations. However, these strips did not appear in the 0% and 5% overlap cases since the dominant noise source is not the rotor-to-rotor BVI, but the rotor upwash wake and blade interaction.

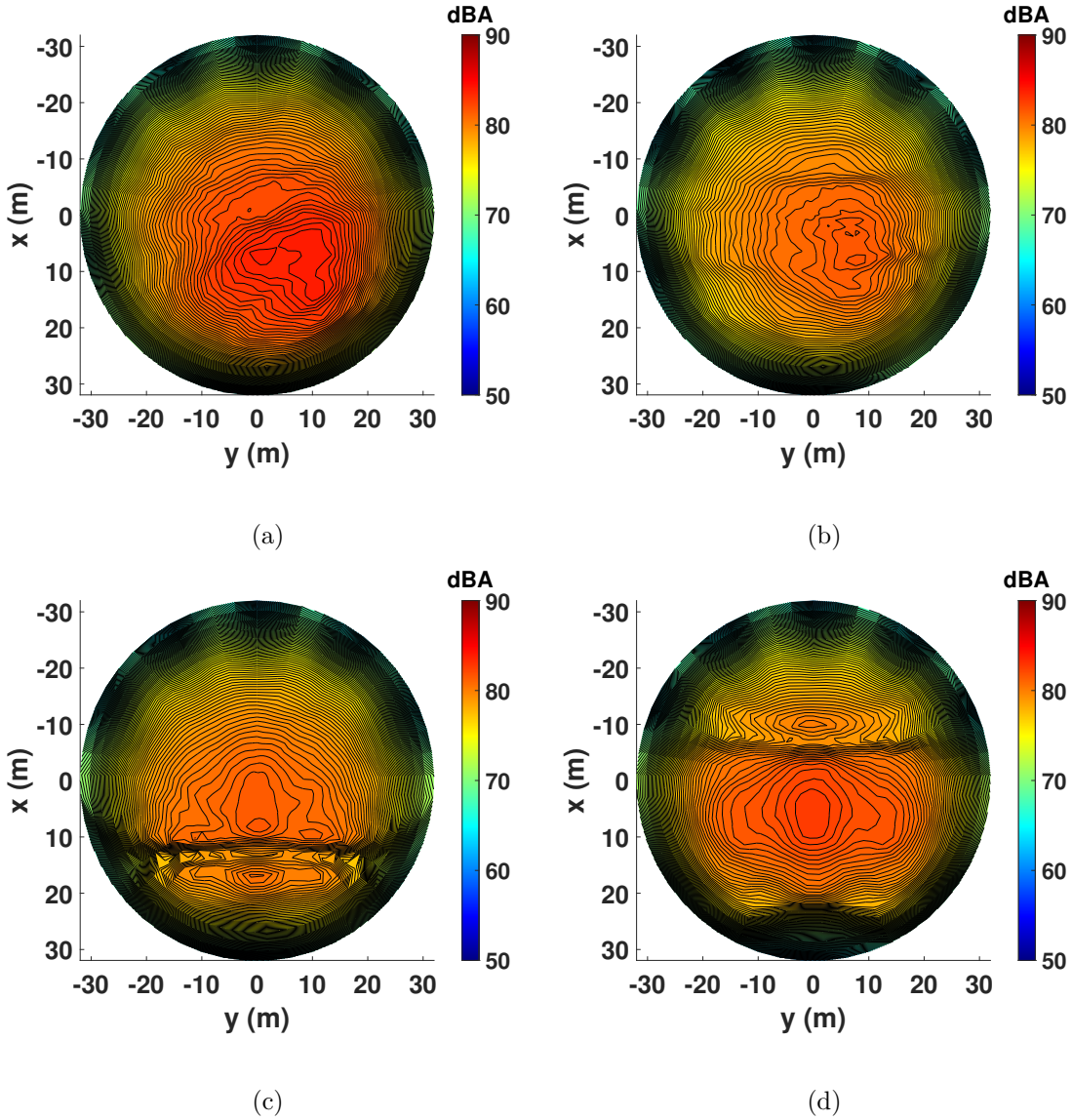

Figure 8.22: Comparison of the A-weighted overall sound pressure level on hemisphere grids: (a) 0% , (b) 5% , (c) 15%, and (d) 25%.

8.6.5 Conclusions

The full configuration of NASA's SbS rotor UAM reference vehicle has been analyzed in hover conditions. High-fidelity CFD simulations using CREATE^{TM}-AV Helios, coupled with acoustics performed by PSU-WOPWOP, were conducted to investigate the performance, aerodynamics, and acoustics of the SbS rotor vehicle with various rotor overlap configura-

tions, including 0%, 5%, 15%, and 25%. The tip vortex and induced velocity were examined, as well as the partial ground effect caused by the fuselage's presence and its influence on the blade sectional aerodynamic loading. The study also investigated the correlation between these factors and the resulting noise. Noise directivity comparisons were made between each of the overlap configurations. The following conclusions can be drawn based on the results presented and analyzed in this work:

1. Incorporating the fuselage revealed a noticeable impact on hover performance, as demonstrated by the increase in FM for all overlap configurations. From the 0% overlap configuration (with no rotor overlap) to the 25% overlap configuration (with a significant percentage of rotor overlap), there was a substantial increase of FM by +10.275% and +12.317%, respectively, compared to cases without the fuselage's presence. Similar increases were observed for other overlap configurations. This indicates that the fuselage exerts considerable influence, and the increase in rotor overlap also affects rotor performance.

2. In the vicinity of the overlap region, there was an increase in the normal force for all overlap configurations, particularly near the mid-span of the blade. Conversely, there was a decrease in the normal force observed beyond mid-span and toward the blade tip with the increased rotor overlap, which are associated with higher induced velocity and less upwash flow.

3. It was observed that the induced velocity exhibits a significant decrease in the overlap region for configurations with little to no rotor overlap. In contrast, the 15% and 25% overlap configurations, which have a considerable amount of rotor overlap, displayed

an increase in induced velocity, thereby reducing the upwash flow generated.

4. The surface pressure across the structure supporting the rotors exhibits significant unsteadiness. Notably, full configurations with little to no rotor overlap tend to display heightened unsteadiness, primarily due to increased upwash compared to cases with greater rotor overlap.

5. In hover conditions, the most dominant source of noise stemmed from blade-tip interactions with tip vortical structures as the blade enters and exits the overlap region for configurations with higher overlap percentages. Additionally, the presence of the fuselage increased the amount of upwash flow, leading to more aerodynamic interactions between rotor wake flows and blades. This resulted in a higher noise level, particularly for configurations with little to no rotor overlap. The 0% and 5% overlap configurations exhibited noise spectrum at all harmonics of BPF, but the 15% and 25% overlap cases showed noise spectrum only at even harmonics, which demonstrates different characteristics of noise source as discussed. Overall, the 25% overlap configuration demonstrated the lowest overall sound pressure level, indicating the benefits of overlap in terms of noise reduction. This contrasts with the isolated rotor case, where the 25% overlap exhibited the highest noise level.

6. Acoustic interference was manifested as a strip in the noise directivity of the 15% and 25% overlap configurations. However, these strips did not appear in the 0% and 5% overlap cases since the dominant noise source is not the rotor-to-rotor BVI, but the rotor upwash wake and blade interaction.

Chapter 9

Concluding Remarks

This chapter provides a summary of this dissertation work including a list of contributions. Thoughts and suggestions for future work are also outlined in this chapter.

9.1 Overview of the Research Work

The investigations carried out in this dissertation work included analyzing aerodynamically induced noise of a SbS rotor UAM aircraft in hover: performance/aerodynamics comparison between various rotor overlap configurations as well as the flow physics associated, the impact of ground effect, and comparisons between with and without the fuselage. A validation study of the methodology employed in the work is also conducted primarily comparing with the acoustic results from the parallel BVI wind tunnel experiment.

Three big key questions were posed in the opening of this dissertation in regard to the contributions from this thesis work are answered here. It has been shown that the current state-of-the-art CFD/acoustics technology is able to accurately model complex problems like BVI, which plays a significant role in the noise generation of UAM aircraft, this was demonstrated in the validation study of the parallel BVI wind tunnel experiment, which is

one of the most impulsive orientation for BVI with the strongest interaction. Good agreement was observed for the acoustics between the predictions and experiment. This is proven further by the previous validation studies that did not capture the vortex in the simulation, but rather they used an analytical model for the vortex. The roll-up an convection of the tip vortex was computed from first principles for the validation study performed in this thesis work, where the vortex was fully captured in the CFD simulation. These validation give us good confidence that current state-of-the-art high-fidelity analyses can be used to make design decisions about rotorcraft performance and noise. Examples of how these high-fidelity simulations can be used for design have been presented throughout the investigations of the SbS rotor UAM aircraft by showing a number of trade-off studies in rotor overlap, ground effect, etc. These examples can provide stimulus for additional ways with the accurate CFD and acoustic models presented here be used to assist with real UAM designs. However, the results presented in this thesis can't exactly pinpoint the the fundamental physics involved in rotor noise for the SbS rotor UAM aircraft or other SbS designs since fixed rotor collective pitch angles were used in all of the simulations as opposed to trimming to a consistent thrust coefficient for all overlap configurations considered. The omission of the latter was to focus more so on the effect of the rotor overlap on the performance, aerodynamics, flow physics, and acoustics. Performance and design trade-offs for specific UAM vehicles will require consistent rotor trim settings in order to provide a true apples to apples comparison.

9.1.1 Validation of Parallel Blade-Vortex Interaction

A validation study of the parallel BVI wind tunnel experiment was carried out to validate the methodology employed in the SbS rotor UAM aircraft studies. The parallel BVI experiment consisted of a wing based vortex generator with a two-bladed rotor positioned downstream. A tip vortex sheds off from the vortex generator convecting downstream hitting the rotor blade at the 180 degree azimuth angle in a parallel manner. Acoustics were recorded through six microphones (two near-field and five far-field). Four primary cases were considered in this validation study. Previously validation studies have considered the same cases, however, they have used an analytical model for the vortex in the simulations meaning the vortex is not captured in the simulation so it does not lose its strength or dissipate. The validation study conducted in this thesis work did not use an analytical model for the vortex. Rather the vortex is fully captured in the CFD simulation followed by the parallel BVI interaction with the rotor where the computed aerodynamic flowfield is used as input for the acoustics simulation. Comparison between the acoustic predictions and measured data showed overall good agreement including the width and amplitude of the resulting acoustic pulses for all four cases simulated. These results show that these high-fidelity computational models are capable of capturing the tip vortex roll-up and formation, vortex convection without excessive numerical dissipation, the correct physics for the vortex interaction with the rotor blade including boundary layer physics and impulsive aerodynamic loading on the rotor blade, and the propagation of the BVI acoustic signals from the rotor blade to the far field microphones.

9.1.2 SbS Rotor UAM Aircraft

High-fidelity CFD simulations were performed for the study of NASA's six-passenger SbS rotor UAM aircraft in hover. Helios, a high-fidelity, multi-disciplinary, and rotary-wing software suite from the U.S. DoD HPC Modernization Program (HPCMP) was used for the CFD simulations. The simulation of the acoustic predictions was conducted with the rotorcraft acoustic prediction tool, PSU-WOPWOP. Simulations of the SbS rotor UAM vehicle consisted of three related CFD studies:

1. Isolated SbS rotors (fuselage and rotor hubs not included) in free air.

2. Isolated SbS rotors (fuselage and rotor hubs not included) in-ground effect.

3. SbS rotors with the fuselage (including rotor hubs) in full configuration in free air.

It should be reiterated that in this work, broadband noise was not accounted for in the acoustic predictions and methodology. There is a possibility of the overall noise level of the SbS rotor UAM vehicle could be higher when factoring in broadband noise.

9.1.2.1 Isolated SbS Rotor in Free air

In the first study, as presented in Chapter 6, four overlap configurations: 0%, 5%, 15%, 25%, and five collective pitch angles: 4°, 6°, 8°, 10°, and 12° were considered in the study of the isolated SbS rotors in free air for the hover condition. The effect of the overlap between the intermeshing rotors was first examined, and it was found that the tip vortices break down quickly within the overlap region resulting in secondary worm-like structures. These intermeshing overlaps also reduce the distance between the rotors leading to a higher

induced velocity beneath the rotor plane. There was a clear reduction in the rotor normal force within the overlap region due to the impact from combined wakes from both rotor systems, inducing higher downwash velocities on the rotor blades. The amount of rotor overlap also showed apparent effects on FM compared to different collective pitch angle. FM was found to experience a significant increase ranging from 1% to 2% at low collective pitch angles with minimal increase of 0.5% experienced at high collective pitch angles.

Acoustics noise sources and their resulting signals from the SbS rotors were then investigated for all overlap configurations at a single collective pitch angle of 8°Ṅoise guidelines from Uber were used to investigate the effect of overlap on the acoustics of the SbS rotors. Noise events like rotor-to-rotor BVIs were identified as a significant source of noise when the rotor blades enter and exit the overlap region resulting in strong noise at even blade passage frequency harmonics. The 25% overlap configuration was found to have the highest noise level compared to other overlap cases due to strong rotor-to-rotor interactions that intensify as the percentage in rotor overlap increases. Acoustic interference was observed in cases with higher percentage of overlap including the 15% and 25% overlap configurations due to destructive interference in the acoustic pressure signals. Sources of the destructive interference were distinct between the 15% and 25% overlap cases showing discrete patterns in the noise directivity.

After completing the analysis of the noise characteristics for the SbS rotor, noise comparisons were not only made between each overlap configuration, but were also compared against data of various background noise including freeways, parks, communities, and rural areas. It was found that none of the overlap cases were able to meet Uber's guideline of 62 dBA at an altitude of 500 ft (152.4 m). As a result, community background noise won't

likely block out the noise generated by the SbS rotor.

9.1.2.2 Isolated SbS Rotor In-Ground Effect

Chapter 7 investigated the significance of the ground plane on the performance, aerodynamics, acoustics on the isolated SbS rotor configurations 0% and 25% overlap at two different heights above the ground plane, half rotor diameter (H = 0.5D) and one rotor diameter (H = 1D). Including the study on the influence of the ground plane, rotor overlap in conjunction with the presence of the ground plane, the effects on the performance and acoustics were investigated.

It was found that clearly the presence of the ground surface has a significant impact on the hover performance after comparing FM between the in- and out-of-ground effect cases of the 0% and 25% overlap configurations at both rotor heights. However, increase in FM was found to be larger for in-ground effect cases of the 0% overlap configuration than the 25% overlap configuration due to the effect of the rotor overlap. The higher increase in FM that is recognized for the 0% overlap cases is a result from the decrease in the induced velocity especially when the distance between the rotor disk plane and ground surface is greatly reduced. Reduction in the rotor height along with the having no rotor overlap results in a large amount of upwash generated. However, increase in the overlap percentage dominates the amount of upwash produced. Increase in the normal force was also observed in H = 0.5D cases of the 0% overlap configuration arises from having no rotor overlap resulting in a significant amount of upwash.

Interactions between the SbS rotor and the upwash especially in H = 0.5D cases with being closer to the ground surface increases the number of aerodynamic interactions including

rotor-to-rotor, rotor and upwash, rotor and wake, upwash and rotor wake, and rotor and tip vortices. The numerous aerodynamic interactions result in higher noise levels at all harmonics, however, it was observed that there is some benefit such as noise reduction due to having rotor overlap even when it is in close proximity to the ground plane.

As observed in the isolated SbS rotor cases in free air, acoustic interference was found in this study and identified as peaks and valleys located at certain observer locations that resulted in constructive (peaks) and destructive interference (valleys). Directivity patterns were also examined and considerable differences between the A-weighted and unweighted OASPL were found. Significant reduction in the peaks and valleys was found for majority of the in-ground effect cases with the exception of the A-weighted 25% overlap configuration at H = 1D near the exit region.

9.1.2.3 SbS Rotor in Full Configuration

In Chapter 8, the study of the SbS rotor in full configuration was conducted for all four overlap cases: 0%, 5%, 15%, and 25% in free air at an 8° collective pitch angle. Influence on the performance, aerodynamics, and acoustics due to the inclusion of the fuselage and rotor hubs was investigated. A substantial impact was observed from adding the fuselage in the rotor performance for each overlap configuration. The presence of the fuselage provides a partial ground effect for the two rotors and many of these full-configuration results for rotor performance and noise were consistent with those from the earlier ground effect studies. In particular, the presence of the fuselage resulted in a significant increase of the FM for the rotor blades, especially for configurations with little to no rotor overlap.

Induced velocity exhibited a significant increase in the 15% and 25% overlap configura-

tions which have a considerable amount of overlap subsequently having less upwash generated compared to the 0% and 5% overlap configurations, which in contrast showed a decrease in induced velocity in the overlap region and having a large increase in upwash flow. Close proximity to the overlap region showed increase in normal force for all overlap cases near mid-span of the rotor blade, however, cases with higher overlap percentage resulted in a reduction in normal force from mid-span and toward the blade tip due to higher induced velocity and less upwash flow. It was also found that the surface pressure across the support structure that span the fuselage and where the rotors are installed showed a considerable amount of unsteadiness which was more evident in the cases that hardly have any rotor overlap mainly because of increased upwash.

After identifying the aerodynamic interactions of the full configuration, the effect of the fuselage on acoustic was investigated. Blade-tip interactions with tip vortical structures were found to the most significant source of noise. These interactions occur when the blades enter and exit the overlap region, especially for the configurations with larger overlap percentages. Moreover, the presence of the fuselage resulted in more upwash flow being generated which led to more aerodynamic interactions between the rotor blades and the wake of the combined rotor system. Increase in aerodynamic interactions led to greater noise level even more so for overlap configurations having little to no overlap. As observed in the 0% and 5% overlap cases, where the noise spectrum can be seen in all harmonics of BPF, conversely the cases for the 15% and 25% overlap configurations, the noise spectrum is only exhibited at even harmonics which indicates the different noise characteristics covered in Chapter 8, Section 8.6.4. The 25% overlap configuration was found to have the lowest overall sound pressure level, demonstrating the advantages of rotor overlap for noise reduction. However, care must

be taken since a large percentage overlap can generate higher noise levels in cruise conditions. It should be reminded that, the isolated SbS rotor in free air study showed the highest of noise at the 25% overlap case. As exhibited in the investigation of the isolated SbS rotor in free air, similar strips in the noise directivity of the 15% and 25% overlap configurations are present in the study of the SbS rotor in full configuration. These strips, however, are not present in the 0% and 5% overlap cases due to the dominant source of noise being the interaction between the rotor blade and upwash flow, and not rotor-to-rotor BVI.

9.2 Research Contributions

This section highlights key contributions of this dissertation to the study of acoustics for multi-rotor configurations and UAM aircraft, more specifically, NASA's six-passenger SbS rotor UAM aircraft. This is the first research study to date on investigating the noise of the SbS rotor UAM aircraft in hover using high-fidelity CFD coupled with acoustics. Majority of other published research studies only conducted investigations in forward flight and without the fuselage or rotor hubs. The research study presented in this dissertation decomposed the SbS rotor UAM vehicle into three separate detailed investigations: isolated rotor, ground effect, and full configuration. The effect of the rotor overlap, ground surface, and fuselage on hover performance, aerodynamics, and acoustics including underlying flow physics were discussed in detail. Important noise sources were identified and analyzed for all four rotor overlap configurations at different collective pitch angles ranging from 4° to 12°. Characterization on the significance of each identified noise source were provided based on a first principles approach using high-fidelity CFD. This dissertation exhibited detailed analysis on the acoustics of the isolated SbS rotor in free air and in-ground effect, a full configuration, and comparisons against various urban background noise. Moreover, the methodology employed in this dissertation was validated against parallel BVI wind tunnel experiments that has a similar acoustic generation process as presented in the investigations of the SbS rotor UAM aircraft. Four cases from the experiment were simulated using the same high-fidelity coupled approach focused on the acoustics methods used for the SbS rotor study. Research findings presented in this dissertation provide an important foundation for the design and analysis of future multi-rotor UAM vehicles, particularly for configurations with intermeshing rotors.

9.3 Future Work Recommendations

Even though the studies include the effect of the rotor overlap, in-ground effect, and full configuration, there is still room for improvement. Recommendations for future research in UAM aircraft noise are discussed in this section. This would help further advance our understanding of multi-rotor configurations, intermeshing rotors, and UAM aircraft noise by considering other aspects that were not covered in this dissertation. Since only tonal noise was predicted in the acoustic study of this dissertation, it is recommended to develop, validate, employ an accurate prediction model for broadband noise not only to study the broadband noise profile of the SbS rotor configuration, but for other proposed or existing UAM aircraft as well. Across the UAM community, a wide variety of proposed configurations have multiple rotors including several with a small rotor radius with higher RPM. It is anticipated that the broadband noise for such a configuration will play a significant role in the overall noise level.

The acoustic methodology employed in the study of the SbS rotor UAM aircraft in full configuration, though it included the fuselage, did not include the effect of acoustic scattering. Exploring an approach with a permeable surface acoustic modeling simulation or acoustic scattering solvers, such as boundary element methods or equivalent source methods would be a useful extension to this work. All of these approaches aim to model acoustic scattering which is important to implement when performing acoustic predictions on the noise of the full vehicle for the SbS rotor UAM with different overlap configurations. Another useful study would be an investigation of the full configuration in forward flight including an analysis of the acoustics and comparisons of the effects of acoustic scattering at different flight conditions.

In addition, any future study of the SbS rotor UAM aircraft should include rotor and aircraft trim as opposed to the current study that used fixed collective pitch angles where all overlap configurations can potentially operate at different thrust levels. Finally, although a validation study was performed for a simple and canonical case in this dissertation, it is essential to perform a validation study against measured data for the SbS rotor configuration.

In terms of parallel BVI validations, detailed grid resolution studies can be performed. It would also be interesting to consider additional cases including near-field acoustic data, oblique BVIS, etc.

Appendix A

NASA SbS Rotor Blade Properties

The blade properties of NASA's six passenger hybrid SbS rotor UAM aircraft were presented here which are obtained from Johnson et al. [34, 35]. In this thesis work, the blades of the SbS UAM aircraft are assumed to be rigid. As shown in Figure A.1, the blade chord and twist distributions as a function of the nondimensional blade radial position. r_b, and nondimensionalized by the rotor radius, R, with the root cutout at 16% span location.

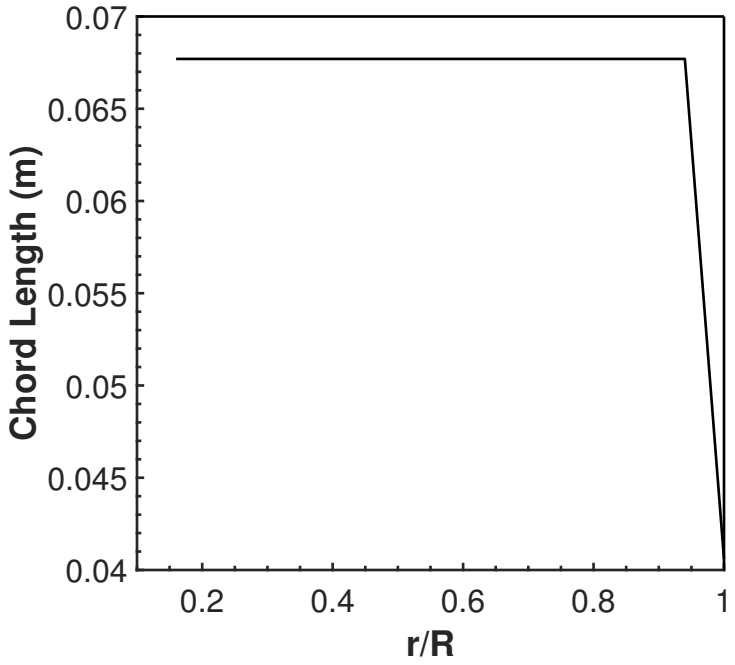

(a)

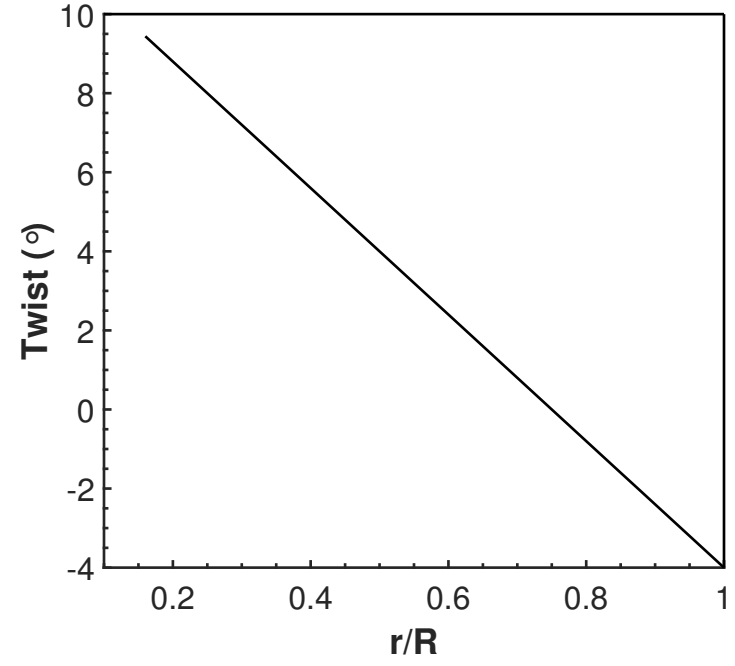

(b)

Figure A.1: Rotor blade properties of the six-passenger SbS UAM vehicle: (a) blade chord distribution and (b) blade twist distribution.

Appendix B

Overlap Fraction

Let $A_{ov} = mA$ [92] be the the overlap area, where d is the shaft separation distance as seen in Figure B.1 and the overlap fraction, m, is defined as:

$$m = \frac{2}{\pi}\left[\cos^{-1}\frac{d}{2R} - \frac{d}{2R}\sqrt{1-\left(\frac{d}{2R}\right)^2}\right] \tag{B.1}$$

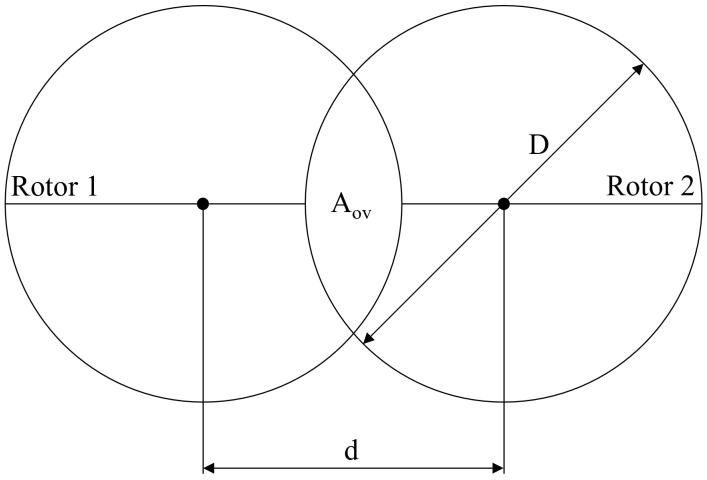

Figure B.1: Overlapping rotor geometry exhibiting the overlap area, A_{ov}. [16]

The projected area equation used in the combined rotors' calculations, $A_{proj} = A(2-m)$, accounts for the overlap of the rotors. This equation was also used in the previous studies of the SbS rotor configuration [37, 64].

Appendix C

FM Convergence

Figure C.1 shows the convergence of FM for four overlap conditions at five different collective angles as a function of rotor revolutions. It can be seen that the convergence is achieved between 9 and 10 rotor revolutions. However, an additional two rotor revolutions are added to make sure the forces and moments have fully converged. As the overlap and collective pitch angle increase, FM fluctuates. This is due to the variances of the thrust and torque that are influenced by the overlap of two rotors over the revolution. It should be noted that this oscillation may play a large role in vibration and acoustics, as studied in detail in the paper.

Using the projected area as the basis for the calculations offers a distinct advantage, as it represents the actual ground footprint area occupied by the overlapping rotors. For this reason, we use A_{proj} in FM, as well as in the thrust and torque coefficients. The equation to obtain the projected area is shown in the following section.

$$FM = \frac{T_{total}}{P_{total}} \sqrt{\frac{T_{total}}{2\rho A_{proj}}} \tag{C.1}$$

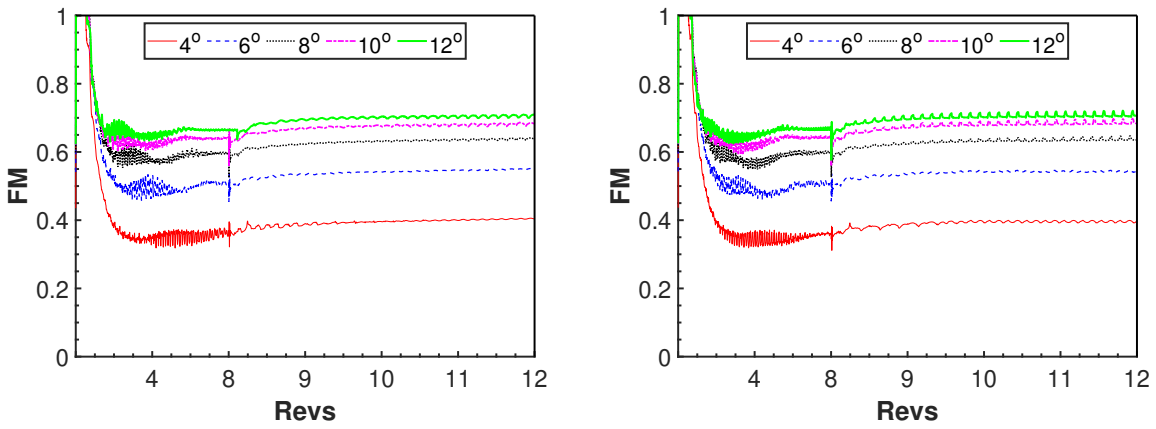

(a)

(b)

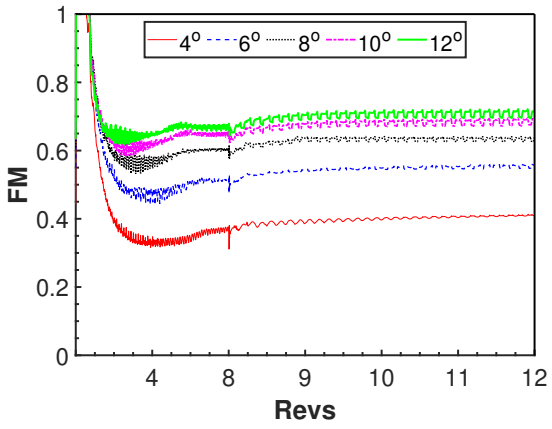

(c)

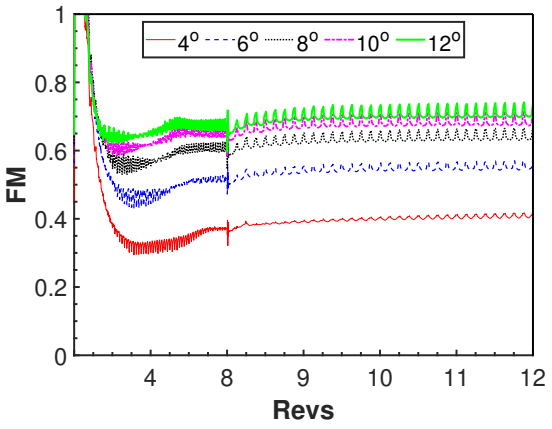

(d)

Figure C.1: Figure of merit convergence plots for all overlap cases and collective pitch: (a) 0% overlap, (b) 5% overlap, (c) 15% overlap, and (d) 25% overlap.

References

[1] Holden, J., and Goel, N., "Fast-Forwarding to a Future of On-Demand Urban Air Transportation," *Uber Elevate*, San Francisco, CA, 2016.

[2] Price, G., Helton, D., Jenkins, K., Kvicala, M., Parker, S., and Wolfe, R., "Urban Air Mobility Operational Concept (OpsCon) Passenger-Carrying Operations," *NASA CR-2020-5001587*, 2020.

[3] Greenwood, E., Brentner, K., Rau, R. F., and Gan, Z. F., "Challenges and Opportunities for Low Noise Electric Aircraft," *International Journal of Aeroacoustics*, Vol. 21, No. 5–7, 2022, pp. 315–381. doi:10.1177/1475472X221107377.

[4] Jia, Z., and Lee, S., "High-Fidelity Computational Analysis on the Noise of a Side-by-Side Hybrid VTOL Aircraft," *Journal of American Helicopter Society*, Vol. 67, No. 2, 2022, pp. 1–14(14). doi:10.4050/JAHS.67.022005.

[5] Johnson, W., and Silva, C., "NASA Concept Vehicles and the Engineering of Advanced Air Mobility Aircraft," *The Aeronautical Journal*, Vol. 126, No. 1295, 2021, pp. 59–91. doi:10.1017/aer.2021.92.

[6] Lee, H., and Lee, D., "Rotor Interactional Effects on Aerodynamic and Noise Characteristics of a Small Multirotor Unmanned Aerial Vehicle," *Physics of Fluids*, Vol. 32, No. 4, 2020, pp. 047107–1–047107–18. doi:10.1063/5.0003992.

[7] Zhou, W., Ning, Z., Li, H., and Hu, H., "An Experimental Investigation on Rotor-to-Rotor Interactions of Small UAV Propellers," AIAA Aviation Forum, National Harbor, MD, June 5–9 2017, AIAA Paper 2017-3744. doi:10.2514/6.2017-3744.

[8] Dingeldein, R., "Wind Tunnel Studies of the Performance of Multirotor Configurations," NASA TN 3236, 1954.

[9] Dekker, H., Ragni, D., Baars, W., and Fulvio, S., "Aerodynamic Interactions of Side-by-Side Rotors in Ground Proximity," *AIAA Journal*, Vol. 60, No. 7, 2022, pp. 4267–4277. doi:10.2514/1.J061105.

[10] Silva, W., C Johnson, and Eduardo, S., "Multidisciplinary Conceptual Design for Reduced-Emission Rotorcraft," *Proceedings of the American Helicopter Society Technical Conference on Aeromechanics Design for Transformative Vertical Flight*, San Francisco, CA, January 16–18, 2018.

[11] Radotich, M., "Conceptual Design of Tiltrotor Aircraft for Urban Air Mobility," *Proceedings of the VFS Aeromechanics for Advanced Vertical Flight Technical Meeting*, San Jose, CA, January 25–27, 2022.

[12] Ffowcs, W., and Hawkings, D. L., "Sound Generation by Turbulence and Surfaces in Arbitrary Motion," *Philosophical Transactions of the Royal Society A: Mathematical, Physical and Engineering Sciences*, Vol. 264, No. 1151, 1969, pp. 321–342. doi: 10.1098/rsta.1969.0031.

[13] Bretner, K., and Farassat, F., "Modeling Aerodynamically Generated Sound of Helicopter Rotors," *Progress in Aerospace Sciences*, Vol. 39, No. 2–3, 2003, pp. 83–120. doi:10.1016/S0376-0421(02)00068-4.

[14] Brentner, K. S., and Jones, H. E., "Noise Prediction for Maneuvering Rotorcraft," 6$^{\text{th}}$ AIAA/CEAS Aeroacoustics Conference, Lahaina, HI, June 12–14, 2000, AIAA Paper 2000-2031. doi:10.2514/6.2000-2031.

[15] Lee, S., Brentner, K. S., and Morris, P. J., "Long-Range and Nonlinear Propagation of Helicopter High-Speed Impulsive Noise," *Journal of American Helicopter Society*, Vol. 62, No. 2, 2017, pp. 1–10(10). doi:10.4050/JAHS.62.022007.

[16] Leishman, J. G., *Principles of Helicopter Aerodynamics*, Cambridge University Press, Cambridge, England, 2006, Chap. 2.

[17] Brooks, T. F., and Burley, C. L., "Blade Wake Interaction Noise for a Main Rotor," *Journal of American Helicopter Society*, Vol. 49, No. 1, 2004, pp. 11–17(17). doi: 10.4050/JAHS.49.11.

[18] Zawodny, N., Boyd, D., and Burley, C., "Acoustic Characterization and Prediction of Representative, Small-Scale Rotary-Wing Unmanned Aircraft System Components," *Proceedings of the 72nd Annual Forum of the American Helicopter Society*, West Palm Beach, FL, May 17–19, 2016.

[19] Intaratep, N., Alexander, W., and Devenport, W., "Experimental Study of Quadcopter Acoustics and Performance at Static Thrust Conditions," AIAA/CEAS Aeroacoustics Conference, Lyon, France, May–June 30–1, 2016, AIAA Paper 2016-2873. doi: 10.2514/6.2016-2873.

[20] Begault, D. R., "Ambient Noise Measurement for UAM Metric Analysis and Research," *Acoustics and Urban Air Mobility Technical Working Group Meeting*, Hampton, vA, 2019.

[21] Edwards, B., and Cox, C., "Revolutionary Concepts for Helicopter Noise Reduction – S.I.L.E.N.T. Program," NASA CR CR-2002-211650, 2002.

[22] Wissink, A. M., Jayaraman, B., Sitaraman, J., Roget, B., Lakshminarayan, V., Leffell, J., and Forsythe, J., "An Assessment of the Dual-Mesh Paradigm Using Different Near-Body Solvers in Helios," AIAA SciTech Forum, Grapevine, TX, May 9–13, 2017, AIAA Paper 2017-0287. doi:10.2514/6.2017-0287.

[23] Sitaraman, J., Jayaraman, B., Datta, A., Potsdam, M., Wissink, A. M., Jain, R., Adamec, S., and Abras, J., "Helios User Guide V.8.0," *Aviation Development Directorate*, 2016.

[24] Nichols, R., and Buning, P., "User's Manual for OVERFLOW," *NASA Langley*, 2018.

[25] Biedron, R. T., Carlson, J., Derlaga, J. M., Gnoffo, P. A., Hammond, D. P., Jones,

W. T., Kleb, B., Lee-Rausch, E. M., Nielsen, E. J., Park, M. A., Rumsey, C. L., Thomas, J. L., and Wood, W. A., "FUN3D Manual, Version 13.2," *NASA TM-2015-218761*, 2015.

[26] Lee, S., Bretner, K., Farassat, F., and Morris, P. J., "Analytic Formulation and Numerical Implementation of an Acoustic Pressure Gradient Prediction," *Journal of Sound and Vibration*, Vol. 319, No. 3–5, 2009, pp. 1200–1221. doi:10.1016/j.jsv.2008.06.028.

[27] Brentner, K. S., Brés, G. A., Perez, G., and Jones, H. E., "Maneuvering Rotorcraft Noise Prediction: A New Code for a New Problem," *Proceedings of the American Helicopter Society Aerodynamics, Acoustics, and Test and Evaluation Technical Specialist Meeting*, San Francisco, CA, January 13–25, 2002.

[28] Brès, G. A., Brentner, K. S., Perez, G., and Jones, H. E., "Maneuvering Rotorcraft Noise Prediction," *Journal of Sound and Vibration*, Vol. 275, No. 3, 2004, pp. 719–738. doi:10.1016/j.jsv.2003.07.005.

[29] Rohit, J., "Hover Predictions on the Sikorsky S-76 Rotor using Helios," AIAA SciTech Forum, National Harbor, MD, January 13–17, 2017, AIAA Paper 2014-0207. doi: 10.2514/6.2014-0207.

[30] Garcia, A., Colonia, S., and Barakos, G., "Accurate Predictions of Hovering Rotor Flows using CFD," AIAA SciTech Forum, Grapevine,TX, January 9–13, 2017, AIAA Paper 2017-1666. doi:10.2514/6.2017-1666.

[31] Garcia, A., and Barakos, G., "Accurate Predictions of Rotor Hover Performance at Low and High Disc Loadings," *Journal of Aircraft*, Vol. 55, No. 1, 2018, pp. 89–110. doi:10.2514/1.C034144.

[32] Healy, R., McCauley, J., Gandhi, F., and Sahni, O., "A Computational Examination of Side-by-Side Rotors in Ground Effect," *Journal of American Helicopter Society*, Vol. 68, No. 3, 2023, pp. 1–18(18). doi:10.4050/JAHS.68.032007.

[33] Smith, B., Healy, R., Gandhi, F., and Lyrintzis, A., "eVTOL Rotor Noise in Ground Effect," *Proceedings of the 77th Annual Forum of the Vertical Flight Society*, Virtual Event, May 10–14, 2021.

[34] Johnson, W., and Silva, C., "Observations from Exploration of VTOL Urban Air Mobility Designs," *NASA Seminar*, Moffett Field, CA, 2018.

[35] Johnson, W., Silva, C., and Eduardo, S., "Concept Vehicles for VTOL Air Taxi Operations," *Proceedings of the American Helicopter Society Technical Conference on Aeromechanics Design for Transformative Vertical Flight*, San Francisco, CA, January 16–18, 2018.

[36] Ventura Diaz, P., and Yoon, S., "High-Fidelity Computational Aerodynamics of Multi-Rotor Unmanned Aerial Vehicles," AIAA SciTech Forum, Kissimmee, FL, June 8–12, 2018, AIAA Paper 2018-1266. doi:10.2514/6.2018-1266.

[37] Ventura Diaz, P., Johnson, W., Ahmad, J., and Yoon, S., "The Side-by-Side Urban Air Taxi Concept," AIAA Aviation Forum, Dallas, TX, June 17–21, 2019, AIAA Paper 2019-2828. doi:10.2514/6.2019-2828.

[38] Ventura Diaz, P., Johnson, W., Ahmad, J., and Yoon, S., "Computational Study of the Side-By-Side Urban Air Taxi Concept," *Proceedings of the 75th Annual Forum of the Vertical Flight Society*, Philadelphia, PA, May 13–16, 2019.

[39] Jia, Z., and Lee, S., "Computational Study on Noise of Urban Air Mobility Quadrotor Aircraft," *Journal of American Helicopter Society*, Vol. 67, No. 1, 2022, pp. 1–15(15). doi:10.4050/JAHS.67.012009.

[40] Li, S., and Lee, S., "Prediction of Urban Air Mobility Multirotor VTOL Broadband Noise Using UCD-QuietFly," *Journal of American Helicopter Society*, Vol. 66, No. 3, 2021, pp. 1–13(13). doi:10.4050/JAHS.66.032004.

[41] Lee, S., Ayton, L., Bertagnolio, F., Moreau, S., Chong, P., and Joseph, P., "Turbulent Boundary Layer Trailing-Edge Noise: Theory, Computation, Experiment, and Application," *Progress in Aerospace Sciences*, Vol. 126, 2021, p. 100737. doi: 10.1016/j.paerosci.2021.100737.

[42] Jia, Z., and Lee, S., "Aeroacoustic Analysis of a Side-by-Side Hybrid VTOL Aircraft," *Proceedings of the 76th Annual Forum of the Vertical Flight Society*, Virtual Event, October 5–8, 2020.

[43] Caradonna, F. X., McCluer, M., Baeder, J., Leishman, J. G., Berezin, V. J., C, Bridgeman, J., Burley, C., Koustsavdis, E., Rahier, G., Delrieux, Y., Rule, J., and Bliss, D., "Methods for the Prediction of Blade-Vortex Interaction Noise," *Journal of American Helicopter Society*, Vol. 45, No. 4, 2000, pp. 303–317(15). doi:10.4050/JAHS.45.303.

[44] Kitaplioglu, C., Caradonna, F. X., and McCluer, M., "An Experimental Study of Parallel Blade-Vortex Interaction Aerodynamics and Acoustics Utilizing an Independently Generated Vortex," *NASA TM–1999-208790*, 1999.

[45] Strawn, R. C., Biswas, R., and Lyrintzis, A. S., "Helicopter Noise Predictions Using Kirchoff Methods," *Journal of Computational Acoustics*, Vol. 4, No. 3, 1996, pp. 321–339. doi:10.1142/S0218396X96000106.

[46] Leishman, J. G., "Aeroacoustics of 2-D and 3-D Blade Vortex Interaction Using the Indicia1 Method," *Proceedings of the 52nd Annual Forum of the American Helicopter Society*, Washington, D.C., June 4–6, 1996.

[47] Leishman, J. G., "Subsonic Unsteady Aerodynamics Caused by Gusts Using the Indicia1 Method," *Journal of Aircraft*, Vol. 33, No. 5, 1996, pp. 869–879. doi:10.2514/3.47029.

[48] Leishman, J. G., "Sound Directivity Generated by Helicopter Rotors Using Wave Tracing Concepts," *Journal of Sound and Vibration*, Vol. 221, No. 3, 1999, pp. 415–441. doi:10.1006/jsvi.1998.1992.

[49] Epstein, R. J., Rule, I. A., and Bliss, D. B., "A Novel Method for Calculating Two-Dimensional Blade Vortex Interactions," *AIAA Journal*, Vol. 35, No. 5, 1997, pp. 909–912. doi:10.2514/2.7466.

[50] Rahier, G., and Delrieux, Y., "Influence of Vortex Models on Blade-Vortex Interaction Load and Noise Predictions," *Journal of American Helicopter Society*, Vol. 44, No. 1, 1999, pp. 26–33. doi:10.4050/JAHS.44.26.

[51] Speigel, P., Rahier, G., and Michea, B., "Blade-vortex Interaction Noise - Prediction and Comparison with Flight and Wind Tunnel Tests," *ONERA TP-1992-126*, 1992.

[52] H, K., and Baeder, J. D., "Coupled Wake/CFD Solutions for Rotors in Hover," *Proceedings of the 52nd Annual Forum of the American Helicopter Society*, Washington, D.C., June 4–6, 1996.

[53] Bridgeman, J. O., Ramachandran, K., Caradonna, F. X., and Prichard, D., "A Computational Analysis of Parallel Blade-Vortex Interactions Using Vorticity Embedding," *Proceedings of the 50th Annual Forum of the American Helicopter Society*, Washington, D.C., May 11–13, 1994.

[54] Torok, M. S., and Berezin, C. R., "Aerodynamic and Wake Methodology Evaluation Using Model UH-60A Experimental Data," *Journal of American Helicopter Society*, Vol. 39, No. 2, 1994, pp. 21–29(9). doi:10.4050/JAHS.39.21.

[55] Baeder, J. D., and Srinivasan, G. R., "Computational Aeroacoustic Study of Isolated Blade-Vortex Interaction Noise," *Proceedings of the American Helicopter Society Aeromechanics Specialists Conference*, San Francisco, CA, January 19–21, 1994.

[56] Kitaplioglu, C., and Caradonna, F. X., "Aerodynamics and Acoustics of Blade-Vortex Interaction Using an Independently Generated Vortex," *Proceedings of the American Helicopter Society Aeromechanics Specialists Conference*, San Francisco, CA, January 19–21, 1994.

[57] Kitaplioglu, C., Caradonna, F. X., and Burley, C. L., "Parallel Blade-Vortex Interactions: An Experimental Study and Comparison with Computations," *Journal of American Helicopter Society*, Vol. 42, No. 3, 1997, pp. 272–281(10). doi:10.4050/JAHS.42.272.

[58] McAlister, K. W., and Takahashi, R. K., "NACA 0015 Wing Pressure and Trailing Vortex Measurements," *NASA TP 3151*, 1991.

[59] Chan, W. M., Pandya, S. A., Rogers, S. E., Jensen, J. C., Lee, H. C., Kao, D. L., Buning, P. G., Meakin, R. L., Boger, D. A., and Nash, S. M., "Chimera Grid Tools User's Manual," *NASA Ames*, 2018.

[60] Beam, R., and Warming, R. F., "An Implicit Finite-Difference Algorithm for Hyperbolic Systems in Conservation Law Form," *Journal of Computational Physics*, Vol. 22, No. 1, 1976, pp. 87–110. doi:10.1016/0021-9991(76)90110-8.

[61] Spalart, P. R., H, J. W., Strelets, M., and Allmaras, S. R., "Comments on the feasibility of LES for wings and on hybrid RANS/LES approach," Proceedings of the 1st AFOSR International Conference on DNS/LES, Columbus, OH, January 1997.

[62] Sagaga, J., and Lee, S., "CFD Hover Predictions for the Side-by-Side Urban Air Taxi Concept Rotor," AIAA Aviation Forum, Virtual Event, June 15–19, 2020, AIAA Paper 2020-2795. doi:10.2514/6.2020-2795.

[63] Leishman, J. G., and M, S., "Figure of Merit Definition for Coaxial Rotors," *Journal of American Helicopter Society*, Vol. 53, No. 3, 2008, pp. 290–300. doi: 10.4050/JAHS.53.290.

[64] Wright, S., and Cummings, H., "Pretest Comprehensive Analysis for the Urban Air Mobility Side-by-Side Test Stand," *Proceedings of the Vertical Flight Society Aeromechanics for Advanced Vertical Flight Technical Meeting*, San Jose, CA, January 25–27, 2022.

[65] Bodling, A., Schwarz, C., Wolf, C., and Gardner, A., "Numerical and Experimental Assessment of Parameters Influencing the Development of Secondary Vortex Structures in Rotor Wakes," *Proceedings of the 79th Annual Forum of the Vertical Flight Society*, West Palm Beach, Florida, May 15–18, 2023.

[66] Abras, J., Hariharan, N. S., and Narducci, R. P., "Wake Breakdown of High fidelity Simulations of a Rotor in Hover," AIAA SciTech Forum, San Diego, CA, January 7–11, 2019, AIAA Paper 2019-0593. doi:10.2514/6.2019-0593.

[67] Hariharan, N. S., Abras, J., and Narducci, R. P., "An Overview of Wake Breakdown in High-Fidelity Simulations ofRotor-in-Hover," *Proceedings of the 76th Annual Forum of the Vertical Flight Society*, Virtual Event, October 5–8, 2020.

[68] Abras, J., Narducci, R. P., and Hariharan, N. S., "Impact of High-Fidelity Simulation Variations on Wake Breakdown ofa Rotor in Hover," AIAA SciTech Forum, San Diego, CA, January 6–10, 2020, AIAA Paper 2020-0531. doi:10.2514/6.2020-0531.

[69] Poggi, C., Bernardini, G., Gennaretti, M., and Camussi, R., "Scalability of Mach Number Effects on Noise Emitted by Side-by-Side Propellers," *Applied Sciences*, Vol. 12, No. 19, 2022, p. 9507. doi:10.3390/app12199507.

[70] Carpenter, P. J., and Friedovich, B., "Effect of a Rapid Blade-Pitch Increase on the Thrust and Induced-Velocity Response of a Full-Scale Helicopter Rotor," NACA TN 3044, 1953.

[71] Li, S., and Lee, S., "Prediction of Rotorcraft Broadband Trailing-Edge Noise and Parameter Sensitivity Study," *Journal of American Helicopter Society*, Vol. 65, No. 4, 2020, pp. 1–14(14). doi:10.4050/JAHS.65.042006.

[72] Li, S., and Lee, S., "Acoustic Analysis and Sound Quality Assessment of a Quiet Helicopter for Air Taxi Operations," *Journal of American Helicopter Society*, Vol. 67, No. 3,

2022, pp. 1–15(15). doi:10.4050/JAHS.67.032001.

[73] Li, S., and Lee, S., "UCD-QuietFly: A New Program to Predict Multi-Rotor eVTOL Broadband Noise," *VFS Aeromechanics for Advanced Vertical Flight Technical Meeting*, San Jose, CA, January 20–23, 2020.

[74] Sagaga, J., and Lee, S., "Acoustic Predictions for the Side-by-Side Air Taxi Rotor in Hover," *Proceedings of the 77th Annual Forum of the Vertical Flight Society*, Virtual Event, May 10–14, 2020.

[75] Sagaga, J., and Lee, S., "Acoustic Predictions for Side-by-Side Air Taxi in Full Configuration," AIAA Aviation Forum, San Diego, CA, June 12–16, 2023, AIAA Paper 2023. doi:10.2514/6.2023-4522.

[76] Pettingill, N., and Zawodny, N., "Identification and Prediction of Broadband Noise for a Small Quadcopter," *Proceedings of the 75th Annual Forum of the Vertical Flight Society*, Philadephia, PA, May 13–16, 2019.

[77] Schiller, N., Pascioni, K., and Zawodny, N., "Tonal Noise Control Using Rotor Phase Synchronization," *Proceedings of the 75th Annual Forum of the Vertical Flight Society*, Philadephia, PA, May 13–16, 2019.

[78] Sarojini, D., Ruh, M., Joshy, A. J., Yan, J., Ivanov, A., Scotzniovsky, L., Fletcher, A., Orndorff, N., Sperry, M., Gandarillas, V., Asher, I., Chambers, J., Gill, H., Lee, S., Cheng, Z., Rodrigues, G., Zhao, S., Mi, C., Nascenzi, T., Cuatt, T., Winter, T., Guibert, A., Cronk, A., Kim, H., Meng, S., and Hwang, J., "Large-Scale Multidisciplinary Design Optimization of an eVTOL Aircraft using Comprehensive Analysis," AIAA SciTech Forum, National Harbor, MD, January 23–27 2023, AIAA Paper 2023-0146. doi:10.2514/6.2023-0146.

[79] Orndorff, N., Sperry, M., Scotzniovsky, L., Gill, H., Sarojini, D., Hwang, J., Lee, S., Cheng, Z., Zhao, S., and Mi, C., "Air-taxi Transition Trajectory Optimization Using Physics-based Aerodynamic, Acoustic, and Motor Models," AIAA SciTech Forum, National Harbor, MD, January 23–27 2023, AIAA Paper 2023-0324. doi:10.2514/6.2023-0324.

[80] Gill, H., Lee, S., Ruh, M., and Hwang, J., "Applicability of Low-Fidelity Tonal and Broadband Noise Models on Small-Scaled Rotors," AIAA SciTech Forum, National Harbor, MD, January 23–27 2023, AIAA Paper 2023-0324. doi:10.2514/6.2023-1547.

[81] Wei, P., Chan, S. N., Lee, S., and Kong, Z., "Mitigating Ground Effect on Mini Quadcopters with Model Reference Adaptive Control," *International Journal of Intelligent Robotics and Applications*, Vol. 3, No. 3, 2019, pp. 283–297. doi:10.1007/s41315-019-00098-z.

[82] Glauert, M. B., "The Wall Jet," *Journal of Fluid Mechanics*, Vol. 1, No. 6, 1956, pp. 625–643. doi:10.1017/S002211205600041X.

[83] Li, S., and Lee, S., "A Machine Learning-Based Fast Prediction of Rotorcraft Broadband Noise," AIAA Aviation Forum, Virtual Event, June 15–19, 2020,AIAA Paper 2020-2588. doi:10.2514/6.2020-2588.

[84] Li, S., and Lee, S., "Predictions and Validations of Small-Scale Rotor Noise Using UCD-QuietFly," *Proceedings of the Vertical Flight Society Technical Conference on Aeromechanics Design for Transformative Vertical Flight*, San Jose, CA, January 25–27, 2022.

[85] Lee, S., Ayton, L., Bertagnolio, F., Moreau, S., Chong, T. P., and Joseph, P., "Turbulent Boundary Layer Trailing-Edge Noise: Theory, Computation, Experiment, and Application," *Progress in Aerospace Sciences*, Vol. 126, 2021, p. 100737. doi: 10.1016/j.paerosci.2021.100737.

[86] Farassat, F., and Succi, G. P., "A Review of Propeller Discrete Frequency Noise Prediction Technology with Emphasis on Two Current Methods for Time Domain Calculations," *Journal of Sound and Vibration*, Vol. 71, No. 3, 1980, pp. 399–419. doi: 10.1016/0022-460X(80)90422-8.

[87] Farassat, F., "Derivation of formulations 1 and 1A of Farassat," *NASA TM–2007-214853*, 2007.

[88] Bodling, A., and Potsdam, M., "Numerical Investigation of Secondary Vortex Structures in a Rotor Wake," 2022, pp. 1–18(18). doi:10.4050/JAHS.67.042007.

[89] Karman, S., and Wyman, N., "Automatic Unstructured Mesh Generation with Geometry Attribution," AIAA SciTech Forum, San Diego, CA, January 7–11, 2019, AIAA Paper 2019-1721. doi:10.2514/6.2019-1721.

[90] Chaderjian, N. M., "Quantitative Approach for the Accurate CFD Simulation of Hover in Turbulent Flow," Proceedings of the 11^{th} International Conference on Computational Fluid Dynamics, Maui, HI, July 1–15, 2022.

[91] Sagaga, J., and Lee, S., "Acoustic Predictions for Side-by-Side Rotor with Ground Effect," *Proceedings of the 79^{th} Annual Forum of the Vertical Flight Society*, West Palm Beach, Florida, May 15–18, 2023.

[92] Johnson, W., *Helicopter Theory*, Princeton University Press, Princeton, NJ, 1980, Chap. 3.